INVESTIGATING THE INITIAL EVENTS OF IGE RECEPTOR SIGNALING BY SUPER-RESOLUTION MICROSCOPY AND COMPUTATIONAL MODELING

A Dissertation

Presented to the Faculty of the Graduate School

of Cornell University

in Partial Fulfillment of the Requirements for the Degree of

Doctor of Philosophy

By

Eshan David Mitra

August 2017

INVESTIGATING THE INITIAL EVENTS OF IGE RECEPTOR SIGNALING BY SUPER-RESOLUTION MICROSCOPY AND COMPUTATIONAL MODELING

Eshan David Mitra, Ph. D.
Cornell University 2017

The IgE receptor signaling system in mast cells is widely studied for its role in the allergic response, and as a model system for immune receptor signaling. In the present studies, we focus on the earliest events in the signaling cascade, in which antigen cross-links IgE receptors (IgE-FcεRI), forming clusters, which couple to the tyrosine kinase Lyn, a cytoplasmic protein anchored by fatty acyl chains to the inner leaflet of the plasma membrane. Biochemical techniques have suggested that the coupling between Lyn and FcεRI is mediated by membrane lipids. Modern microscopy and computational methods enable a more detailed study of these cell signaling processes at the nanoscale, allowing us to investigate the specific molecular events that are required for cell stimulation.

We use super-resolution fluorescence microscopy (PALM/STORM) to quantify the redistribution of IgE-FcεRI upon simulation with antigen. Using structurally defined trivalent ligands, built on rigid dsDNA scaffolds, we generate IgE-FcεRI clusters of a well-defined spatial configuration. We use PALM/STORM to quantitatively measure the size and density of clusters, and two-color PALM/STORM to measure the colocalization of Lyn and other membrane components with the clusters. We show that IgE-FcεRI clusters with a higher receptor density are more effective at recruiting Lyn, and stimulating downstream signaling events. Though the change in Lyn concentration is

small, it leads to cellular degranulation and other major functional consequences. In addition to the well-known mast cell responses, we describe a novel mechanism by which the activity of Lyn leads to an increase in IgE-FcεRI clustering, providing positive feedback on the signal initiation process.

We find lipid reorganization due to IgE-FcεRI clustering to be too subtle to detect in our PALM/STORM system, but using computational modeling in conjunction with previous work, we gain new insight to the role that lipids might play. Using the Ising model, we compute the binding energy for recruitment of a kinase into a receptor cluster, assuming that both proteins partition into the same membrane phase. We extend this model into a full phase diagram for membranes, computed using machine learning techniques, and examine how kinase binding energy depends on the phase state of the membrane. We predict a modest binding energy for membranes that exist as a microemulsion or near a critical phase transition, and a much larger binding energy if the membrane exists near a tricritical point.

Taken together, our results provide new, molecular-level insight about protein-mediated and lipid-mediated processes that contribute to the initiation of IgE-FcεRI signaling.

BIOGRAPHICAL SKETCH

Eshan Mitra was born August 13, 1990 in Rochester, New York. He graduated from Brighton High School in 2008, and went on to attend Brown University in Providence, Rhode Island. While at Brown, Eshan had his first research experience in the chemical biology lab of Sarah Delaney, studying the mechanism of DNA trinucleotide repeat expansion. Eshan completed his undergraduate degree in Chemical Biology, with additional coursework focused on mathematics and computer science. After graduating from Brown in 2012, Eshan moved to Cornell to begin in the graduate program in Chemistry and Chemical Biology. He joined the Baird-Holowka group, where he has spent the past five years on the project contained in the present volume.

Outside of the lab, Eshan is involved in writing comics, designing board and computer games, and writing and solving puzzles. His fifth major comic series, The Story of Salira, is scheduled for self-publication within the current year. His latest board game, Blob Battle, is as of this writing playable online at blobbattle.com .

Following his time at Cornell, Eshan will be starting a post-doctoral position with Bill Hlavacek at Los Alamos National Laboratory, on software development for systems biology applications.

ACKNOWLEDGEMENTS

I owe thanks to many people who have helped me to reach this point, and provided me with support throughout my five years in graduate school.

First, I would like to thank my advisors Barbara and Dave for the guidance they have provided in all of my work in the lab. They have been excellent mentors, and have been supportive during the difficult stretches of my graduate career. I would also like to acknowledge all of my colleagues in the Baird-Holowka group over the years: Sarah Shelby, Devin Wakefield, Lily Chylek, Marcus Wilkes, Alice Wagenknecht-Wiesner, Jordan Mohr, Roselynn Cordero, Meraj Ramezani, Arianna Gagnon, Nirmalya Bag, and Felix Chin. Special thanks to Sarah and Nirmalya, my fellow microscopists over the years, with whom I spent many days making the scope reliable enough to collect our data. And thanks to Jordan, Meraj, and Arianna, who led the effort to boost the lab's social activity during my later years in the group.

I have been fortunate to have excellent theoretical collaborators. Jim Sethna, the Sethna group, and Sam Whitehead have been great to work with on my theoretical projects, and also understanding of my limitations as only a part-time theorist.

I would like to thank my parents and my extended family for their unending support of my pursuit of higher education, including my decision to attend graduate school.

Lastly, I would like to thank all of my friends, from this setting and previous ones, who have been supportive during these difficult years of graduate school. Thanks to Cornell chemistry students and biophysics students, residents and friends of Perkins

House at Brown, and graduates from Brighton High School who have kept in touch all this time.

TABLE OF CONTENTS

LIST OF FIGURES

LIST OF TABLES

LIST OF ABBREVIATIONS

ADAP	Adhesion- and degranulation-promoting adaptor protein
AF488	Alexa Fluor 488
AF568	Alexa Fluor 568
AF647	Alexa Fluor 647
B1E3	An anti-IgE antibody
BLNK	B cell linker protein
BSA	Bovine serum albumin
BSS	Buffered salt solution
CD3	An anti-FcεRI antibody
cSMAC	Central supramolecular activation cluster
DAG	Diacylglycerol
DNA	Deoxyribonucleic acid
DNP	2,4-dinitrophenyl
dsDNA	Double-stranded DNA
dsRed	Discosoma red fluorescent protein
dSTORM	Direct STORM
Dy654	Dyeomics 654
EDTA	Ethylenediaminetetraacetic acid
EGFP	Enhanced green fluorescent protein
EMCCD	Electron-multiplying charge-coupled device
FACS	Fluorescence-activated cell sorting
FcεRI	High affinity IgE receptor
FFT	Fast Fourier Transform
FPALM	Fluorescence PALM
fps	Frames per second
FRET	Fluorescence (or Förster) resonance energy transfer
GBF	Gads binding fragment
GG	Geranylgeranyl

GPI	Glycosylphosphatidylinositol
GPMV	Giant plasma membrane vesicle
Grb2	Growth factor receptor-bound protein 2
GTPase	Guanosine triphosphatase
GUV	Giant unilamellar vesicle
HEPES	4-(2-hydroxyethyl)-1-piperazineethanesulfonic acid
IgE	Immunoglobulin E
IgG	Immunoglobulin G
IP3	Inositol trisphosphate
ITAM	Immunoreceptor tyrosine-based activation motif
kB	Boltzmann's constant
kT	Boltzmann's constant times temperature
LAT	Linker for activation of T cells
Ld	Liquid disordered
Lo	Liquid ordered
mEos	Monomeric Eos fluorescent protein
MIMODIS	3-(1-Methyl-1H-indol-3-yl-methylene)-2-oxo-2,3-dihydro-1H-indole-5-sulfonamide
mRFP	Monomeric red fluorescent protein
PALM	Photoactivated localization microscopy
PBS	Phosphate buffered saline
PIP2	Phosphatidylinositol 4,5 bisphosphate
PLCγ	Phospholipase C gamma
PM	Palmitoyl, myrisotyl
PTPα	Protein tyrosine phosphatase alpha
RBL	Rat basophilic leukemia
SH2	Src homology 2
SIM	Structured illumination microscopy
SLP-76	SH2 domain-containing leukocyte phosphoprotein of 76 kDa
SPT	Single particle tracking
ssDNA	Single-stranded DNA

STED	Stimulated electron depletion
STORM	Stochastic optical reconstruction microscopy
Syk	Spleen tyrosine kinase
TIRF	Total internal reflection fluorescence
Y16	Y-shaped trivalent ligand made from 16-base DNA oligonucleotides
Y16bi	Y-shaped bivalent ligand made from 16-base DNA oligonucleotides
Y46	Y-shaped trivalent ligand made from 46-base DNA oligonucleotides
Y46bi	Y-shaped bivalent ligand made from 46-base DNA oligonucleotides
YFP	Yellow fluorescent protein
ZAP70	Zeta-chain associated protein kinase of 70 kDa

CHAPTER ONE

INTRODUCTION

1.1 Signaling by the IgE-FcεRI receptor in mast cells

Biomedical Motivation

The high affinity immunoglobulin E (IgE) receptor (FcεRI) in mast cells and basophils is the molecular trigger for allergic inflammation as part of an immune response. Mast cell mediated allergies can present an inconvenience in the case of hay fever, or a more serious, even life-threatening risk in the case of asthma and anaphylaxis (1). The prevalence of allergies is widespread, with respiratory allergies affecting about 17% of children under age 18 in the United States, and food allergies affecting 5% and rising (2). To combat this growing health concern, there is a continuing effort to understand the biochemical mechanisms by which allergies are triggered, in order to inform the development of effective allergy treatments. At the fundamental level, this requires an understanding of the initial stages of signaling through the receptor, IgE-FcεRI.

Overview of signaling by IgE-FcεRI

FcεRI is a transmembrane receptor expressed in mast cells and basophils, consisting of one α, one β, and two γ subunits. The α subunit of FcεRI binds an IgE antibody that confers specificity to a particular antigen. Physiologically, an individual's serum contains IgE of numerous types, specific to antigens that the individual is allergic to, such as the allergens found in pollen or peanuts. The signaling proteins involved in this process have been characterized, reviewed in (3, 4). A stimulating antigen is

multivalent, binding to several IgE-FcεRI and creating a cluster of receptors. The first signaling partner to interact with the clustered IgE-FcεRI is the kinase Lyn. Lyn, a Src family tyrosine kinase anchored to the inner leaflet of the plasma membrane by acyl chains, is recruited to the IgE-FcεRI cluster, and phosphorylates cytoplasmic immunoreceptor tyrosine-based activation motifs (ITAMs) on the β and γ subunits of FcεRI. Following the initial coupling of Lyn to FcεRI, Lyn associates more stably to the phosphorylated β subunit by means of its Src homology 2 (SH2) domain. The activity of Lyn provides the binding site for the cytoplasmic tyrosine kinase Syk on the phosphorylated γ subunit (Fig. 1.1a). At the same stage, the Src family kinase Fyn activates a complementary signaling pathway (5–7), though our work focuses on the more canonical Lyn pathway.

Extensive studies of Lyn suggest that it plays a complicated role in mast cell signaling. Lyn clearly plays an activating role in the initial stages of signaling, enhancing phosphorylation of FcεRI (8, 9) and Syk (5, 8, 10). However, when tested for downstream degranulation responses, cells from Lyn-/- knockout mice tend to show an increased response (5, 10–12) (though a decreased response has also been observed (8)). This suggests Lyn also plays a regulatory role in the later stages of signaling.

Lyn is expressed at a relatively high level in mast cells, but can exist in different states of activity. When the C-terminal tyrosine 508 is phosphorylated, Lyn adopts a closed conformation in which its SH2 domain is inaccessible, making it unable to bind to FcεRI β. Dephosphorylation of tyrosine 508 favors an open state in which the SH2 domain is available, and phosphorylation of tyrosine 397 enhances the catalytic kinase activity (3, 13). The kinase Csk and phosphatase CD45 are thought to assist in the

Figure 1.1 Schematic of IgE-Mediated signaling. (a) Schematic of the initial events of IgE-FcεRI signaling. IgE-FcεRI is cross-linked by antigen, stimulating the recruitment of Lyn, and the recruitment and activation of Syk. These events occur within the Lo phase of the plasma membrane, represented as phospholipids with orange head groups and straight tails. (b) Schematic of more downstream events of IgE-FcεRI signaling. Activated Syk phosphorylates LAT, which facilitates the activation of subsequent signaling partners. Activation of PLCγ leads to Ca^{2+} mobilization and degranulation, while SLP-76 mediates the reorganization of actin and integrins.

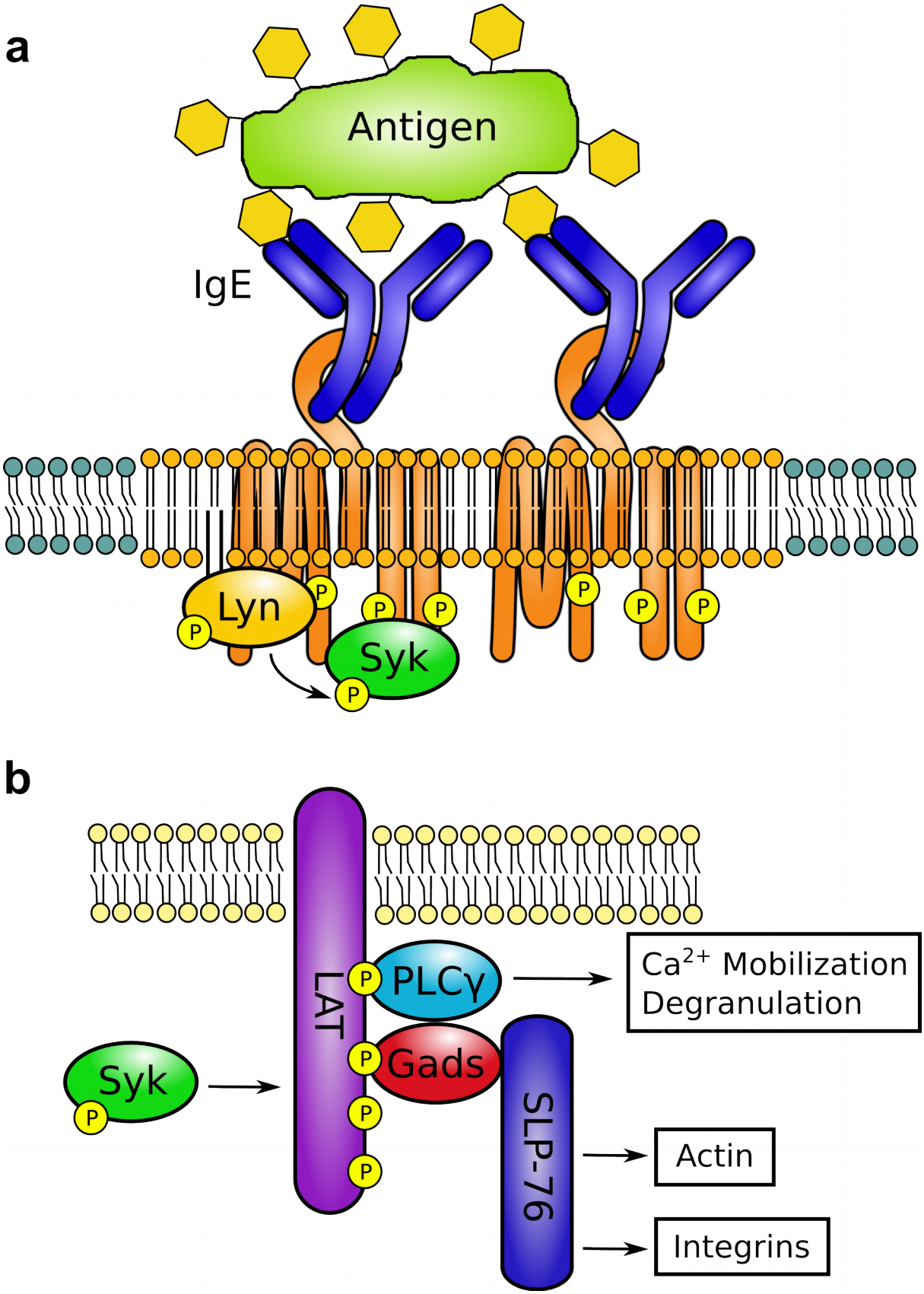
a
Antigen
IgE
Lyn
Syk
P
b
LAT
PLCγ
Gads
Syk
SLP-76
Ca2+ Mobilization
Degranulation
Actin
Integrins

interconversion between the active and inactive states (3). Theoretical work found that a low quantity of Lyn in the active state, relative to the number of receptors, was consistent with observed phosphorylation time courses (14, 15). We provide further insights on the role of Lyn in the present work.

The next stage of signal propagation (Fig. 1.1b) occurs at a transmembrane scaffold protein, the linker for activation of T cells (LAT) (reviewed in (16)). Activated Syk phosphorylates LAT at four key tyrosine sites (17). One of these sites serves as a docking site for phospholipase C γ (PLCγ). PLCγ exists as two isoforms, PLCγ1 and PLCγ2, both of which contribute to cell activation, but PLCγ1 is thought to be predominant (7, 18). Activated PLCγ is responsible for the hydrolysis of phosphatidylinositol 4,5 bisphosphate (PIP2) into the secondary messengers inositol trisphosphate (IP3) and diacylglycerol (DAG). IP3 promotes the increase in intracellular Ca^{2+} concentration by the process of store-operated Ca^{2+} entry, followed by degranulation, the release of inflammatory mediators stored in the cell's secretory lysosomes. A different phosphorylated site on LAT serves as the docking site for Gads. Gads binds to SLP-76, forming the start of a chain of signaling partners that link to the actin cytoskeleton (16). The connection between LAT and the actin cytoskeleton has been demonstrated in a reconstituted in vitro system (19). Another associator with SLP-76, ADAP, couples to integrins on the plasma membrane (16).

IgE-FcεRI as a Model System

Many questions about IgE-FcεRI signaling can be addressed using rat basophilic leukemia 2H3 (RBL-2H3) cells, a model mast cell line (20).

In addition to the specific biomedical applications for understanding IgE-FcεRI

signaling, the receptor serves as a useful model system for more general principles of cell biology. Many cell membrane proteins propagate an external stimulus into the cell by some form of clustering (21), and there are likely to be commonalities in the physical basis of these mechanisms. More specifically, FcεRI is a member of the immunoglobulin superfamily (22), which has other members found on other immune cells, including the T cell receptor on T cells and the B cell receptor on B cells. Subsequent signaling partners are homologous in all three cell types. In T cell receptor signaling, reviewed in (23), the Src family kinase Lck and cytoplasmic kinase Zap70 play the roles of Lyn and Syk respectively, while the LAT scaffold along with SLP-76 and Gads are common to both T cells and mast cells. In B cell receptor signaling, reviewed in (24, 25), Lyn and Syk play the same roles as in mast cells, while the cytosolic scaffold protein BLNK plays a similar role to LAT, in that it recruits PLCγ and Grb2. Therefore, a model for signaling in mast cells has important broader applications, providing insight into the function of related immune signaling processes, and also more general features of cell signaling through membrane receptors.

1.2 Super-resolution fluorescence microscopy

Overview of Fluorescence Localization Microscopy

A long-standing challenge in studying cellular processes including IgE-FcεRI signaling is the resolution limit of conventional fluorescence microscopy, which is bound by the diffraction limit. A point source of light in a sample appears in an image as a point-spread function of finite size. The diameter (full width at half maximum) of the point-spread function is roughly equal to the wavelength of the light divided by twice the

numerical aperture of the microscope objective (26). With typical fluorophores and objectives, this width is at least 200 nm. As a result, structures with a typical size of under 200 nm, including IgE-FcεRI receptor clusters, cannot be imaged quantitatively with fluorescence microscopy.

Starting in 2006, several related super-resolution microscopy techniques were developed that used photo-switching and single-molecule localization to escape the diffraction limit. These included photoactivation localization microscopy (PALM) (27), stochastic optical reconstruction microscopy (STORM) (28), fluorescence PALM (FPALM) (29), and direct STORM (dSTORM) (30). The class of techniques is more generally referred to as PALM/STORM. These techniques are all based on the same optical principles, but differ in the types of dyes used – fluorescent proteins in the case of PALM/FPALM and organic dyes in the case of STORM/dSTORM – and in how the required photochemical behavior of dyes (photo-switching) is achieved. In all cases, the sample is subjected to conditions such that almost all of the fluorescent probes are in a non-fluorescent dark state, leaving a few spatially isolated fluorescent molecules. For each isolated molecule, the entire point-spread function is isolated in the image. The point-spread function is fit, such as with a two-dimensional Gaussian, to give a precise localization of the molecule. Over the course of imaging, fluorophores stochastically “blink” on and off, allowing for the acquisition of more localizations, and with sufficient imaging time, a well-sampled super-resolved image is reconstructed (Fig. 1.2a). The best-case resolution of the image depends on the number of photons collected per localization in order to generate a high quality point-spread function; specifically, it is the diffraction limit divided by the square root of the number of photons. In practice, typical

Figure 1.2 PALM/STORM imaging and analysis. (a) Schematic of STORM imaging. In a simulated diffraction-limited TIRF image, the image is too blurred to discern the high-resolution detail. In each frame of STORM imaging, a small number of fluorophores are turned on, and those fluorophores are precisely localized. After acquiring a sufficient number of frames, a high resolution image is reconstructed from the localizations. (b) Schematic of calculating an autocorrelation function to quantify a PALM/STORM image. To calculate the autocorrelation function g(r) at radius r with a bin size of dr, a disc of radius r and width dr is drawn around a probe, as shown, and the density of probes within that disc is computed. This process is repeated, centered at each probe in the image, and the average density among all of these discs is computed. This average is divided by the bulk density of the entire region of interest (green polygon) to give the value of g(r). g(r) will have a value greater than 1 if the image contains clusters of size r or larger. Note that in practice, g(r) is computed by a more efficient algorithm than described here, through the use of fast Fourier transforms.

a

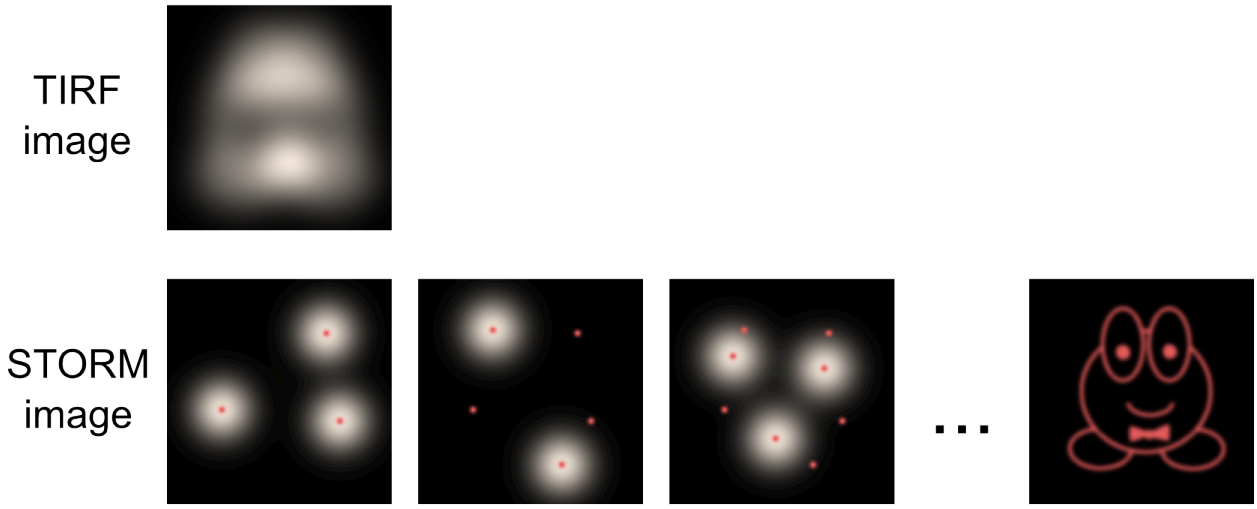

b

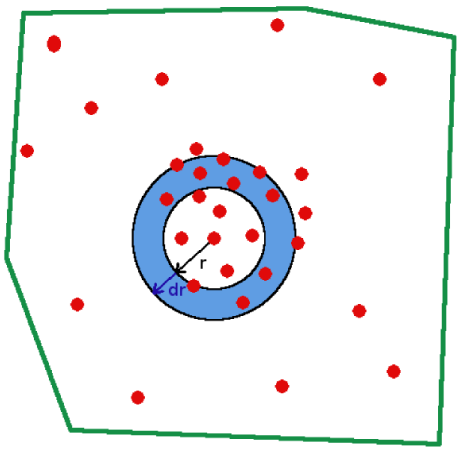

$$g(r) = \frac{\langle \text{density at radius } r \rangle_{probes}}{\text{bulk density}}$$

PALM/STORM resolution is ~ 20-30 nm, roughly a tenfold improvement upon the diffraction limit.

For imaging of the membrane, PALM/STORM is commonly used in conjunction with total internal reflection fluorescence (TIRF) (31), which confines the illumination to an evanescent field within ~ 100 nm of the cover glass surface. This is sufficient to illuminate the ventral membrane of a cell on a glass slide, while reducing background fluorescence coming from the cell interior. For other applications, three-dimensional PALM/STORM has also been achieved (32).

Technical advancement of PALM/STORM

Since the inception of PALM/STORM over a decade ago, there has been great interest in the technique, which has led to numerous innovations that improve upon it.

There has been a great effort to improve the time resolution of PALM/STORM, typically a weakness of the technique due to the requirement to collect many frames of raw data per reconstructed image. The earliest PALM/STORM images published were limited to chemically fixed samples, while localization-based microscopy on live samples could be done with single particle tracking (SPT) (33), measuring long diffusion trajectories for a smaller number of particles. The two approaches have been combined (SPT-PALM) (34) to obtain a large number of short trajectories from a single sample, in a data set containing both spatial and dynamic information. New analysis approaches such as multi-emitter fitting (35–37) and time-resolved cross-correlation (38) continue to push the temporal resolution limit of PALM/STORM.

The high-resolution information provided in a PALM/STORM image has led to the need for quantitative analysis methods for reliable interpretation. Frequently, these

include the quantification of protein clusters within images. One class of approaches uses cluster finding algorithms (39, 40) to explicitly label clusters within the image. A second approach calculates the value of a function for the image as a whole, such as Ripley's K function (41) or a pair correlation function (42), and extracts from the function parameters that quantify structural properties of the average cluster. In the present studies, our analysis method of choice is the pair correlation function (Fig. 1.2b). This has the advantage over cluster finding algorithms in that it gives an unbiased quantification of the image, relying on no user-defined parameters. In addition, as an advantage over Ripley's K function, the correlation function can be fit to an exponential function with parameters that intuitively relate to structural features of the clusters in the image: The y-intercept gives the average cluster density, the decay length gives the average cluster radius, and the integral is proportional to the average number of probes per cluster. The correlation function is therefore a useful and unbiased method to quantify the spatial organization of clusters in PALM/STORM images.

When performing quantification of one-color PALM/STORM images, there is always the concern of over-counting (43). If single labeled molecules are localized multiple times over the course of a PALM/STORM experiment, due to blinking off and on during the imaging time necessary to reconstruct one image, it gives the false appearance of clusters. Photochemically, this is unavoidable; there are no available dyes that reliably go through a single “on” cycle, then turn off permanently without further blinking. Some strategies have been suggested for over-counting correction during analysis (42, 44, 45). In practice, it often is more useful to simply analyze results with over-counting in mind, as the dye-specific parameters required for an accurate

over-counting correction can be difficult to estimate. A sample that is close to unclustered, such as IgE-FcεRI on an unstimulated cell, gives some baseline level of autocorrelation, and other samples can be evaluated in comparison to that control. A better, but more technically demanding approach is to assess clustering by two-color colocalization. Two populations of the protein of interest labeled in different colors will colocalize only if there is true clustering of the protein, regardless of over-counting (42). In our studies, we make use of both the one-color and two-color methods, addressing specific issues of over-counting.

There is a large interest in performing multicolor PALM/STORM (46) to eliminate issues of one-color over-counting, and also to simultaneously visualize multiple species within the cell. Multicolor PALM/STORM has been achieved through simple splitting of channels (46), and more recently by ratiometric measurements between channels (47) or by collecting the full spectrum of each molecule (48). These techniques are potentially very powerful in observing interactions between molecular species at high resolution. However, they come with new technical challenges including the precise alignment of channels to within the resolution of the technique, as well as issues of cross-talk between color due to bleed-through of fluorescent signal (49) or an impurity in one of the dyes used (50). The latter concerns about channel cross-talk are only recently becoming understood.

The contribution of PALM/STORM to the imaging field

PALM/STORM has an important place in this era of rapidly advancing microscopy techniques. Compared to other fluorescence-based techniques, PALM/STORM has the highest possible x-y spatial resolution, with moderate time resolution. There is also

moderate concern of sample integrity with the high laser power and reducing buffer conditions necessary for the technique. Structured Illumination Microscopy (SIM) (51) and Lattice Light Sheet microscopy (52) trade off some spatial resolution for greatly improved temporal resolution and non-damaging imaging conditions very suitable for use on cells in their native environment. Stimulated electron depletion (STED) microscopy (53) offers comparable spatial resolution to PALM/STORM and better temporal resolution than PALM/STORM, at the cost of higher, more disruptive laser powers.

PALM/STORM provides information that is useful in specific contexts, and is often complementary to data provided by other advanced microscopy techniques. The technique's strengths make it especially suited to study our biological system of interest consisting of clustering IgE receptors on the plasma membrane. PALM/STORM in TIRF is well-suited for imaging of the ventral membrane, where axial resolution less of a concern. Moreover, the ultra high resolution of PALM/STORM is valuable for characterizing IgE-FcεRI clusters, which can be even smaller than SIM or lattice light sheet resolution. PALM/STORM stands to provide data on IgE-FcεRI that are distinct from other techniques, and useful in combination with other techniques to gain insight on IgE-FcεRI signaling.

1.3 Lipid Phase Separation in Cell Signaling

Membrane Domains are Important in Cell Signaling

Accumulating evidence supports the role of lipid domains in the initial stages of cell signaling. Lipid phase separation can be clearly seen on a macroscopic scale in

giant unilamellar vesicles (GUVs): model membranes of defined composition, consisting of two or three types of phospholipid molecules along with cholesterol. The liquid ordered (Lo) phase is enriched in cholesterol and in a higher melting point phospholipid with saturated fatty acyl chains, while the liquid disordered (Ld) phase is enriched in the lower melting point phospholipid with unsaturated fatty acyl chains. Phase diagrams have been studied for three- (54, 55) and four-component (56) GUVs. Depending on temperature and composition, the vesicles can be macroscopically (micron-scale) phase-separated, mixed in a single disordered phase, or nanoscopically phase-separated, with domains that are detectable by FRET or neutron scattering, but not optically resolvable.

It is thought that analogous Lo-like and Ld-like lipid phases exist on the plasma membrane of cells, though at a smaller length scale than is found on macroscopically phase-separated model membranes. Lo-like membrane domains are often called lipid rafts, but the term remains controversial, in part due to ambiguity in its definition. For the purposes of this work, we use the physical definition suggested in (57): lipid rafts are Lo-like membrane domains, enriched in cholesterol and lipids with saturated acyl chains including sphingolipids, with sizes ranging 10 to 200 nm. We add to this a functional definition, that the function of the membrane domains is to colocalize membrane proteins of similar lipid phase preference, or separate those of different phase preference. The function of lipid rafts has important implications for cell signaling: The cell can harness this mechanism to bring together proteins that are necessary for a particular signaling process. The notion that membrane composition affects cell signaling exists for many cell types (58). Lipid domains are proposed to play important

roles in triggering of T cells (59) and B cells (60), as well as in non-immunological processes such as the localization of isoforms of the GTPase Ras (61).

The lipid raft hypothesis (58, 62) has been studied in depth for IgE-mediated signaling in mast cells (63). Initial evidence included the coalescence of large, optically resolvable domains when cells were cooled below room temperature (64). Resistance to solubilization by detergent was another early biochemical readout for localization to Lo domains (65). Though concerns have arisen about the exact interpretation of the assay (66), partitioning to detergent resistant membranes remains one piece of evidence suggesting a protein is likely to prefer Lo membrane (67). In RBL mast cells, IgE-FcεRI, upon cross-linking with stimulating antigen, has an increased partitioning into detergent resistant membranes (68), and Lyn also partitions into detergent resistant membranes (69). As Lyn is anchored to the membrane by saturated palmitoyl and myristoyl chains, this partitioning is not surprising. PTPα, a phosphatase that dephosphorylates FcεRI, was found to be excluded from detergent resistant membranes (70). This led to a model in which clustered IgE-FcεRI stabilizes a Lo-like domain that recruits Lyn and excludes PTPα (63). A theoretical reaction network model based on this picture was developed and found consistent with experimental phosphorylation results (71). Phase separation is also seen in giant plasma membrane vesicles (GPMVs) extracted from the membranes of cells, and considered a more realistic representation of the cell membrane's composition, compared to GUVs. However, observations of GPMVs found that both IgE and Lyn colocalize with a Ld probe (72). Patterned ligand surfaces have been another useful tool for analysis of IgE clusters by artificially forming large clusters of an optically resolvable (micron-scale)

size. This showed the recruitment of both an ordered membrane probe and a disordered membrane probe to IgE clusters, leaving the membrane's phase properties unclear (73). Electron Spin Resonance experiments, on cells and cell membrane derived preparations, support the existence of Lo and Ld phases on the plasma membrane (74). Most recently, two-color PALM/STORM experiments showed a more clear enrichment of a Lo probe but not an Ld probe in proximity of IgE receptor clusters (75). In summary, lipid redistribution in mast cells, and its effect on the coupling of kinase to the receptor, appears to be a subtle process, detectable by some but not all of the previously attempted methods. The model of lipid-mediated coupling between IgE-FcεRI and Lyn is compelling, but remains controversial, and demands further work with modern technology and a solid theoretical framework to more directly examine the model.

The physical basis of membrane domains

While there is general agreement that membrane heterogeneity exists in some form, supported by vast experimental data on mast cells and other cell types, the physical basis of membrane heterogeneity remains a subject of wide-ranging debate. Some examples of proposed models and their limitations are reviewed in (76); a consensus has been difficult to achieve due to the limited number of methods available to measure features at the nanoscopic length scale, and difficulty in reconciling various types of data collected on different cell types. Some have suggested that protein islands, stabilized by purely protein-protein interactions, are a driving force behind membrane heterogeneity, in addition to, or instead of, lipid composition (77, 78). There is additional support for a role of the cortical actin cytoskeleton in organizing the

membrane (further discussed below). Even within the scope of membrane heterogeneity arising purely from lipid composition, there is a large diversity of opinion. Estimates vary on the size of Lo-like domains, their persistence time, percent coverage of the membrane, as well as which plasma membrane molecules are part of Lo domains (76, 79).

Another open question is how the phase behavior of membrane lipids might lead to the reported properties of Lo domains. To this end, one attractive explanation is the proximity of the membrane to a critical phase transition (80, 81). A critical phase transition, reviewed in (81) in the context of membranes, occurs at a critical point within the phase diagram, at a particular critical temperature and membrane composition. At the critical point, two phases (Lo and Ld) become identical: the order parameter that distinguishes each phase (e.g. the percentage of ordered-like lipids they contain) converges to the same value (e.g. 50%) for both phases. Since the two phases are near equivalent, thermal fluctuations in energy are sufficient to tip regions of the system from one phase to the other. As a result, just above the critical temperature, one sees the two phases interleaved and fluctuating, with long length-scale domains of both phases present. Fluctuating domains consistent with a critical point have been observed in giant plasma membrane vesicles extracted from RBL cells (Fig. 1.3 a-b) (82).

If the plasma membrane indeed exists near a critical point, it becomes possible to gain new theoretical insights. Universality in statistical mechanics states that any critical point within the same universality class (i.e. having the same scaling exponents on physical quantities as the critical point is approached) exhibits the same universal properties, independent of the molecular details of how that phase transition is

Figure 1.3 Critical and first order phase transitions. (a) A giant plasma membrane vesicle (GPMV) extracted from an RBL cell membrane undergoes a critical phase transition. At the transition temperature, large, fluctuating domains are visible. (b) A synthetic giant unilamellar vesicle (GUV) that does not have the correct composition to pass through a critical point. It instead undergoes a normal, first-order phase transition. At its transition temperature, no fluctuating domains appear. Panels a and b are reproduced from reference (82).

(c) The Ising model is used as a model for a critical phase transition. As it goes through a critical phase transition, the Ising model shows fluctuating domains, similar to (a). (d) At a different set of parameters, the Ising model goes through a first order phase transition, as in (b).

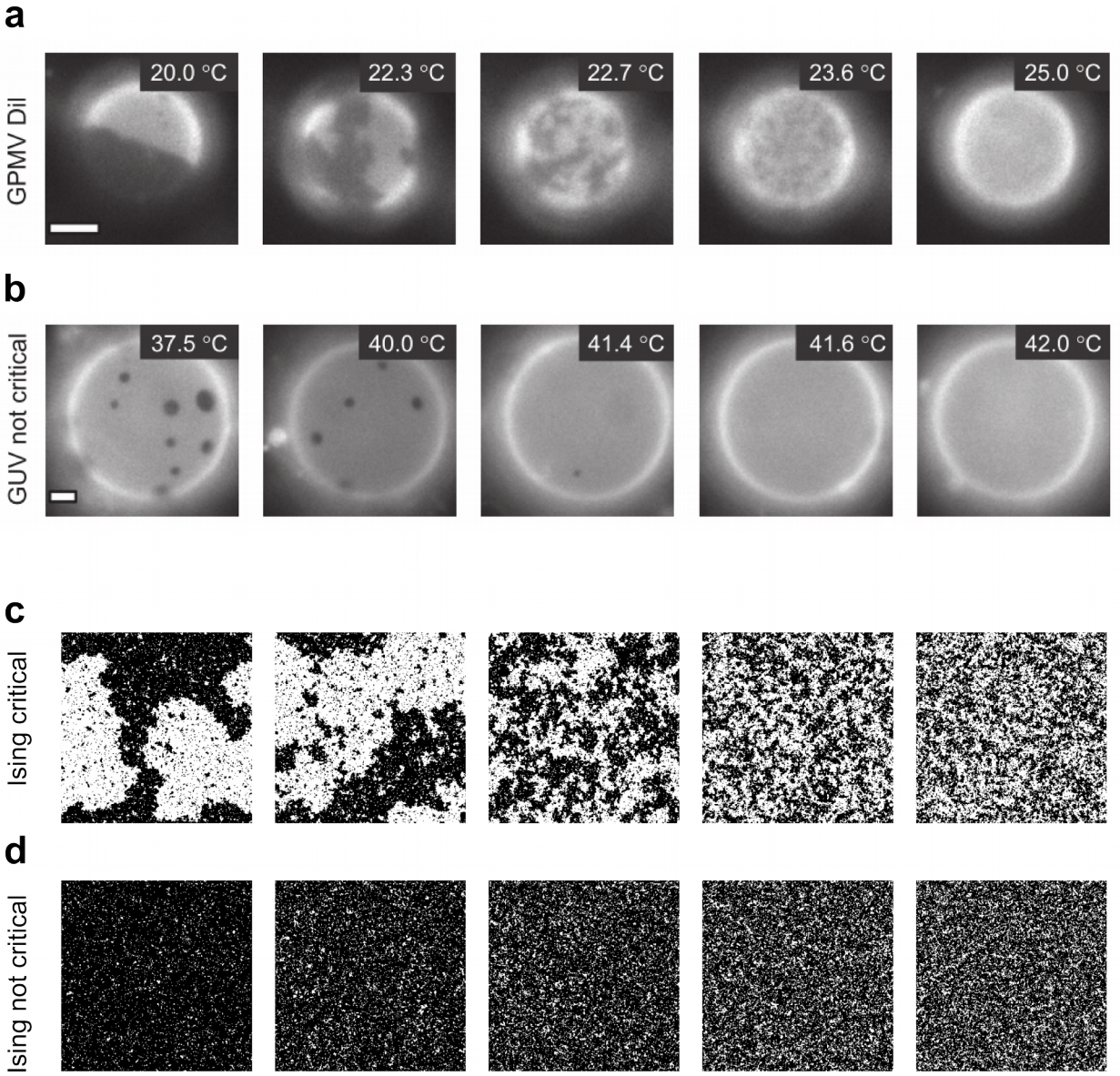
a
GPMV DiI
20.0 °C
22.3 °C
22.7 °C
23.6 °C
25.0 °C
b
GUV not critical
37.5 °C
40.0 °C
41.4 °C
41.6 °C
42.0 °C
c
Ising critical
d
Ising not critical

achieved. In the case of membranes, the universality class is that of the two-dimensional Ising model. This suggests that the 2D Ising model should be useful in for modeling the physics of the membrane (see *Modeling Lipid Phase Separation*, below).

An alternate hypothesis to the critical point is the presence of more stable nanodomains (54, 83, 84). These small domains of a particular characteristic size would be distributed over a background consisting of the second phase. It might be possible for this to occur on a kinetically trapped membrane that thermodynamically would be phase-separated (81). More frequently (e.g., (54)), it is suggested that the nanodomains are thermodynamically stable. In this case, the membrane is a microemulsion (81). Some new energetic interaction is required to stabilize the nanodomains of a microemulsion at a particular size: In theoretical membrane models, microemulsions can be generated in the presence of an amphiphilic species (85), or by including an energetic contribution due to membrane curvature (86, 87). The latter was also able to reproduce a modulated phase state found experimentally in model membranes (86). Dipole-dipole repulsion has also been proposed for stabilizing small domains (88). Microemulsions, or nanodomains are widely proposed, more often than the critical point, and are more consistent with the conventional depiction of lipid domains. Sometimes in discussion of lipid domains, a microemulsion-like picture is assumed implicitly. For example, experimental evidence of confined diffusion, assuming that confinement is solely lipid-mediated, is consistent with a microemulsion but not a critical point (80). Another argument for microemusions is that they are easier to achieve than a critical point. While a critical point has co-dimension 2 in the phase diagram (i.e. a single point in a 2D phase diagram or a line in a 3D phase diagram), microemulsions potentially

cover a larger region of phase space (85, 87). The microemulsion would therefore require less fine-tuned manipulation of lipid composition by the cell to maintain the correct phase state, and is in this sense, a simpler way to achieve nanoscopic membrane heterogeneity.

The actin cytoskeleton could additionally play a role in controlling the size of lipid domains. In a widely proposed model, the cortical actin meshwork couples to the plasma membrane, restricting diffusion of membrane proteins and potentially directing lipids of a particular phase preference to the location of the meshwork (89). This has been studied theoretically in combination with the Ising model (90), showing that actin-mediated partitioning can lead to nanoscopic domain sizes, even under conditions that would otherwise be completely phase-separated. This model has been validated in *in vitro* experiments (91). It has also been suggested that active remodeling of cortical actin could in turn remodel membrane domains (92). In the context of mast cells, studies with patterned surfaces (73) found that actin plays a complicated set of roles: Actin was recruited to sites of micron-sized IgE clusters, while inhibition of actin polymerization reduced Lyn recruitment to below the detection limit, but increased FcεRI phosphorylation. More recently by PALM/STORM, it was observed inhibition of actin polymerization leads to an increased colocalization of both Lyn and a label for ordered membrane with IgE clusters, suggesting that actin sequesters a reservoir of order-preferring components (75). Thus, the cortical actin cytoskeleton adds a further layer of complexity to the lipid phase behavior that exists in the membrane.

The diversity of hypotheses on the physical chemistry of membrane domains: critical points, microemulsions, or even phase-separated states partitioned by other

means like the cytoskeleton, creates the need for new experimental and theoretical approaches to evaluate and distinguish between them.

Modeling Lipid Phase Separation

Because plasma membrane domains exist on length and time scales that remain challenging to access experimentally, theoretical modeling and computational simulations are powerful complementary tools to address questions about membranes. Computational studies of membranes typically fall into two classes: molecular dynamics and Monte Carlo simulations. Molecular dynamics simulations (93, 94) explicitly model the molecules that make up the membrane, atomistically or with coarse graining (95), and apply classical mechanics to propagate the system in femtosecond time steps. This is a powerful tool, providing a molecular-level picture of lipids in a membrane, even one with physological composition (96). However, molecular dynamics is computationally expensive, limited to ~ millisecond time scales in the best case on a supercomputer (94). Properties pertaining to longer time scales, like phase separation and thermodynamic quantities, are inaccessible.

Monte Carlo simulations, such as in the present work, omit much of the molecular detail, instead working with a simplified model that still encompasses key physical properties of the membrane. This is an especially powerful approach for a critical phase transition, where, by universality, a simple two-dimensional Ising model has the essential properties of the critical phase transition (Fig. 1.3 c-d). The Ising model consists of a square lattice with white and black pixels, which, in the application to membranes, represent molecules preferring the Lo and Ld phases, respectively. This model is very simple compared to a real membrane, as it consists of only two types of

molecules, but, by universality, exhibits the same phase transition physics as are proposed for real membranes. Monte Carlo simulations of the Ising model are straightforward and efficient to run, and provide an ensemble of thermodynamically probable snapshots. Established methods can use such snapshots to calculate differences in free energy among conditions of interest (97, 98). Previous work has used the Ising model in membranes to predict protein-protein forces (99) and protein localization (75, 100).

Moreover, the Ising model and related models have been widely studied in statistical mechanics, allowing many predictions coming from theory alone. The two-dimensional Ising model has been solved exactly (101). Several relevant extensions on the Ising model have been described. The Blume-Capel (102, 103) and Blume Emery Griffiths (104) models add a third type of pixel, which could represent molecules of an intermediate phase preference. While these lack exact solutions, they are well characterized by finite size scaling (105, 106) and renormalization group (107) methods. Some Ising-like lattice models have also included surfactants, giving phase diagrams that include microemulsion states (85, 108, 109). In the present work, such extended models prove useful in bridging the differences between critical point, microemulsion, and other models of membrane phase separation.

1.4 Scope of this thesis

In this work, we apply super-resolution imaging and theoretical modeling to study the initial stages of IgE-mediated signaling. We consider protein-mediated effects specific to FcεRI, as well as more general phase properties of the plasma membrane,

and how this phase behavior might control the localization of membrane proteins.

In Chapter 2, we ask how the spatial configuration of IgE-FcεRI relates to the elicited functional response. Experimentally, we use structurally defined ligands to form IgE-FcεRI clusters with known structural characteristics, and characterize the spatial configuration of clusters by PALM/STORM imaging. We then relate the structure to the capacity of the clusters to recruit other membrane components. We specifically establish that a high density of receptors can be a key structural feature that allows a receptor cluster to signal effectively. We use the Ising model to show how lipids may play a role in mediating this observed trend. Under the assumption of an Ising critical point, we show how receptor density, as well as membrane composition relate to the energetic capacity of clusters to recruit kinase.

In Chapter 3, we extend our lattice model for the role of lipids in recruiting kinase to receptor clusters when both have the same phase preference. We relax the assumption of Ising criticality, and instead consider a model that, depending on parameter choices, can exist at a critical point, phase-separated state, microemulsion, or tricritical point. This covers almost every proposed thermodynamic picture for the state of biological membranes. We calculate the phase diagram of this model using modern machine learning techniques based on neural networks, and direct our attention to the parts of the phase diagram that are likely to be most biologically relevant. In this analysis, we arrive at the exciting discovery that a membrane at a tricritical point, not previously discussed in the context of membranes, would in fact enable a stronger kinase-receptor coupling than any of the other currently proposed models.

Our results in Chapters 2 and 3 make it tempting to suggest a simple model in

which antigen cross-links IgE-FcεRI in a particular configuration, then that configuration dictates kinase recruitment and downstream signaling. In Chapter 4, we show that in fact, additional layers of complexity may be present. We give evidence for a novel positive feedback mechanism through which IgE-FcεRI clustering is enhanced by the activity of downstream signaling proteins. Lyn is especially important in this process, as overexpression of Lyn leads to a higher level of IgE-FcεRI clustering. We have not yet identified the specific mechanism responsible for the increase in IgE-FcεRI, but show that it is activated downstream in the IgE signaling system, downstream of both Syk and PLCγ. The discovery of this mechanism creates a new paradigm for IgE clustering associated with signaling. As opposed to the canonical model in which IgE clusters simply lead to a response, we observe that IgE clustering is part of a more complex, regulated process, mediated not only by the external antigen, but also by intracellular signaling processes.

In sum, we use molecular-level experimental and theoretical tools to achieve several new insights into lipid-mediated and protein-mediated mechanisms of signal initiation by FcεRI.

References

1. Stone, K.D., C. Prussin, and D.D. Metcalfe. 2010. IgE, mast cells, basophils, and eosinophils. J. Allergy Clin. Immunol. 125: S73–S80.

2. Jackson, K.D., L.D. Howie, and L.J. Akinbami. 2013. Trends in Allergic Conditions Among Children : United States, 1997-2011. In: NCHS Data Brief 121. Hyattsville, MD: National Center for Health Statistics.

3. Gilfillan, A.M., and J. Rivera. 2009. The tyrosine kinase network regulating mast cell activation. Immunol. Rev. 228: 149–169.

4. Blank, U., and J. Rivera. 2004. The ins and outs of IgE-dependent mast-cell exocytosis. Trends Immunol. 25: 266–273.

5. Parravicini, V., M. Gadina, M. Kovarova, S. Odom, C. Gonzalez-Espinosa, Y. Furumoto, S. Saitoh, L.E. Samelson, J.J. O'Shea, and J. Rivera. 2002. Fyn kinase initiates complementary signals required for IgE-dependent mast cell degranulation. Nat. Immunol. 3: 741–8.

6. Kraft, S., and J.P. Kinet. 2007. New developments in FcεRI regulation, function and inhibition. Nat Rev Immunol. 7: 365–378.

7. Gilfillan, A.M., and C. Tkaczyk. 2006. Integrated signalling pathways for mast-cell activation. Nat. Rev. Immunol. 6: 218–230.

8. Kawakami, Y., J. Kitaura, A.B. Satterthwaite, R.M. Kato, K. Asai, S.E. Hartman, M. Maeda-Yamamoto, C.A. Lowell, D.J. Rawlings, O.N. Witte, and T. Kawakami. 2000. Redundant and opposing functions of two tyrosine kinases, Btk and Lyn, in mast cell activation. J. Immunol. 165: 1210–1219.

9. Pribluda, V.S., C. Pribluda, and H. Metzger. 1994. Transphosphorylation as the mechanism by which the high-affinity receptor for IgE is phosphorylated upon aggregation. PNAS. 91: 11246–11250.

10. Nishizumi, H., and T. Yamamoto. 1997. Impaired tyrosine phosphorylation and Ca2+ mobilization, but not degranulation, in lyn-deficient bone marrow-derived mast cells. J. Immunol. 158: 2350–2355.

11. Odom, S., G. Gomez, M. Kovarova, Y. Furumoto, J.J. Ryan, H. V. Wright, C. Gonzalez-Espinosa, M.L. Hibbs, K.W. Harder, and J. Rivera. 2004. Negative Regulation of Immunoglobulin E–dependent Allergic Responses by Lyn Kinase. J. Exp. Med. 199: 1491–1502.

12. Hernandez-Hansen, V., A.J. Smith, Z. Surviladze, A. Chigaev, T. Mazel, J. Kalesnikoff, C.A. Lowell, G. Krystal, L.A. Sklar, B.S. Wilson, and J.M. Oliver. 2004.

Dysregulated Fcε RI Signaling and Altered Fyn and SHIP Activities in Lyn-Deficient Mast Cells. J. Immunol. 173: 100–112.

13. Ingley, E. 2008. Src family kinases: regulation of their activities, levels and identification of new pathways. Biochim. Biophys. Acta. 1784: 56–65.

14. Wofsy, C., C. Torigoe, U.M. Kent, H. Metzger, and B. Goldstein. 1997. Exploiting the difference between intrinsic and extrinsic kinases: implications for regulation of signaling by immunoreceptors. J. Immunol. 159: 5984–5992.

15. Wofsy, C., B.M. Vonakis, H. Metzger, and B. Goldstein. 1999. One lyn molecule is sufficient to initiate phosphorylation of aggregated high-affinity IgE receptors. PNAS. 96: 8615–8620.

16. Balagopalan, L., N.P. Coussens, E. Sherman, L.E. Samelson, and C.L. Sommers. 2010. The LAT story: a tale of cooperativity, coordination, and choreography. Cold Spring Harb. Perspect. Biol. 2.

17. Saitoh, S., R. Arudchandran, T.S. Manetz, W. Zhang, C.L. Sommers, P.E. Love, J. Rivera, and L.E. Samelson. 2000. LAT Is Essential for FcεRI-Mediated Mast Cell Activation. Immunity. 12: 525–535.

18. Barker, S.A., K.K. Caldwell, J.R. Pfeiffer, and B.S. Wilson. 1998. Wortmannin-Sensitive Phosphorylation, Translocation, and Activation of PLCgamma 1, but Not PLCgamma 2, in Antigen-stimulated RBL-2H3 Mast Cells. Mol. Biol. Cell. 9: 483–496.

19. Su, X., J.A. Ditlev, E. Hui, S. Banjade, and J. Okrut. 2016. Phase separation of signaling molecules promotes T cell receptor signal transduction. Science. 9964.

20. Passante, E., and N. Frankish. 2009. The RBL-2H3 cell line: Its provenance and suitability as a model for the mast cell. Inflamm. Res. 58: 737–745.

21. Nussinov, R., H. Jang, and C.J. Tsai. 2015. Oligomerization and nanocluster organization render specificity. Biol. Rev. 90: 587–598.

22. Williams, A.F., and A.N. Barclay. 1988. The Immunoglobulin Superfamily — Domains for Cell Surface Recognition. Annu. Rev. Immunol. 6: 381–405.

23. Brownlie, R.J., and R. Zamoyska. 2013. T cell receptor signalling networks: branched, diversified and bounded. Nat. Rev. Immunol. 13: 257–269.

24. Dal Porto, J.M., S.B. Gauld, K.T. Merrell, D. Mills, A.E. Pugh-Bernard, and J. Cambier. 2004. B cell antigen receptor signaling 101. Mol. Immunol. 41: 599–613.

25. Packard, T.A., and J.C. Cambier. 2013. B lymphocyte antigen receptor signaling:

initiation, amplification, and regulation. F1000Prime Rep. 5: 40.

26. 2009. Beyond the diffraction limit. Nat. Photonics. 3: 361–361.

27. Betzig, E., G.H. Patterson, R. Sougrat, O.W. Lindwasser, S. Olenych, J.S. Bonifacino, M.W. Davidson, J. Lippincott-Schwartz, and H.F. Hess. 2006. Imaging intracellular fluorescent proteins at nanometer resolution. Science. 313: 1642–1645.

28. Rust, M.J., M. Bates, and X. Zhuang. 2006. Sub-diffraction-limit imaging by stochastic optical reconstruction microscopy (STORM). Nat. Methods. 3: 793–795.

29. Hess, S.T., T.P.K. Girirajan, and M.D. Mason. 2006. Ultra-high resolution imaging by fluorescence photoactivation localization microscopy. Biophys. J. 91: 4258–4272.

30. Owen, D.M., C. Rentero, J. Rossy, A. Magenau, D. Williamson, M. Rodriguez, and K. Gaus. 2010. PALM imaging and cluster analysis of protein heterogeneity at the cell surface. J. Biophotonics. 3: 446–54.

31. Axelrod, D. 2003. Total Internal Reflection Fluorescence Microscopy in Cell Biology. Methods Enzymol. 361.

32. Huang, B., W. Wang, M. Bates, and X. Zhuang. 2008. Three-Dimensional Super-Resolution Imaging by Stochastic Optical Reconstruction Microscopy. Science. 319: 810–813.

33. Manzo, C., and M.F. Garcia-Parajo. 2015. A review of progress in single particle tracking: from methods to biophysical insights. Reports Prog. Phys. 78: 124601.

34. Manley, S., J.M. Gillette, G.H. Patterson, H. Shroff, H.F. Hess, E. Betzig, and J. Lippincott-Schwartz. 2008. High-density mapping of single-molecule trajectories with photoactivated localization microscopy. Nat. Methods. 5: 155–157.

35. Mukamel, E.A., H. Babcock, and X. Zhuang. 2012. Statistical deconvolution for superresolution fluorescence microscopy. Biophys. J. 102: 2391–2400.

36. Huang, F., S.L. Schwartz, J.M. Byars, and K.A. Lidke. 2011. Simultaneous multiple-emitter fitting for single molecule super-resolution imaging. Biomed. Opt. Express. 2: 1377–93.

37. Huang, F., T.M.P. Hartwich, F.E. Rivera-Molina, Y. Lin, W.C. Duim, J.J. Long, P.D. Uchil, J.R. Myers, M.A. Baird, W. Mothes, M.W. Davidson, D. Toomre, and J. Bewersdorf. 2013. Video-rate nanoscopy using sCMOS camera-specific single-molecule localization algorithms. Nat. Methods. 10: 653–8.

38. Stone, M.B., and S.L. Veatch. 2015. Steady-state cross-correlations for live two-colour super-resolution localization data sets. Nat. Commun. 6: 7347.

39. Sneath, P.H.A. 1957. The application of computers to taxonomy. J. Gen. Microbiol. 17: 201–226.

40. Ester, M., H.P. Kriegel, J. Sander, and X. Xu. 1996. A Density-Based Algorithm for Discovering Clusters in Large Spatial Databases with Noise. Proc. 2nd Int. Conf. Knowl. Discov. Data Min. : 226–231.

41. Kiskowski, M.A., J.F. Hancock, and A.K. Kenworthy. 2009. On the use of Ripley's K-function and its derivatives to analyze domain size. Biophys. J. 97: 1095–1103.

42. Veatch, S.L., B.B. Machta, S.A. Shelby, E.N. Chiang, D.A. Holowka, and B.A. Baird. 2012. Correlation functions quantify super-resolution images and estimate apparent clustering due to over-counting. PLoS One. 7: e31457.

43. Annibale, P., S. Vanni, M. Scarselli, U. Rothlisberger, and A. Radenovic. 2011. Identification of clustering artifacts in photoactivated localization microscopy. Nat. Methods. 8: 527–8.

44. Baumgart, F., A.M. Arnold, K. Leskovar, K. Staszek, M. Fölser, J. Weghuber, H. Stockinger, and G.J. Schütz. 2016. Varying label density allows artifact-free analysis of membrane-protein nanoclusters. Nat. Methods. 13: 661–4.

45. Annibale, P., S. Vanni, M. Scarselli, U. Rothlisberger, and A. Radenovic. 2011. Quantitative photo activated localization microscopy: unraveling the effects of photoblinking. PLoS One. 6: e22678.

46. Bates, M., B. Huang, G.T. Dempsey, and X. Zhuang. 2007. Multicolor super-resolution imaging with photo-switchable fluorescent probes. Science. 317: 1749–53.

47. Bossi, M., J. Föiling, V.N. Belov, V.P. Boyarskiy, R. Medda, A. Egner, C. Eggeling, A. Schönle, and S.W. Hell. 2008. Multicolor far-field fluorescence nanoscopy through isolated detection of distinct molecular species. Nano Lett. 8: 2463–2468.

48. Zhang, Z., S.J. Kenny, M. Hauser, W. Li, and K. Xu. 2015. Ultrahigh-throughput single-molecule spectroscopy and spectrally resolved super-resolution microscopy. Nat. Methods. 12: 935–938.

49. Kim, D., N.M. Curthoys, M.T. Parent, and S.T. Hess. 2013. Bleed-through correction for rendering and correlation analysis in multi-colour localization microscopy. J. Opt. 15: 094011.

50. Stone, M.B., and S.L. Veatch. 2014. Far-red organic fluorophores contain a

fluorescent impurity. Chemphyschem. 15: 2240–2246.

51. Gustafsson, M.G.L. 2000. Surpassing the lateral resolution limit by a factor of two using structured illumination microscopy. J. Microsc. 198: 82–87.

52. Chen, B.-C., W.R. Legant, K. Wang, L. Shao, D.E. Milkie, M.W. Davidson, C. Janetopoulos, X.S. Wu, J.A. Hammer, Z. Liu, B.P. English, Y. Mimori-Kiyosue, D.P. Romero, A.T. Ritter, J. Lippincott-Schwartz, L. Fritz-Laylin, R.D. Mullins, D.M. Mitchell, J.N. Bembenek, A.-C. Reymann, R. Bohme, S.W. Grill, J.T. Wang, G. Seydoux, U.S. Tulu, D.P. Kiehart, and E. Betzig. 2014. Lattice light-sheet microscopy: Imaging molecules to embryos at high spatiotemporal resolution. Science. 346: 1257998.

53. Hell, S.W., and J. Wichmann. 1994. Breaking the Diffraction Resolution Limit By Stimulated-Emission - Stimulated-Emission-Depletion Fluorescence Microscopy. Opt. Lett. 19: 780–782.

54. Feigenson, G.W. 2009. Phase diagrams and lipid domains in multicomponent lipid bilayer mixtures. Biochim. Biophys. Acta. 1788: 47–52.

55. Konyakhina, T.M., and G.W. Feigenson. 2016. Phase diagram of a polyunsaturated lipid mixture: Brain sphingomyelin/1-stearoyl-2-docosahexaenoyl-sn-glycero-3-phosphocholine/cholesterol. Biochim. Biophys. Acta - Biomembr. 1858: 153–161.

56. Goh, S.L., J.J. Amazon, and G.W. Feigenson. 2013. Toward a better raft model: modulated phases in the four-component bilayer, DSPC/DOPC/POPC/CHOL. Biophys. J. 104: 853–862.

57. Pike, L.J. 2006. Rafts defined: a report on the Keystone symposium on lipid rafts and cell function. J. Lipid Res. 47: 1597–1598.

58. Simons, K., and M.J. Gerl. 2010. Revitalizing membrane rafts: new tools and insights. Nat. Rev. Mol. Cell Biol. 11: 688–699.

59. Van der Merwe, P.A., and O. Dushek. 2011. Mechanisms for T cell receptor triggering. Nat. Rev. Immunol. 11: 47–55.

60. Gupta, N., and A.L. DeFranco. 2007. Lipid rafts and B cell signaling. Semin. Cell Dev. Biol. 18: 616–626.

61. Hancock, J.F. 2003. Ras proteins: different signals from different locations. Nat. Rev. Mol. Cell Biol. 4: 373–385.

62. Simons, K., and D. Toomre. 2000. Lipid rafts and signal transduction. Nat. Rev. Mol. Cell Biol. 1: 31–39.

63. Holowka, D., J.A. Gosse, A.T. Hammond, X. Han, P. Sengupta, N.L. Smith, A. Wagenknecht-Wiesner, M. Wu, R.M. Young, and B. Baird. 2005. Lipid segregation and IgE receptor signaling: a decade of progress. Biochim. Biophys. Acta. 1746: 252–259.

64. Thomas, J.L., D. Holowka, B. Baird, and W.W. Webb. 1994. Large-Scale Co-aggregation of Fluorescent Lipid Probes with Cell Surface Proteins. J. Cell Biol. 125: 795–802.

65. Brown, D.A., and J.K. Rose. 1992. Sorting of GPI-anchored proteins to glycolipid-enriched membrane subdomains during transport to the apical cell surface. Cell. 68: 533–544.

66. Babiychuk, E.B., and A. Draeger. 2006. Biochemical characterization of detergent-resistant membranes: a systematic approach. Biochem. J. 397: 407–16.

67. Brown, D.A. 2006. Lipid rafts, detergent-resistant membranes, and raft targeting signals. Physiology. 21: 430–439.

68. Field, K.A., D. Holowka, and B. Baird. 1997. Compartmentalized Activation of the High Affinity Immunoglobulin E Receptor within Membrane Domains. J. Biol. Chem. 272: 4276–4280.

69. Field, K.A., D. Holowka, and B. Baird. 1995. FcεRI-mediated recruitment of p53/56lyn to detergent-resistant membrane domains accompanies cellular signaling. PNAS. 92: 9201–9205.

70. Young, R.M., X. Zheng, D. Holowka, and B. Baird. 2005. Reconstitution of regulated phosphorylation of FcεRI by a lipid raft-excluded protein-tyrosine phosphatase. J. Biol. Chem. 280: 1230–1235.

71. Barua, D., and B. Goldstein. 2012. A mechanistic model of early FcεRI signaling: lipid rafts and the question of protection from dephosphorylation. PLoS One. 7: e51669.

72. Baumgart, T., A.T. Hammond, P. Sengupta, S.T. Hess, D.A. Holowka, B.A. Baird, and W.W. Webb. 2007. Large-scale fluid/fluid phase separation of proteins and lipids in giant plasma membrane vesicles. PNAS. 104: 3165–3170.

73. Wu, M., D. Holowka, H.G. Craighead, and B. Baird. 2004. Visualization of plasma membrane compartmentalization with patterned lipid bilayers. PNAS. 101: 13798–13803.

74. Swamy, M.J., L. Ciani, M. Ge, A.K. Smith, D. Holowka, B. Baird, and J.H. Freed. 2006. Coexisting domains in the plasma membranes of live cells characterized by

spin-label ESR spectroscopy. Biophys. J. 90: 4452–4465.

75. Shelby, S.A., S.L. Veatch, D.A. Holowka, and B.A. Baird. 2016. Functional nanoscale coupling of Lyn kinase with IgE-FcεRI is restricted by the actin cytoskeleton in early antigen-stimulated signaling. Mol. Biol. Cell. 27: 3645–3658.

76. Klotzsch, E., and G.J. Schutz. 2013. A critical survey of methods to detect plasma membrane rafts. Philos Trans R Soc B. 368: 20120033.

77. Lillemeier, B.F., J.R. Pfeiffer, Z. Surviladze, B.S. Wilson, and M.M. Davis. 2006. Plasma membrane-associated proteins are clustered into islands attached to the cytoskeleton. PNAS. 103: 18992–18997.

78. Lillemeier, B.F., M.A. Mörtelmaier, M.B. Forstner, J.B. Huppa, J.T. Groves, and M.M. Davis. 2010. TCR and Lat are expressed on separate protein islands on T cell membranes and concatenate during activation. Nat. Immunol. 11: 90–96.

79. Sezgin, E., I. Levental, S. Mayor, and C. Eggeling. 2017. The mystery of membrane organization: composition, regulation and roles of lipid rafts. Nat. Rev. Mol. Cell Biol. : Advance Online Publication.

80. Levental, I., and S.L. Veatch. 2016. The Continuing Mystery of Lipid Rafts. J. Mol. Biol. 428: 4749–4764.

81. Honerkamp-Smith, A.R., S.L. Veatch, and S.L. Keller. 2009. An introduction to critical points for biophysicists; observations of compositional heterogeneity in lipid membranes. Biochim. Biophys. Acta. 1788: 53–63.

82. Veatch, S.L., P. Cicuta, P. Sengupta, A. Honerkamp-Smith, D. Holowka, and B. Baird. 2008. Critical fluctuations in plasma membrane vesicles. ACS Chem. Biol. 3: 287–293.

83. Veatch, S.L.L., I.V. V Polozov, K. Gawrisch, and S.L.L. Keller. 2004. Liquid Domains in Vesicles Investigated by NMR and Fluorescence Microscopy. Biophys. J. 86: 2910–2922.

84. Silvius, J. 2005. Lipid microdomains in model and biological membranes: how strong are the connections? Q. Rev. Biophys. 38: 373.

85. Palmieri, B., and S.A. Safran. 2013. Hybrid Lipids Increase the Probability of Fluctuating Nanodomains in Mixed Membranes. Langmuir. 29: 5246–5261.

86. Amazon, J.J., S.L. Goh, and G.W. Feigenson. 2013. Competition between line tension and curvature stabilizes modulated phase patterns on the surface of giant unilamellar vesicles: A simulation study. Phys. Rev. E. 87: 22708.

87. Schick, M. 2015. Theories of Equilibrium Inhomogeneous Fluids. .

88. Usery, R.D., T.A. Enoki, S.P. Wickramasinghe, M.D. Weiner, W.-C. Tsai, M.B. Kim, S. Wang, T.L. Torng, D.G. Ackerman, F.A. Heberle, J. Katsaras, and G.W. Feigenson. 2017. Line Tension Controls Liquid-Disordered + Liquid-Ordered Domain Size Transition in Lipid Bilayers. Biophys. J. 112: 1431–1443.

89. Kusumi, A., T.K. Fujiwara, N. Morone, K.J. Yoshida, R. Chadda, M. Xie, R.S. Kasai, and K.G.N. Suzuki. 2012. Membrane mechanisms for signal transduction: The coupling of the meso-scale raft domains to membrane-skeleton-induced compartments and dynamic protein complexes. Semin. Cell Dev. Biol. 23: 126–144.

90. Machta, B.B., S. Papanikolaou, J.P. Sethna, and S.L. Veatch. 2011. Minimal model of plasma membrane heterogeneity requires coupling cortical actin to criticality. Biophys. J. 100: 1668–1677.

91. Honigmann, A., S. Sadeghi, J. Keller, S.W. Hell, C. Eggeling, and R. Vink. 2014. A lipid bound actin meshwork organizes liquid phase separation in model membranes. Elife. 3: e01671.

92. Rao, M., and S. Mayor. 2014. Active organization of membrane constituents in living cells. Curr. Opin. Cell Biol. 29: 126–132.

93. Feller, S.E. 2000. Molecular dynamics simulations of lipid bilayers. Curr. Opin. Colloid Interface Sci. 5: 217–223.

94. Dror, R.O., R.M. Dirks, J.P. Grossman, H. Xu, and D.E. Shaw. 2012. Biomolecular Simulation: A Computational Microscope for Molecular Biology. Annu. Rev. Biophys. 41: 429–452.

95. Marrink, S.J., H.J. Risselada, S. Yefimov, D.P. Tieleman, and A.H. De Vries. 2007. The MARTINI Force Field : Coarse Grained Model for Biomolecular Simulations The MARTINI Force Field : Coarse Grained Model for Biomolecular Simulations. J. Phys. Chem. B. 111: 7812–7824.

96. Ingólfsson, H.I., M.N. Melo, F.J. van Eerden, C. Arnarez, C.A. Lopez, T.A. Wassenaar, X. Periole, A.H. de Vries, D.P. Tieleman, and S.J. Marrink. 2014. Lipid organization of the plasma membrane. J. Am. Chem. Soc. 136: 14554–14559.

97. Bennett, C.H. 1976. Efficient Estimation of Free Energy Differences from Monte Carlo Data. J. Comput. Phys. 22: 245–268.

98. Jarzynski, C. 1997. Nonequilibrium Equality for Free Energy Differences. Phys. Rev. Lett. 78: 2690–2693.

99. Machta, B.B., S.L. Veatch, and J.P. Sethna. 2012. Critical Casimir Forces in Cellular Membranes. Phys. Rev. Lett. 109: 138101.

100. Veatch, S.L., E.N. Chiang, P. Sengupta, D.A. Holowka, and B.A. Baird. 2012. Quantitative nanoscale analysis of IgE-FcεRI clustering and coupling to early signaling proteins. J. Phys. Chem. B. 116: 6923–6935.

101. Onsager, L. 1943. A Two-Dimensional Model with an Order-Disorder Transition. Cryst. Stat. 65: 117–149.

102. Blume, M. 1966. Theory of the First-Order Magnetic Phase Change in UO2. Phys. Rev. 141: 517–524.

103. Capel, H.W. 1966. On the possibility of first-order transitions in Ising systems of triplet ions with zero-field splitting. Physica. 32: 966–988.

104. Blume, M., V.J. Emery, and R.B. Griffiths. 1971. Ising Model for the λ Transition and Phase Separation in He3-He4 Mixtures. Phys. Rev. A. 4: 1071–1077.

105. Beale, P.D. 1986. Finite-size scaling study of the two-dimensional Blume-Capel model. Phys. Rev. B. 33: 1717–1720.

106. Alcaraz, F.C., J.R. Drugowich de Felício, R. Köberle, and J.F. Stilck. 1985. Hamiltonian studies of the Blume-Emery-Griffiths model. Phys. Rev. B. 32: 7469–7475.

107. Berker, A.N., and M. Wortis. 1976. Blume-Emery-Griffiths-Potts model in two dimensions: Phase diagram and critical properties from a position-space renormalization group. Phys. Rev. B. 14: 4946–4963.

108. Gompper, G., and M. Schick. 1990. Lattice model of microemulsions: The effect of fluctuations in one and two dimensions. Phys. Rev. A. 42: 2137–2149.

109. Widom, B. 1984. A model microemulsion. J. Chem. Phys. 81: 1030.

CHAPTER TWO

INVESTIGATING THE MOLECULAR BASIS OF IGE RECEPTOR SIGNALING WITH STRUCTURALLY DEFINED LIGANDS AND SUPER-RESOLUTION MICROSCOPY

2.1 Summary

Advances in microscopy enable the study of the initiation of mast cell signaling at a new level of molecular detail. We utilized PALM/STORM super-resolution imaging in conjunction with dsDNA-based structurally defined ligands to examine how the spatial configuration of IgE-FcεRI within a cluster relates to the capacity of the cluster to initiate transmembrane signaling. dSTORM imaging of IgE on live cells revealed ligand-dependent differences in clustering parameters of receptor density, cluster radius, and number of receptors per cluster. We identify the density of IgE-FcεRI in clusters , and in limiting cases the number of IgE-FcεRI per cluster, as the most important parameters that correlate with the functional capacity of clusters. Two-color imaging of IgE and Lyn suggests that Lyn recruitment is subtle – a ~ 20% increase in Lyn concentration for the most potent ligand – but correlates with the density of IgE-FcεRI. We show that this density dependence is consistent with a lipid-mediated mechanism for the initial Lyn coupling to IgE-FcεRI, which we model quantitatively with the Ising model. The predicted lipid-mediated binding energy of ~-0.6 k_BT at a receptor spacing of 5 nm is sufficient to fully explain the measured extent of Lyn partitioning. Our results suggest that lipids may have a crucial role in the initial stages of IgE-FcεRI signaling.

2.2 Introduction

Signaling through the high affinity immunoglobulin E (IgE) receptor (FcεRI) in

mast cells is of biomedical interest due to its role in allergic responses. In addition, the mast cell serves as a model system for a more general paradigm in cell biology, in which membrane receptors receive an external stimulus, form clusters, and transmit the received signal into the cell (1, 2). More specifically, the molecular components present in mast cell signaling are analogous to those found in other immune signaling systems including those found in T cells (3) and B cells (4). For these reasons, there is a large interest in understanding the mechanisms underlying mast cell signal initiation.

The signal in mast cells is initiated when IgE-FcεRI is cross-linked and clustered by a multivalent ligand (antigen) for which the bound IgE has specificity. Commonly used model IgE is specific for 2,4-dinitrophenyl (DNP), and can be cross-linked with BSA multiply conjugated with DNP (DNP-BSA). Cross-linking can lead to the formation of clusters consisting of a large number of IgE-FcεRI. The size of the typical cluster is smaller than the diffraction limit, so characterization of the clusters has been challenging until the advent of super-resolution imaging, which gave an estimate of ~70 nm clusters containing ~120 receptors under a strong DNP-BSA stimulus (5). Clusters formed due to a highly multivalent antigen such as DNP-BSA become immobilized (5, 6), although this immobilization is not required for stimulation (7).

Following clustering, the association is enhanced between FcεRI and the Src-family tyrosine kinase Lyn, which catalyzes the initial phosphorylation of the immunoreceptor tyrosine-based activation motifs (ITAMs) of the β and γ subunits of FcεRI (8). This allows for the subsequent stabilized binding of Lyn to phosphorylated ITAMs of the β subunit, and recruitment and phosphorylation of Syk tyrosine kinase. Syk in turn propagates the signal by phosphorylating the linker for activation of T cells (LAT)

scaffold, engaging further downstream signaling partners, eventually leading to the activation of phospholipase C γ (PLCγ), stimulated Ca^{2+} mobilization, and the cellular release of pre-formed inflammatory mediators, known as degranulation (9).

While much of this signaling pathway and the proteins involved have been characterized, the molecular basis behind the initial signaling events, namely the aggregation-induced coupling between Lyn and the IgE receptor, remains a subject of ongoing investigation. Lyn binds to the phosphorylated β subunit of FcεRI via its SH2 domain, but the initial association between Lyn and receptor must occur before phosphorylation, leading to the interest in additional mechanisms (8). Theoretical modeling of the Lyn/FcεRI interaction suggest that it is subtle: One Lyn molecule is sufficient to activate a dimer of FcεRI (10), and only 10-15% of the total Lyn in the cell is available to bind FcεRI (11). As a result, direct measurement of the Lyn/IgE interaction has been challenging, undetectable by conventional fluorescence microscopy. However association of Lyn and IgE receptor has been detected using micron-sized patterned ligand systems (12), fluorescence correlation spectroscopy (FCS) (6), and super-resolution imaging (13).

Substantial evidence supports the role of membrane lipids to mediate the initial kinase recruitment in IgE receptor signaling, although the subject remains controversial due to the subtle nature of the lipid contribution. Structurally, Lyn is anchored to the plasma membrane by one palmitoyl and one myristoyl group, both saturated fatty acid chains, which confers some preference to partition into liquid ordered (Lo)-like lipid phase of the membrane. Studies using detergent-resistant membranes (14) support this notion, and further suggest that Lyn and cross-linked IgE-FcεRI colocalize in a Lo

phase. Transmembrane phosphatases such as PTPα partition into a more liquid disordered (Ld)-like phase (15). This led to a model in which clustered FcεRI stabilize a local Lo environment that tips the kinase/phosphatase balance in favor of phosphorylation and downstream signaling (16).

More recently it has been suggested that the physical basis behind lipid nanodomains is a critical phase transition, in which Lo and Ld regions of the membrane coexist, and exhibit long-range fluctuations (17). The properties of this phase transition are well described by the two-dimensional Ising model (18), which has been used to analyze electron microscopy (19) and super-resolution fluorescence microscopy (13, 20) images of mast cell signaling. This model is attractive because it allows for the possibility of long-range Casimir forces, attractive forces between distant proteins of the same phase preference (21).

Recent advances in single molecule localization imaging techniques, including photoactivated localization microscopy and stochastic optical reconstruction microscopy (which we refer to collectively as PALM/STORM) (22–24) and single particle tracking (25), have allowed this system to be studied in more detail at the nanoscale. Studies have been successful at characterizing the structure and dynamics of IgE-FcεRI clusters (5), dynamics of the FcεRI-γ subunit (26), and roles of actin (13, 27) in the initial stages of FcεRI clustering and FcεRI/Lyn coupling.

Structurally defined ligands provide molecular-level control of how IgE-FcεRI are cross-linked and simulated. Bivalent (28) and trivalent (29) ligands based on double-stranded DNA (dsDNA), as well as trivalent protein-based ligands (30) and bivalent antibodies (31) have been characterized. Due to the long persistence length of dsDNA

(~ 50 nm), dsDNA scaffolds are rigid, and have the advantage of maintaining a fixed spacing between receptor binding sites, tunable in the range of 5 to 13 nm depending on the length of the scaffold used. Until this study, dsDNA ligands were not evaluated in conjunction with ultra resolution microscopy techniques.

Here, we address the question of how the structural configuration of IgE-FcεRI within a cluster affect the capacity of the cluster to initiate a signal, by combining the power of PALM/STORM with structurally defined ligands. Hence, we were able to stimulate cells by forming clusters with a well-defined receptor spacing, and quantitatively measure the resulting changes in protein localization. Finally, we used these experiments as context for theoretical simulations using the Ising model. With this, we evaluated, at molecular-level resolution, the potential role of membrane lipids at a critical phase transition in mediating the initial recruitment of kinase to receptor clusters.

2.3 Results

Structurally defined ligands control the spatial organization of IgE receptor clusters

We utilized rigid Y-shaped trivalent ligands Y16 and Y46, as described previously (29). The ligands consist of a Y-shaped double-stranded DNA scaffold to which DNP is conjugated to each 5' end (Fig. 2.1a). As measured by fluorescence resonance energy transfer (FRET) the rigid dsDNA scaffold holds the DNP groups at a fixed spacing apart, 5.2±0.9 nm for Y16, and 13.1±2.5 nm for Y46 (slightly aplanar scaffolds accounts for the uncertainty values) (29). As both ligands are trivalent and interact with a bivalent IgE,

both can form an extensive cross-linked network of IgE-FcεRI (Fig. 2.1a), albeit with different distances between IgE binding sites. The differences between Y16 and Y46 are functionally relevant: Y16 is more potent than Y46 in stimulating degranulation in sensitized RBL-2H3 cells (Fig. 2.2), consistent with previous results (29). To investigate the structural basis for this distinctive capacity to stimulate a cellular response, we used direct stochastic optical reconstruction microscopy (dSTORM) (32) to examine spatial and dynamic features of IgE-FcεRI cross-linked by trivalent Y16 and Y46 or multivalent DNP-BSA in live RBL cells. Cells were sensitized with anti-DNP IgE labeled with Dyeomics 654 (Dy654) and imaged over time by dSTORM before and after the addition of stimulating ligand. We reconstructed high resolution images from sets of 500 raw frames acquired approximately every 20 s (Fig. 2.1b).

We quantified IgE-FcεRI clustering in each reconstructed image with a pair autocorrelation function, g(r), which can be fit with an exponential function (20). Autocorrelation functions at selected time points are shown in Fig. 2.3a. With this analysis (Materials and Methods) we obtain the correlation amplitude, which is a measure of the receptor density in clusters, the correlation length, which is a measure of the average radius of clusters, and the average number of receptors per cluster. We use these three parameters – amplitude, correlation length and number per cluster – to quantitatively describe the structure of the IgE-FcεRI clusters that are formed (Fig. 2.1c and Table 2.1). As established previously, auto-correlation of images obtained with PALM/STORM is subject to errors of over-counting due to fluorophore blinking (20) (Materials and Methods). For our live cell imaging, this is mitigated by diffusion over distances larger than the point spread function during the time that a fluorophore

Figure 2.1 Trivalent structurally defined ligands form large, immobile receptor clusters of well-defined structure. (a) Schematic representation of ligands Y16 and Y46, and the IgE-FcεRI clusters they are predicted to form. (b) Example dSTORM images at several time points of Dy654-IgE on a live cell at room temperature. The cell was stimulated at time 0 with 20 nM Y16. Scale bars are 5 μm in the main panels, and 500 nm in the insets. (c) Fitting parameters from autocorrelation analysis of dSTORM data. Cells were stimulated at time 0 with 20 nM Y16, 20 nM Y46, or 1 μg/mL DNP-BSA. Autocorrelation functions were calculated for one reconstructed image per 500 imaging frames (9-16 s), then all fits recorded within a one-minute time bin were averaged. Average ± standard error shown for 7 cells each of Y16, Y46, and 6 cells of DNP-BSA. (d) Diffusion coefficients, obtained separately by single particle tracking dSTORM of AF647-IgE under the same stimulation conditions as a-c. Average ± standard error shown for 4 cells per condition.

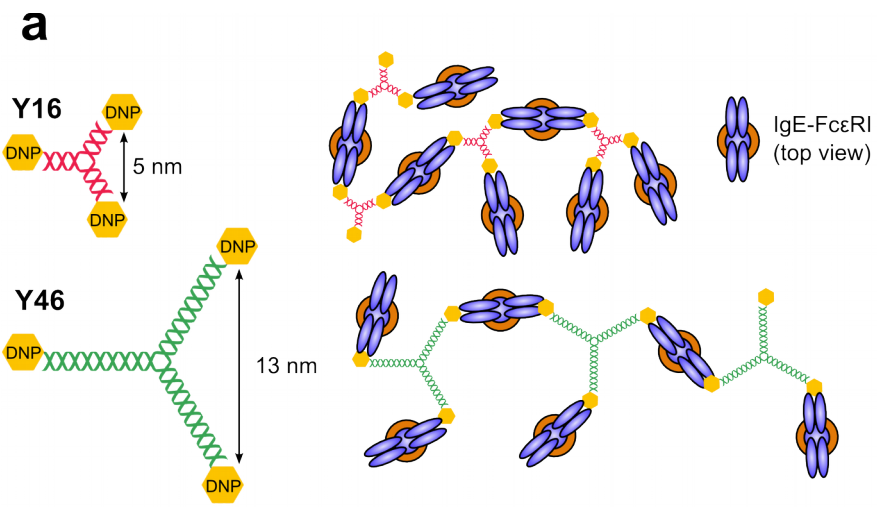
a
Y16
DNP
DNP
DNP
5 nm
Y46
DNP
DNP
DNP
13 nm
IgE-FcεRI
(top view)

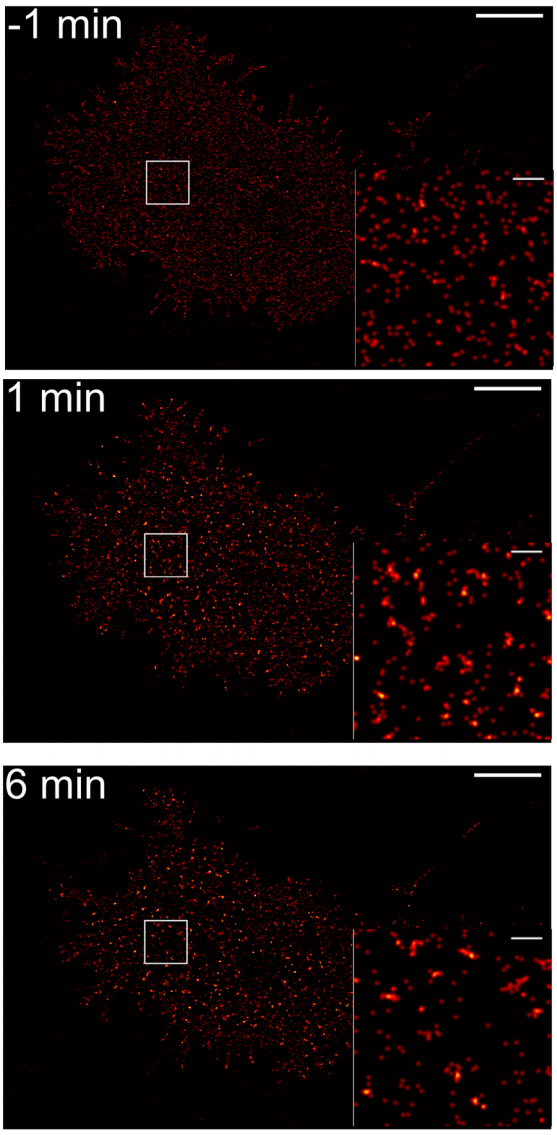
b
-1 min
1 min
6 min

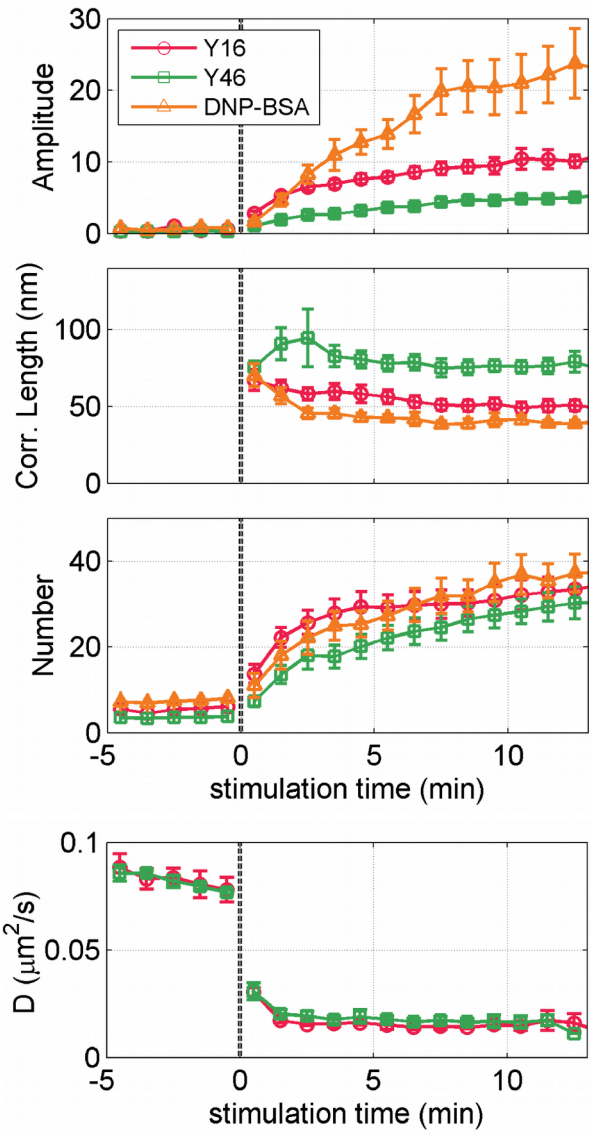
c
Amplitude
Y16
Y46
DNP-BSA
Corr. Length (nm)
Number
stimulation time (min)
D (μm²/s)
stimulation time (min)

	n	Amplitude	g(30 nm)	Correlation Length (nm)	Number per Cluster
Y16	9	10.1 ± 0.8	6.5 ± 0.4	50.8±3.5	33.4±3.5
Y46	8	5.0 ± 0.5	4.4 ± 0.3	79.1±6.7	30.2±3.7
DNP-BSA	7	23.7 ± 4.8	11.3 ± 1.3	39.0±2.0	37.2±4.4
Y16bi	5	5.7 ± 0.7	3.5 ± 0.2	38.1 ± 2.5	13.4 ± 1.8

	n	Diffusion ($\mu m^2/s$)
Unstim	8	0.077 ± 0.003
Y16	4	0.017 ± 0.004
Y46	4	0.017 ± 0.003

Table 2.1: Average correlation function parameters at steady state, in one-color live cell STORM experiments, as shown in Fig. 2.1 and Fig. 2.4. Amplitude and correlation length come from an exponential fit to equation 2. Values are tabulated based on the last time point in the time traces (12.5 min, or 11.5 min for diffusion coefficient). g(30 nm) indicates the value of the correlation function at a radius of 30 nm. The unstimulated diffusion coefficient is determined from the time point immediately before stimulation, from the same time traces that are tabulated for the stimulated cases. Values given are mean ± standard error of the mean.

Figure 2.2 Bulk degranulation assays serve as a readout of downstream functional responses in response to stimulation with ligand. Readout is beta-hexosaminidase release in response to 30 min stimulation with ligand at 37 °C, as a percentage of the total content released after detergent permeabilization. Error bars give ± standard error of at least 5 technical replicates. One representative run is shown for (a) trivalent ligands, and (b) bivalent ligands. Trends are consistent with prior work with these ligands. The absolute signal obtained in this assay varies from one run to the next; a DNP-BSA response is included in each run to aid in comparison between runs.

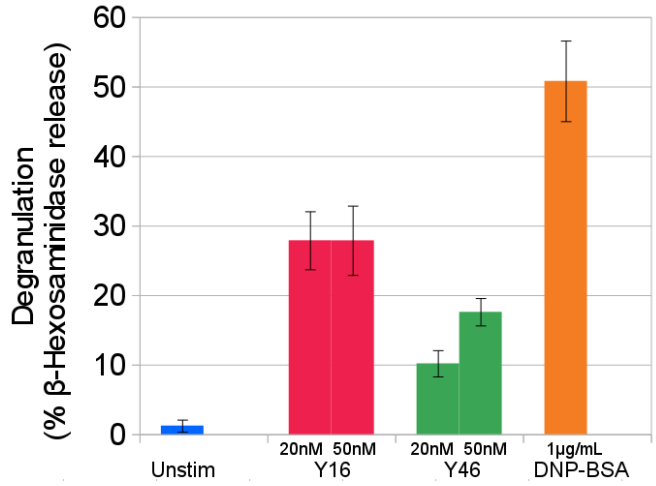
Degranulation
(% β-Hexosaminidase release)
60
50
40
30
20
10
0
Unstim
20nM 50nM
Y16
20nM 50nM
Y46
1µg/mL
DNP-BSA

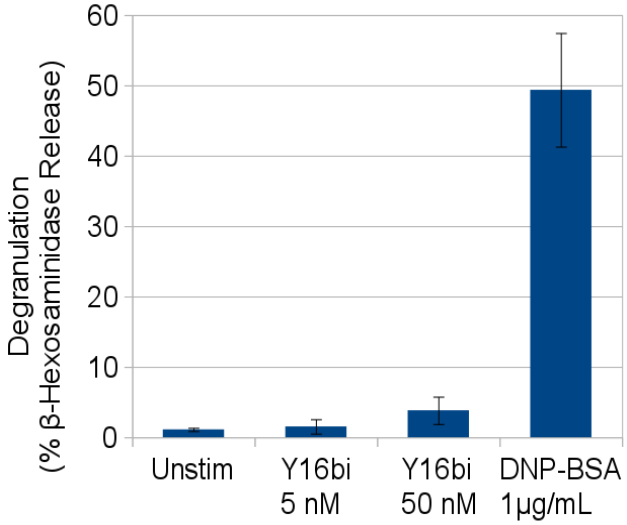
Degranulation
(% β-Hexosaminidase Release)
60
50
40
30
20
10
0
Unstim
Y16bi
5 nM
Y16bi
50 nM
DNP-BSA
1µg/mL

Figure 2.3 Correlation functions and example trajectories at selected time points from 1-color live cell dSTORM experiments. (a) IgE autocorrelation functions at selected time points, from Y16 and Y46 experiments tabulated in Fig. 2.1c, top three panels. Each curve gives the correlation function at that time point, averaged over the 8 or 9 cells imaged with that condition. Error bars indicate standard error of the mean. (b) Example trajectories acquired from Y16 and Y46 experiments tabulated in Fig. 2.1c, bottom panel. The gray background image is the reconstructed dSTORM image for the given time interval. The overlaid colored lines show trajectories acquired during that time interval. The color of the trajectory indicates the calculated diffusion coefficient for that trajectory.

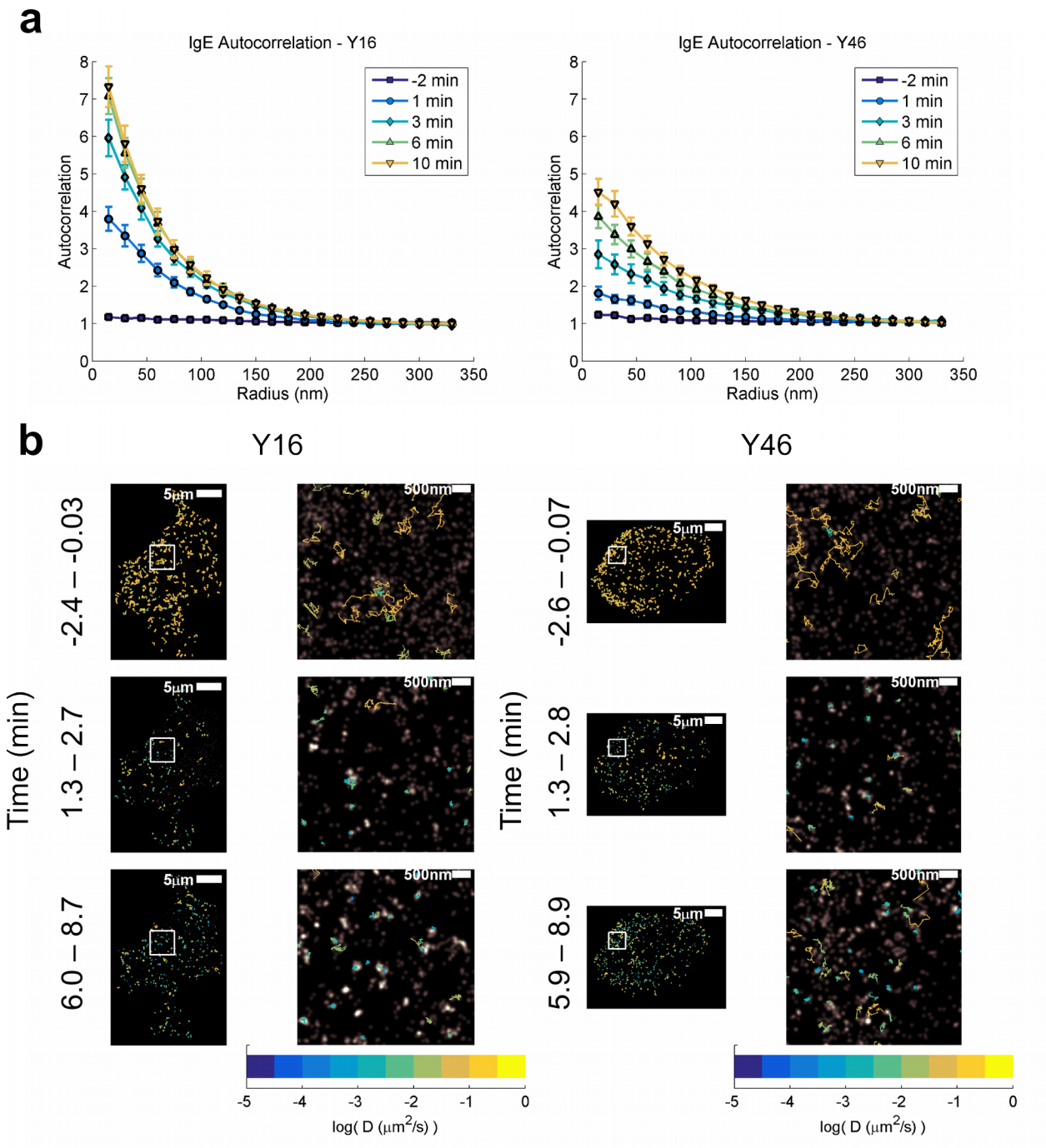
a
IgE Autocorrelation - Y16
IgE Autocorrelation - Y46
Autocorrelation
Radius (nm)
-2 min
1 min
3 min
6 min
10 min
b
Y16
Y46
Time (min)
-2.4 – -0.03
1.3 – 2.7
6.0 – 8.7
-2.6 – -0.07
1.3 – 2.8
5.9 – 8.9
5μm
500nm
log(D (μm²/s))

labeling an individual IgE-FcεRI remains in the dark state. This may be less true for IgE-FcεRI stabilized in large clusters. For comparison purposes, we list in Table 2.1 both amplitude (g(0) from the exponential fit) and g(30 nm) values, as most of the over-counting contribution has decayed by r=30 nm (~1/e radius of point spread function). We emphasize that any over-counting error in these measurements does not affect our conclusions based on the relative differences in spatial correlation parameters measured for different samples.

We find that Y16 and Y46 form stable clusters with a similar number of IgE-FcεRI per cluster. Stimulation by either of these trivalent ligands increases this number, up to a steady state of about 30. However, the plots of correlation amplitude and correlation length reveal differences in the structure of the clusters formed by the two ligands. Compared to Y46, Y16 reaches a steady state with a higher amplitude (~ 10 for Y16 compared to ~ 5 for Y46) and a lower correlation length (~ 50 nm compared to ~ 80 nm). These comparative values indicate that Y16 forms receptor clusters with, on average, a higher receptor density and a lower radius. We also evaluated these spatial correlation parameters for DNP-BSA cross-linking IgE-FcεRI on live RBL cells. This structurally ill-defined BSA ligand, with a nominal valency of 15 DNP, shows a time course for clustering IgE-FcεRI similar to that for the trivalent ligands, but the autocorrelation function converges to a higher correlation amplitude of ~ 24 and a lower correlation length of ~ 40 nm. Functionally, DNP-BSA elicits a stronger degranulation response than either Y16 or Y46 (Fig. 2.2). Together, the results suggest that the receptor density predominates over cluster area or number of receptors per cluster as the spatial feature important for initiating transmembrane signaling, such that DNP-BSA

is more potent than Y16, which is more potent than Y46. We note that the kinetics of cluster density increase appear slower for DNP-BSA than for the trivalent ligands (Fig. 2.1c, top panel), and this may result from the conjugated DNP groups being initially less exposed than for the dsDNA ligands (33).

Live cell STORM imaging allowed single particle tracking of individual IgE-FcεRI, after small changes in imaging conditions such that many individual fluorophores remain in a fluorescent state for multiple sequential frames. Example trajectories are shown in Fig. 2.3b Our measured diffusion coefficient for IgE-FcεRI on unstimulated cells is 0.08 $\mu m^2/s$, as determined by mean square displacement analysis, and this is similar to the value measured in previous STORM experiments (5). IgE-FcεRI complexes show a large reduction in mobility after addition of either Y16 or Y46 to a measured diffusion coefficient of 0.02 $\mu m^2/s$, indicating near immobility. This is similar to the immobilization of IgE-FcεRI on RBL cells measured previously after addition of DNP-BSA (5). For comparison, completely immobile probes would appear to diffuse at 0.003-0.006 $\mu m^2/s$ based on our resolution (Materials and Methods).

Ligands with more limited valency form IgE-FcεRI clusters that are smaller and less signaling competent

A variety of bivalent ligands have been used in the past to investigate structural features of IgE-FcεRI cross-linking important for transmembrane signaling (28, 31). We compared valency using Y16bi, a variant of Y16 that has DNP attached to only two of the three 5' ends (Fig. 2.4a). We performed the same dSTORM measurements and analysis, and found that Y16bi yields clusters with a lower steady state correlation amplitude (5.7), corresponding to lower density, and lower number of IgE-FcεRI per

Figure 2.4 Ligands of limited valency form smaller receptor clusters. (a) Schematic representation of Y16bi, which is predicted to form linear chains of IgE-FcεRI. (b) Fitting parameters from autocorrelation analysis of dSTORM imaging of Dy654-IgE on live cells stimulated with Y16bi at room temperature. Cells were stimulated at time 0 with 30 nM Y16bi. Fitting parameters shown for individual cells (colored points), and average ± standard error (black line), 5 cells.

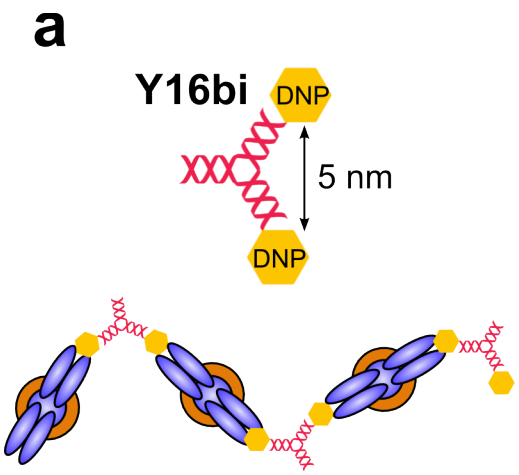
a
Y16bi
DNP
5 nm
DNP

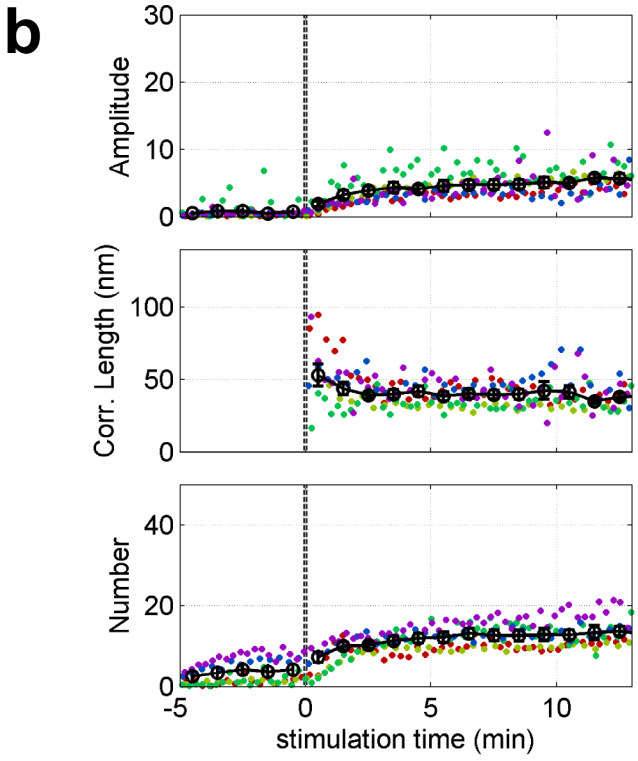
b
Amplitude
30
20
10
0
Corr. Length (nm)
100
50
0
Number
40
20
0
-5
0
5
10
stimulation time (min)

cluster (13.4) than the Y16 trivalent ligand (Fig. 2.4b and Table 2.1). The two other bivalent ligands we evaluated – a bivalent version of Y46 and the anti-IgE antibody B1E3 (34) – show a qualitatively consistent low level of stimulated IgE-FcεRI clustering (data not shown). These results are consistent with the expectation that bivalent ligand forms only non-branched IgE-FcεRI chains that may extend randomly (Fig. 2.4a) but not as densely spaced as a cross-linked network (Fig. 2.1a). The total number of receptors in the cluster formed by the chain is limited because there are only two points at the ends of the chain by which the cluster can grow, and a single unbinding event within the chain is sufficient to break apart the cluster. As assessed by the degranulation assay, Y16bi stimulates less transmembrane signaling than its trivalent Y16 counterpart (Fig. 2.2). This result indicates the functional consequences of a smaller number of clustered receptors, which becomes an important structural feature when the cluster is small.

Dense IgE-FcεRI clusters formed by Y16 and DNP-BSA more effectively recruit Lyn

We investigated the relationship between structural features of IgE-FcεRI clusters that we observe with super resolution imaging and the clusters' capacity to initiate transmembrane signaling. Association of FcεRI with Lyn kinase, which is anchored to the inner leaflet of the plasma membrane is known to be the first of these events. This coupling results in tyrosine phosphorylation of the FcεRI-β and –γ subunits, and Lyn then binds reversibly to phosphorylated FcεRI-β (13). We use recruitment of Lyn as a readout for effectively signaling IgE-FcεRI clusters.

Although Lyn association with clustered IgE-FcεRI has been observed in experiments where the clusters are highly stabilized, the transient nature of the Lyn

coupling and binding (10) causes its interaction with IgE-FcεRI to be challenging to detect with PALM/STORM imaging (see Discussion). Significant technical development was necessary in order to accurately detect and quantify the subtle colocalization of Lyn and IgE-FcεRI in our cell samples. Most notably, we uncovered a form of channel cross-talk, not previously reported, for one dye used to label IgE (Dy654), or the batches that we tested in these experiments. Therefore, we tested several others and finally selected a better-behaved dye pair (Alexa Fluor 647 (AF647) / mEos). Our detailed characterization is described in a Supplementary note. Additional procedures to optimize channel alignment and control samples is detailed in the Materials and Methods. These precautions and technical improvements allowed us to move forward and detect the subtle association between clustered IgE-FcεRI and Lyn.

We collected two-color PALM/STORM images of AF647-IgE and Lyn-mEos on chemically fixed cells (Fig. 2.5a), which were well-sampled as reconstructed over 10000 raw frames. We quantified images of cells fixed before and after addition of DNP-ligands for 6 min at 37 °C. For each image, each of the two color channels was first analyzed individually by an autocorrelation function (Fig. 2.5b; values for spatial parameters with errors are provided in Table 2.2). The IgE-FcεRI autocorrelation functions before and after addition of DNP-ligands show trends similar to the one-color live cell experiments (Fig. 2.1b, Table 2.1), such that the autocorrelation amplitudes trend DNP-BSA > Y16 > Y46. The amplitude values at g(0) are larger than in the live cell experiments, as expected, because there is a higher over-counting contribution when blinking probes are fixed and may be localized multiple times in the same position. Values for g(25 nm), for which the over-counting error is largely reduced, are

also shown in Table 2.2. The Lyn autocorrelation function does not show a stimulation-dependent change for any of the samples, indicating that Lyn does not form detectable clusters after IgE-FcεRI are cross-linked into clusters by the stimulating ligands. If we make the reasonable assumption that Lyn is completely unclustered before addition of ligand, then all of the auto-correlation curves, before and after stimulus, are dominated by over-counting.

We quantified colocalization of IgE-FcεRI and Lyn before and after addition of ligands using pair cross-correlation functions (Fig. 2.5c, Table 2.2), for which over-counting error does not occur (20). The amplitude of cross-correlation corresponds to the relative density of colocalization. For a negative control, we randomly and covalently labeled a surface with AF647-IgE and streptavidin conjugated to Alexa Fluor 568. We observe a higher cross-correlation amplitude between IgE-FcεRI and Lyn for cells stimulated with Y16 (0.21±0.03) or DNP-BSA (0.21±0.02), compared to Y46 (0.10±0.01). The measured average amplitudes for Y16 and DNP-BSA indicates that for both there is roughly a 20% increase in Lyn density in the proximity of IgE-FcεRI clusters, compared to the average density of Lyn across the cell. The significantly lower cross-correlation amplitude for Y46 stimulated samples is similar to that of the randomly distributed control sample (0.08±0.04); however, the longer decay length (correlation length = 129 ± 15 nm) compared to the control (38 ± 13 nm), indicates a low level of Lyn/IgE-FcεRI colocalization. The significant difference in Lyn cross-correlation with IgE-FcεRI comparing stimulation by Y16 vs Y46 is consistent with the view that a higher density of receptors facilitates stronger kinase recruitment.

Previous studies provide strong evidence that Lyn coupling with clustered IgE-

Figure 2.5 Two-color PALM/STORM imaging of AF647-IgE and Lyn-mEos on chemically fixed cells. (a) Example 2-color PALM/STORM images of fixed cells stimulated 6 min at 37 °C with 50 nM Y16. Though the trend is difficult to visually discern, some colocalization events are visible (white arrows). (b) Cross-correlation functions averaged over many PALM/dSTORM samples, stimulated 6 min at 37 ° C with 50 nM Y16, 50 nM Y46, or 1 μg/mL DNP-BSA. Control sample is a random distribution of labels on a non-cell surface (see Materials and Methods). Average ± standard error is shown for each point in the cross-correlation function, and the exponential fit (equation 3) is plotted based on the average amplitude and correlation length. (c) Cross-correlation amplitudes from (b) give a readout of Lyn/IgE colocalization. *, $p<0.05$; **, $p<0.01$; ***, $p<0.001$ by Wilcoxon rank-sum test.

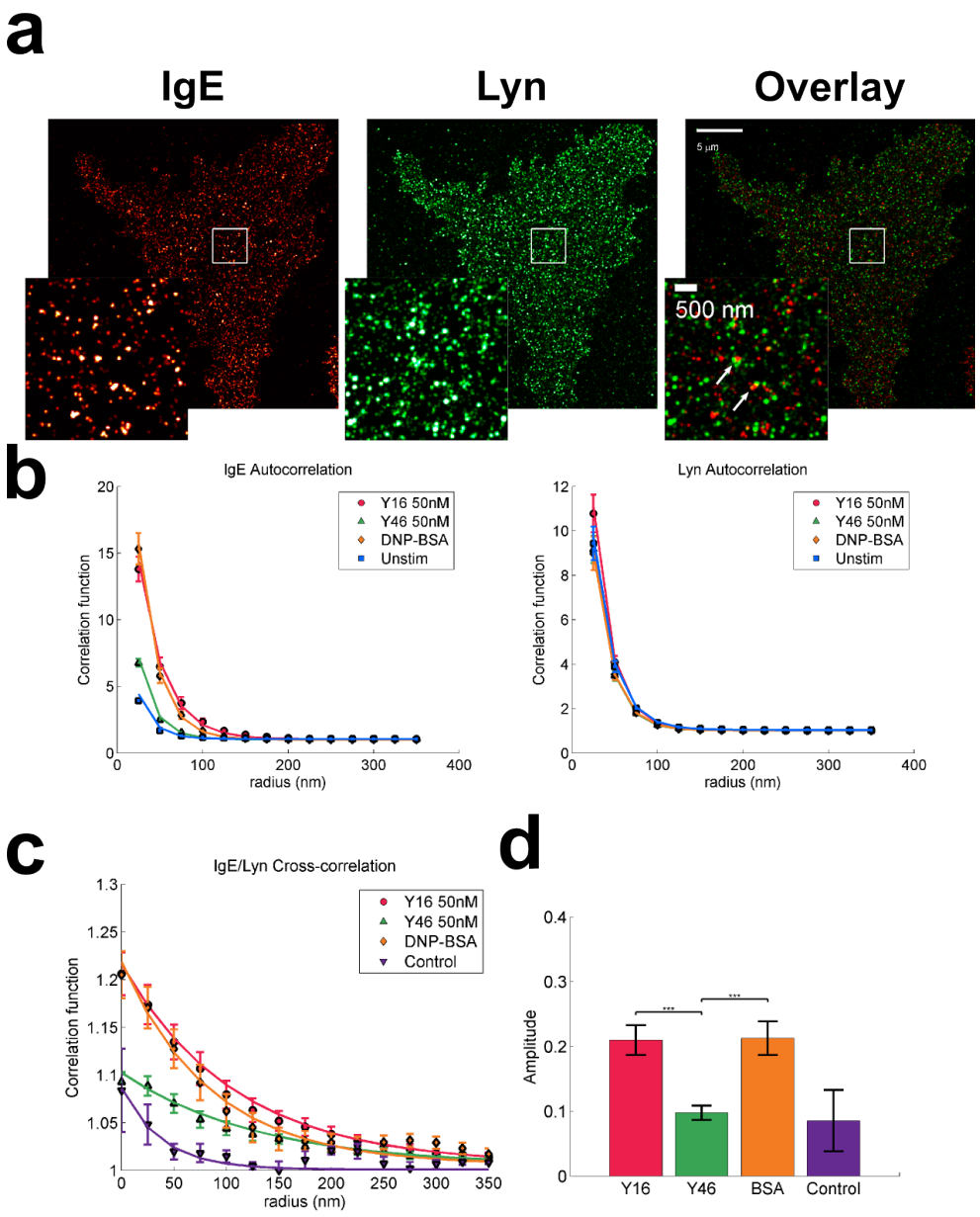
a
IgE
Lyn
Overlay
5 μm
500 nm
b
IgE Autocorrelation
Y16 50nM
Y46 50nM
DNP-BSA
Unstim
Correlation function
radius (nm)
Lyn Autocorrelation
Y16 50nM
Y46 50nM
DNP-BSA
Unstim
Correlation function
radius (nm)
c
IgE/Lyn Cross-correlation
Y16 50nM
Y46 50nM
DNP-BSA
Control
Correlation function
radius (nm)
d
Amplitude
***
***
Y16
Y46
BSA
Control

Table 2.2 Values extracted from correlation functions from two-color PALM/STORM experiments. Average correlation amplitudes are presented for the IgE / Lyn cross-correlation function, and IgE and Lyn autocorrelation functions, from the two-color experiments as shown in Fig. 2.5. Cross-correlation parameters are also presented for a control sample (Random) consisting of AF647-IgE and AF568-Streptavidin randomly, uniformly conjugated to a glass surface. As an alternate metric that is less susceptible to overcounting artifacts, we also present g(25 nm), the average values of the correlation function at a radius of 25 nm. Finally, we present the correlation lengths of the auto- and cross-correlation functions. Note that the correlation length of the autocorrelation function is affected by over-counting, giving it a value close to the radius of the super-resolved point-spread function. The correlation length of the cross-correlation function is not affected by over-counting.

Amplitude

	n	IgE / Lyn Cross-correlation	IgE Auto-correlation	Lyn Auto-correlation
Y16	20	0.21 ± 0.02	31.2±2.2	31.5±3.0
Y46	20	0.10 ± 0.01	22.3±1.9	27.3±2.0
DNP-BSA	14	0.21 ± 0.03	43.3±3.6	25.4±2.5
Random	4	0.08 ± 0.04		

g(25 nm)

		IgE / Lyn Cross-correlation	IgE Auto-correlation	Lyn Auto-correlation
Y16	20	1.17 ± 0.02	13.8 ± 1.0	10.8 ± 0.8
Y46	20	1.09 ±0.01	6.7 ± 0.3	9.1 ± 0.6
DNP-BSA	14	1.17 ± 0.02	15.3 ± 1.2	9.0 ± 0.8
Random	4	1.04 ± 0.02		

Correlation length (nm)

		IgE / Lyn Cross-correlation	IgE Auto-correlation	Lyn Auto-correlation
Y16	20	108 ± 12	29.7 ± 1.9	21.8 ± 0.5
Y46	20	129 ± 15	19.3 ± 0.7	20.9 ± 0.5
DNP-BSA	14	85 ± 17	23.1 ± 1.0	21.7 ± 0.5
Random	4	38 ± 13		

FcεRI occurs within ordered lipid (Lo-like) membrane domains (Introduction). We carried out PALM/STORM measurements in an effort to detect these domains with our DNP-ligands that cause IgE-FcεRI clusters of different densities. For this purpose, we tested a variety of fluorescently labeled probes that were previously characterized as having some preference for ordered or disordered (Ld-like) lipid domains (Fig. 2.6). We carried out two-color PALM/STORM experiments as described above, except using one of these probes instead of Lyn-mEos. Comparing cross-correlation amplitudes, we did not observe an obvious trend within the detection limits of the experimental configuration we used for these studies (Fig. 2.6). Together, these results indicate that the significant Lyn/IgE-FcεRI cross-correlation we observe after stimulating cells with Y16 or DNP-BSA is due to Lyn that has phosphorylated and then bound to FcεRI-β subunit. The results further point to the subtlety of lipid redistribution mediated by clustered IgE-FcεRI that facilitates the initial coupling with Lyn kinase. Our previously demonstrated capacity to detect it (13) appears to be highly dependent on details including the population of cells evaluated, the detection limits of the PALM/STORM system, and the degree of partitioning of the membrane probes used.

The 2D Ising model predicts lipid-mediated kinase recruitment

We took a theoretical approach to address the potential role of lipids in mediating signaling caused by clustered receptors. We considered the model in which the membrane exists near a critical phase transition (17), and asked how such phase behavior could facilitate recruitment of a kinase to receptor cluster if both prefer the same phase. We apply our model in the context of mast cell signaling and our experimental data, but note that the same model could be applied to any situation that

Figure 2.6 Cross-correlation amplitudes under numerous conditions using markers for liquid ordered and liquid disordered membrane. Palmitoyl, myristoyl-mEos (PM), a fragment of Lyn containing only the sites of palmitoyl and myristoyl modification, is a marker for liquid ordered phase. mEos-GPI (GPI) is a GPI-anchored construct which serves as another liquid ordered marker. Flaer (51) is the protein aerolysin labeled with Alexa Fluor 488, added as a soluble reagent to label cells before stimulation; Flaer labels endogenous GPI-anchored proteins, and so serves as another liquid ordered marker. mEos-geranylgeranyl is a geranygeranylated construct, and serves as a marker for the liquid disordered phase. For comparison we also plot the amplitude from the randomly distributed sample, shown as the purple curve in Fig. 2.5c (Uniform). (a) Cross-correlation amplitude between AF647-IgE and the indicated labels as measured in PALM/STORM experiments as in Fig. 2.5, with stimulation with DNP-BSA for 6 minutes at 37 °C. We see that the liquid ordered markers PM and GPI show hints of the same trend found for Lyn, namely a higher cross-correlation for Y16 and DNP-BSA compared to Y46, while this is not seen for liquid disordered marker GG. This would suggest that the clusters formed with Y16 or DNP-BSA, due to their higher density, are more effective at stabilizing a local liquid ordered-like phase. However, these signals are low compared to that from the uniform, non-cell surface, and so cannot be confidently distinguished from the noise inherent to the imaging system. Flaer shows the highest cross-correlation signal, especially under DNP-BSA stimulation, and is clearly above the level of background noise. his too suggests a stabilization of liquid ordered phase by clustered receptors, but raises the question why the same high signal was not detected with mEos-GPI.

(Figure 2.6, continued) It is possible that overexpression of the mEos-GPI construct changes the overall distribution of GPI on the membrane, making Flaer the more realistic probe. Alternatively, Flaer might be detecting some specific endogenous GPI-anchored protein that is located near receptor clusters by either lipid-mediated or protein-mediated interactions. The cross-correlation with DNP-BSA for Lyn and PM is low compared to previously published results (13). We attribute the differences to changes over time in the population of RBL cells used in the lab. For the transient changes we are observing, this population-level variation can affect whether the colocalization is detectable above the baseline. (b) Cells were instead stimulated at room temperature (RT) for 15 minutes. This universally increased the cross-correlation amplitude in all conditions tested, but did not preserve the relative trend between DNP-BSA, Y16, and Y46. These results are reasonable based on the Ising model: at a lower temperature, the membrane will be closer to phase transition, with a larger typical domain size. This makes lipid redistribution more prominent, but makes differences in receptor density less important, as even a low density cluster could effectively stabilize domains. (c) Cells were preincubated with the inhibitor of actin polymerization Cytochalasin D (CD), for 5 minutes before stimulation for 6 minutes at 37°C. This treatment also universally increased the cross-correlation with Lyn or PM for all ligands, consistent with previous results (13). However, this treatment also did not preserve the relative differences between ligands.

The number of cells imaged for each condition is given below each bar on the graph. Error bars show standard error of the mean.

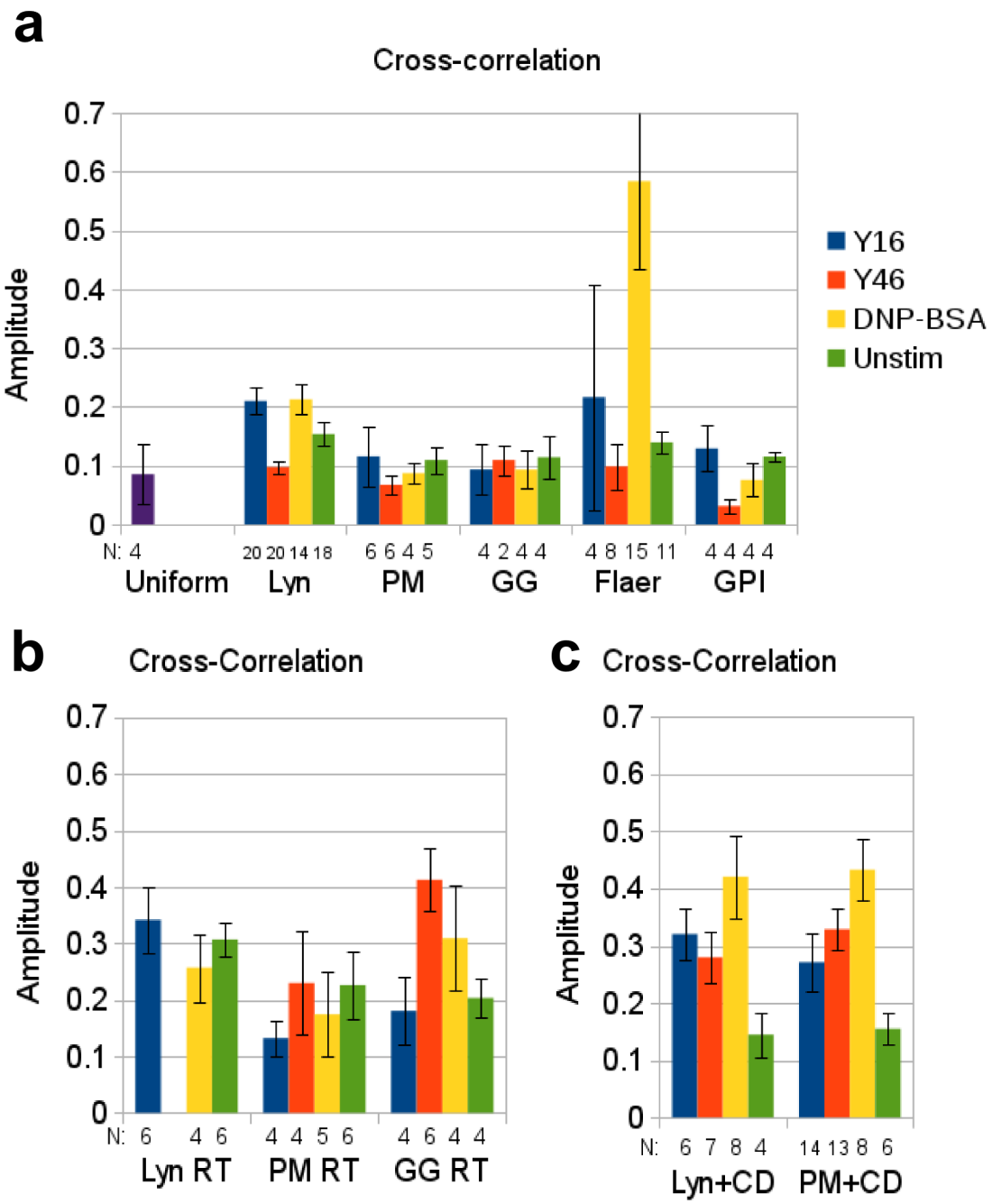
a
Cross-correlation
Amplitude
0.7
0.6
0.5
0.4
0.3
0.2
0.1
0
N: 4 20 20 14 18 6 6 4 5 4 2 4 4 4 8 15 11 4 4 4 4
Uniform
Lyn
PM
GG
Flaer
GPI
Y16
Y46
DNP-BSA
Unstim
b
Cross-Correlation
Amplitude
N: 6 4 6 4 4 5 6 4 6 4 4
Lyn RT
PM RT
GG RT
c
Cross-Correlation
Amplitude
N: 6 7 8 4 14 13 8 6
Lyn+CD
PM+CD

includes clustered membrane receptors.

We used the two-dimensional Ising model to model a membrane near a critical phase transition, in which black pixels represent Ld-preferring membrane components and white pixels represent Lo-preferring membrane components. We consider a receptor and a kinase that both prefer the Lo phase, as is thought to be the case for IgE-FcεRI and Lyn (16). The receptor is represented as a block of white pixels of diameter 4, and the palmitoyl and myristoyl membrane anchors of Lyn are represented as a single white pixel. In a Monte Carlo simulation, these proteins of interest are held fixed while the rest of the lattice pixels are allowed to flip between white and black. This generates thermodynamically probable snapshots of how the membrane phases might look, with the proteins set in the chosen positions (Fig. 2.7b). In our first set of simulations, we wanted to consider the difference between Y16 and Y46, so we configured the receptors in a cluster of three, with spacing either 5 nm (Y16) or 13 nm (Y46). We also compared these against a case with just one receptor present, representing an unstimulated receptor not cross-linked with antigen.

We first used Monte Carlo snapshots with no kinase present, and computed average images (Fig. 2.7a), which give a visual representation of how the cluster affects its local environment via the membrane. In all cases, the cluster forms a local region of membrane that is on average more ordered, but the nature of this ordered region depends on the configuration of receptors used. Note that for Y16, the interior of the cluster is on average more ordered than for Y46.

To calculate how this affects kinase recruitment, we ran simulations with kinase located at each possible position along a transect (black lines, Fig. 2.7a) moving into the

cluster. From this series of simulations, we calculated a free energy profile associated with moving the kinase along the transect (Fig. 2.7c) (Materials and Methods). For a free energy value ΔF, the partition coefficient $e^{-\Delta F}$ gives the factor by which the concentration of kinase is predicted to increase at that position, compared to the bulk kinase concentration on the membrane.

Biologically, the important part of this profile is at low position coordinates on the x-axis (Fig. 2.7c, blue box), where the kinase would be close enough to the receptors to interact with and phosphorylate them. Within this region, the kinase has the lowest free energy within the Y16 cluster. The minimum free energy is about -0.6 k_BT, compared to values at the same radius of -0.3 k_BT for Y46 and -0.2 – -0.3 k_BT for the unclustered case. The minimum free energy for the Y16 cluster of -0.6 k_BT corresponds to a partition coefficient of $e^{0.6} \approx 1.8$, meaning that the kinase concentration is 1.8 times higher inside the cluster than outside the cluster. The partition coefficient for the Y46 cluster is $e^{0.3} \approx 1.3$, and the Y16 cluster is predicted to recruit $e^{0.6-0.3} \approx 1.3$ times more kinase than the Y46 cluster. This energy difference provides a purely lipid-mediated contribution to the increased density of kinase in Y16 clusters.

Our simulations were run at 1.07 times the critical temperature. This is reasonable based on experiments showing the true critical temperature can vary from 11 °C to 27 °C (35), implying physiological temperature is 1.03-1.09 times the critical temperature. To assess the temperature sensitivity of our simulations, we also ran them at 1.04 times the critical temperature, and found the energy wells extended to a longer distance from the cluster, had a higher minimum, and preserved the qualitative difference between Y16 and Y46 (Fig. 2.8).

Figure 2.7 The Ising model illustrates how a cluster of receptors may affect its local environment via the membrane lipids. All simulations were performed at 1.07 times the critical temperature. (a) Average images resulting from Monte Carlo simulations with receptors placed at spacing 5 nm (Y16) or 13 nm (Y46), or a single receptor. (b) Example snapshot of an Ising simulation in which 3 receptors (red) and one kinase (blue) are placed in the membrane. (c) Profile showing the free energy associated with moving a kinase along transects drawn in b. A lower free energy in the region of the profile close to receptors (blue box) indicates a higher predicted kinase concentration encountered by the receptors. Note that the sharp drop at position ≤ 2 is dominated by lattice-specific effects due to being very close to a single protein, and the plateaus in the Y16 and Y46 curves at position ≈ 3-10 are due to the regions of the transect passing between the two receptors, on the right side of the cluster in panel (a). (d-e) Average images (d) and energy profiles (e) for a case where the clusters contain a larger number of receptors at the same 5 or 13 nm spacing. (f-g) Average images (f) and energy profiles (g) for a cluster at 5 nm spacing, at varied average lipid composition, ranging from 5% to 80% white. The average image for 50% white is shown in (a). The lowest free energy is achieved at 20% white.

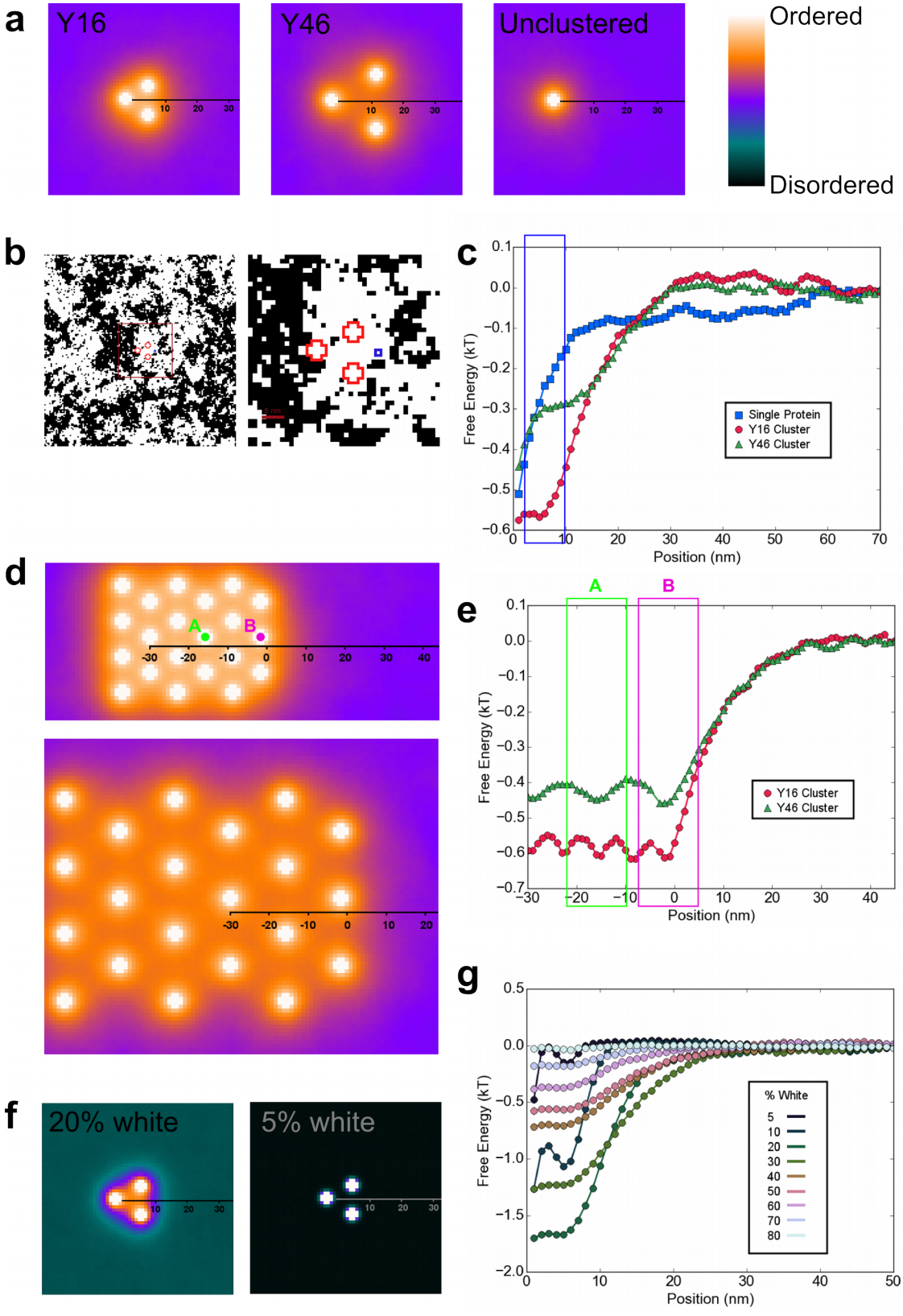
a
Y16
Y46
Unclustered
Ordered
Disordered
b
c
Free Energy (kT)
Position (nm)
Single Protein
Y16 Cluster
Y46 Cluster
d
A
B
e
Free Energy (kT)
Position (nm)
Y16 Cluster
Y46 Cluster
f
20% white
5% white
g
Free Energy (kT)
Position (nm)
% White
5
10
20
30
40
50
60
70
80

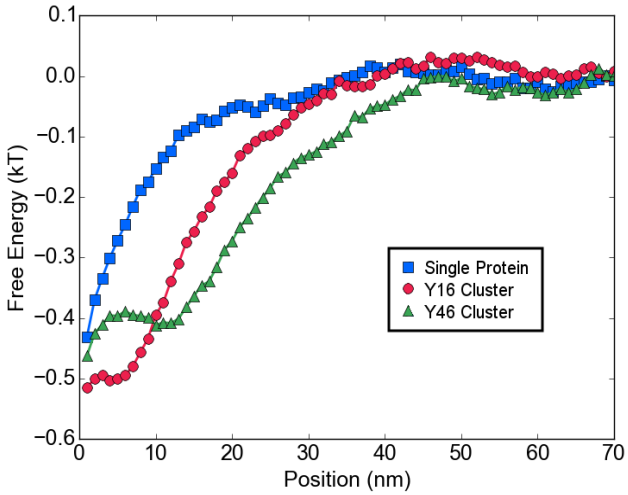

Figure 2.8 Free energy profiles, as in Fig. 2.7c, from Ising model simulations run at 1.04 times the critical temperature.

Physiological IgE clusters can vary in the number of IgE-FcεRI per cluster, and in our Y16/Y46 system, contain many more than just 3 receptors (Table 2.1). Therefore, we next considered how total number of receptors in a cluster affects kinase recruitment to that cluster. We assume the total number of clustered receptors on the cell remains constant (in many small clusters, or fewer large clusters), and so focus on how the kinase concentration per receptor changes. We performed simulations on a large array of receptors at either 5 nm (Y16) or 13 nm (Y46) spacing, and as before, computed average images (Fig. 2.7d) and free energy profiles (Fig. 2.7e). We found that compared to the three-receptor cluster there is a similar minimum free energy achieved by the kinase within this larger cluster. That is, the maximum kinase concentration within a receptor cluster depends on only the receptor density, not the number of receptors. This is consistent with our experimental results: Clusters from Y46 were less effective at signaling than Y16, even though they were similar in number of receptors per cluster.

However, this case reveals an important advantage of having large clusters. Compare a receptor in the interior of the large cluster (Fig. 2.7d, top panel, labeled A) to one at the edge of the cluster (labeled B). On the free energy profile (Fig. 2.7e), the receptors might be able to interact with any kinase located within boxes A and B, respectively. We see that receptor A will encounter more total kinase because the minimum free energy is achieved throughout box A, whereas on one side of box B, the free energy has already started to increase due to being outside the cluster. More generally, receptors located on the edge of the cluster encounter less total kinase than those in the interior. This implies that very small clusters, where most receptors are on the edge, will be worse at signaling than large clusters. This relates to our experimental

results with bivalent ligands, which form small clusters and are less effective in signaling. On the other extreme, in very large clusters, most of the receptors already are in the interior. Further increases in the number of receptors are less helpful, and receptor density becomes the most important feature, as we observed with the trivalent ligands.

The calculated free energy changes are sufficient to explain the changes in Lyn localization in our system, but are still rather small in magnitude compared to thermal energy k_BT. We were curious whether this is an upper bound in general for lipid-mediated protein localization in a two-phase system described by a lattice model. We found that in fact, a larger free energy change can be achieved by varying the composition of the membrane (Fig. 2.7f-g). A minimum free energy of -1.6 k_BT is achieved in a membrane with 20% white pixels. This picture could be biologically relevant if a certain subpopulation of lipids, totaling 20% of the membrane, had an especially strong interaction with the receptors and kinase. This would not be the entire Lo phase, which covers upwards of 50% of the membrane according to some estimates (36, 37), but perhaps could be a subset of the lipids that have an especially strong attraction to the receptors and kinase.

2.4 Discussion

Using super-resolution imaging in conjunction with structurally defined ligands, we have identified how the spatial configuration of IgE-FcεRI – in particular the density of receptors, and in limiting cases the number of receptors per cluster – relates to the capacity of the cluster to recruit Lyn kinase, and mediate transmembrane signaling

leading to a cellular response. Based on our theoretical modeling with the Ising model, we suggest a lipid-mediated mechanism consistent with the observed density and number dependence.

A high density of IgE-FcεRI leads to more effective signaling

Our comparison of structurally defined ligands Y16 and Y46 identify the density of IgE-FcεRI in clusters as a key structural feature in determining IgE-FcεRI signaling capacity, with a higher receptor density leading to a stronger functional response. By design, these ligands hold the receptors at different spacing – ~ 5 nm for Y16 and ~ 13 nm for Y46 – in order to create IgE-FcεRI clusters of different spatial configurations. In terms of a downstream cellular response, we show that Y16 stimulates stronger degranulation than Y46 (Fig. 2.2), which is consistent with the initial characterization of these ligands (29) . Our correlation function analysis of the one-color, live cell imaging data (Fig. 2.1c) quantifies the configurational difference that correlates with this functional difference, and indicates that it is mainly based on density. Y16 clusters have a higher receptor density than Y46 clusters, as quantified by the correlation amplitude (10 versus 5) or the value of the correlation function at a small radius (g(30 nm) equal to 6 versus 4). In contrast, other structural features of clusters – the number of receptors, mobility of the clusters, and area of the clusters – appear less important in distinguishing the signaling capacity of these clusters, as Y16 and Y46 clusters have similar diffusion coefficients and number of receptors per cluster, and the weaker stimulant Y46 has the larger cluster area as quantified by the correlation length.

DNP-BSA, which has been characterized by dSTORM here and previously (5), is consistent with the trend of density dependence. DNP-BSA is chemically

heterogeneous, making it less clear how the IgE-FcεRI clusters are formed structurally, but our measured correlation amplitude of 24 and g(30 nm) = 11 for DNP-BSA indicates that, at least on average, DNP-BSA forms clusters of an even higher density than Y16. This is intuitively reasonable, given that DNP-BSA contains an average of about 15 DNP groups on a protein of longest dimension ~ 14 nm, it is likely that some of these groups have a closer spacing than the Y16 spacing of ~ 5 nm. The clusters of high receptor density generated by DNP-BSA correlate with a larger degranulation response than Y16 (Fig. 2.2). We note that the degranulation response stimulated by DNP-BSA may be further enhanced due to the higher valency of DNP-BSA, if the higher binding avidity leads to more stable, long-lived IgE-FcεRI clusters. The limited time resolution of dSTORM makes it difficult to precisely measure cluster lifetime in order to test for this potential difference.

A lipid-based mechanism explains the connection between IgE-FcεRI density and signaling capacity

We seek to understand the mechanism behind the observed dependence on FcεRI density for downstream function. Transphosphorylation has been proposed as one possibility (29). In this mechanism, Lyn associated with one FcεRI – either transiently in the earliest stages of Lyn/FcεRI coupling (38), or more stably after initial FcεRI phosphorylation via binding the FcεRI-β ITAM (29) – phosphorylates another FcεRI in close proximity. In either case, receptors would have to be positioned close enough to each other for transphosphorylation to occur, which would give a dependence on receptor density. In T cell receptor signaling, density dependence has also been observed, and a mechanism was proposed based on receptor conformational changes

(39). Here, we present another potential mechanism based on lipid reorganization. This lipid-based contribution potentially exists in addition to, and perhaps enhances, the other proposed mechanisms for density dependence. However, as we describe below, the lipid-mediated mechanism may be strong enough to entirely account for the experimentally measured Lyn partitioning.

Our model is based on a few assumptions, which have reasonable basis in existing literature. We assume that the membrane exists near a critical phase transition, as suggested in studies with giant plasma membrane vesicles (17), and we assume that both cross-linked IgE-FcεRI and Lyn have a preference for the Lo phase, as supported by detergent-resistant membrane studies (14) and previous super-resolution imaging (13). The general concept is that when several IgE-FcεRI, each with some preference for the Lo phase, are brought in close proximity, a larger Lo domain is stabilized (visualized in Fig. 2.7a), and promotes the partitioning of Lyn to that region of the membrane. Our model is explicit and quantitative through our use of simulations to calculate energy profiles (Fig. 2.7c), showing a stronger free energy change for recruitment of Lyn to a IgE-FcεRI spacing consistent with Y16 (-0.6 k_BT) than one consistent with Y46 (-0.3 k_BT). It is important to note that this partitioning is entirely lipid-mediated, depending only on the phase properties of the membrane and the preferential partitioning of Lyn and FcεRI, and occurs before any specific phosphorylation or binding interactions between Lyn and FcεRI.

A sufficient number of IgE-FcεRI per cluster is necessary for effective signaling

Studies with the bivalent ligand Y16bi suggest that the number of IgE-FcεRI per cluster is a secondary feature that contributes to the signaling capacity of the stimulus.

Y16bi has the same ligand spacing as Y16, but stimulates a considerably lower degranulation response, consistent with other bivalent ligands studied previously (28, 31). Our one-color, live cell STORM results show, unsurprisingly, that the number of receptors per cluster is smaller for Y16bi (Table 2.1, 13 for Y16bi compared to 30 for Y16). In addition, the density as measured by correlation amplitude is also smaller for Y16bi, even though the ligand spacing is the same as for Y16. The difference is in part because a single chain of receptors, arranged roughly in a random walk, will likely have less tight receptor packing, on average, than a highly cross-linked network of receptors. A second contribution to the amplitude difference is explored in Fig. 2.7d-e: Receptors that sit on the edge of the cluster (e.g. Fig. 2.7d, receptor B) do not experience the maximum receptor density possible for the ligand spacing, and in small clusters, most receptors sit on the edge. In this way, a high (low) number of receptors per cluster can be seen as a means to achieve a high (low) average density of receptors. Therefore, our suggested mechanism based on receptor density can also be used to explain the secondary dependence on number of receptors per cluster.

Lyn cross-correlation with IgE-FcεRI clusters is a detectable consequence of lipid-mediated partitioning

Our two-color PALM/STORM imaging of cells fixed after stimulation shows that high- and low-density IgE-FcεRI clusters are distinguished at the earliest stages of signaling in the recruitment of the kinase Lyn, and suggest that the differential recruitment of Lyn leads to the differences in magnitude of the downstream degranulation response. Clusters due to Y16 or DNP-BSA show an average cross-correlation amplitude of 0.21, compared to 0.10 for Y46. We emphasize that this Lyn

coupling is extremely subtle – in the strongest cases of Y16 and DNP-BSA, only a 21% increase in the concentration of Lyn above random background. Yet these small differences in Lyn coupling correlate with large differences in the degranulation response. This reinforces the idea that only a small perturbation is necessary to tip the balance in favor of signaling. This is consistent with theoretical work (11) that found only a small proportion (5-10%) of Lyn needs to couple with IgE-FcεRI clusters to explain measured time courses for FcεRI phosphorylation.

In our proposed model of IgE-FcεRI initiation of transmembrane signaling, the initial, lipid-mediated association of Lyn and FcεRI depends on receptor density, and leads to the phosphorylation by Lyn of the FcεRI-β subunit. Following phosphorylation, a more stable association between Lyn and FcεRI-β is possible via binding of the Lyn SH2 domain to the β subunit's phosphorylated ITAMs. It is this more stable association that we are able to detect by IgE/Lyn cross-correlation at an amplitude of 0.21. Given that this cross-correlation amplitude already sits near the lower detection limit of two-color PALM/STORM (amplitude ~ 0.1), it is not surprising that the redistribution of lipids, a weaker phenomenon than the stable association, is below the detection limit.

Still, we argue based on our theoretical modeling that a lipid-mediated mechanism for the initial coupling of Lyn with FcεRI is compelling. Our model predicts a maximum partition coefficient of 1.8 for the Y16 cluster. The actual partition coefficient we would predict based on a IgE/Lyn cross-correlation of 0.21 is a value smaller than 1.21, well below our maximum value of 1.8. This means that even if the membrane, IgE-FcεRI, and Lyn are not perfectly described by the Ising model, making the actual partitioning less than optimal, it is still reasonable to expect the lipid-mediated

partitioning to be high enough to mediate the required extent of Lyn/FcεRI coupling.

Related modeling work with the Ising model by Veatch et al. (19) emphasizes the distinction between the early, weak lipid-mediated Lyn coupling and the more stable association following the phosphorylation of FcεRI-β. Veatch et al. use the more indirect readout of Lyn clustering (if Lyn is highly associated with clustered IgE-FcεRI, then Lyn, too, should appear clustered), and show that Lyn clustering is only detectable when a very strong protein-mediated Lyn/FcεRI interaction is included in addition to the normal lipid-mediated Ising model interactions. Veatch et al. chose a Lyn/FcεRI coupling energy of 10 times the Ising coupling J, or ~ 4.2 k_BT, which led almost all Lyn in the simulation to be associated with FcεRI. Our experimental cross-correlation amplitude of only 0.21 suggests that the Lyn/FcεRI coupling is more limited, but we agree with the concept that the stronger protein-mediated coupling is more readily detectable than the initial lipid-mediated coupling.

We note that previous two-color PALM/STORM studies (13), a considerably larger cross-correlation was detected between IgE and Lyn (amplitude ~ 1.3 compared to 0.21) upon simulation with DNP-BSA. In this case, the weaker lipid reorganization was also detectable by cross-correlation of IgE-FcεRI and the Lo marker PM-mEos at a lower amplitude of ~ 0.7. We attribute the differences from the present study to the variability in the cell population used in the study. While RBL-2H3 cells are highly reliable in eliciting clear functional responses such as Ca^{2+} mobilization and degranulation, they remain heterogeneous in terms of more subtle processes such as Lyn coupling, and PALM/STORM is a sufficiently powerful technique to detect these subtle differences. The results from the previous study give additional support to our

model that the initial stages of Lyn coupling are lipid-mediated. The present study suggests that the higher level of Lyn coupling previously reported is not required, as the cell population evaluated in the present study exhibits a similar degranulation response with a more limited extent of Lyn coupling. At this lower level of Lyn coupling, the lipid reorganization drops to below the detection limit.

Technical considerations for two-color imaging

The technical development associated with this study (Supplementary Note) serves as a cautionary tale in the use of PALM/STORM to detect subtle biological phenomena as we have done here. While it is exciting to use super-resolution imaging to detect processes that were previously elusive, an appropriate amount of caution is necessary to prevent channel cross-talk artifacts from leading to erroneous conclusions. In the case of the present study, one dye that we considered, Dy654, would have generated artifactual cross-correlation at an amplitude similar to our true signal. Had we used this label, we would have incorrectly concluded that every protein tested shows stimulation-dependent colocalization with IgE, and been unable to extract the true signal from Lyn/IgE colocalization. Consideration of channel cross-talk is especially important when the true colocalization signal is low, such as in this study. There is an additional risk when the dye in question is clustered, as with cross-linked IgE, because then a small amount of cross-talk can lead to a large apparent colocalization.

We further stress that the particular fluorophores that are acceptable on our microscope system differ from what others have reported previously (40), due to differences in either the individual dye stock, or in the optical components of the microscope. This suggests that, rather than looking to an increasingly long list of “bad

STORM dyes," each research group should perform the necessary control experiments to verify that for the particular microscope, the dyes used do not exhibit channel cross-talk at a level that would interfere with the conclusions of the study.

We would recommend the following minimal test. Once near the start of the study, a 1-color control sample such as in Fig. 2.13 should be prepared and analyzed in parallel to the two-color experiments of interest. Then, Supplementary Note equation 13 should be applied to determine how any cross-talk affects the true colocalization signal. The STORM dye should only be used in the study if the cross-talk signal is acceptably small in comparison to the true colocalization signal to be detected.

2.5 Conclusion

In summary, we have applied complementary experimental and theoretical techniques to probe the molecular basis of transmembrane signaling initiated by antigen-clustered IgE-FcεRI. We showed that the density of IgE receptors within a cluster is a key structural feature that affects the capacity of that cluster to signal, both at the earliest stage of kinase recruitment and in downstream functional responses. We propose a model for a lipid-mediated contribution to this density dependence, in which clusters of a higher receptor density more effectively stabilize a Lo-like membrane domain, which then promotes the recruitment of Lyn kinase.

2.6 Materials and Methods

Reagents

Anti-DNP IgE was prepared as described in (41). Organic dyes were conjugated

to IgE by reaction with a N-hydroxy-succidimidyl ester of the dye (Alexa Fluor 647, Dyeomics 654, or Alexa Fluor 488) overnight in borate buffered saline (200 mM boric acid, 160 mM NaCl, pH adjusted to 8.5 with NaOH) at room temperature, followed by dialysis for 3-7 days at 4°C to remove unreacted dye. The average dye:protein ratio measured by UV-vis spectroscopy was 1.3 for AF647-IgE, 1.1 for Dy-654 IgE, and 7.6 for AF-488 IgE. All labeled IgE preparations were tested by degranulation assays to verify that they elicit the same functional response as unlabeled IgE.

Lyn-mEos, mEos-GG, and PM-mEos constructs were described previously (13). mEos-GPI (42) was a gift from Dr. Sarah Veatch (University of Michigan).

Y16 and Y46 ligands were prepared from ssDNA (IDT), sequences listed in (29), with a dinitrophenyl moiety attached to the 5' end of each strand. Strands were annealed on a thermal cycler (Bio-rad) by heating to 95°C for 5 min, then 60 °C 4 min, then cooled to 4 °C at a rate of 1°C/min, in a buffer consisting of 50 mM NaCl, 1 mM EDTA, 10 mM Tris pH 8. For Y16, the NaCl concentration was increased to 500 mM.

DNP-BSA, containing of roughly 15 DNP groups, on average, per BSA molecule, was prepared as described in (43).

B1E3 antibody (34) was a gift from Dr. Daniel Conrad (Virginia Commonwealth University).

Cell Sample Preparation

RBL-2H3 cells were cultured in media consisting of 80% Minimal Essential Medium, 20% Fetal Bovine Serum, and 50 µg/mL gentimicin. On the day prior to sample preparation, MatTek imaging dishes (35 mm dishes with 14 mm microwell and no. 1.5 coverglass) were plasma cleaned for 6 min, plated with 110,000 cells per dish, and

incubated overnight to allow cells to adhere to the glass and spread.

For samples requiring genetically encoded constructs, cells were chemically transfected. For each MatTek dish to be transfected, media was replaced with 1 mL OptiMEM (Gibco), then a transfection solution consisting of 2 µg plasmid, 6 µL Fugene (Promega) in 100 µL OptiMEM per dish was added. After 1 hour incubation, 1 mL of 0.1 µg/mL phorbol dibutyrate in OptiMEM was added. After an additional 3 hours, cells were returned to normal media, and incubated overnight before use.

Fluorescently labeled IgE (AF647-IgE, Dy654-IgE, or AF488-IgE) was diluted in buffered salt solution (BSS; 135 mM NaCl, 5 mM KCl, 1 mM $MgCl_2$, 1.8 mM $CaCl_2$, 5.6 mM glucose, 20 mM HEPES pH 7.4) plus 1 mg/mL bovine serum albumin (BSA) to a final concentration of 2 µg/mL. Cell samples were incubated with labeled IgE solutions for 40 minutes at room temperature, then excess IgE solution was rinsed off with BSS.

Live cell samples were imaged immediately following IgE sensitization.

For cell samples to be chemically fixed, IgE solution was rinsed off and replaced with antigen solution at the desired concentration in BSS. The sample was incubated at the specified temperature for the specified time (37°C, 6 minutes unless otherwise indicated), then fixed with a solution of 4% paraformaldehyde and 0.4% gluteraldehyde, for 10 minutes. Fixative was quenched with blocking buffer (10 mg/mL BSA, 0.02% NaN_3 in phosphate buffered saline (PBS)) for 10 minutes, then buffer was removed and replaced with 1 mL fresh blocking buffer for storage. Fixed samples were imaged within two weeks of preparation.

Microscope

Imaging was performed on a home-built system consisting of a Leica DM-IRB

inverted microscope, 405 nm, 488 nm and 561nm (Coherent) and 642 nm (CrystaLaser) lasers, 100x NA 1.47 TIRF objective (Leica), Optosplit (89 North), and a Andor iXon DU-897 EMCCD camera. Data were collected using home-built MATLAB camera control software.

One-color super-resolution imaging of live cells

Imaging buffer consisted of 15 mg/mL glutathione, 9 mg/mL glucose, 0.5 mg/mL glucose oxidase, 0.04 mg/mL catalase in Tris buffered salt solution (135 mM NaCl, 5 mM KCl, 1 mM $MgCl_2$, 1.8 mM $CaCl_2$, 5.6 mM glucose, 30 mM Tris pH 8.0-8.5). This buffer supports cell signaling (5).

1 mL imaging buffer was added to cells sensitized with fluorescent IgE. A cell was located under the microscope. The cell was imaged for at least 5 min prior to stimulation. Antigen was diluted in 1 mL imaging buffer to 2 times the desired final concentration. The antigen solution was added to the sample on the microscope, and the time of addition was noted. The cell was imaged for at least 13 min following stimulation.

Raw data were collected in blocks of 500 frames, with each block used to reconstruct one final image. The frame rate varied between cells in the range of 31-54 fps, using the fastest frame rate possible with our EMCCD given the size of the chosen field of view. Illumination consisted of a 100 mW 642 nm excitation laser, with a neutral density filter of 0.14 for Dy654-IgE samples used for rendering well-sampled images, or a neutral density filter of 0.9 for AF647-IgE samples used for acquiring single-molecule trajectories.

Two-color super-resolution imaging of chemically fixed cells

In order to perform two-color PALM/STORM, it was necessary to achieve channel alignment to a higher accuracy than our ~ 30 nm resolution. An alignment sample was used consisting of 200 μm tetraspeck beads (ThermoFisher) adhered to a MatTek imaging dish at a density giving 10-50 beads per field of view. 80-100 2-color TIRF images of the alignment sample were acquired before and after each cell imaged to enable acceptable channel alignment (Fig. 2.11).

Imaging buffer consisted of 10μL/mL beta mercaptoethanol, 50 mg/mL glucose, 0.5 mg/mL glucose oxidase, 0.04 mg/mL catalase in 0.1 M Tris buffer, pH adjusted to 8.0-8.5.

A mercury arclamp was used to identify cells expressing mEos 3.2 constructs by eye. Cells were imaged simultaneously in red (mEos) and far red (AF647) channels. A total of 10000 frames per cell were collected at 10 ms exposure time, 31 frames per second. Illumination consisted of 642 nm and 561 nm excitation lasers each at 100 mW with a neutral density filter of 0.44, and 405 nm activation laser, adjusted to achieve optimal signal density, in the range 0.3-1.0 mW with a neutral density filter of 1.44.

To verify that our microscope was adequately aligned and capable of detecting two-color cross-correlation, we imaged a positive control sample (Fig. 2.9), in which cells were sensitized with a 1:1 mixture of AF488-IgE and AF647-IgE, and either unstimulated or stimulated with 0.5 μg/mL DNP-BSA, 6 min at 37 °C. In the stimulated case, AF488-IgE and AF647-IgE should co-cluster, giving a large cross-correlation. The high measured cross-correlation of amplitude ~ 11-14 (Fig. 2.9b) indicates the microscope is well aligned.

Two-color control sample

Figure 2.9 Imaging of cells sensitized with two colors of IgE serves as a positive control for the two-color PALM/STORM setup. Separate populations of IgE were labeled with AF488 and AF647. Upon cross-linking with DNP-BSA, IgE-FcεRI forms large clusters containing both colors of IgE, so a high level of colocalization is expected. (a) 2-color image of Alexa Fluor 488 IgE and Alexa Fluor 647 IgE on a cell stimulated 6 min with 0.5 μg/mL DNP-BSA. Colocalization in clusters of the two colors is clearly visible. (b) Cross-correlation functions from the two-color experiments. Functions are plotted for 2 individual cells per condition. A very high cross-correlation is detected in the stimulated case, comparable in amplitude to IgE autocorrelation as shown in Fig. 2.5b. These results validate that our system is capable of detecting strong cross-correlation. Therefore the weak cross-correlation shown in Fig. 2.5c is not a microscope limitation, but rather reflects that there is weak colocalization between the two proteins.

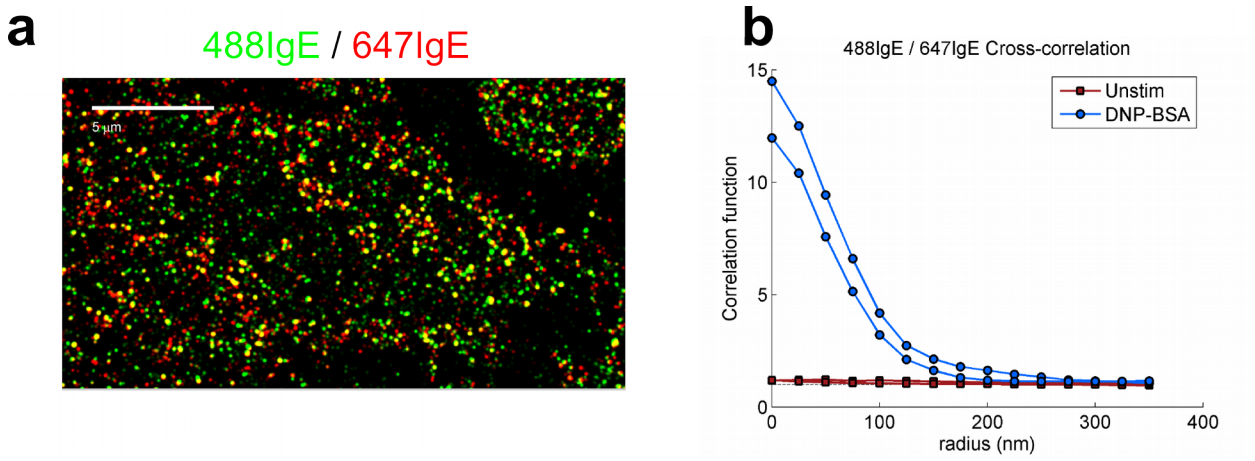
a
488IgE / 647IgE
5 µm
b
488IgE / 647IgE Cross-correlation
Unstim
DNP-BSA
Correlation function
radius (nm)
0
5
10
15
0
100
200
300
400

Figure 2.10: Membrane topography contributes to cross-correlation functions in unstimulated cells. (a) Example two-color PALM/STORM image of AF647-IgE and Lyn-mEos on an unstimulated cells. Large regions of slightly higher signal intensity are marked with yellow ovals. We identify these structures as podosomes. The increased signal in both channels is likely because, due to the topography of the membrane, more total membrane is present at those positions. (b) Cross-correlation functions for AF647-IgE / Lyn-mEos from Fig. 2.5c are shown again here, and the average cross-correlation for unstimulated cells (blue curve) is included. A podosome contribution to cross-correlation is apparent for the unstimulated case, in that it does not decrease to 1 at large radii. In contrast, for all stimulated cases, cross-correlation functions are close to 1 at a radius of 350 nm, suggesting that these large topgraphical structures disappear upon stimulation.

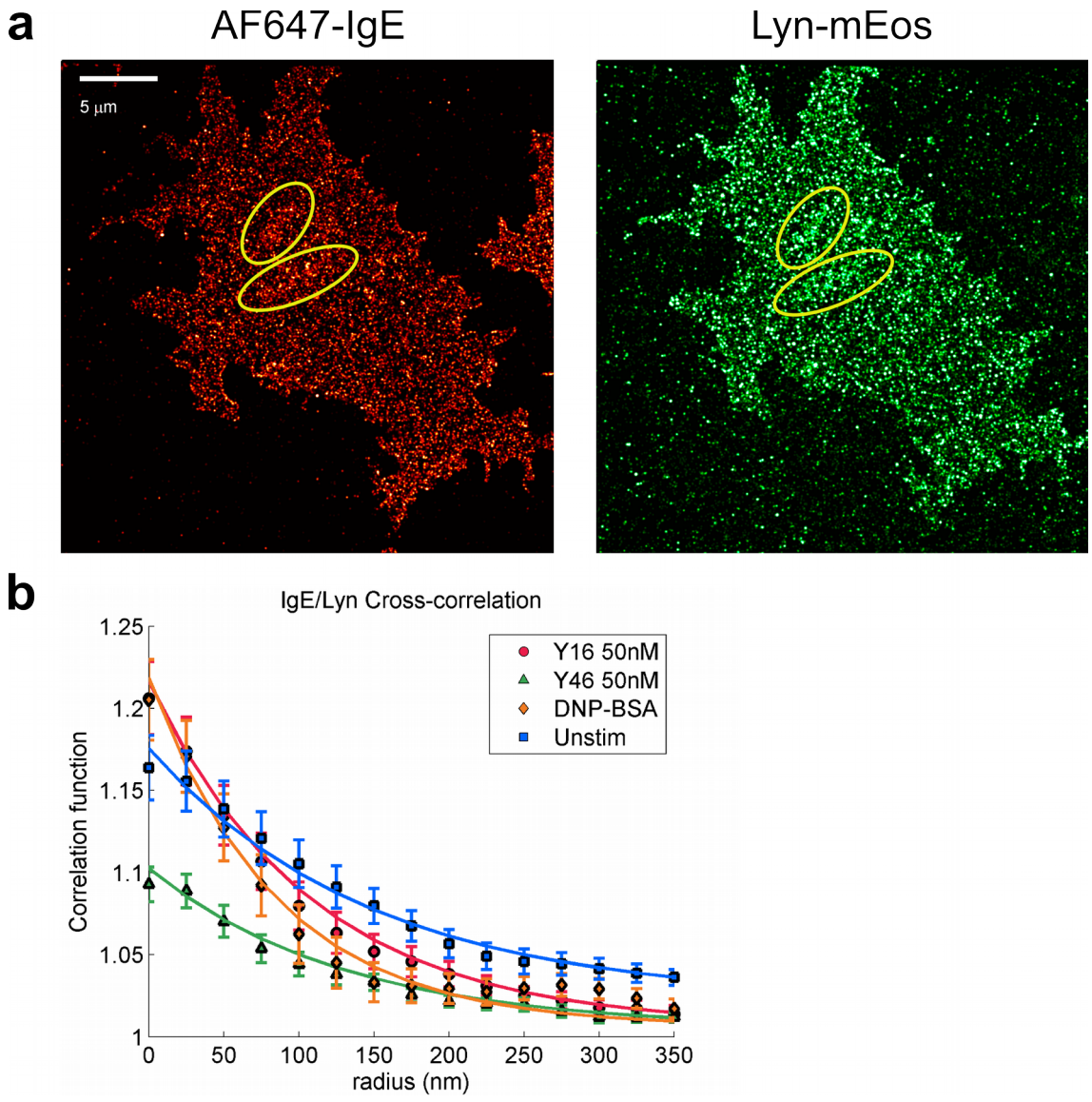
a
AF647-IgE
Lyn-mEos
5 µm
b
IgE/Lyn Cross-correlation
Y16 50nM
Y46 50nM
DNP-BSA
Unstim
Correlation function
radius (nm)
1.25
1.2
1.15
1.1
1.05
1
0
50
100
150
200
250
300
350

The intuitive negative control for comparison to the stimulated colocalization of Lyn-mEos and AF647 IgE (Fig. 2.5) would be the corresponding unstimulated cell sample. However, such a comparison was difficult due to the presence in unstimulated cells of membrane morphology such as podosomes, which contribute to the cross-correlation function with an amplitude comparable to our true colocalization signal (Fig. 2.10). This membrane morphology was not present in stimulated samples, likely because of cell spreading.

As an alternate control, we turned to a synthetically made surface that has a uniform distribution of fluorescent labels, namely fluorescent proteins covalently bound randomly to a silanized glass surface. This control still captures any cross-correlation contribution inherent to the microscope setup, although does not capture any baseline association between Lyn and FcεRI.

Glass coverslips were cleaned overnight in a 1:1 solution of methanol and 30% HCl. Coverslips were plasma cleaned twice for 30 s, dried, rinsed in toluene, then incubated 30 min at room temperature in a solution of 4% (3-mercaptopropyl)trimethoxysilane in toluene. A 1M stock solution of N-(γ-maleimidobutyryloxy)succidimide ester was diluted to 4 mM in ethanol. Coverslips were incubated with the 4 mM solution for 30 min at room temperature. A coverslip was rinsed in ethanol, dried and attached to a MatTek imaging dish (35 mm dish with 10 mm hole) with Norland Optical Adhesive 68T. A protein solution was prepared in PBS consisting of 10 μg/mL AF647 IgE, 10 μg/mL AlexaFluor 568 (AF568) streptavidin, and 30 μg/mL BSA. Streptavidin was used simply as a conveniently available protein with a red label, and BSA was used to dilute the density of the fluorescent labels. The

coverslip was incubated with the protein solution for 2 hours at room temperature, allowing primary amines on the proteins to covalently bind at random to the functionalized glass. After incubation, the sample was incubated for 5 minutes with 1 mg/mL BSA in PBS to quench any remaining open binding sites, and then the sample was stored for future imaging.

The control sample was imaged according to the same protocol as for two-color cell samples.

Rendering super-resolution images

Image processing was performed on home-built MATLAB software. Prior to fitting, a time-averaged image over 500 frames was subtracted from each individual frame, to prevent the localization of non-blinking background. To to identify candidate localizations, images were subjected to Gaussian bandpass filtering, blurring events on short (0.75 px = 109 nm) and long (10 px = 1450 nm) length scales, to emphasize events on the length scale of the expected point spread function. Local maxima in the blurred image, which were at least 5 standard deviations above the mean intensity (or 7 standard deviations in the case of AF488 channels), were selected as candidate localizations. Candidates were localized in the unblurred image by a least squares fit to a two-dimensional Gaussian. Localizations that were abnormal in intensity, width, aspect ratio, or localization error were culled from the dataset. For two-color imaging, a transform was calculated based on images of the Tetraspeck alignment sample as previously described (13). Briefly, the localizations from the alignment sample were used to make a piecewise, nonlinear transform from coordinates of points in the Eos channel to the correct location in the far red channel. We achieved an average channel

Figure 2.11 Color channels are aligned with high precision. To test the precision of the two-color PALM/STORM channel alignment, the localizations of fiducial markers in the alignment sample were arbitrarily split into two groups. The channel transform was calculated from group 1 only, and the resulting transform was applied to the group 2 localizations. We measure the error of each transformed group 2 marker position from the true position of that marker. (a) Histogram of alignment errors for all markers used in one example channel alignment. The alignment is acceptable because the vast majority of markers show an error less than our STORM resolution of ~ 30 nm. (b) Plot of all localizations used in (a) according to their position within the field of view and alignment error. Note that many of the poorly aligned markers are at the edges of the field of view, areas which were not used for the actual cell imaging. A smaller number of poorly aligned markers in the center are likely due to markers that were poorly localized. (c) Average alignment error per cell, for all cells used for Fig. 2.5c. For all cells, the alignment error is acceptably low compared to STORM resolution. To assess how much the channel alignment drifts over the course of imaging, we performed an alternate analysis (red curve) in which group 1 contained all the markers imaged before STORM imaging, and group 2 contained all the markers imaged after. The calculated error was still below STORM resolution, indicating there was not excessive alignment drift during imaging. However, this error is worse than the simple alignment error, indicating that the alignment does have some drift, and therefore it is useful to image the alignment sample before and after imaging every cell.

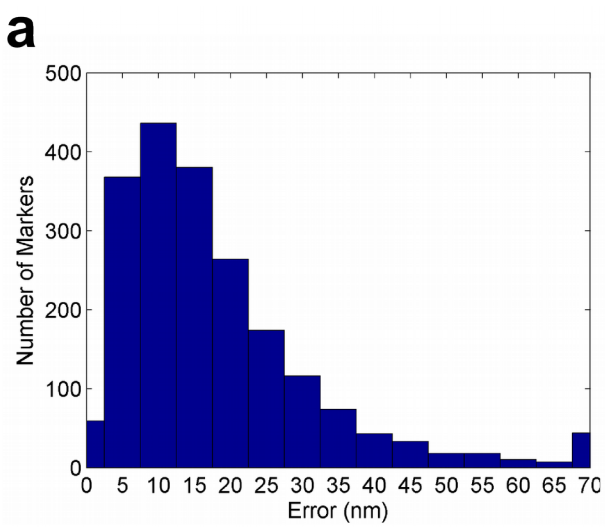
a
Number of Markers
Error (nm)
0
100
200
300
400
500
0 5 10 15 20 25 30 35 40 45 50 55 60 65 70

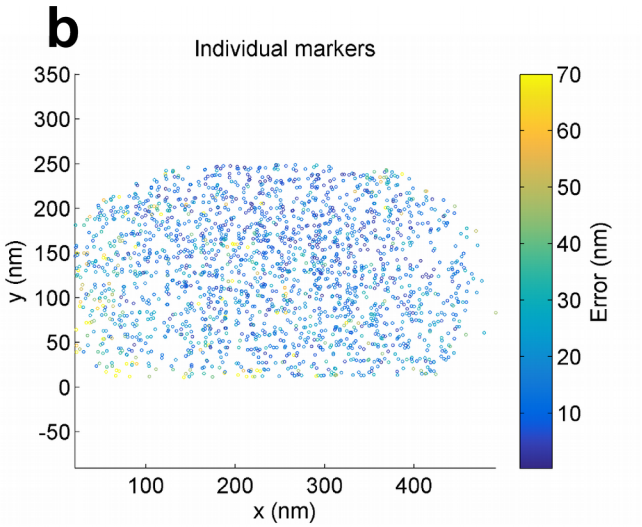
b
Individual markers
y (nm)
x (nm)
Error (nm)
350
300
250
200
150
100
50
0
-50
100 200 300 400
70
60
50
40
30
20
10

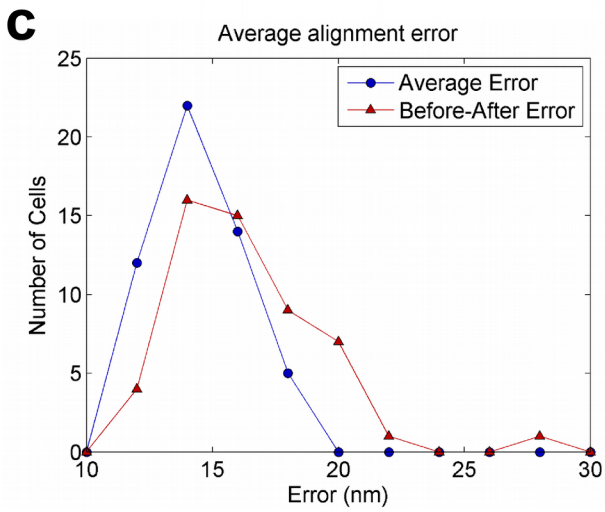
c
Average alignment error
Average Error
Before-After Error
Number of Cells
Error (nm)
25
20
15
10
5
0
10 15 20 25 30

alignment error in the range of 10-20 nm (Fig. 2.11). The alignment sample was imaged before and after imaging each cell, and the two sets of images were combined to compute the transform, to correct for any drift in alignment that occurred during imaging. We detected that the channel alignment does indeed worsen in the time needed to image one cell (Fig. 2.11c), indicating that it is important to realign the channels this frequently. The image was corrected for stage drift by optimizing the cross-correlation between consecutive blocks of 500 frames of localizations. Finally, images were rendered by binning localizations into pixels of 25 nm by 25 nm. For display purposes, the image was convolved with a 30 nm Gaussian to reflect the uncertainty of localization.

Correlation function analysis of super-resolution images

Pair correlation functions (Chapter 1, Fig. 1.2b) were calculated for a manually drawn region of interest including the entire cell, using fast Fourier transform (FFT) methods as previously described (20). We took the image I containing the PALM/STORM localizations, subjected to a mask M defining the shape of the cell (equal to 1 on the cell and 0 off of the cell), and the density of localizations in the masked image ρ. A two-dimensional autocorrelation function $g_{2D}(r)$ was computed according to the equation

$$g_{2D}(r) = \frac{1}{\rho^2} \frac{FFT^{-1}\left(\left|FFT(I)\right|^2\right)}{FFT^{-1}\left(\left|FFT(M)\right|^2\right)} \quad (1)$$

For cross-correlation analysis, the computation of $g_{2D}(r)$ takes a similar form, but includes images I1 and I2, with densities ρ1 and ρ2, from channels 1 and 2 respectively (overline denotes the complex conjugate):

$$g_{2D}(r)=\frac{1}{\rho_1\rho_2}\frac{FFT^{-1}\left(FFT(I_1)\overline{FFT(I_2)}\right)}{FFT^{-1}\left(\left|FFT(M)\right|^2\right)} \quad (2)$$

$g_{2D}(r)$ was radially averaged to give the correlation function g(r) that we use for analysis. g(r) was fit to the form

$$g(r)=Ae^{-r/\xi}+C \quad (3)$$

From this fit, we extracted the amplitude, A, which represents the density of receptors in clusters, and the correlation length ξ, which represents the length scale (radius) of clusters. The constant C was always close to 1, but included as a parameter to be fit. Additionally, we scale the integral of the correlation function according to an assumed total density of IgE-FcεRI of 200 per μm^2 (44) to obtain average the number of receptors per cluster N.

One-color PALM/STORM measurements carry the concern of over-counting due to multiple localizations of the same molecule (20). For live cell measurements, the concern is lessened because the molecules are diffusing, and will not likely yield multiple localizations at the same location. Still, it is possible some over-counting exists, which would lead to an overestimate of amplitude and number per cluster, and an underestimate of correlation length. There is some variation in the absolute numbers for amplitude and number per cluster if imaging conditions are varied, e.g. using AF647 IgE, which yields a lower number of localizations (data not shown), which we attribute to higher over-counting. However, under the same imaging conditions, any over-counting contribution would be the same for all samples tested, so the relative differences we observe in autocorrelation parameters are robust.

We calculated the localization precision of our one- and two-color PALM/STORM imaging, and found that our super-resolved point-spread has a 1/e radius of 30-40 nm in

Figure 2.12 Quantification of PALM/STORM localization precision. The super-resolved point spread function was calculated as previously described (20), by subtracting the autocorrelation function the STORM image from the autocorrelation function of the same image in which probes are intentionally over-counted. (a) Example point spread function from a 1-color live cell experiment. The PSF was rendered using 1500 frames of raw data from the time course, from a section of the time course roughly 2 minutes after stimulation. (b) The radially averaged PSF (black) is well fit by an exponential decay (red), and the 1/e radius (correlation length) ξ is reported. (c) Histogram of 1/e radius calculated by the same analysis method on all cells used in Fig. 2.1c. Note that our typical STORM point spread function (ξ = 25-35 nm) is smaller than the typical size of the IgE-FcεRI clusters we are imaging (ξ = 40-80 nm), which allows us to resolve the structure of the clusters. (d-f) The same analysis is performed on the AF647 channel of the 2-color data reported in Fig. 2.5. (g-i) A similar analysis is performed on the Lyn-mEos channel of the 2-color data reported in Fig. 2.5. However, for this channel, the intentionally over-counted autocorrelation function is roughly equal to the regular autocorrelation function (which is dominated by unintentional over-counting), so the subtraction method cannot be used. Instead, we simply take the intentionally over-counted autocorrelation function to be the point spread function. This gives an upper bound on the true localization precision.

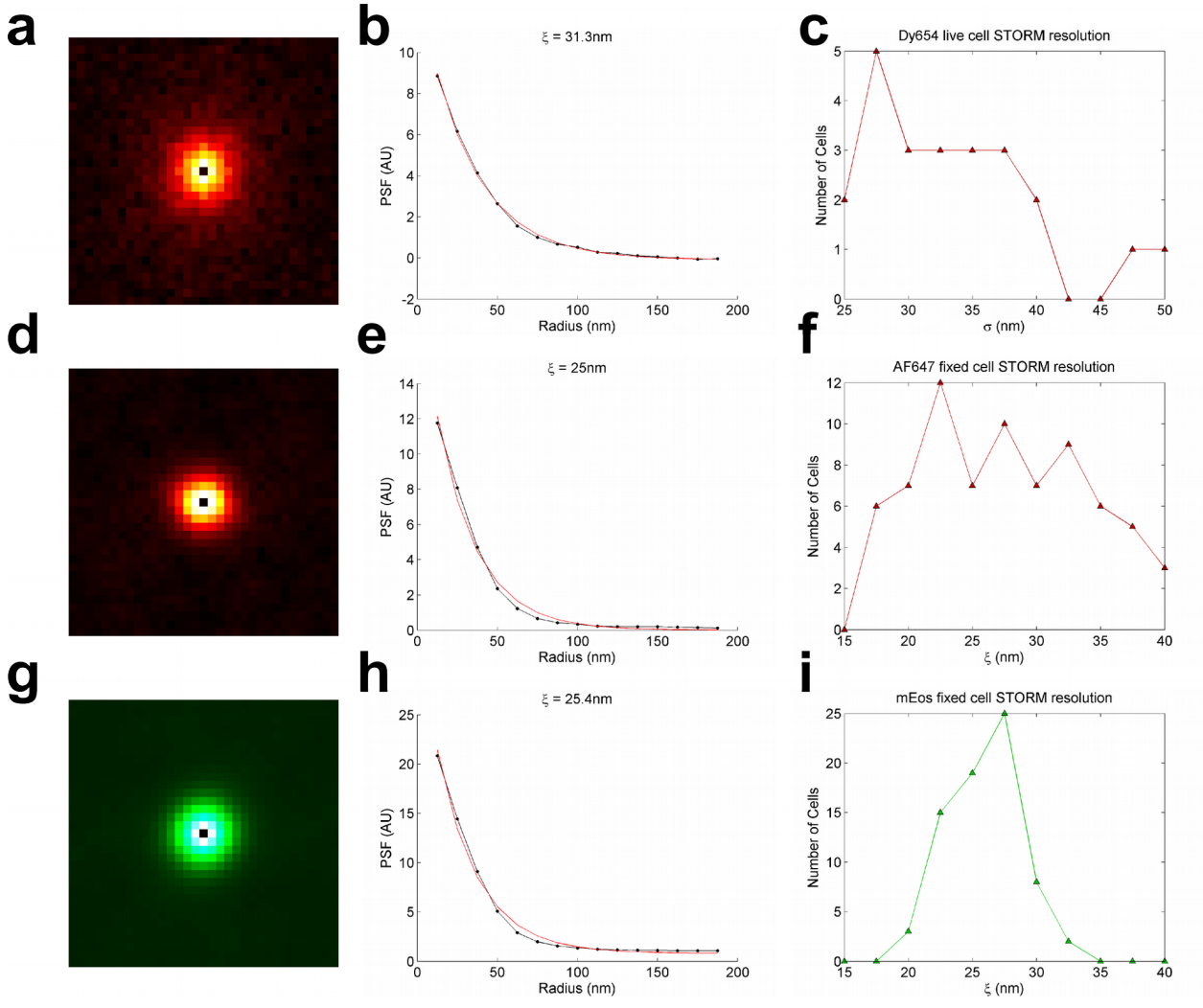
a
b
ξ = 31.3nm
PSF (AU)
Radius (nm)
c
Dy654 live cell STORM resolution
Number of Cells
σ (nm)
d
e
ξ = 25nm
PSF (AU)
Radius (nm)
f
AF647 fixed cell STORM resolution
Number of Cells
ξ (nm)
g
h
ξ = 25.4nm
PSF (AU)
Radius (nm)
i
mEos fixed cell STORM resolution
Number of Cells
ξ (nm)

the case of 1-color, live cell imaging, and 20-30 nm in the case of two-color, fixed cell imaging (Fig. 2.12).

Single particle tracking in live cell STORM images

For live cell imaging, a simple tracking algorithm was applied to the set of STORM localizations. A localization was added to a trajectory if it appeared within 4 imaging frames and 400 nm of the previous localization in the trajectory. Trajectories were examined visually in 3-dimensional plots of x, y, and time, to confirm that cutoff choices led to reasonable linking of trajectories. For rendering and correlation function analysis of live cell data, each trajectory was treated as a single localization, located at the first recorded position in that trajectory. The mean squared displacement was calculated for time delays of 2 through 4 raw imaging frames, combining all displacements recorded in trajectories in a block of 500 raw imaging frames. This was fit with MSD = 4Dt to extract the average diffusion coefficient.

When interpreting our computed value for D, we note that if the displacements measured are smaller than the STORM resolution, then the probes are effectively immobile to within the detection limit of the technique. Using our STORM resolution of ~ 30 nm, and a frame rate of ~ 50 fps, the resolution-limited squared displacement, a lower bound for 4D, would be in the range $(0.030\mu m)^2$ / (2/50 s) = 0.023 $\mu m^2/s$ to $(0.030\mu m)^2$ / (4/50 s) = 0.011 $\mu m^2/s$. This implies a measured D in the range of 0.003-0.006 $\mu m^2/s$ would be consistent with completely immobilized probes.

Degranulation assay

Degranulation assays were performed as previously described (45). Briefly, cells in a 96-well plate were incubated with antigen in BSS for 30 min at 37 °C, then

supernatants were reacted with metylumbelliferyl-N-acetyl-β-D-glucosaminide to generate a fluorescent signal proportional to β-hexosiminidase concentration. Signal was recorded with a Tecan SPECTRAFluor plate reader, and normalized based on a negative control with no cells, and a positive control in which cells were permeablized with 0.1 % Triton-X 100. At least 5 technical replicates were averaged for each condition in each run of the assay.

Ising Monte Carlo Simulations

Ising simulations were run using home-built Python code. Snapshots were generated using a Metropolis algorithm: random moves were proposed consisting of changing the color of a single pixel, and moves were accepted with probability $min\left(1, e^{-\Delta U/k_B T}\right)$. Note that this method allows for fluctuations in the number of white versus black pixels; it can be thought of as a grand canonical ensemble, representing a small section of the whole cell membrane whose composition can fluctuate. We use the standard Ising model Hamiltonian,

$$U = -H\sum \sigma_i - J\sum_{neighbors} \sigma_i \sigma_j \quad (4)$$

Simulations were run on a 150x150 lattice with periodic boundary conditions. We equate one pixel to a size of 1 nm x 1 nm, which is close to the area occupied by a single membrane lipid (46).

Positions of proteins were predefined in the simulation, and pixels at these positions were not allowed to change color. For the results shown in the main text, simulations were run at a temperature of 2.4280 J/k_B, or 1.07 times the critical temperature.

We controlled the average percentage of white pixels in the simulation by

applying existing calculations (47) to precompute the value of H necessary to achieve the desired percentage. Note that for 50:50 white:black, H = 0.

To calculate free energy profiles, we applied Jarzynski's equality (48), an extension of Bennett's acceptance ratio (49), which states that a free energy change (ΔF) can be calculated from a thermodynamic ensemble of snapshots each showing an internal energy change (ΔU) according to the relationship

$$\exp(-\Delta F / k_B T) = \langle \exp(-\Delta U / k_B T) \rangle \quad (5)$$

where angled braces denote the average over all Monte Carlo snapshots. The same approach has been used with the Ising model previously (21) to compute the interaction energy between two proteins.

In our application, we have a single white pixel representing a kinase, placed at a position along the transect of interest. This pixel, like the pixels representing receptors, was forced to remain white. With each simulation snapshot, we calculated the ΔU associated with exchanging the kinase pixel with the pixel to its right. We then used equation 5 to calculate ΔF associated with this move, that is moving the kinase from position x to position x+1. Likewise, we performed a set of simulations with the kinase at position x+1, and calculated ΔF to move from position x+1 to position x, providing a second, independent measurement of the same ΔF value. This process was repeated, with a new simulation set performed at each possible kinase position along the transect. The individual, stepwise ΔF values calculated were used to build the complete free energy profile, with F at the farthest position from the cluster assumed to be zero. As a measure of precision, we calculated $e^{-\Delta F(x \text{ to } x+1)} * e^{\Delta F(x+1 \text{ to } x)}$, which should equal 1. For each free energy profile measured (Fig. 2.7 and Fig. 2.8) we calculated the average

deviation from 1 over all points in the profile; this average error ranged from 0.6% to 1.6% for all free energy profiles calculated.

2.7 Supplementary Note: Evaluation of Channel Cross-Talk in Two-color Imaging

For confidence in our quantitative two-color super-resolution data, we needed to verify that we have sufficiently small channel cross-talk. In our application, this is of particular concern if signal from the far red (IgE) channel appears in the red (mEos) channel. Since the IgE in our stimulated samples is highly clustered, even a small amount of cross-talk into the mEos channel could create a spurious cross-correlation. Furthermore, since stimulation involves clustering of the far red dye, any cross-correlation generated due to cross-talk would appear stimulation-dependent.

To test for such an artifact, we prepared one-color samples with the fluorescent IgE of interest (Dy654-IgE or AF647-IgE) cross-linked with antigen, and imaged as if they were two-color samples. In image processing, we applied the same absolute fluorescence intensity cutoffs that we would have used in a two-color experiment with Lyn-mEos, to determine which blink events were counted. (This is different from just applying the usual 5 standard deviation cutoff to the blank channel, which would be a lower cutoff, detecting more noise than would be relevant to a real two-color imaging situation) . If there is no cross-talk, there should be no cross-correlation between IgE and the empty red channel. However, we detected a large cross-correlation amplitude with Dy654, and a small cross-correlation amplitude with AF647 (Fig. 2.13b).

We investigated the basis of this potential artifact in order to adequately address it. We determined that this is not a case of “bleed-through” (50) in which single probes

Figure 2.13 Evidence for channel cross-talk due to a fluorescent impurity in Dy654-IgE samples. (a) Images of one-color fixed samples sensitized with Dyeomics 654 IgE or Alexa Fluor 647 IgE and stimulated 6 min with 0.5 μg/mL DNP-BSA (Ag) at 37 °C. No fluorophore was used in the second channel, but images were processed as if they were Far red / mEos two-color samples. With Dy654, small areas of strong colocalization (white arrows) are visible in some but not all of the clusters. Each of these could conceivably come from a single Dy654 molecule that is repeatedly localized in the wrong channel. This artifact is not visible in the AF647 sample. (b) Cross-correlation functions between far red IgE and an empty red channel; results from two single cell experiments per condition shown. The fluorescent impurity in Dy654 causes a large, stimulation-dependent cross-correlation artifact. The cross-correlation artifact for AF647 is much lower, but still nonzero.

a

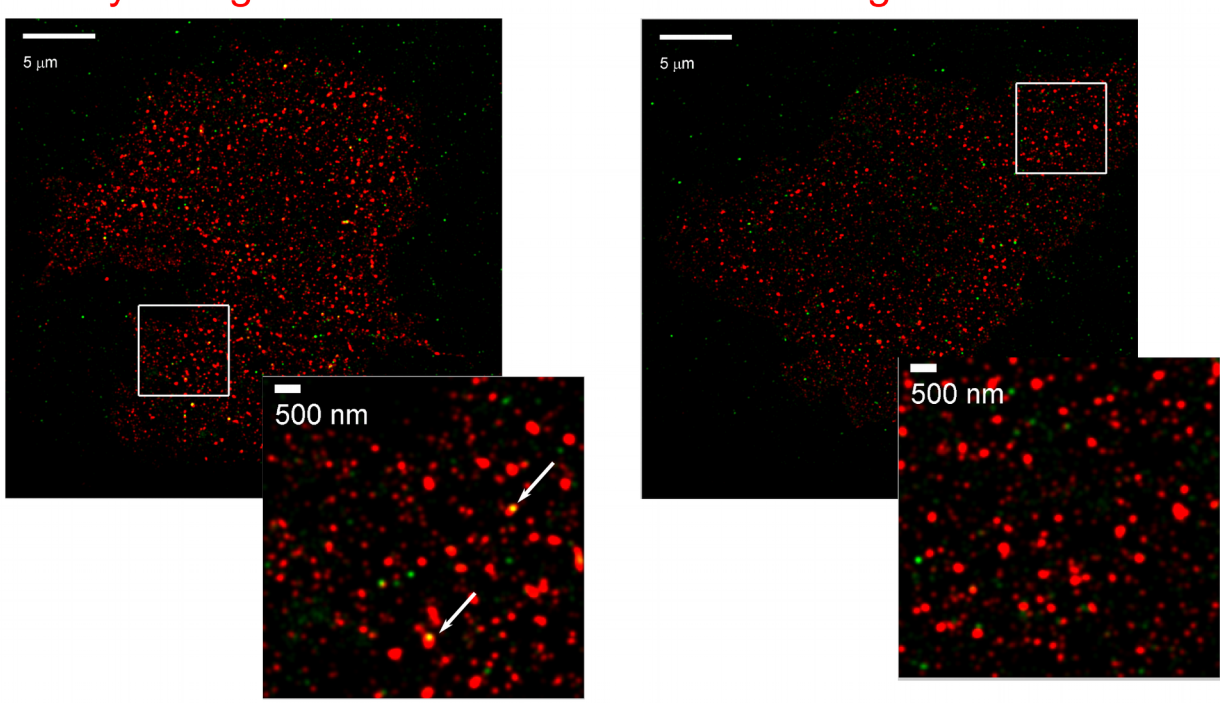
Dy654-IgE / Blank
AF647-IgE / Blank
5 μm
500 nm
5 μm
500 nm

b

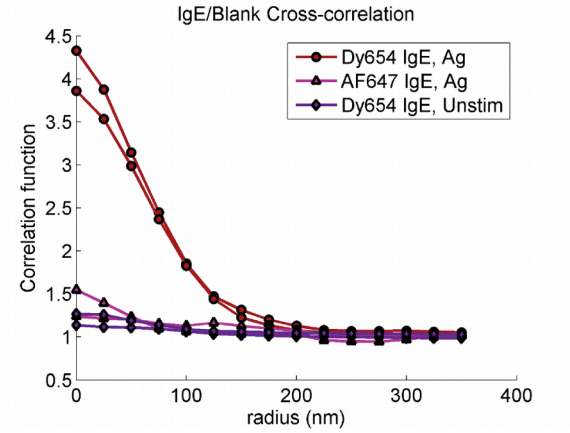
IgE/Blank Cross-correlation
Dy654 IgE, Ag
AF647 IgE, Ag
Dy654 IgE, Unstim
Correlation function
radius (nm)
4.5
4
3.5
3
2.5
2
1.5
1
0.5
0
100
200
300
400

Figure 2.14: The cross-talk artifact is different from bleed through. We performed the published test for bleed through (50): for each blink event, we measure the proportion of the intensity that is in the far red channel. Results from single cell experiments with (a) Dy654 / Lyn-mEos and (b) AF647 / Lyn-mEos show that this is not an issue: There is not a detectable population that splits its fluorescence between the two channels. Rather, most events are either near 0% far red (a red molecule) or near 100% far red (a far red molecule)

Dy654-IgE

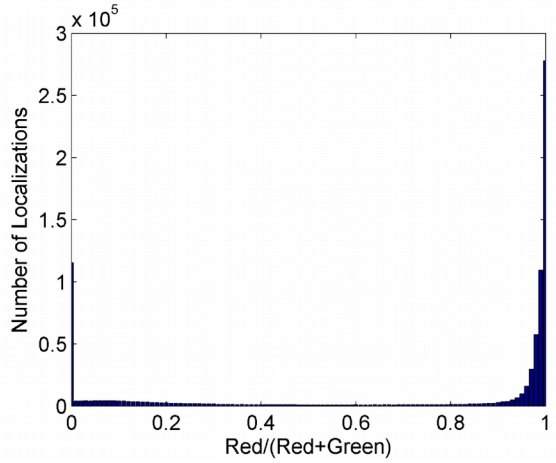

AF647-IgE

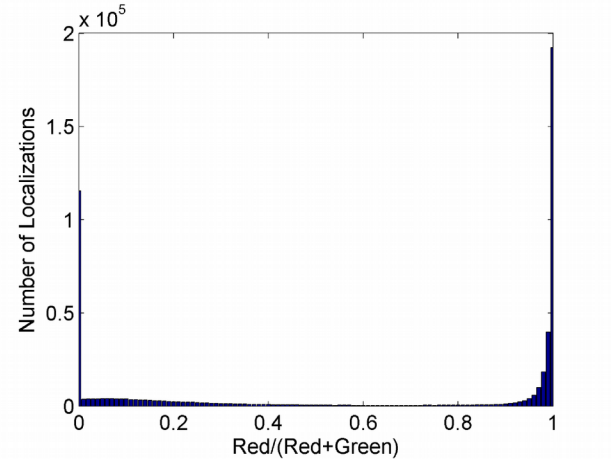

give fluorescence detected simultaneously in both channels. Rather, when our data is analyzed in this way, most localizations appear exclusively in one channel or the other (Fig. 2.14).

A close study of the STORM images collected from 1-color control samples provides more insight into the cause of this issue. We see that many IgE clusters in the image have no visible cross-talk, but occasionally, a cluster contains a bright spot of the opposite color (Fig. 2.13a). This is consistent with a picture in which a small subset of the Dy654 molecules are fluorescent in the wrong color. Such a species might be an existing impurity within the Dy654 stock used, or generated during imaging by the high laser power needed to achieve STORM. The repeated localization of one such molecule leads to one bright, colocalized spot in the STORM image.

A similar phenomenon has been described previously for a different far red organic dye (40). Surprisingly, Stone and Veatch observed fluorescent impurity with AF647 but not Dy654. We therefore suspect that these issues are specific to the particular microscope system used – including the exact emission filters present, and/or the particular batch of organic dye used. We would encourage other groups relying on colocalization analysis of STORM data to perform a similar cross-correlation analysis to what we describe here, to determine which dyes are adequate for their own imaging systems.

It is useful to quantify how much this cross-talk would affect the reported cross-correlation functions. Note that the contribution will be much lower than the amplitudes shown in Fig. 2.13b, which contains only the cross-talk signal. A real cell experiment

would contain this signal mixed with true signal, with most of the signal being true signal. To state this rigorously, we can write the true cross-correlation function as

$$g_{true}(r)=\frac{\langle \rho_G(r)\rangle}{bulkG} \tag{6}$$

where $<\rho_G(r)>$ is the local density of green probes at radius r from a given red probe, averaged over all red probes, and *bulkG* is the bulk density of green probe (We refer to a "red" channel that might generate cross-talk in a "green" channel, but these could be any colors). Suppose a proportion ε of the red signal is a fluorescent impurity that actually appears in the green channel. Then the observed correlation function would be

$$g_{obs}(r)=\frac{\langle \rho_G(r)\rangle+\varepsilon\langle \rho_R(r)\rangle}{bulkG+\varepsilon\, bulkR} \tag{7}$$

with $<\rho_R(r)>$and *bulkR* referring to the analogous quantities in the red channel. One strategy to quantify or correct for the fluorescent impurity is to try to estimate the value of ε. We note that the autocorrelation function of the red channel $ac_R(r)$ can be calculated from the same two-color imaging experiment and is given by

$$ac_R(r)=\frac{\langle \rho_R(r)\rangle}{bulkR} \tag{8}$$

From algebraic manipulation of the above equations we have

$$g_{true}(r)=[g_{obs}(r)-\frac{bulkR}{bulkG+\varepsilon\, bulkR}\varepsilon\, ac_R(r)]\frac{bulkG+\varepsilon\, bulkR}{bulkG} \tag{9}$$

Everything on the right-hand side of equation 9, with the exception of ε, can be obtained from the experiment. (Note that the measured bulk density in the green channel is *bulkG* + ε *bulkR*, and *bulkG* alone can be calculated with knowledge of ε and *bulkR*) Therefore, one strategy to quantify or correct for the fluorescent impurity is to try to estimate the value of ε. This ε, representing the proportion of fluorescent impurity

signal present, should be a constant for a particular dye pair and imaging conditions.

We can estimate ε by applying heuristics to data from a one-color control sample such as in Fig. 2.13. One strategy is to programmatically identify the impurity-generated events as marked in Fig. 2.13a. We consider each connected component of green pixels in the image as a candidate molecule that might represent the fluorescent impurity. The molecule is confirmed to be a fluorescent impurity if 1) it generated a threshold number of green counts – we chose a cutoff of 10, and 2) it is colocalized with red signal – we chose a cutoff of 30 red counts. ε is computed by dividing the number of counts of fluorescent impurity found in this way by the total amount of red signal in clusters (defined as connected components of over 30 counts). We found two Dy654 cells gave ε of 0.0069 and 0.0074, while two AF647 cells gave ε of 0 and 0.0015. These values can vary by ~ 0.002 depending on the choices of cutoffs. An alternate method is to simulate the impurity on the AF647 image in Fig. 2.13, counting the proportion of signal that must be moved from the red channel to green channel to reach the same level of cross-correlation as in the Dy654 sample (Of course, this approach is only possible if one already has a dye with a lower fluorescent impurity!). This gave a similar result of ε ≈ 0.01 for Dy654 samples.

One remaining weakness of this approach is that $<\rho_R>$ in equation 8 is comes from an autocorrelation function and it subject to an over-counting artifact (20), while the $<\rho_R>$ in equation 7 has no overcounting. Therefore the calculated g_{true} will be an underestimate if the over-counting contribution is significant.

An alternate approach to quantification is to use the cross-correlation functions in

Fig. 2.13b directly. The correlation function shown, assuming the signal came from only the fluorescent impurity,

would be given by

$$g_{1c}(r)=\frac{\varepsilon\langle\rho_R(r)\rangle}{\varepsilon\, bulkR} \tag{10}$$

However, this is clearly inaccurate, as this is identical to equation 8 for any ε, but our measured cross-correlation function is in fact lower than the red autocorrelation function. More accurately, the signal in Fig. 2.13b comes from a combination of the fluorescent impurity, and any other randomly distributed impurities on the sample – such as a small amount of dust that remains on the sample even after plasma cleaning and exhibits blinking under high laser power. We refer to all such random, uniformly distributed sources of signal collectively as "dust" with the subscript D. Since the dust is by assumption uniform, $<\rho_D(r)>$ = *bulkD*

$$g_{1c}(r)=\frac{\varepsilon\langle\rho_R(r)\rangle+\langle\rho_D(r)\rangle}{\varepsilon\, bulkR+bulkD}=\frac{\varepsilon\langle\rho_R(r)\rangle+bulkD}{\varepsilon\, bulkR+bulkD} \tag{11}$$

Note that in equation 7, ρ_G and *bulkG* more accurately include both true green signal and a contribution from the dust.

$$g_{obs}(r)=\frac{\langle\rho_G(r)\rangle+bulkD+\varepsilon\langle\rho_R(r)\rangle}{bulkG+bulkD+\varepsilon\, bulkR} \tag{12}$$

Algebraic manipulation of equations 6, 11, and 12 gives the following result.

$$g_{true}(r)=[\,g_{obs}(r)-\frac{\varepsilon\, bulkR+bulkD}{bulkG+\varepsilon\, bulkR+bulkD}\,g_{1c}(r)]\,\frac{bulkG+\varepsilon\, bulkR+bulkD}{bulkG} \tag{13}$$

Equation 13 gives another method by which it is possible to quantify or correct for a fluorescent impurity, as all quantities on the right hand side can be obtained from imaging both a two-color sample to be tested, and a one-color control sample imaged in

Figure 2.15: Example application of fluorescent impurity correction on cross-correlation data. Example correction is shown for two single-cell experiments: one with Dy654-IgE and mEos-GG (left panel), and one with AF647-IgE and mEos-GG (right panel). For demonstration purposes, cells were chosen with similar, above-average cross-correlation functions. Red curves give the original, uncorrected cross-correlation functions. Blue curves apply equation 13 using data from one-color control samples. Green curves apply equation 9 using an estimated impurity proportion ε of 0.01 for Dy654 and 0.001 for AF647. Note that this method over-corrects at small radius because the autocorrelation function used in equation 9 has contributions from over-counting.

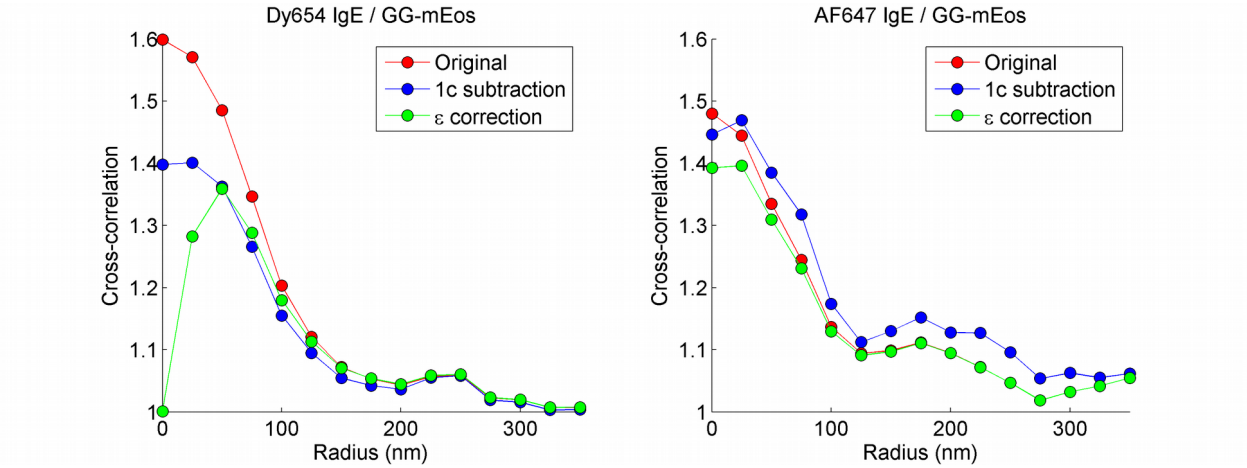
Dy654 IgE / GG-mEos
Original
1c subtraction
ε correction
Cross-correlation
Radius (nm)
1.6
1.5
1.4
1.3
1.2
1.1
1
0
100
200
300
AF647 IgE / GG-mEos
Original
1c subtraction
ε correction
Cross-correlation
Radius (nm)

both channels. The bulk density in the green channel of the two-color sample gives the quantity $bulkG + \varepsilon\, bulkR + bulkD$, and the bulk density in the (nearly empty) green channel of the one-color sample gives the quantity $\varepsilon\, bulkR + bulkD$. Note that with this method, we never have to directly know ε or $bulkD$. However, we do need a 1-color sample that matches the two-color sample not just in imaging conditions, but in every detail of sample preparation such that the amount of background dust in the two samples match. This is only possible if the one-color sample is prepared in parallel to the two-color sample to be corrected. In practice, this would lead to much more work for the microscopist compared to finding a dye that does require a fluorescent impurity correction.

We used the above formulas to analyze the cross-correlation functions in two-color imaging experiments (Fig. 2.15). Both of our proposed methods agree at radii of ~ 50 nm and higher, giving us improved confidence in the validity of these methods. Below 50 nm, equation 9 appears to over-correct due to the over-counting contribution discussed above. We find for the example Dy654 cell, the fluorescent impurity contributes an amplitude of ~ 0.2, while the correction necessary for AF647 is negligible. This analysis indicates that use of Dy654 could lead to incorrect conclusions, as the fluorescent impurity has a contribution of comparable size to our true signal (Fig. 2.5c), and justifies our decision to use AF647, for which we observe little to no effect of any fluorescent impurity.

In summary, we showed that fluorescent impurities in dyes can contribute significantly to a measured cross-correlation function, and lead to incorrect notions of

colocalization if adequate analysis is not done. In our application, we rejected the use of Dy654 because its fluorescent impurity could contribute a cross-correlation amplitude of ~ 0.2, comparable in magnitude to the actual signal we were trying to observe. While the above equations could in principle be used to correct correlation functions for a fluorescent impurity, we would not recommend this, as it adds additional degrees of assumption and estimation to the processing, and it would always be better to instead use a more well behaved dye if one is available. This analysis is useful, however, for quantifying the extent to which a fluorescent impurity may affect a cross-correlation analysis. This can in turn be used to judge whether a particular dye is acceptable to use in a particular biological system.

Acknowledgements

James P. Sethna, David Holowka, and Barbara Baird made contributions to this work.

EM, DH, and BB were supported by National Institutes of Health grants R01-AI018306 followed by R01-GM117552. JPS was supported by the National Science Foundation grant DMR-1312160. EM was additionally supported by the National Institutes of Health under Ruth L. Kirschstein National Research Service Award (2T32GM008267) from the National Institute of General Medical Sciences.

We are grateful to Sarah Veatch (University of Michigan) for the STORM analysis code that was adapted for use in this study, to Ben Machta for the Monte Carlo simulation code that was adapted for use in this study, to Sam Hess (University of Maine) for bleed-through correction code. We thank Sarah Shelby for assistance with

super-resolution microscopy experiments, and for useful discussions. We additionally thank Alice Wagenknecht-Wiesner for performing the molecular cloning of constructs used in this study.

References

1. Nussinov, R., H. Jang, and C.J. Tsai. 2015. Oligomerization and nanocluster organization render specificity. Biol. Rev. 90: 587–598.

2. Metzger, H. 1992. Transmembrane Signaling : the Joy of Aggregation. J. Immunol. 149: 1477–1487.

3. Brownlie, R.J., and R. Zamoyska. 2013. T cell receptor signalling networks: branched, diversified and bounded. Nat. Rev. Immunol. 13: 257–269.

4. Dal Porto, J.M., S.B. Gauld, K.T. Merrell, D. Mills, A.E. Pugh-Bernard, and J. Cambier. 2004. B cell antigen receptor signaling 101. Mol. Immunol. 41: 599–613.

5. Shelby, S.A., D. Holowka, B. Baird, and S.L. Veatch. 2013. Distinct stages of stimulated FcεRI receptor clustering and immobilization are identified through superresolution imaging. Biophys. J. 105: 2343–54.

6. Larson, D.R., J.A. Gosse, D.A. Holowka, B.A. Baird, and W.W. Webb. 2005. Temporally resolved interactions between antigen-stimulated IgE receptors and Lyn kinase on living cells. J. Cell Biol. 171: 527–36.

7. Andrews, N.L., J.R. Pfeiffer, A.M. Martinez, D.M. Haaland, R.W. Davis, T. Kawakami, J.M. Oliver, B.S. Wilson, and D.S. Lidke. 2009. Small, mobile FcεRI receptor aggregates are signaling competent. Immunity. 31: 469–479.

8. Gilfillan, A.M., and J. Rivera. 2009. The tyrosine kinase network regulating mast cell activation. Immunol. Rev. 228: 149–169.

9. Blank, U., and J. Rivera. 2004. The ins and outs of IgE-dependent mast-cell exocytosis. Trends Immunol. 25: 266–273.

10. Wofsy, C., B.M. Vonakis, H. Metzger, and B. Goldstein. 1999. One lyn molecule is sufficient to initiate phosphorylation of aggregated high-affinity IgE receptors. PNAS. 96: 8615–8620.

11. Wofsy, C., C. Torigoe, U.M. Kent, H. Metzger, and B. Goldstein. 1997. Exploiting the difference between intrinsic and extrinsic kinases: implications for regulation of signaling by immunoreceptors. J. Immunol. 159: 5984–5992.

12. Wu, M., D. Holowka, H.G. Craighead, and B. Baird. 2004. Visualization of plasma membrane compartmentalization with patterned lipid bilayers. PNAS. 101: 13798–13803.

13. Shelby, S.A., S.L. Veatch, D.A. Holowka, and B.A. Baird. 2016. Functional nanoscale coupling of Lyn kinase with IgE-FcεRI is restricted by the actin

cytoskeleton in early antigen-stimulated signaling. Mol. Biol. Cell. 27: 3645–3658.

14. Field, K.A., D. Holowka, and B. Baird. 1995. FcεRI-mediated recruitment of p53/56lyn to detergent-resistant membrane domains accompanies cellular signaling. PNAS. 92: 9201–9205.

15. Young, R.M., X. Zheng, D. Holowka, and B. Baird. 2005. Reconstitution of regulated phosphorylation of FcεRI by a lipid raft-excluded protein-tyrosine phosphatase. J. Biol. Chem. 280: 1230–1235.

16. Holowka, D., J.A. Gosse, A.T. Hammond, X. Han, P. Sengupta, N.L. Smith, A. Wagenknecht-Wiesner, M. Wu, R.M. Young, and B. Baird. 2005. Lipid segregation and IgE receptor signaling: a decade of progress. Biochim. Biophys. Acta. 1746: 252–259.

17. Veatch, S.L., P. Cicuta, P. Sengupta, A. Honerkamp-Smith, D. Holowka, and B. Baird. 2008. Critical fluctuations in plasma membrane vesicles. ACS Chem. Biol. 3: 287–293.

18. Honerkamp-Smith, A.R., S.L. Veatch, and S.L. Keller. 2009. An introduction to critical points for biophysicists; observations of compositional heterogeneity in lipid membranes. Biochim. Biophys. Acta. 1788: 53–63.

19. Veatch, S.L., E.N. Chiang, P. Sengupta, D.A. Holowka, and B.A. Baird. 2012. Quantitative nanoscale analysis of IgE-FcεRI clustering and coupling to early signaling proteins. J. Phys. Chem. B. 116: 6923–6935.

20. Veatch, S.L., B.B. Machta, S.A. Shelby, E.N. Chiang, D.A. Holowka, and B.A. Baird. 2012. Correlation functions quantify super-resolution images and estimate apparent clustering due to over-counting. PLoS One. 7: e31457.

21. Machta, B.B., S.L. Veatch, and J.P. Sethna. 2012. Critical Casimir Forces in Cellular Membranes. Phys. Rev. Lett. 109: 138101.

22. Betzig, E., G.H. Patterson, R. Sougrat, O.W. Lindwasser, S. Olenych, J.S. Bonifacino, M.W. Davidson, J. Lippincott-Schwartz, and H.F. Hess. 2006. Imaging intracellular fluorescent proteins at nanometer resolution. Science. 313: 1642–1645.

23. Rust, M.J., M. Bates, and X. Zhuang. 2006. Sub-diffraction-limit imaging by stochastic optical reconstruction microscopy (STORM). Nat. Methods. 3: 793–795.

24. Hess, S.T., T.P.K. Girirajan, and M.D. Mason. 2006. Ultra-high resolution imaging by fluorescence photoactivation localization microscopy. Biophys. J. 91: 4258–4272.

25. Manzo, C., and M.F. Garcia-Parajo. 2015. A review of progress in single particle tracking: from methods to biophysical insights. Reports Prog. Phys. 78: 124601.

26. Schwartz, S.L., Q. Yan, C. a. Telmer, K. a. Lidke, M.P. Bruchez, and D.S. Lidke. 2015. Fluorogen-activating proteins provide tunable labeling densities for tracking FcεRI independent of IgE. ACS Chem. Biol. 10: 539–546.

27. Andrews, N.L., K.A. Lidke, J.R. Pfeiffer, A.R. Burns, B.S. Wilson, J.M. Oliver, and D.S. Lidke. 2008. Actin restricts FcεRI diffusion and facilitates antigen-induced receptor immobilization. Nat. Cell Biol. 10: 955–963.

28. Paar, J.M., N.T. Harris, D. Holowka, and B. Baird. 2002. Bivalent ligands with rigid double-stranded DNA spacers reveal structural constraints on signaling by FcεRI. J. Immunol. 169: 856–864.

29. Sil, D., J.B. Lee, D. Luo, D. Holowka, and B. Baird. 2007. Trivalent ligands with rigid DNA spacers reveal structural requirements for IgE receptor signaling in RBL mast cells. ACS Chem. Biol. 2: 674–684.

30. Mahajan, A., D. Barua, P. Cutler, D.S. Lidke, F.A. Espinoza, C. Pehlke, R. Grattan, Y. Kawakami, C.-S. Tung, A.R.M. Bradbury, W.S. Hlavacek, and B.S. Wilson. 2014. Optimal Aggregation of FcεRI with a Structurally Defined Trivalent Ligand Overrides Negative Regulation Driven by Phosphatases. ACS Chem. Biol. 9: 1508–1519.

31. Posner, R., K. Subramanian, B. Goldstein, J.L. Thomas, T. Feder, D. Holowka, and Baird. 1995. Simultaneous Cross-Linking by Two Nontriggering Bivalent Ligands Causes Synergistic Signaling of IgE FcεRI Complexes. J. Immunol. 155: 3601–3609.

32. Heilemann, M., S. van de Linde, M. Schüttpelz, R. Kasper, B. Seefeldt, A. Mukherjee, P. Tinnefeld, and M. Sauer. 2008. Subdiffraction-resolution fluorescence imaging with conventional fluorescent probes. Angew. Chem. Int. Ed. Engl. 47: 6172–6176.

33. Xu, K., B. Goldstein, D. Holowka, and B. Baird. 1998. Kinetics of multivalent antigen DNP-BSA binding to IgE-FcεRI in relationship to the stimulated tyrosine phosphorylation of Fc epsilon RI. J. Immunol. 160: 3225–3235.

34. Keegan, A.D., C. Fratazzi, B. Shopes, B. Baird, and D.H. Conrad. 1991. Characterization of new rat anti-mouse IgE monoclonals and their use along with chimeric IgE to further define the site that interacts with FcεRII and FcεRI. Mol. Immunol. 28: 1149–1154.

35. Gray, E.M., G. Díaz-Vázquez, and S.L. Veatch. 2015. Growth conditions and cell

cycle phase modulate phase transition temperatures in RBL-2H3 derived plasma membrane vesicles. PLoS One. 10: e0137741.

36. Swamy, M.J., L. Ciani, M. Ge, A.K. Smith, D. Holowka, B. Baird, and J.H. Freed. 2006. Coexisting domains in the plasma membranes of live cells characterized by spin-label ESR spectroscopy. Biophys. J. 90: 4452–4465.

37. Mukherjee, S., and F.R. Maxfield. 2004. Membrane Domains. Annu. Rev. Cell Dev. Biol. 20: 839–866.

38. Pribluda, V.S., C. Pribluda, and H. Metzger. 1994. Transphosphorylation as the mechanism by which the high-affinity receptor for IgE is phosphorylated upon aggregation. PNAS. 91: 11246–11250.

39. Pageon, S. V, T. Tabarin, Y. Yamamoto, P.R. Nicovich, J.S. Bridgeman, A. Cohnen, C. Benzing, Y. Gao, D. Michael, K. Tungatt, G. Dolton, A.K. Sewell, D.A. Price, O. Acuto, R.G. Parton, J.J. Gooding, J. Rossy, J. Rossjohn, and K. Gaus. 2016. Functional role of T-cell receptor nanoclusters in signal initiation and antigen discrimination. PNAS. 113: E6905–E6905.

40. Stone, M.B., and S.L. Veatch. 2014. Far-red organic fluorophores contain a fluorescent impurity. Chemphyschem. 15: 2240–2246.

41. Posner, R.G., B. Lee, D.H. Conrad, D. Holowka, B. Baird, and B. Goldstein. 1992. Aggregation of IgE-receptor complexes on rat basophilic leukemia cells does not change the intrinsic affinity but can alter the kinetics of the ligand-IgE interaction. Biochemistry. 31: 5350–5356.

42. Edwald, E., M.B. Stone, E.M. Gray, J. Wu, and S.L. Veatch. 2014. Oxygen depletion speeds and simplifies diffusion in HeLa cells. Biophys. J. 107: 1873–1884.

43. Weetall, M., D. Holowka, and B. Baird. 1993. Heterologous Desensitization of the High Affinity Receptor for IgE (FcεRI) on RBL Cells. J. Immunol. 150: 4072–4083.

44. Erickson, J., B. Goldstein, D. Holowka, and B. Baird. 1987. The effect of receptor density on the forward rate constant for binding of ligands to cell surface receptors. Biophys. J. 52: 657–662.

45. Naal, R.M.Z.G., J. Tabb, D. Holowka, and B. Baird. 2004. In situ measurement of degranulation as a biosensor based on RBL-2H3 mast cells. Biosens. Bioelectron. 20: 791–796.

46. Petrache, H.I., S. Tristram-Nagle, K. Gawrisch, D. Harries, V.A. Parsegian, and J.F. Nagle. 2004. Structure and Fluctuations of Charged Phosphatidylserine Bilayers in the Absence of Salt. Biophys. J. 86: 1574–1586.

47. Chen, Y.-J., N.M. Paquette, B.B. Machta, and J.P. Sethna. 2013. Universal scaling function for the two-dimensional Ising model in an external field: A pragmatic approach. arXiv. : 1307.6899.

48. Jarzynski, C. 1997. Nonequilibrium Equality for Free Energy Differences. Phys. Rev. Lett. 78: 2690–2693.

49. Bennett, C.H. 1976. Efficient Estimation of Free Energy Differences from Monte Carlo Data. J. Comput. Phys. 22: 245–268.

50. Kim, D., N.M. Curthoys, M.T. Parent, and S.T. Hess. 2013. Bleed-through correction for rendering and correlation analysis in multi-colour localization microscopy. J. Opt. 15: 094011.

51. Brodsky, R.A., G.L. Mukhina, S. Li, K.L. Nelson, P.L. Chiurazzi, J.T. Buckley, and M.J. Borowitz. 2000. Improved detection and characterization of paroxysmal nocturnal hemoglobinuria using fluorescent aerolysin. Am. J. Clin. Pathol. 114: 459–66.

CHAPTER THREE

COMPUTATION OF A THEORETICAL MEMBRANE PHASE DIAGRAM, AND THE ROLE OF PHASE IN LIPID RAFT-MEDIATED PROTEIN ORGANIZATION

3.1 Summary

Lipid phase heterogeneity in the plasma membrane is thought to be crucial for many aspects of cell signaling, but the physical basis of such “lipid rafts” or other membrane domains remains controversial. Here we consider a lattice model with a phase diagram that includes several states proposed to be relevant for the cell membrane, including microemulsion and Ising critical behavior. Using a neural network-based machine learning approach, we compute the full phase diagram of the model. We then analyze selected regions of the phase diagram in the context of recruitment of the membrane-anchored kinase Lyn to a cluster of IgE-FcεRI receptors in mast cell signaling. We find that microemulsion and Ising critical states can mediate roughly equal levels of kinase recruitment (binding energy ~ -0.6 k_BT), while a membrane near a tricritical point can mediate much stronger kinase recruitment (-1.7 k_BT). By comparing several lipid phase models within a single modeling framework, this work points to testable differences between existing models, and also suggests the tricritical point as a new hypothesis for the basis of membrane domains that facilitate preferential partitioning of signaling components. .

3.2 Introduction

The lateral organization of cell membranes contributes crucially to their function. While previous models suggested that cell membranes were largely homogeneous on

length scales much larger than the size of a constituent lipid (1 nm), a bulk of recent experimental evidence suggests that mammalian plasma membranes contain organized phase domains on the order of 10-200 nm in length (1–4). The plasma membrane is thought to contain phases of liquid ordered (Lo)-like and liquid disordered (Ld)-like character. The phase domains are thought to play an essential role in cell signaling by colocalizing membrane proteins that partition into the same phase, and separating those that partition into different phases (4, 5). The term that has emerged for the phase domains is “lipid rafts,” although the literature describing these is conflicting and controversial. For the purposes of this study, we define lipid rafts as membrane domains of Lo-like character (i.e. containing a higher than bulk concentration of cholesterol and lipids with saturated fatty acyl chains), of size 10-200 nm, that serve to control the spatial organization of membrane proteins. Lipid-mediated phenomena have been implicated in many mechanisms of membrane protein signaling, including immune receptors (6, 7), G-protein coupled receptors (8), the oncogenic GTPase Ras (9), and others.

Despite the centrality of lipid membranes to biology, there remains no consensus on the physical basis of lipid domains. The formation of lipid rafts has been tied to the observation of phase separation in model membranes, including giant unilamellar vesicles (GUVs) (10–12) and giant plasma membrane vesicles (GPMVs) (13, 14). These systems exhibit a rich variety of phase behavior, including two-phase coexistence, microemulsions (11, 15), modulated or lamellar phases (16), and critical phenomena (14). However, despite recent advances in experimental techniques (for recent review, see (7)), lipid rafts in real mammalian cell membranes remain a difficult

system to investigate – the complexity of these systems notwithstanding, the characteristic size of rafts prevents direct observation via conventional light microscopy. Thus, the goal for a theoretical consideration of lipid raft physics should provide hypotheses that are amenable to testing with the currently available tools.

Towards this end, various theoretical models have been proposed to describe raft-like phenomena. Importantly, due to the lack of direct experimental data on lipid rafts, the set of theories that are consistent with observation is relatively unconstrained – models that disagree on the fundamental physics of raft formation can give qualitatively similar results that agree with extant experimental work. Prominent among these theories is the view that lipid rafts are the domains of a microemulsion phase. In this microemulsion framework, phase domains of a characteristic size – like rafts – are stabilized by a surfactant-like interaction – either a literal surfactant species (17) or an interaction mediated by membrane curvature (18–20)– which makes the interface between immiscible phase regions more energetically stable. An alternate hypothesis suggests that rafts are instead critical fluctuations in membrane composition, a result of the membrane's proximity to a 2D Ising critical point (14, 21). Experimental studies have provided support for both an Ising critical point (14) and surfactant-like interactions consistent with a microemulsion (15, 16).

Due to the ambiguities in the physics of lipid raft formation, we make use of a lattice microemulsion model originally described by Gompper and Schick (22, 23), which can be used to study both microemulsions and critical phenomena. In addition, the phase diagram of this model captures features such as modulated phase and two phase coexistence observed in other membrane studies, as well as a tricritical point,

which we show has interesting implications for cell signaling.

When the microemulsion model of Gompper and Schick was initially described, it was possible to extract some key features of the phase diagram, most notably the location of the critical line, by finite size scaling (22). With the great increase in the power of computational resources since then, it has become possible for us to address the model more globally by simulation. In addition, neural networks have become a powerful machine learning technique, leading to the development of computational tools to address challenging problems such as image recognition (24). Such classifiers have recently been applied with considerable success to assist in drawing phase diagrams (25, 26).

With this powerful technique for generating full phase diagrams at low computational cost, we investigate membrane phase behavior, and the possible consequences on cell signaling. As described above, lipid rafts are important for the localization of membrane proteins. To analyze this functional manifestation in depth, we focus on the tractable example of signaling through the IgE-FcεRI receptor in mast cells, a signaling pathway involved in the allergic immune response (reviewed in (27–29)). The mast cell is stimulated when an external allergen physically cross-links several IgE-FcεRI receptors together. This enables the recruitment of the kinase Lyn, which phosphorylates the receptor, activating downstream signaling events. This kinase recruitment is thought to be raft-mediated: both the cross-linked receptors and the kinase preferentially partition into more ordered membranes, making it favorable to find the kinase and receptor in the same location on the membrane (6). The mast cell system serves as an example of a more general paradigm in cell biology, in which the

clustering of membrane proteins due to an external stimulus leads to transmembrane initiation of downstream events (9).

3.3 Results

Model

We use the two-dimensional square lattice model described by Gompper and Schick (22) with the Hamiltonian

$$\mathcal{H} = \sum_i \left(H \sigma_i + \Delta \sigma_i^2 \right) + \sum_{i,j} \left(-J \sigma_i \sigma_j - K \sigma_i^2 \sigma_j^2 \right) + \sum_{i,j,k} L \sigma_i \left(1 - \sigma_j^2 \right) \sigma_k$$

The spin σ at each lattice site can take a value of -1, 0, or 1. Throughout the study, we refer to these as black, gray, and white pixels, respectively. Spin values of -1 and 1 represent membrane molecules favoring the Ld and Lo phases, respectively. Spin 0 represents a surfactant when L > 0, or simply a molecule with neutral phase preference when L = 0. The summation over i is over all spins in the lattice, i,j is over all nearest neighbors, and i,j,k is over all groups of three adjacent spins in a straight horizontal or vertical line. We equate one lattice unit to a length of 1 nm, the approximate diameter occupied by one membrane lipid molecule.

Each of the five parameters of this model – H, Δ, J, K, and L – has units of energy. We consider only non-negative values for J, K, and L, while H and Δ can take any value. The external fields H and Δ control the composition of the lattice. H controls the relative abundance of -1 and 1, while larger Δ increases the concentration of 0. We consider this model in the grand canonical ensemble: our simulation box represents one section of the membrane, so it makes sense that the number of each type of molecule can fluctuate, analogous to molecules diffusing in and out of the box. The spin-spin

coupling J represents the usual Ising spin-spin coupling, which, for a membrane model, is the preference for Lo phase to be adjacent to other Lo phase, not Ld phase. J can also be thought of as equal to the line tension times a distance of 1 lattice unit (1 nm). K is a two-spin interaction that gives a favorable energy to adjacent nonzero spins. For a particular concentration of 0 spins, a higher value of K makes it more favorable to have those 0 spins adjacent to each other. L controls the strength of 0 spins as a surfactant; note that this term contributes a nonzero value only when a 0 spin sits between two nonzero spins, and is favorable when the two nonzero spins have different signs. Thus, this term makes it preferable for spin 0 to sit between spin 1 and spin -1.

In our implementation, rather than choosing a value for J, we choose a value for temperature T in units of J/k_B, and J is set accordingly. The other parameters H, Δ, K and L are chosen in units of J. Boltzmann's constant k_B is set to unity.

Note that when L=0 this reduces to the Blume-Emery-Griffiths model (30). With K also set to 0, this becomes the Blume-Capel model (31, 32). With $\Delta = -\infty$ in addition, it reduces to the Ising model.

Neural Network Phase Identification

We trained neural networks to classify the output of a Monte Carlo simulation according to the phase that the simulation represents. A schematic of the network is shown in Fig. 3.1. The spin values from a 30 by 30-pixel Monte Carlo snapshot (generated by the standard Metropolis method (33)) were used as 900 inputs to the network. Training data consisted of 15600 such snapshots, which represented typical examples of each phase of interest (Fig. 3.14). The network was trained with 2 hidden layers of 100 nodes each, and an output layer of 6 nodes, corresponding to the six

Figure 3.1 Schematic of the neural network used for phase prediction. The pixel values from a Monte Carlo simulation on a 30x30 lattice serve as inputs. The network is trained using 2 hidden layers of 100 nodes each. The network contains 6 outputs, corresponding to its confidence that the input represents each of the 6 possible phases.

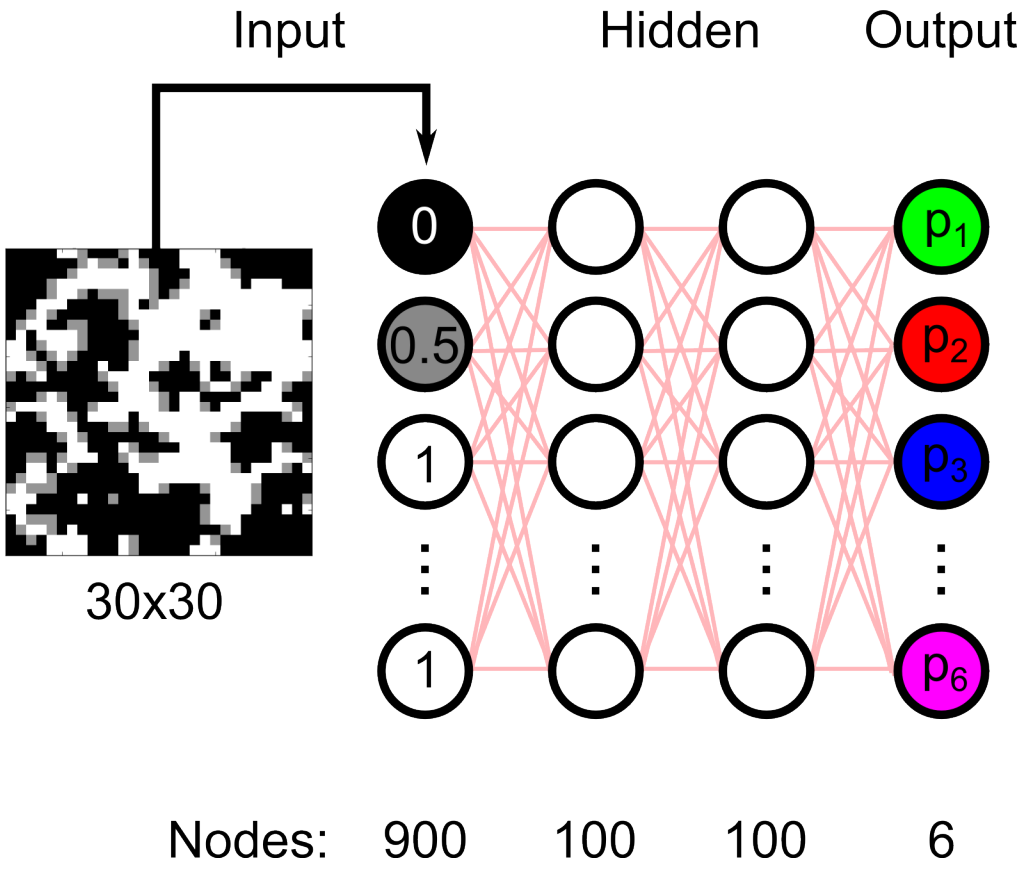
Input
Hidden
Output
0
0.5
1
1
p_1
p_2
p_3
p_6
30x30
Nodes: 900 100 100 6

Figure 3.2 Phase diagram of the microemulsion lattice model. The color of each pixel indicates the phase at that point, as determined by the neural network. Pixels with a higher brightness indicate a higher level of confidence in the classification. Snapshots show typical examples of each of the phases, corresponding to the black points on the phase diagram.

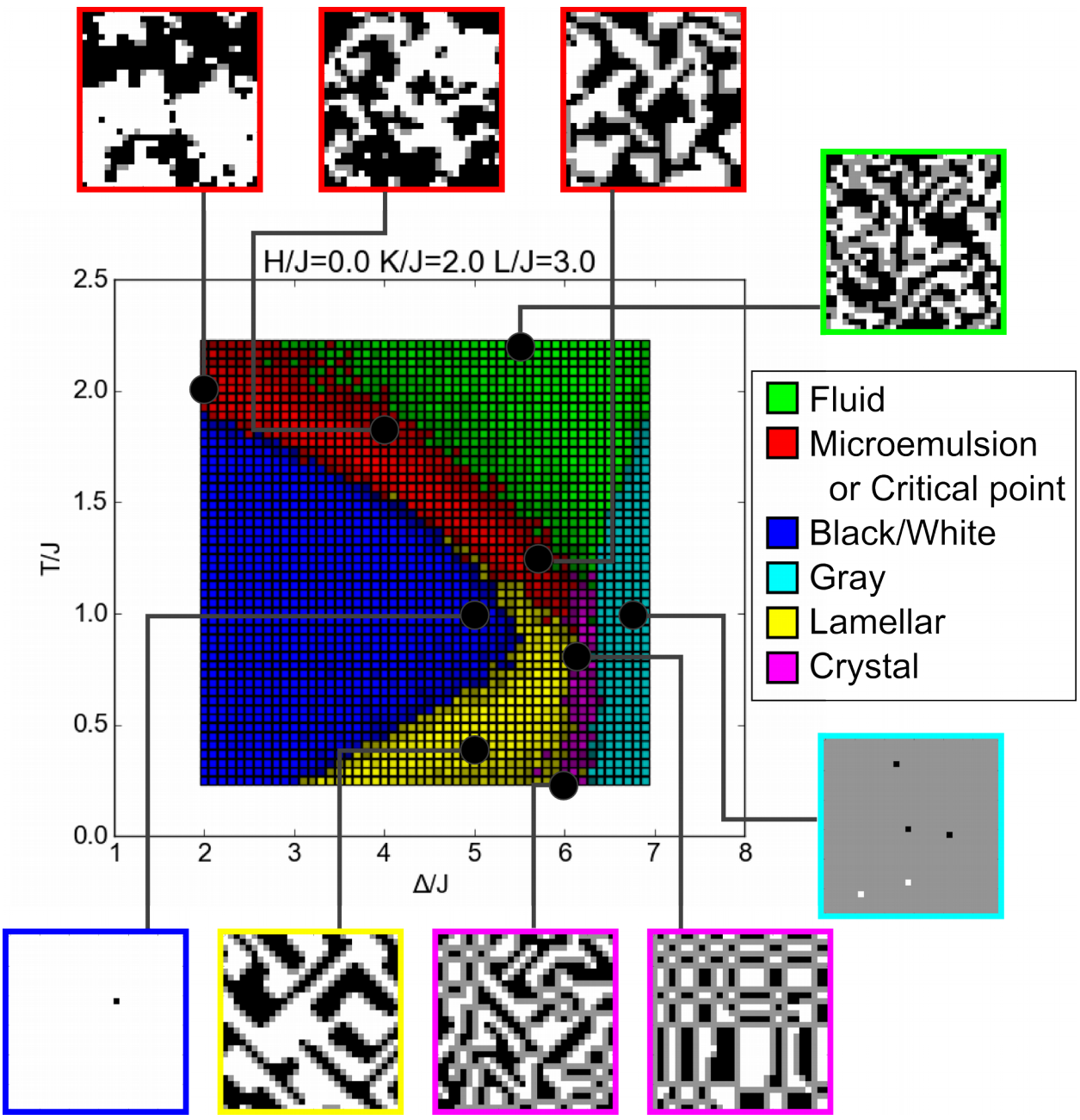
H/J=0.0 K/J=2.0 L/J=3.0
T/J
Δ/J
0.0
0.5
1.0
1.5
2.0
2.5
1
2
3
4
5
6
7
8
Fluid
Microemulsion
or Critical point
Black/White
Gray
Lamellar
Crystal

phases of interest in the phase diagram. Alternatively, instead of single Monte Carlo snapshots, we used input consisting of the average of 10 correlated snapshots from consecutive simulation steps. This method tended to be more accurate in most cases, and our final reported phase diagrams make use of some output from both types of networks. Further information on the setup and training of the neural networks is described in Methods.

Our neural network was able to confidently label 6 distinct regions of the phase diagram (Fig. 3.2). We have named these phases according to what each appears to represent. The fluid phase (green) is a disordered phase containing all three types of spins, with only short-range interactions between them. The microemulsion / critical region (red) contains two types of behaviors that the network was not able to distinguish. At larger values of Δ, the region is a microemulsion, while, at smaller values of Δ, the system shows fluctuating domains consistent with sitting near an Ising critical point. There does not appear to be a clear boundary between the critical fluctuation and microemulsion states, but rather a continuous transition from one to the other. It is also important to note that the microemulsion / critical region is not truly a phase. Thermodynamically, it is the same as the fluid phase (34), and the location of the red-green boundary is subjective (in our case, subjectively chosen by the neural network based on the training data set). However, it remains an important *region* of the phase diagram, with interesting properties for lipid membranes. In fact, both mainstream models to explain lipid rafts – microemulsion and critical point – are included within this region, making it the most important to consider for membrane-related questions. The black/white phase (blue) is a fully phase-separated state, consisting of all -1 or all 1

spins. With H=0, this is a region of two-phase coexistence (black and white), although an individual snapshot of our small 30x30 simulation box typically contains only one phase or the other. The gray phase (cyan) is another phase-separated state, this one containing all 0 spins. The lamellar phase, or modulated phase, (yellow) is similar to a microemulsion phase in that the surfactant separates the black and white phases, but instead of enclosed, roughly round domains, the two phases exist as long stripes. Finally, the crystal phase (magenta) includes the strange state in which rectangular regions of black and white exist, separated by a meshwork of surfactant. The network applied the same classification to the limit of the lamellar phase in which the phases alternate with period of one lattice unit.

Exploring the Phase Diagram

We used our neural network to compute other cross-sections of the phase diagram, to gain a more complete perspective on the entire parameter space. Remarkably, it was not necessary to retrain the network to work with these other cross-sections. The original network trained at H=0, K=2, L=3 is able to accurately identify the phases elsewhere in the phase diagram, for all H, K, and L values considered in this study.

Varying the surfactant strength L changes the topology of the phase diagram (Fig. 3.3). At zero or low L (L/J = 1.5), the lamellar phase does not exist, and the black/white phase directly borders the gray phase. At zero L, a tricritical point exists at the intersection of the fluid, black/white and gray phases. At higher L (L/J = 3), we reach the case shown in Fig. 3.2, in which the lamellar and crystal phases exist between the black/white and gray phases. At extremely high L (L/J = 6), the system becomes a

crystal for nearly all values of Δ and T tested in order to maximize the number of surfactant interactions.

The same sequence of topologies appears when L is varied with K=0 (Fig. 3.4), although the phase boundaries occur at lower Δ. Note that we show the K=0, L=0 case, which is equivalent to the Blume-Capel model. In our diagram, the transition between black/white coexistence and the fluid phase can be identified as a critical line by virtue of the red critical region appearing between the blue and green regions. Note that microemulsions are not possible with L=0, and therefore the entire red region in this cross-section represents Ising critical behavior. The critical line occurs at the boundary between the blue and red regions.

Finally, we examined the effect of adding an external field H, changing the composition of black versus white, in both cases of zero and positive L. (Fig. 3.5) Notably, the red critical region separating the black/white and fluid phases disappears, correctly showing that at L=0, H>0, this is no longer a critical phase transition. However, in the L=3 case, some red region remains at high Δ. Presumably this indicates a microemulsion phase, which is still expected to exist at nonzero H.

Quantifying Protein Recruitment

Having calculated the phase diagram for the lattice microemulsion model, we turned to address our questions related to biological function. In particular, we wanted to compare the effectiveness of lipid raft-mediated protein reorganization at various points on the phase diagram. Our simulated case is the same one we have investigated previously (Chapter 2): we suppose that 3 receptors (such as IgE-FcεRI) have been cross-linked to form a cluster, and need to recruit a kinase (such as Lyn) to become

Figure 3.3 Cross-sections of the phase diagram at varying values of the surfactant strength. Surfactant strength L/J is varied 0 to 6, with constant H/J = 0, K/J = 2. Colors have the same meaning as in Fig. 3.2.

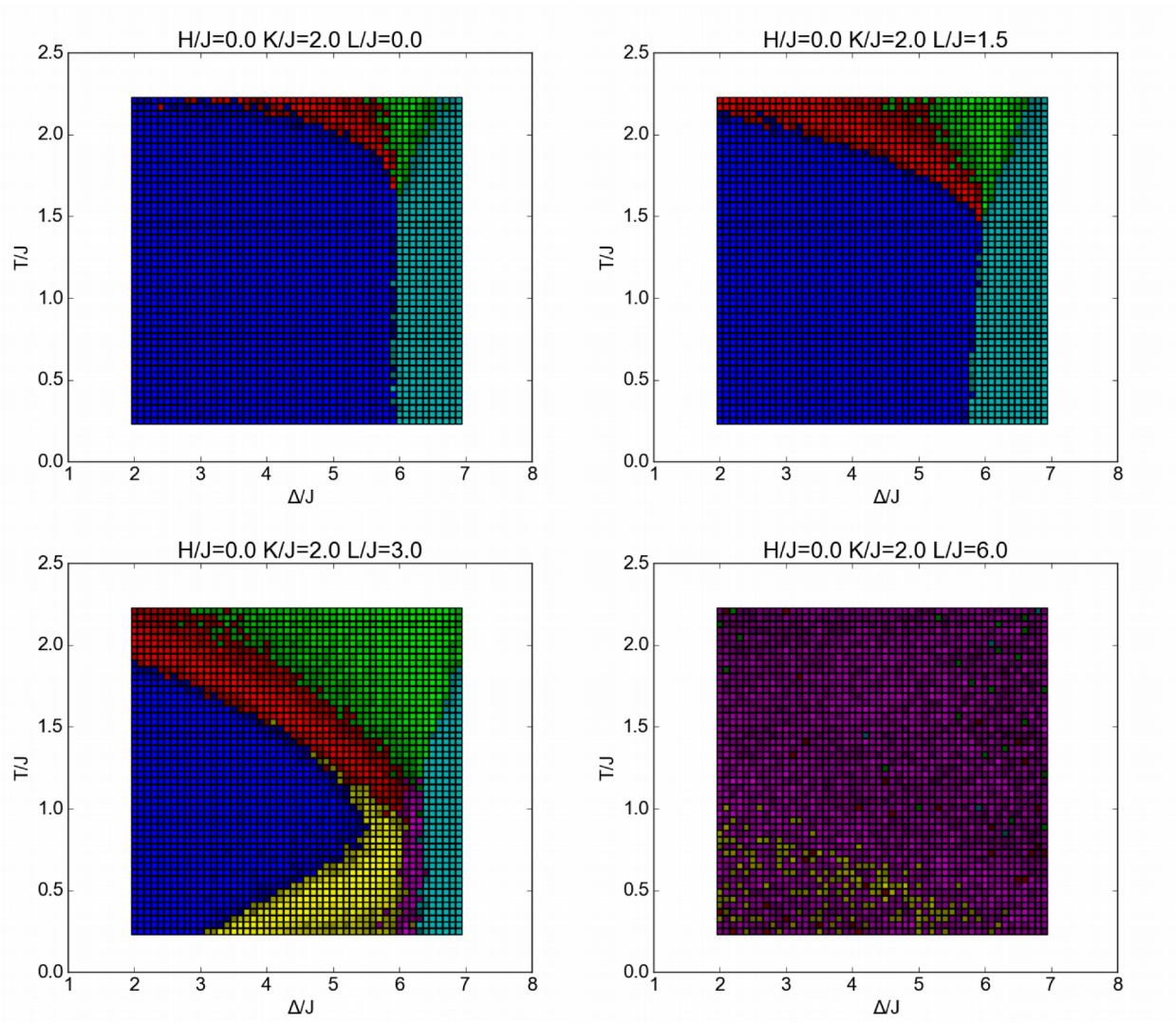
H/J=0.0 K/J=2.0 L/J=0.0
H/J=0.0 K/J=2.0 L/J=1.5
H/J=0.0 K/J=2.0 L/J=3.0
H/J=0.0 K/J=2.0 L/J=6.0
T/J
Δ/J
0.0
0.5
1.0
1.5
2.0
2.5
1
2
3
4
5
6
7
8

Figure 3.4 Cross-section of the phase diagram, with H=0 and K=0. L/J is varied from 0 to 2. The case of K=0, L=0 (top left) gives the phase diagrams for the Blume-Capel model. Colors have the same meaning as in Fig. 3.2.

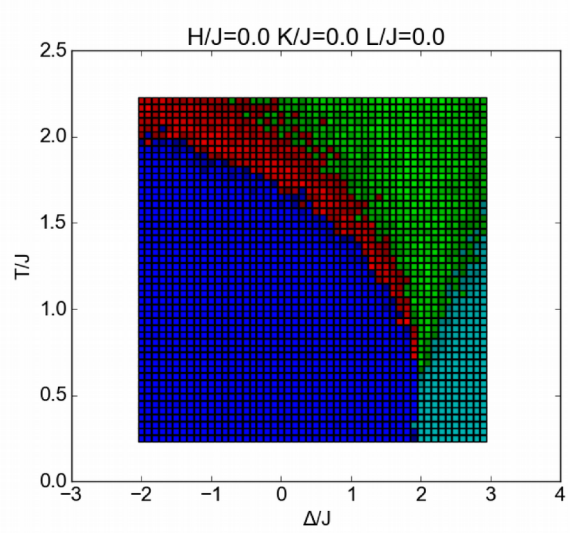
H/J=0.0 K/J=0.0 L/J=0.0
T/J
Δ/J
2.5
2.0
1.5
1.0
0.5
0.0
−3
−2
−1
0
1
2
3
4

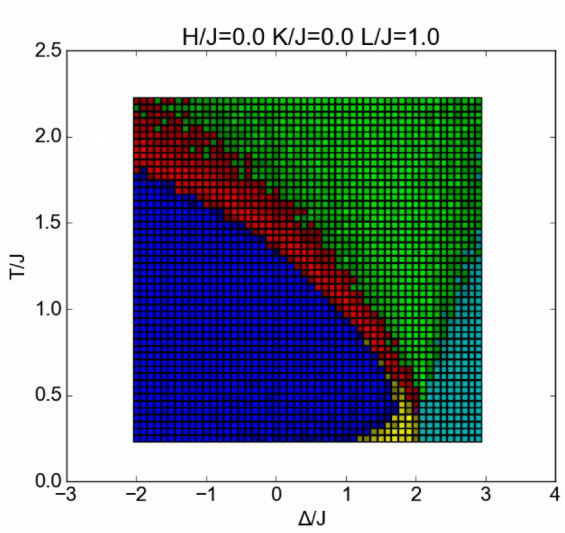
H/J=0.0 K/J=0.0 L/J=1.0
T/J
Δ/J
2.5
2.0
1.5
1.0
0.5
0.0
−3
−2
−1
0
1
2
3
4

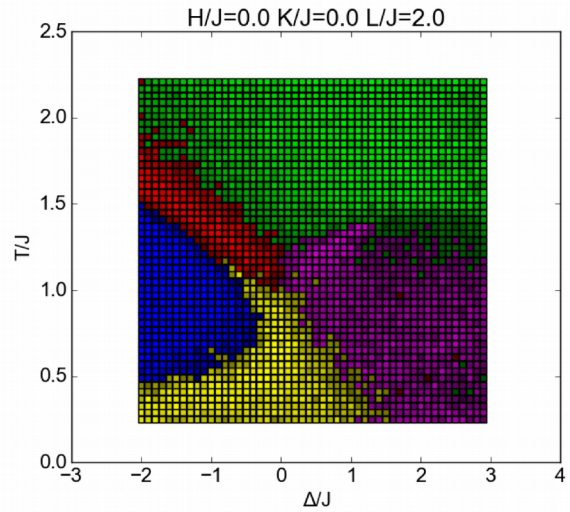
H/J=0.0 K/J=0.0 L/J=2.0
T/J
Δ/J
2.5
2.0
1.5
1.0
0.5
0.0
−3
−2
−1
0
1
2
3
4

Figure 3.5 Cross-sections of the phase diagram at nonzero external field H. H/J = 0.1 or 0.5, and L/J = 0 or 3. Colors have the same meaning as in Fig. 3.2.

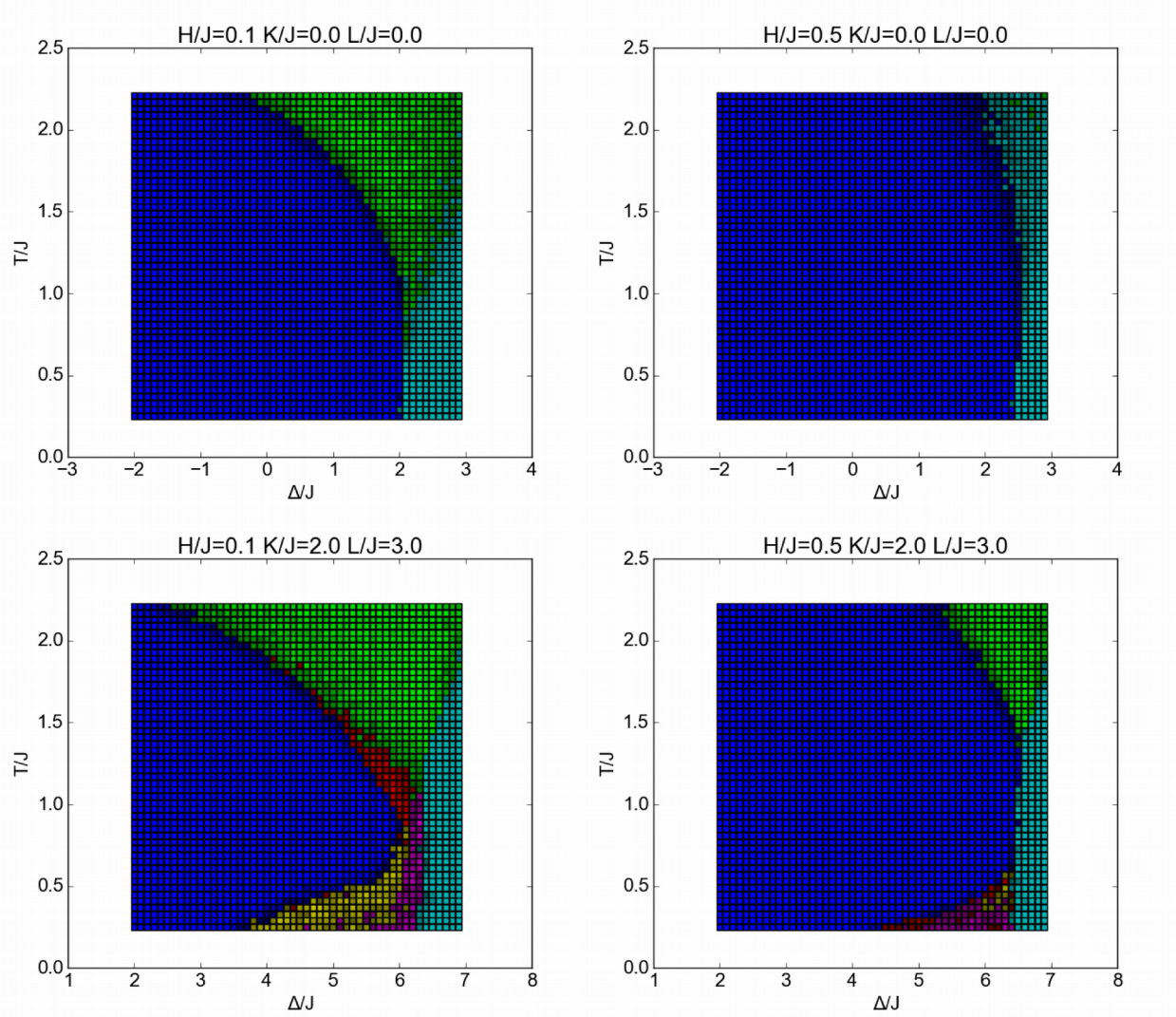
H/J=0.1 K/J=0.0 L/J=0.0
H/J=0.5 K/J=0.0 L/J=0.0
H/J=0.1 K/J=2.0 L/J=3.0
H/J=0.5 K/J=2.0 L/J=3.0
T/J
Δ/J

activated. We assume both the receptors and the kinase prefer the Lo phase. We would like to compute the free energy associated with moving the kinase into the middle of the receptor cluster (binding energy). A larger magnitude negative value indicates a stronger contribution of lipid rafts to protein colocalization at the particular point in the phase diagram.

Similar to what we and others have done previously (Chapter 2 and (35)), we use Bennett's method (36) to calculate the free energy change. We do so here in a more computationally efficient method than in previous studies. Previously, we computed the energy change stepwise, moving the kinase out of the cluster, one lattice unit at a time, and generating a profile of energy versus position in the process (Chapter 2, Fig. 2.7). Here, we instead calculate the entire energy in one step. Our simulated system (Fig. 3.6) consists of two separate boxes, one containing the receptor cluster (left), and the other representing membrane at infinite distance from the cluster (right). By Bennett's method, we compute the free energy to move the kinase from the box at infinite distance to the center of the cluster (position of kinase in Fig. 6, bottom left).

We used the phase diagram to assist in choosing points for Bennett simulations – we ran a simulation at each point marked with a diamond in Fig. 3.7. We focused our simulations primarily on the microemulsion / critical region of the phase diagram (red), and for comparison, we performed simulations at a smaller number of points elsewhere in the phase diagram as well.

Our results are shown in Fig. 3.7 (colors of diamonds). In the Blume-Capel (H = K = L = 0) phase diagram (Fig. 3.7a), we see roughly the same binding energy of ~ -0.6 k_BT at all points along the Ising critical line. This corresponds to a modest increase in

Figure 3.6 Schematic of simulations using Bennett's method to calculate kinase binding energy. The simulated system consists of two separate boxes, one representing the membrane near the receptor cluster (left), and another representing a section of the membrane at infinite distance (right). The red and green proteins' spins are fixed white, while the rest of the lattices are Monte Carlo sampled. We use Bennett's method to compute the free energy difference between State 1 (kinase at infinity) and State 2 (kinase inside cluster).

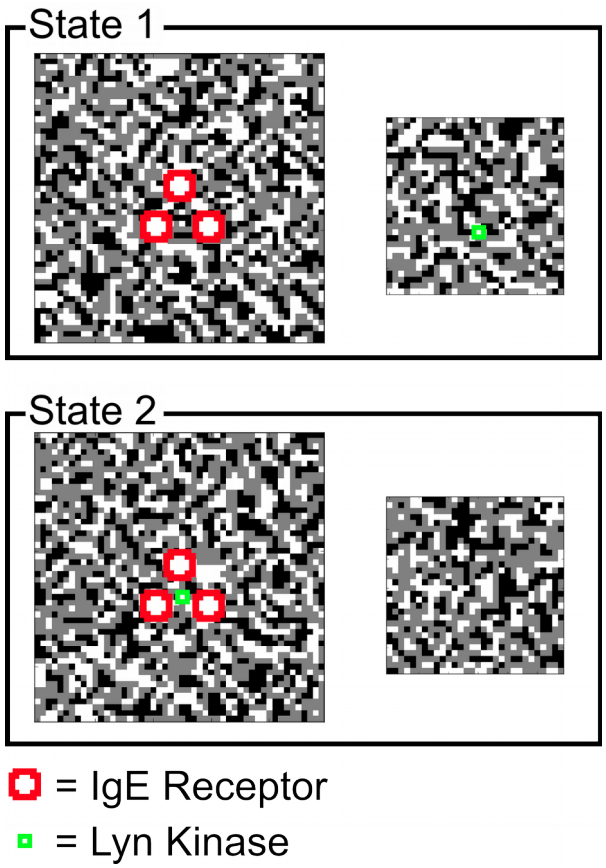
State 1
State 2
= IgE Receptor
= Lyn Kinase

Figure 3.7 Kinase binding energy at selected points in the phase diagram. Each colored diamond indicates the free energy change associated with moving a kinase into a cluster of receptors (as in Fig. 3.6) at that point in the phase diagram. The phase diagram colors are rendered paler than in other figures to make the diamonds more clearly visible. (a) Binding energy in the Blume-Capel model cross-section. (b) Inset of (a) in the region around the tricritical point (black box). The indicated point (black arrow) with the minimum free energy of -1.7 k_BT occurs at the tricritical Δ and 1.04 times the tricritical temperature. (c) Binding energy in a cross-section in which the external field $H/J = 0.1$ favors spins opposite to the kinase and receptor preference. (d) Binding energy in a cross-section that includes microemulsions and lamellar phases ($K/J = 2$, $L/J = 3$). At certain points here (purple color scale), the positive binding energy indicates that it is energetically unfavorable to bring the kinase into the cluster.

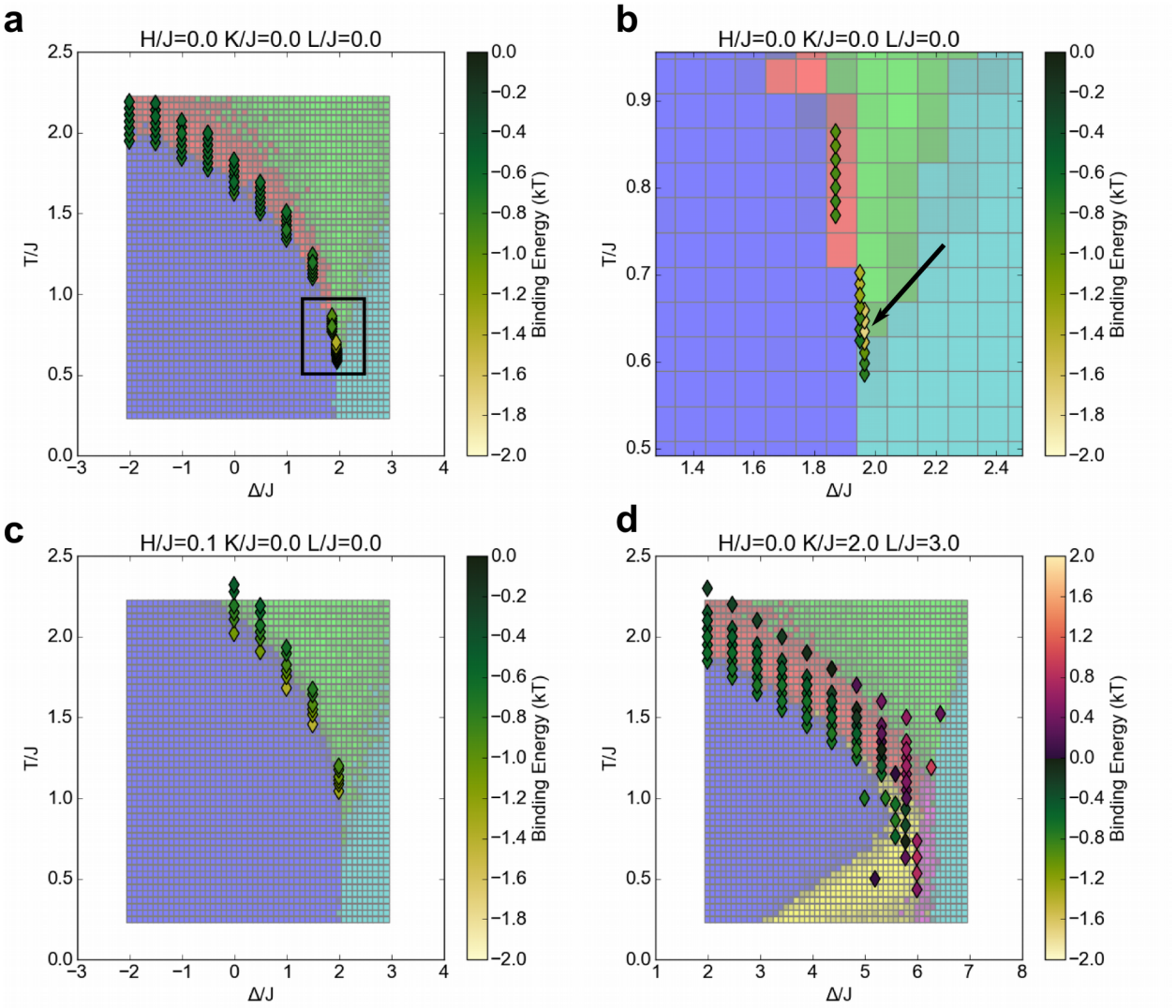
a
H/J=0.0 K/J=0.0 L/J=0.0
T/J
Δ/J
Binding Energy (kT)
b
H/J=0.0 K/J=0.0 L/J=0.0
T/J
Δ/J
Binding Energy (kT)
c
H/J=0.1 K/J=0.0 L/J=0.0
T/J
Δ/J
Binding Energy (kT)
d
H/J=0.0 K/J=2.0 L/J=3.0
T/J
Δ/J
Binding Energy (kT)

kinase concentration, by a factor of $e^{0.6} \approx 1.8$. Along the critical line, the binding energy does not show a dramatic difference above, versus below, the transition temperature (blue-red boundary). Strikingly, as the tricritical point is approached, we see a dramatic, nearly threefold increase in the magnitude of the binding energy. The minimum free energy of -1.7 k_BT, is achieved at the tricritical Δ (1.9655 J) and 1.04 times the tricritical temperature (0.6344 J/k_B). The corresponding increase in kinase concentration by a factor of $e^{1.7} \approx 5.5$ is much more significant than the 1.8 factor at an ordinary critical point. We suspect that the distance of the optimum above the tricritical temperature, 1.04 times, is a finite size effect, as this value increases if the simulation box is made smaller. The true optimum might occur at exactly the tricritical temperature.

To further investigate the finite size effect, and also validate our new application of Bennett's method (Fig. 3.6), we also calculated the energy profile at the tricritical point stepwise by Jarsynski's method (37), identical to the method used in Chapter 2 and (35) (Fig. 3.8). This gave a binding energy of ~ -1.5 k_BT, comparable to our result at 1.02 times the tricritical temperature (Fig. 3.7b). However, at the tricritical temperature, our application of Bennett's method gives a binding energy of only -1.0 k_BT, presumably due to finite size effects at this temperature.

We compare these results to the first-order phase transition that occurs at a positive field H (Fig. 3.7c), where we have a higher concentration of black, Ld pixels than white, Lo pixels. Based on our previous work with varied membrane compositions (Chapter 2, Fig. 2.7f-g), we expected to see a stronger binding energy here. We found a similar binding energy of ~ -0.6 k_BT above the transition temperature in the fluid phase. However, we see a substantially stronger binding energy as low as ~ -1.4 k_BT upon

Figure 3.8 Alternate method for computing kinase binding energy. We use the method described in (35) and Chapter 2. (a-b) Example simulation at the tricritical point, in which the kinase sits at a position 95 nm from the cluster. Receptors (red) and kinase (green) were held fixed as white, and the rest of the lattice was Monte Carlo sampled. (a) shows one simulation snapshot, and (b) shows the average of all snapshots acquired. The simulation was repeated at every possible kinase position from 0 to 95, stepwise, in order to generate (c), the profile showing the free energy of the kinase in every position. The position axis in (c) corresponds to the axis shown in (a). The free energy at position 3 nm of ~ -1.4 k_BT is in good agreement with the computationally cheaper method used in the rest of the study (Fig. 3.7, Fig. 3.9).

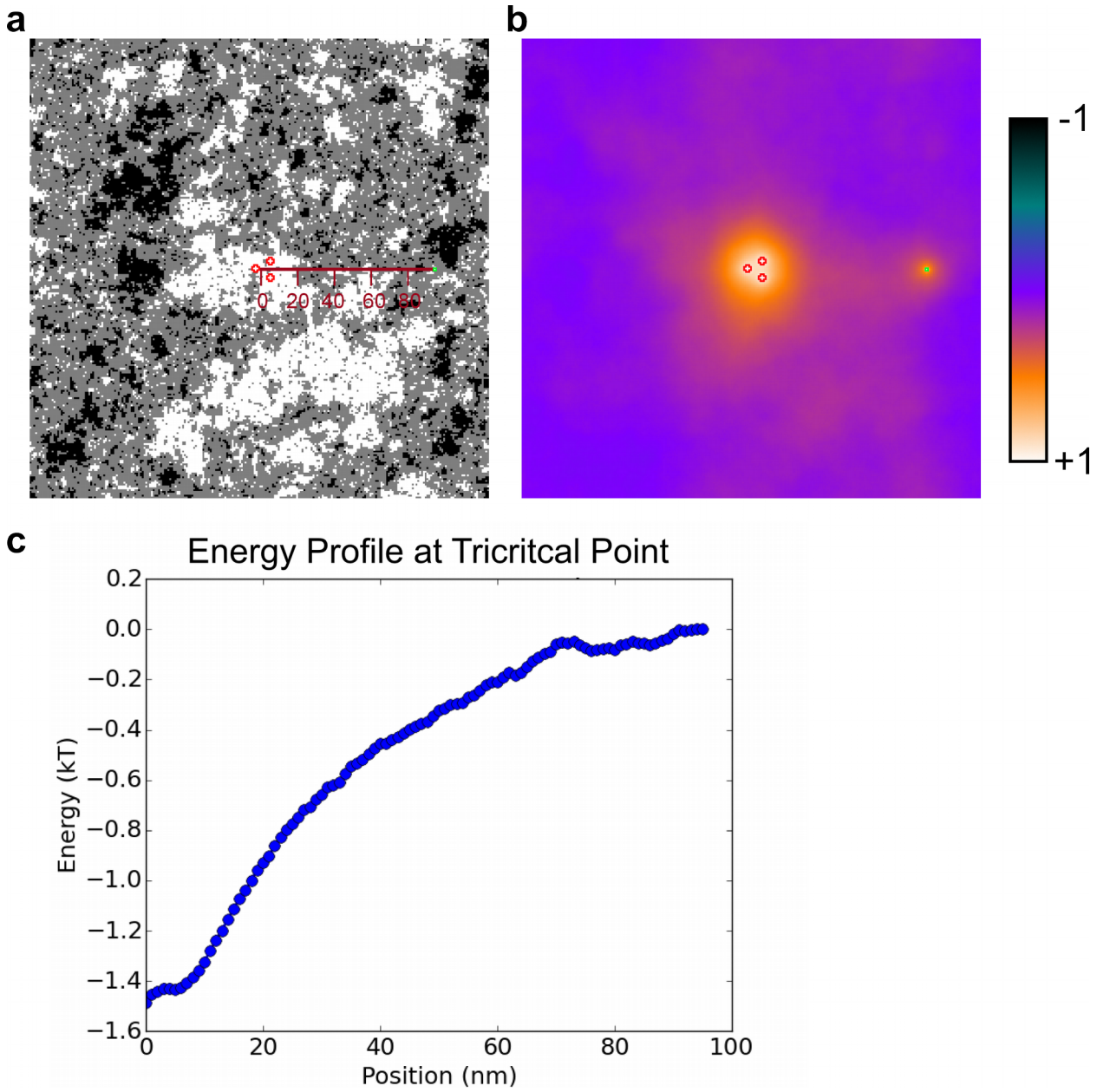
a
b
0
20
40
60
80
-1
+1
c
Energy Profile at Tricritcal Point
Energy (kT)
Position (nm)
0.2
0.0
−0.2
−0.4
−0.6
−0.8
−1.0
−1.2
−1.4
−1.6
0
20
40
60
80
100

entering the phase-separated state. In the context of membranes, this would correspond to a situation in which most lipids on the membrane favor Ld phase, but our proteins of interest favor Lo. The stronger binding energy in this case is consistent with our conclusions in Chapter 2.

Finally, we consider the binding energy in the full microemulsion model (Fig. 3.7d). In the Ising critical region (i.e. the red region at low values of Δ), we again see a binding energy of ~ -0.6 k_BT, the same as the case with no surfactant strength L (Fig. 3.7a). As we move to higher Δ, and the Ising critical region becomes instead a microemulsion region, we see a striking change. The binding energy at certain points becomes much weaker, even turning positive (unfavorable). Intuitively, this happens when the characteristic length scale of the microemulsion is smaller than the size of the cluster. This is not to say that a microemulsion state cannot lead to strong kinase binding – it depends on how the characteristic length scale of the microemulsion compares to the spacing of the clustered receptors. Indeed, some of our measurements within the microemulsion and lamellar regions achieve a binding energy of -0.6 k_BT, comparable to that at an Ising critical point. It is also possible that a microemulsion exists at a length scale larger than our 30x30 nm simulation box. This would likely appear as phase-separated in our diagram, and indeed would look equivalent to phase-separated from the perspective of a cluster of size less than 30 nm. Based on our simulated results at phase-separated points, this case would also likely yield a value of around -0.6 k_BT.

What is lacking in the Fig. 3.7d cross-section is a dramatic tricritical point. At nowhere in this parameter cross-section do we beat the “typical” value of ~ -0.6 k_BT

(except perhaps biologically irrelevant points at very low temperature). This remains true if we more densely sample the entire length of the phase boundaries (data not shown). We are not convinced that a tricritcal point exists at this cross-section, but if it does, it seems to be less biologically exciting than the one in Fig. 3.7a. Among all of the phase states tested, the tricritical point with no surfactant leads to the strongest possible kinase binding energy.

In future work, it might be possible to develop a universal scaling theory to describe the increase in binding energy magnitude as the tricritical point is approached. For such work, it would be preferable to consider the simpler case, in which, instead of considering a receptor cluster, we simply find the attractive energy between two white pixels. We performed simulations for this case by the same method, and found qualitatively similar results, with unsurprisingly lower magnitudes (Fig. 3.9).

3.4 Discussion

Comparison to Published Results

We have generated the phase diagram for the Gompper and Schick microemulsion lattice model using relatively new neural network techniques. It is important to consider how this method compares to other more established methods for phase diagram determination. We examine certain special cases of the model that allow for comparison of our phase diagram to published phase diagrams obtained by other methods.

By taking Δ to $-\infty$, we have the Ising model, with the well-known critical transition temperature of $2 / \log(1 + \sqrt{2}) \approx 2.269\ J/k_B$. Applying our existing network to this

Figure 3.9 Free energy change (binding energy) due to moving two +1 spins to a spacing of 3 lattice units. Simulations were run on a system similar to that shown in Fig. 3.6, but with the box on the left containing, instead of the 3 IgE receptors, a single fixed white pixel. Each diamond indicates the free energy computed by Bennett's method at that point in the phase diagram. (a) Binding energy in the Blume-Capel model (H=0, K=0, L=0) cross-section. (b) Inset of (a) in the area of the tricritical point (black box). Similar to the more complicated case of a cluster of receptors (Fig. 3.7 a-b), the binding energy is considerably higher close to the tricritical point. (c) Binding energy in a cross-section that includes microemulsions (K/J = 2, L/J = 3). Similar to the more complicated case (Fig. 3.7d), certain microemulsions give a positive binding energy.

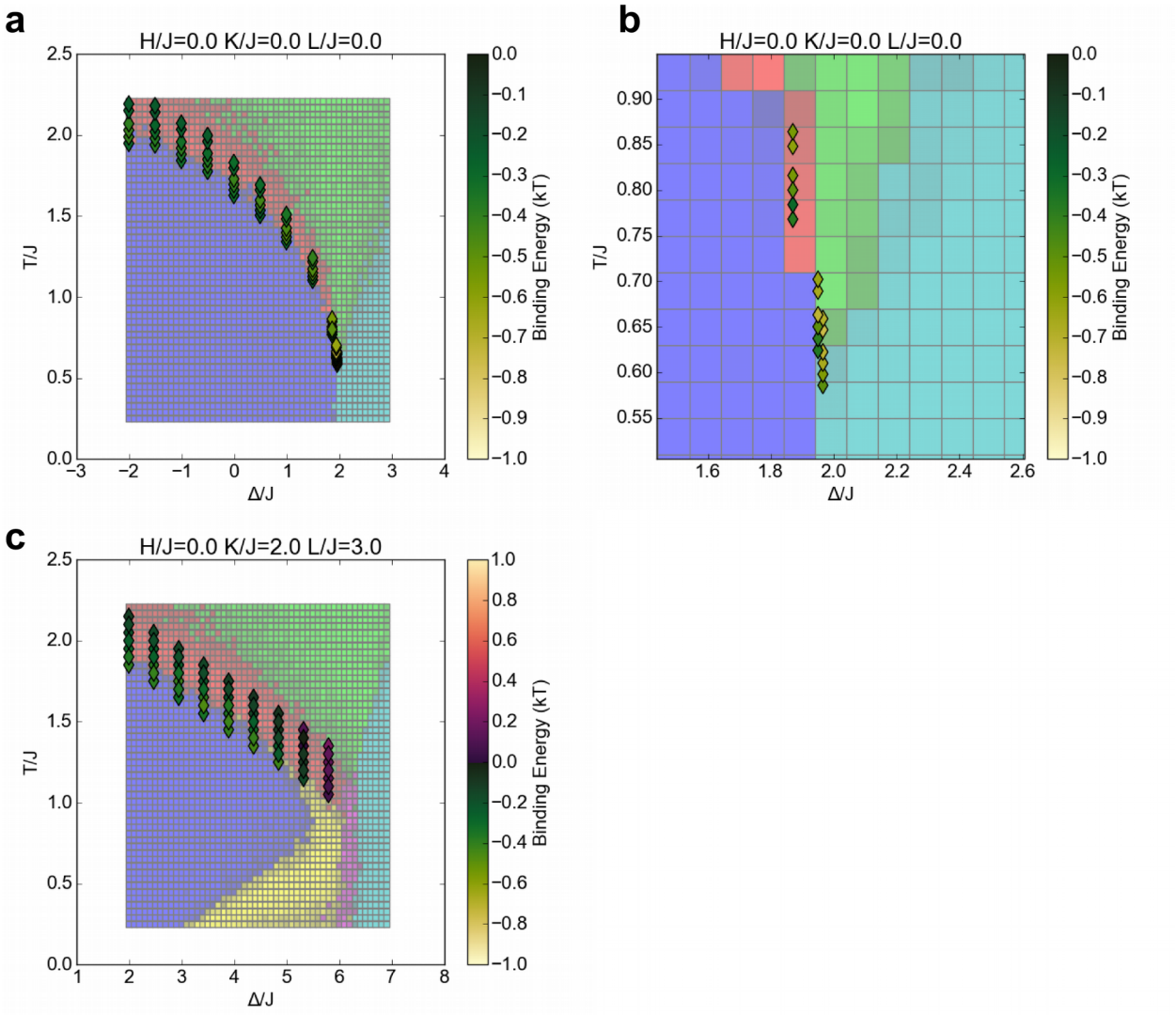
a
H/J=0.0 K/J=0.0 L/J=0.0
T/J
Δ/J
Binding Energy (kT)
b
H/J=0.0 K/J=0.0 L/J=0.0
T/J
Δ/J
Binding Energy (kT)
c
H/J=0.0 K/J=2.0 L/J=3.0
T/J
Δ/J
Binding Energy (kT)

case, we see the phase transition at close to the correct temperature (Fig. 3.10a). The network's confidence level for the Ising model is worse than optimal because this network was trained to perform a more complicated classification on 6 phases, instead of the 2 phases relevant to the Ising model. A different approach is to train a network, solely on Ising model examples, to classify between only the fluid and phase-separated states. With this model, we distinguish the phases with high confidence, and nearly perfectly identify the transition temperature (Fig. 3.10b). This level of accuracy is comparable to previous neural network work on the Ising critical transition (25).

The result for the Blume-Capel model (Fig. 3.4, K=0, L=0) is comparable to results with this model from other methods. We find good quantitative agreement on the location of phase boundaires with Beale's phase diagram from finite size scaling (38), and obtain a much better result than the mean field theory solution (30) (Fig. 3.11).

Our diagrams can also be compared to those obtained in Gompper and Schick's original description of the model (22) (Fig. 3.12). Note that to make this comparison it was necessary to add the parameter K2, the equivalent of K between second nearest neighbors in a straight line. This had no effect on the overall shape of the phase diagram, but shifted the phase boundaries slightly. We find very good agreement on the location of the critical line in all cross-sections with Gompper and Schick's transfer matrix approach. The original phase diagram included a Lifshitz line, which the authors defined as the separation between Ising and microemulsion regions. This helps us better interpret the combined microemulsion/critical region in our phase diagram, which is in fact a microemulsion to the right of the Lifshitz line. In other aspects of the phase diagram, the neural network approach provided new information, and revealed

Figure 3.10 Neural network computation of the Ising model phase diagram. Graphs show the outputs of the neural network corresponding to each phase, indicating the network's level of confidence that the system represents that phase. At each temperature value, the network's prediction is the phase for which the network output is the highest. The true Ising transition temperature is indicated by the dashed line; an accurate network should give “Separated” as the highest output below this temperature, and “Critical” or “Fluid” as the highest output above this temperature. (a) Output of the neural network used in the rest of this study. The predicted transition temperature is close to, but slightly above, the true transition temperature (b) Output of a neural network specialized for the Ising model only. This network was trained on examples from the Ising model, and only distinguishes between the fluid and phase separated states. This network's predicted transition temperature almost exactly matches the true transition temperature.

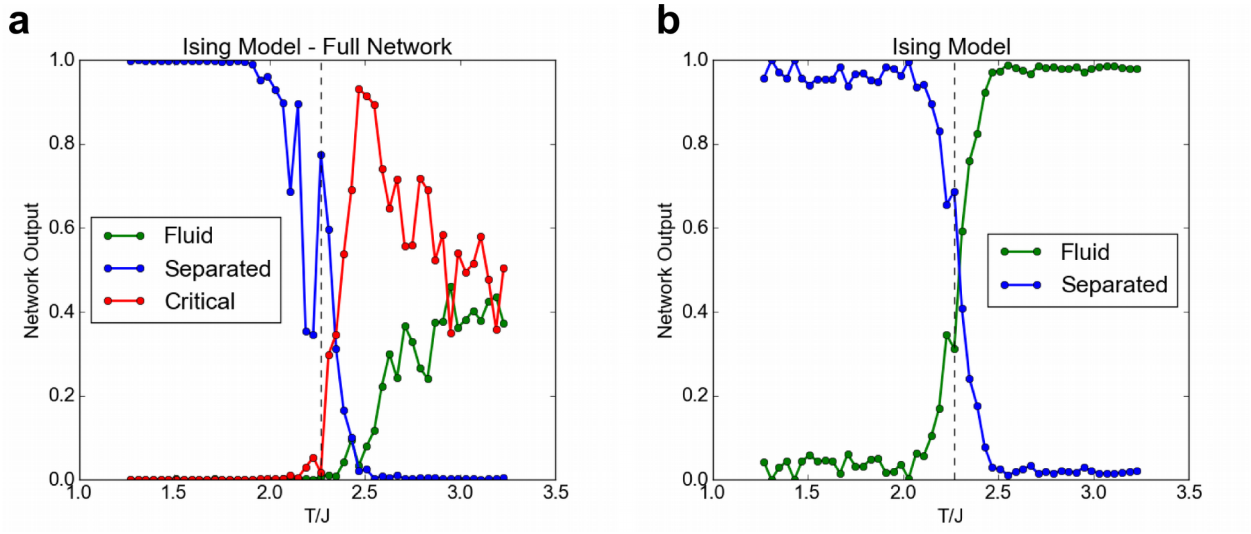
a
Ising Model - Full Network
Network Output
T/J
Fluid
Separated
Critical
b
Ising Model
Network Output
T/J
Fluid
Separated

Figure 3.11: Comparison to other methods for calculation of the Blume-Capel phase diagram. The neural network's phase diagram follows the same key as in Fig. 3.2. Overlaid in gray is the phase boundary as determined by finite size scaling in (38). The dashed line represents a critical phase transition, solid represents a first-order transition, and the transition from dashed to solid is the tricritical point. Dotted line in yellow is the critical line as determined by mean field theory in (30).

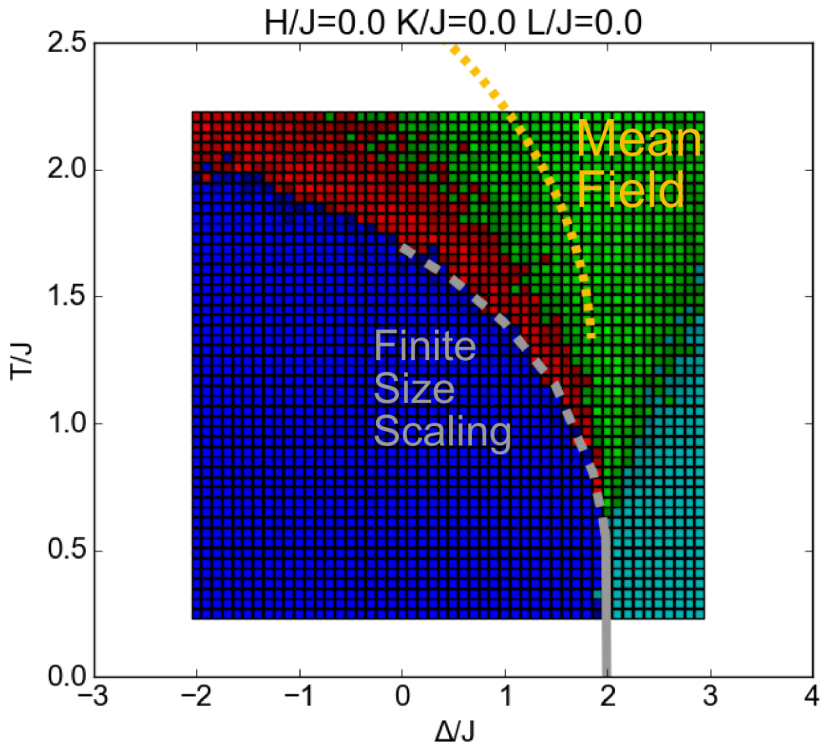
H/J=0.0 K/J=0.0 L/J=0.0
Mean
Field
Finite
Size
Scaling
T/J
Δ/J
2.5
2.0
1.5
1.0
0.5
0.0
−3
−2
−1
0
1
2
3
4

shortcomings of the original phase diagram. We note our new placement of the lamellar phase (yellow) is qualitatively different from the Gompper and Schick diagram, including a lobe that sits below the phase-separated state on the temperature axis. We give a new boundary between the gray phase (cyan) and the fluid phase (green). Our identification of the rectangular crystal phase (magenta) is entirely new, not addressed in the original study (the diagonal crystal that our network labeled as part of this phase arguably belongs in the lamellar phase, but the rectangular features are clearly their own phase).

Some of these novel features are relevant to the biological system of interest, while others are not (such as the rectangular crystal phase, which likely exists only due to the use of a square lattice), but all point to the strengths of global computational approaches in phase diagram prediction. Theoretical techniques like finite size scaling frequently focus on particular interesting regions of the phase diagram, such as the critical line. In our neural network approach, we instead indiscriminately analyzed entire slices of the phase diagram, extracting features in both critical and non-critical regions. This is especially valuable for a problem such as membranes, for which many groups believe the most relevant states are not located near a critical point.

Finally, to further validate the application of this model to the study of lipid membranes, we compare our neural-network-derived phase diagrams with the numerical and mean-field phase diagrams produced in previous studies on the formation of lipid rafts (as defined in the Introduction). We focus our comparison on microemulsion-based models for lipid raft formation, which propose that either surfactant-like lipid species (17) or membrane curvature (19, 20, 39) stabilize the

Figure 3.12: Comparison of results for the microemulsion phase diagram to the original study. Gray overlays are reproduced from the original study (22). Solid lines indicate first order phase transitions, dashed lines indicate critical phase transitions, and dotted lines are Lifshitz lines.

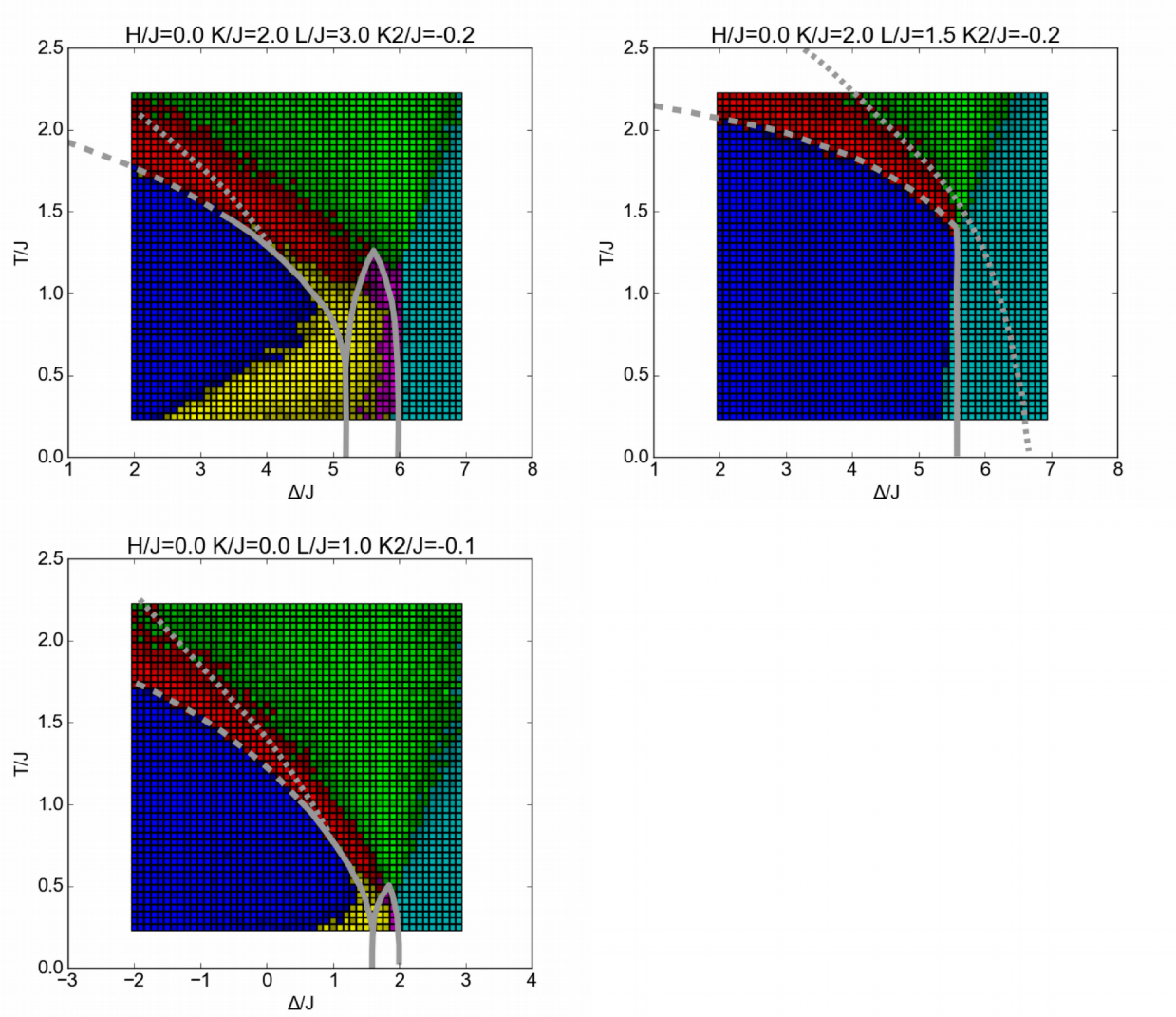
H/J=0.0 K/J=2.0 L/J=3.0 K2/J=-0.2
H/J=0.0 K/J=2.0 L/J=1.5 K2/J=-0.2
H/J=0.0 K/J=0.0 L/J=1.0 K2/J=-0.1
T/J
Δ/J

interface between different phase domains. In general, for both aforementioned microemulsion models, we find good agreement between the phase diagrams in the literature and those generated by our neural network approach (Fig. 3.13). Our phase diagrams reproduce all of the features found in these other model frameworks, including Ising critical transitions, modulated phases, two-phase coexistence and tricritical phenomena. Moreover, the general topology of the phase diagrams is consistent regardless of model choice—for instance, all models considered here predict a modulated phase-separated from a microemulsion phase by an Ising critical line, with the microemulsion phase in turn separated from an ordinary fluid phase by a non-phase-transition boundary. This consistency with previous work speaks to the generality of our approach, which allows us to describe and compare a wide variety of raft phenomenologies using a single model framework.

Application to Lipid Rafts

We set out with this model to analyze competing hypotheses on the physical basis of lipid rafts: does lipid heterogeneity arise from proximity to a critical phase transition, or from nanodomains of a characteristic size, as in a microemulsion? We found that in some ways, the two hypotheses are much alike. If we say that the main purpose of a lipid raft is to recruit proteins to the correct place on the membrane, such as our example of Lyn recruitment into an IgE-FcεRI cluster, then the two states are equally beneficial for the cell, thermodynamically. As we showed, both give about the same optimal binding energy of -0.6 k_BT. We also showed it is possible to sit in a region between microemulsion and critical point with a classification that is subjective. Gompper and Schick chose the Lifshitz line as an arbitrary distinction for what qualifies

Figure 3.13 Schematic comparison of our phase diagram with those from the microemulsion literature. (a) Mean-field phase diagram from a model with hybrid lipid species acting as a surfactant. Adapted from (50). (b) Mean-field phase diagram from a model with curvature coupled to membrane composition to produce a surfactant-like interaction. Adapted from (39). (c) Phase diagram generated by our neural network approach. Note the similarity in structure of the three different phase diagrams. X coordinate gives strength of surfactant-like interaction in (b), or concentration of surfactant species in (a) and (c). Y coordinate represents temperature. Note that this is a schematic representation, so the actual axes from the source papers differ in scale and representation. Color coding of phase diagrams is similar to previous figures: yellow = modulated or lamellar phase, blue = two-phase coexistence, green = ordinary fluid, and red = microemulsion. Solid lines denote first-order phase transitions, dashed lines denote critical (second-order) phase transitions, and dotted lines denote Lifshitz lines. For the sake of comparison to the other models, we use red here to represent only microemulsions, not Ising critical behavior. The red-green gradient in (c) is used to schematize the ambiguity between microemulsion and ordinary fluid phase, and represents our best interpretation of the location of the microemulsion state, taking into account the neural network output (Fig. 3.2), snapshots within the phase diagram (Fig. 3.2, red-bordered panels), and the location of the Lifshitz line from (22) shown in Fig. 3.12.

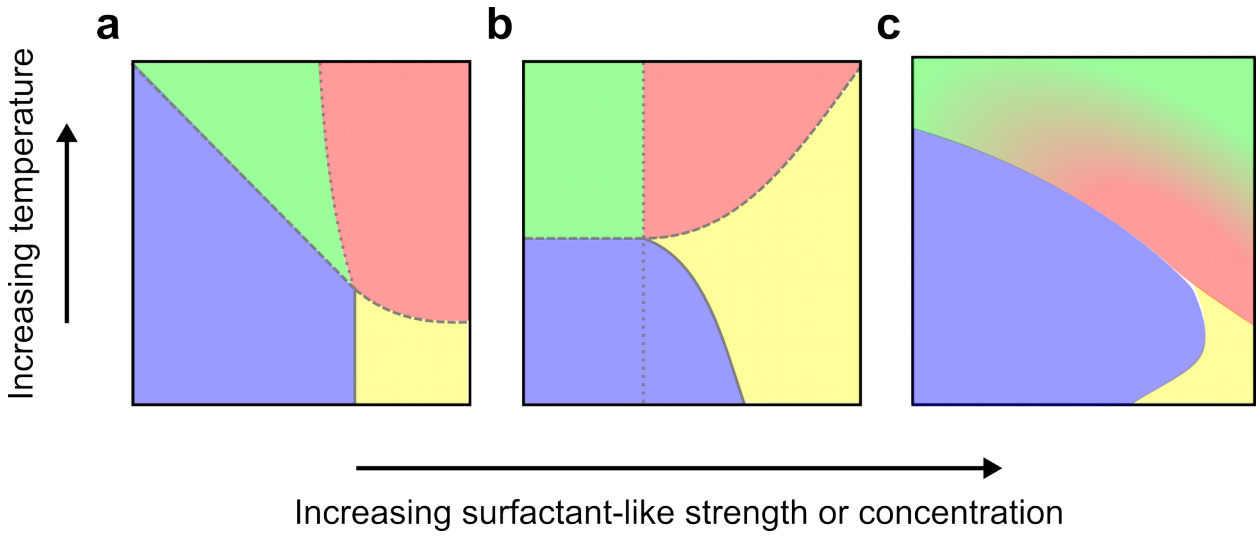
a
b
c
Increasing temperature
Increasing surfactant-like strength or concentration

as a microemulsion, while our neural network was unable to distinguish the two behaviors.

Our energy calculations make a clear prediction for a difference between clearly critical and clearly microemulsion states. Microemulsions carry the requirement of a particular characteristic size, and can only effectively stabilize lipid domains smaller than that size. If a cluster is larger than the microemulsion length scale, then there is actually *exclusion* of other components of like phase from the cluster (Fig. 3.7d). In contrast, the Ising critical point stabilizes lipid rafts at all length scales, and never excludes components of like phase. If the membrane indeed exists as a microemulsion, then in principle it should be possible to experimentally exceed the correct length scale, and cause a reversal of the lipid mediated signaling. To our knowledge, this experiment has not been achieved, and would remain challenging to implement. However, in mast cells, a structurally defined ligand with spacing 13 nm has been studied (Chapter 2 and (40)), and the resulting large receptor spacing lowers but does not eliminate the signaling response. This suggests that, if the mast cell signaling response relies on a microemulsion-mediated kinase recruitment, that microemulsion must have a size larger than 13 nm.

One argument sometimes used in favor of microemulsions is that they are easier to achieve, requiring less cell-directed tuning of the membrane. From our phase diagrams, this is hard to say. Microemulsions and critical points occupy roughly similar areas on the phase diagram, but this likely depends greatly on the details of the specific microemulsion model used. We can, however, point out that cell-directed tuning to achieve a microemulsion may be more difficult than expected. The cell not only has to

tune the membrane composition to a microemulsion, but also must tune the length scale to the characteristic size necessary for the correct biological function, which may be highly variable, depending on the signaling pathway.

What about the actin cytoskeleton? It is widely thought that cortical actin couples to the membrane, forming “corrals” that add further complexity to the heterogeneity of the membrane. However, in many ways this does not affect our conclusions, as typical size estimates for actin corrals (41) are above our simulation size of 50x50 nm (Fig. 3.6). A small cluster sitting within one corral sees a particular membrane composition, regardless of the corrals that exist elsewhere. However, actin involvement motivates two other considerations. First, we should not entirely ignore the phase-separated state in the phase diagram (blue, Figs. 3.2-3.7), as the membrane perhaps has a phase-separating composition, driven below the diffraction limit only by actin-mediated partitioning (42, 43). We see that this would give a similar binding energy to the microemulsion or critical point pictures (Fig. 3.7a,d). Second, we note that due to actin, the membrane composition encountered by receptors might not be the global composition of the membrane. Actin has been proposed to preferentially recruit and sequester certain types of lipids (42, 44), which would deplete these from a cluster in the middle of a corral.

The most striking new discovery from our phase diagram and energy calculations is the power of a membrane at a tricritical point. Our computations show that near the tricritical point, the potential binding energy due to lipid rafts increases by a factor of 3 compared to any of the other proposed models: critical point, microemulsion, or phase-separated two-phase coexistence. Likely the benefit of the tricritical point comes from

the different critical exponents of this universality class. In particular the correlation function g(r) scales as $r^{-0.25}$ at the Ising critical point, but as $r^{-0.15}$ at the tricritical point. The smaller tricritical exponent (η=0.15) allows attraction between proteins to remain stronger at a longer distance.

To our knowledge, a tricritical point has not previously been considered as a serious proposition for the basis of lipid rafts, and perhaps for a good reason: tricritical points are even harder for a cell to achieve than Ising critical points. In the three-dimensional phase space of the Blume-Capel model, only a single point is a tricritical point. However, we note that in a many-component cell membrane with many more than 3 degrees of freedom, it should be possible to tune to a tricritical composition. Furthermore, we argue that if effective lipid rafts provide a strong enough evolutionary advantage for the cell, it might be to the cell's advantage to maintain a tricritical composition, and gain the massive improvement in lipid raft energetics that follows. Conversely, the optimal lipid raft strength for regulated signaling in the cell might be weaker than what is generated by the tricritical point, in which case we would expect the membrane to exist in one of the other phase states explored in this study.

It is also reasonable to ask whether lipid rafts could mediate the formation of the receptor cluster itself. This is less relevant in mast cells, in which clustering occurs primarily due to physical cross-linking of the IgE-FcεRI receptors with antigen, but in T cell receptor signaling, for example, clusters form in the absence of cross-linking by a mechanism that remains unclear (45). The Ising critical point or microemulsion binding energy of -0.6 k_BT may be sufficient for biologically relevant kinase recruitment, but receptor clustering requires considerably stronger interactions. We previously have

performed calculations and simulations based on the formulas for Casimir forces given in (35) and concluded that these forces, at an Ising critical point, are not large enough to mediate receptor clustering (Milka Doktorova and Eshan Mitra, unpublished observations). However, we now note that the stronger binding energies found near the tricritical point may be sufficient to mediate receptor clustering.

We further note that the concept of a membrane at a tricritical point is potentially still consistent with observations of GPMVs showing ordinary Ising critical exponents (14). From renormalization group theory, the tricritical point is an unstable fixed point, such that when a system near tricritical composition is coarse-grained, it begins to look like an ordinary Ising critical point (46). It is therefore possible that the membrane appears to be near an Ising critical point on the long length scale observed in GPMV studies, but is tricritical on the short length scale that is relevant for protein organization.

While our work with this microemulsion model has been useful in addressing many hypotheses on lipid organization (and proposing a new one!), it has some limitations. In particular, this is a thermodynamic model, operating under the assumption of a steady state. Kinetic hypotheses about lipid organization, such as active actin remodeling (47), would require a different theoretical framework in order to compare to the cases that we have explored, although our neural network-based methods should allow similar morphological classification. It is possible for active processes to still be described by an Ising critical point, as was shown in fireflies (48), although GPMV membrane studies (14) show that membranes remain close to an Ising critical point even after any active processes have likely been disrupted in sample preparation.

Another future direction for theory is to convert the phase diagrams shown here

using external fields H and Δ into diagrams based on the concentration of each component. We chose to use a model with fixed external fields and variable composition to enable efficient simulations on small system sizes, and to easily compare with existing theory literature. These external fields could be converted to the corresponding compositions of each component, transforming the phase diagram to one of fixed compositions. This would allow more direct comparison to experimental membrane phase diagrams such as (11).

3.5 Methods

Monte Carlo Simulations

Snapshots of the lattice model were generated by the Metropolis algorithm. The length of the simulation was counted in sweeps, where in each sweep, each lattice site has on average 100 opportunities to be flipped (total of 90000 individual proposed moves for a 30x30 lattice). Each proposed move consisted of randomly choosing a lattice site and a target spin value (one of {-1, 0, 1} that was not the current value of the spin). The move was performed with probability $\min(1, e^{-\Delta U/T})$ where ΔU is the change in the Hamiltonian resulting from the move.

To generate a single independent snapshot, the lattice was randomized, then 100 sweeps were run to equilibrate, with the final result saved. To generate correlated snapshots, additional sweeps were run after equilibration, with a sample saved after each sweep.

Neural Network Training

We chose the cross-section H/J=0, K/J=2, L/J=3 for training because this is

close to the cross-section described by Gompper and Schick (22) as containing examples of all major phases of the model. Generation of the neural network training data was a somewhat heuristic and iterative process. We started by sparsely sampling a large region of space in the H.J=0, K/J=2, L/J=3 plane, and labeling phases manually, to get a general sense of the layout of the phase diagram. This allowed us to find regions where we were highly confident about the correct classification, which we used for training data. In the case of the microemulsion phase, this included checking that the structure factor (Fourier transform of the correlation function) had a nonzero peak, as per Gompper and Schick's definition of a microemulsion. After the first round of training and testing, we examined snapshots from different points in the phase diagram to evaluate where errors occurred, and added further training data at appropriate points in order to reduce these errors. For example, we initially did not include the crystal phase consisting of black and white rectangles, as this phase was not described in previous work. We discovered this phase after it was labeled as fluid phase in earlier tests. The final training data set is shown in Fig. 3.14, overlaid on the final phase diagram. At each chosen set of training parameters (156 in total), 100 independent samples were acquired for training, for a total of 15600 samples in the training set.

Note that despite the heuristic approach to generating the training data, it is not the case that we could generate an arbitrary different phase diagram simply by changing the training data. Rather, the phase diagram reflects real, qualitative differences in the behavior of the system. In our experience, training with a bad training set (e.g. containing different phases labeled as the same phase) leads to an obviously bad phase diagram, in which some regions contain different adjacent pixels classified

Figure 3.14 Training the neural network. (a) Each circle represents a parameter set at which training data was acquired. The color indicates the human-generated classification of the phase at that point. These points are overlaid on the final phase diagram computed by the neural network. (b-c) Phase diagrams generated by two types of neural network. (b) is trained on averages of correlated Monte Carlo snapshots to identify all 6 phases, while (c) is trained on individual Monte Carlo snapshots to identify 4 phases. Our final phase diagram is based mostly on (b), but we take the classification of the gray phase from (c) due to its high confidence in that phase.

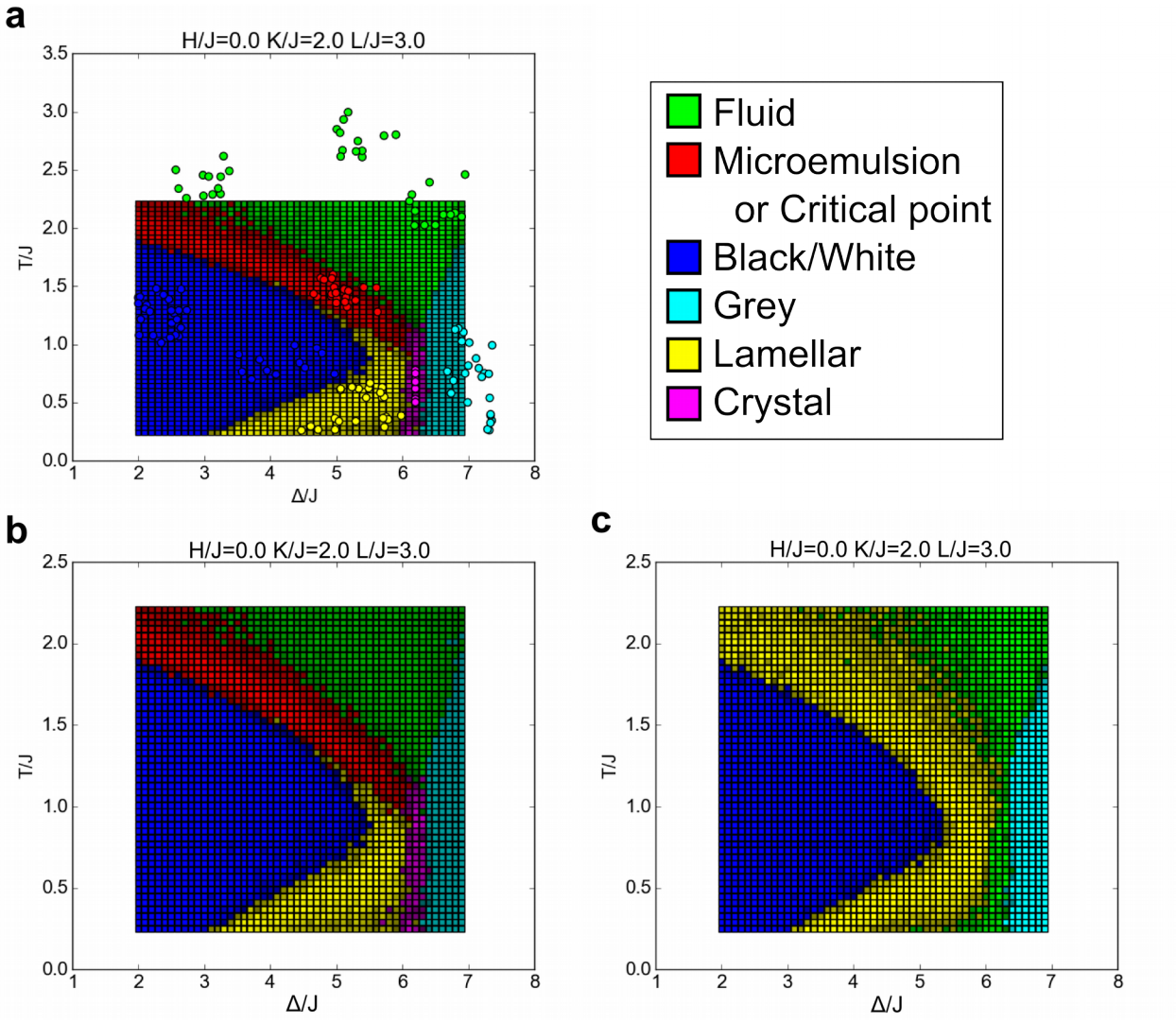
a
H/J=0.0 K/J=2.0 L/J=3.0
T/J
Δ/J
Fluid
Microemulsion
or Critical point
Black/White
Grey
Lamellar
Crystal
b
H/J=0.0 K/J=2.0 L/J=3.0
T/J
Δ/J
c
H/J=0.0 K/J=2.0 L/J=3.0
T/J
Δ/J

as different phases with low confidence.

Two types of training data were acquired, for use in training two separate networks. In one data set (the snapshot approach), simply 100 independent snapshots per parameter set were saved. In a second data set (the averaged approach), 100 independent groups of 10 correlated snapshots each were acquired. The 10 snapshots were averaged to give one average image for the data set. Broadly speaking, this averaging has the effect of smoothing out random fluctuations, allowing the network training to focus on more constant aspects of each phase.

The neural network code used is the implementation of (49), also available online at https://github.com/mnielsen/neural-networks-and-deep-learning . Each training sample was converted into an input vector of length 900 containing the values at each site of the 30x30 lattice, and a target output vector of length 6 consisting of a 1 at the index of the correct phase, and 0 for all other values. The feed-forward neural network contained two hidden layers of size 100 each, made up of sigmoid neurons. 25 epochs of training were performed. In each epoch, the training data were randomly divided into mini batches of size 10. With each mini batch, stochastic gradient descent was performed by a backpropagation algorithm with a learning rate $\eta = 0.06$. We use a cross-entropy cost function, with an L2 regularization parameter of $\lambda = 0.04$ to avoid overfitting .To avoid stopping the stochastic training at a bad point, if the final classification accuracy was worse than 0.85, extra epochs were run, one at a time, until 0.85 was reached. For the snapshot approach, we instead used a threshold of 0.9 . This method resulted in at most 5 (typically 0-2) extra epochs added. 10 instances of the neural network were trained independently on the same training data set. When working

with the test data, we took the average output of the 10 instances.

Neural Network Phase Diagram Generation

Test data were generated by the same Metropolis method as the training data. At each point in parameter space where we wished to determine the phase, 5 snapshots or correlated averages were generated. These were fed as input into the neural networks. Output vectors were averaged over the 5 samples and 10 network instances to arrive at a single final output vector. The point was classified as the phase corresponding to the maximum value in the output vector. The classification confidence was calculated as the maximum value in the output vector divided by the sum of the output vector. When rendering the phase diagrams, the phase classification determined the color – red, green, blue, cyan, magenta, or yellow. The RGB value of the base color was multiplied by the classification confidence, making a brighter color represent more confident classification. For example, a point classified as lamellar (yellow, RGB = (1.0, 1.0, 0.0)) with confidence 0.8 would be rendered as RGB = (0.8, 0.8, 0.0).

The averaged approach was more effective than the snapshot approach. With the snapshot approach, we could only distinguish 4 phases: Fluid, Black/White, Gray, and a single region covering Lamellar, Microemulsion, and Critical (Fig. 3.14b). With the averaged approach, we could distinguish all 6 phases, but had low confidence in the distinction between the Fluid and Gray phases (unsurprisingly, since both averages look gray) (Fig. 3.14c). To combine these, on testing data, we used the gray output from the snapshot approach, and the other 5 outputs from the averaged approach. This gave the final phase diagram that we believe most completely describes our understanding of it after our work with both of these approaches.

Binding Energy Computation

To compute binding energy by Bennett's method, simulations were performed on the four separate lattices shown in Fig. 3.6: A 50x50 lattice containing a cluster of receptors, a 30x30 lattice containing a kinase of size one spin, a 50x50 lattice containing the kinase within the cluster of receptors, and a 30x30 empty lattice. Note for the 30x30 boxes (Fig. 3.6, right), the smaller lattice size was permissible because these boxes only ever contain one white pixel, which affects the lattice on a shorter length scale than the full receptor cluster. Samples were generated by the Metropolis algorithm in the same way as the neural network training data, but the predefined proteins were required to remain white. Any proposed move that attempted to flip one of these spins was automatically rejected.

The free energy *ΔF* is computed according to the formula

$$e^{-(\Delta F - C)/(k_B T)} = \frac{\langle f((\Delta U_{1\to 2} - C)/(k_B T))\rangle_1}{\langle f((\Delta U_{2\to 1} + C)/(k_B T))\rangle_2}$$

We choose *f* as the Fermi-Dirac function $f(x) = 1/(1+e^x)$, as suggested in (36), and choose our guess *C* for the free energy as -0.5 $k_B T$. The numerator is calculated as an ensemble average from simulations of state 1 (Fig. 3.6). $\Delta U_{1\to 2}$ for each sample is the energy change associated with exchanging the kinase and a spin at the center of the cluster (at what is the kinase's position in state 2). Likewise, the denominator is calculated from simulations of state 2, and $\Delta U_{2\to 1}$ is the energy change associated with exchanging the kinase and the spin at what would be its state 1 position.

Note that the two separate boxes that make up each state can be generated independently, and we use this to our advantage. We initially generated the same number of samples of the 50x50 box and the 30x30 box. Then each 50x50 box was

paired with 10 different 30x30 boxes, increasing the number of samples of the state by a factor of 10. These samples are not independent, but still follow the correct Monte Carlo statistics.

At each point to be tested, simulations were performed for 5000 sweeps, a sample was saved every sweep, and the lattice was reshuffled every 10 sweeps. After data expansion, this gave 50000 non-independent samples of each state, to be used in the Bennett calculation.

Acknowledgements

Samuel Whitehead, David Holowka, Barbara Baird, and James P. Sethna made contributions to this work.

EM, DH, and BB were supported by National Institutes of Health grants R01-AI018306 followed by R01-GM117552. SW was supported by the Department of Defense through the National Defense Science Engineering Graduate Fellowship (NDSEG) Program. JPS was supported by the National Science Foundation grant DMR-1312160. EM was additionally supported by the National Institutes of Health under Ruth L. Kirschstein National Research Service Award (2T32GM008267) from the National Institute of General Medical Sciences.

We are grateful to Frank Zhang for discussions on the use of neural networks for phase diagram prediction, and to Archishman Raju, Colin Clement, and Benjamin Machta for discussions on critical phenomena and scaling analysis.

References

1. Munro, S. 2003. Lipid Rafts. Cell. 115: 377–388.

2. Pike, L.J. 2006. Rafts defined: a report on the Keystone symposium on lipid rafts and cell function. J. Lipid Res. 47: 1597–1598.

3. Sengupta, P., D. Holowka, and B. Baird. 2007. Fluorescence resonance energy transfer between lipid probes detects nanoscopic heterogeneity in the plasma membrane of live cells. Biophys. J. 92: 3564–3574.

4. Lingwood, D., and K. Simons. 2010. Lipid rafts as a membrane-organizing principle. Science. 327: 46–50.

5. Simons, K., and M.J. Gerl. 2010. Revitalizing membrane rafts: new tools and insights. Nat. Rev. Mol. Cell Biol. 11: 688–699.

6. Holowka, D., J.A. Gosse, A.T. Hammond, X. Han, P. Sengupta, N.L. Smith, A. Wagenknecht-Wiesner, M. Wu, R.M. Young, and B. Baird. 2005. Lipid segregation and IgE receptor signaling: a decade of progress. Biochim. Biophys. Acta. 1746: 252–259.

7. Sezgin, E., I. Levental, S. Mayor, and C. Eggeling. 2017. The mystery of membrane organization: composition, regulation and roles of lipid rafts. Nat. Rev. Mol. Cell Biol. : Advance Online Publication.

8. Chini, B., and M. Parenti. 2004. G-protein coupled receptors in lipid rafts and caveolae: How, when and why do they go there? J. Mol. Endocrinol. 32: 325–338.

9. Nussinov, R., H. Jang, and C.J. Tsai. 2015. Oligomerization and nanocluster organization render specificity. Biol. Rev. 90: 587–598.

10. Veatch, S.L., and S.L. Keller. 2005. Seeing spots: Complex phase behavior in simple membranes. Biochim. Biophys. Acta - Mol. Cell Res. 1746: 172–185.

11. Feigenson, G.W. 2009. Phase diagrams and lipid domains in multicomponent lipid bilayer mixtures. Biochim. Biophys. Acta. 1788: 47–52.

12. Konyakhina, T.M., and G.W. Feigenson. 2016. Phase diagram of a polyunsaturated lipid mixture: Brain sphingomyelin/1-stearoyl-2-docosahexaenoyl-sn-glycero-3-phosphocholine/cholesterol. Biochim. Biophys. Acta - Biomembr. 1858: 153–161.

13. Baumgart, T., A.T. Hammond, P. Sengupta, S.T. Hess, D.A. Holowka, B.A. Baird, and W.W. Webb. 2007. Large-scale fluid/fluid phase separation of proteins and lipids in giant plasma membrane vesicles. PNAS. 104: 3165–3170.

14. Veatch, S.L., P. Cicuta, P. Sengupta, A. Honerkamp-Smith, D. Holowka, and B.

Baird. 2008. Critical fluctuations in plasma membrane vesicles. ACS Chem. Biol. 3: 287–293.

15. Stanich, C.A., A.R. Honerkamp-Smith, G.G. Putzel, C.S. Warth, A.K. Lamprecht, P. Mandal, E. Mann, T.-A.D. Hua, and S.L. Keller. 2013. Coarsening dynamics of domains in lipid membranes. Biophys. J. 105: 444–454.

16. Konyakhina, T.M., S.L. Goh, J. Amazon, F.A. Heberle, J. Wu, and G.W. Feigenson. 2011. Control of a nanoscopic-to-macroscopic transition: modulated phases in four-component DSPC/DOPC/POPC/Chol giant unilamellar vesicles. Biophys. J. 101: L8–L10.

17. Palmieri, B., and S.A. Safran. 2013. Hybrid Lipids Increase the Probability of Fluctuating Nanodomains in Mixed Membranes. Langmuir. 29: 5246–5261.

18. Schick, M. 2012. Membrane heterogeneity: Manifestation of a curvature-induced microemulsion. Phys. Rev. E. .

19. Sadeghi, S., M. Müller, and R.L.C.L.C. Vink. 2014. Raft Formation in Lipid Bilayers Coupled to Curvature. Biophys. J. 107: 1591–1600.

20. Amazon, J.J., S.L. Goh, and G.W. Feigenson. 2013. Competition between line tension and curvature stabilizes modulated phase patterns on the surface of giant unilamellar vesicles: A simulation study. Phys. Rev. E. 87: 22708.

21. Honerkamp-Smith, A.R., S.L. Veatch, and S.L. Keller. 2009. An introduction to critical points for biophysicists; observations of compositional heterogeneity in lipid membranes. Biochim. Biophys. Acta. 1788: 53–63.

22. Gompper, G., and M. Schick. 1990. Lattice model of microemulsions: The effect of fluctuations in one and two dimensions. Phys. Rev. A. 42: 2137–2149.

23. Gompper, G., and M. Schick. 1990. Lattice model of microemulsions. Phys. Rev. B. 41: 9148–9162.

24. Krizhevsky, A., I. Sutskever, and G.E. Hinton. 2012. ImageNet Classification with Deep Convolutional Neural Networks. Adv. Neural Inf. Process. Syst. : 1097–1105.

25. Carrasquilla, J., and R.G. Melko. 2016. Machine learning phases of matter. arXiv. 1605.01735.

26. Wang, L. 2016. Discovering phase transitions with unsupervised learning. Phys. Rev. B - Condens. Matter Mater. Phys. 94: 195105.

27. Blank, U., and J. Rivera. 2004. The ins and outs of IgE-dependent mast-cell

exocytosis. Trends Immunol. 25: 266–273.

28. Gilfillan, A.M., and J. Rivera. 2009. The tyrosine kinase network regulating mast cell activation. Immunol. Rev. 228: 149–169.

29. Rivera, J., and A.M. Gilfillan. 2006. Molecular regulation of mast cell activation. J. Allergy Clin. Immunol. 117: 1214–1225.

30. Blume, M., V.J. Emery, and R.B. Griffiths. 1971. Ising Model for the λ Transition and Phase Separation in He3-He4 Mixtures. Phys. Rev. A. 4: 1071–1077.

31. Blume, M. 1966. Theory of the First-Order Magnetic Phase Change in UO2. Phys. Rev. 141: 517–524.

32. Capel, H.W. 1966. On the possibility of first-order transitions in Ising systems of triplet ions with zero-field splitting. Physica. 32: 966–988.

33. Metropolis, N., A.W. Rosenbluth, M.N. Rosenbluth, A.H. Teller, and E. Teller. 1953. Equation of State Calculations by Fast Computing Machines. J. Chem. Phys. 21: 1087–1092.

34. Gompper, G., and M. Schick. 1990. Lattice model of microemultions. Phys. Rev. B. 41: 9148–9162.

35. Machta, B.B., S.L. Veatch, and J.P. Sethna. 2012. Critical Casimir Forces in Cellular Membranes. Phys. Rev. Lett. 109: 138101.

36. Bennett, C.H. 1976. Efficient Estimation of Free Energy Differences from Monte Carlo Data. J. Comput. Phys. 22: 245–268.

37. Jarzynski, C. 1997. Nonequilibrium Equality for Free Energy Differences. Phys. Rev. Lett. 78: 2690–2693.

38. Beale, P.D. 1986. Finite-size scaling study of the two-dimensional Blume-Capel model. Phys. Rev. B. 33: 1717–1720.

39. Schick, M. 2015. Theories of Equilibrium Inhomogeneous Fluids. .

40. Sil, D., J.B. Lee, D. Luo, D. Holowka, and B. Baird. 2007. Trivalent ligands with rigid DNA spacers reveal structural requirements for IgE receptor signaling in RBL mast cells. ACS Chem. Biol. 2: 674–684.

41. Kusumi, A., T.K. Fujiwara, N. Morone, K.J. Yoshida, R. Chadda, M. Xie, R.S. Kasai, and K.G.N. Suzuki. 2012. Membrane mechanisms for signal transduction: The coupling of the meso-scale raft domains to membrane-skeleton-induced compartments and dynamic protein complexes. Semin. Cell Dev. Biol. 23: 126–144.

42. Machta, B.B., S. Papanikolaou, J.P. Sethna, and S.L. Veatch. 2011. Minimal model of plasma membrane heterogeneity requires coupling cortical actin to criticality. Biophys. J. 100: 1668–1677.

43. Honigmann, A., S. Sadeghi, J. Keller, S.W. Hell, C. Eggeling, and R. Vink. 2014. A lipid bound actin meshwork organizes liquid phase separation in model membranes. Elife. 3: e01671.

44. Shelby, S.A., S.L. Veatch, D.A. Holowka, and B.A. Baird. 2016. Functional nanoscale coupling of Lyn kinase with IgE-FcεRI is restricted by the actin cytoskeleton in early antigen-stimulated signaling. Mol. Biol. Cell. 27: 3645–3658.

45. Sherman, E., V. Barr, and L.E. Samelson. 2013. Super-resolution characterization of TCR-dependent signaling clusters. Immunol. Rev. 251: 21–35.

46. Cardy, J. 1996. Scaling and Renormalization in Statistical Physics. New York, New York, USA: Cambridge University Press.

47. Rao, M., and S. Mayor. 2014. Active organization of membrane constituents in living cells. Curr. Opin. Cell Biol. 29: 126–132.

48. Noble, A.E., J. Machta, and A. Hastings. 2015. Emergent long-range synchronization of oscillating ecological populations without external forcing described by Ising universality. Nat. Commun. 6: 6664.

49. Nielsen, M.A. 2015. Neural Networks and Deep Learning. .

50. Palmieri, B., M. Grant, and S.A. Safran. 2014. Prediction of the dependence of the line tension on the composition of linactants and the temperature in phase separated membranes. Langmuir. 30: 11734–11745.

CHAPTER FOUR

A NOVEL POSITIVE FEEDBACK MECHANISM FOR IGE-FCεRI CLUSTERING REVEALED BY SUPER-RESOLUTION IMAGING

4.1 Summary

In the canonical mast cell signaling pathway, antigen cross-links IgE-FcεRI, forming a cluster that couples with Lyn kinase to initiate subsequent signaling events. We describe a novel positive feedback mechanism that serves to enhance the antigen-dependent clustering of IgE-FcεRI. dSTORM super-resolution imaging of IgE detects a significantly higher level of IgE-FcεRI clustering in cells transfected with Lyn constructs compared to those transfected with other constructs. Pharmacological inhibitors for Lyn, Syk, and PLCγ reduce the level of IgE clustering, suggesting that the positive feedback mechanism acts downstream of PLCγ. Our results further suggest that the activity of Lyn plays a key, limiting role in the mechanism, such that overexpression of Lyn, but not of Syk or LAT, enhances the entire process. This mechanism is an important addition to the current understanding of IgE-FcεRI clustering in the initiation of mast cell signaling.

4.2 Introduction

Signaling through the high affinity receptor for IgE (FcεRI) in mast cells and basophils is responsible for the initiation of an allergic immune response, and an understanding of the mechanism behind this signal initiation is of biomedical importance, in part to enable development of better targeted allergy treatments (1).

In the initial stages of signaling (reviewed in (2, 3)), IgE specific to a particular

antigen binds to its transmembrane receptor, FcεRI, forming a stable IgE-FcεRI complex. IgE-FcεRI is cross-linked by a multivalent antigen, forming a cluster of IgE-FcεRI. Lyn, a Src family tyrosine kinase anchored by fatty acyl chains to the plasma membrane, is the first kinase recruited to the cluster. Lyn phosphorylates immunoreceptor tyrosine-based activation motifs (ITAMs) on the β and γ subunits of the receptor, and subsequently associates to the phosphorylated β subunit via its Src homology 2 (SH2) domain. Lyn can exist in inactive and active conformations, depending on its phosphorylation state (3, 4). When tyrosine 508 is phosphorylated, it adopts a closed, inactive conformation in which the SH2 domain is inaccessible. The active state consists of dephosphorylated tyrosine 508, stabilizing an open conformation, and phosphorylated tyrosine 397, activating the catalytic domain. Phosphorylation of the FcεRI γ subunit by Lyn enables Syk, a cytoplasmic tyrosine kinase, to bind to the γ subunit and become activated via phosphorylation by Lyn. Activated Syk phosphorylates the linker for activation of T cells (LAT) (5), which propagates and amplifies the signal.

LAT is a scaffold protein well studied in the context of T cells, and LAT is also required for mast cell signaling (6). The LAT scaffold recruits several signaling proteins, which enables the activation of multiple downstream pathways (reviewed in (7)). One phosphotyrosine site of LAT (Y132) serves as a binding site for PLCγ1. A second isoform, PLCγ2, is also found in mast cells (discussed in (8)); we refer to both here as simply PLCγ. PLCγ is responsible for the hydrolysis of phosphotidylinositol 4,5 bisphosphate (PIP2) into secondary messengers inositol trisphosphate (IP3) and diacylglycerol (DAG), which promote the well-known functional responses in mast cells

of Ca^{2+} influx and degranulation. Three other phosphotyrosine sites of LAT (Y171, Y191, and Y226) bind to members of the Grb2 family, including Gads. Gads recruits SLP-76, an additional scaffold protein, which in turn recruits signaling partners including PI3K, Vav, Itk, Nck, and ADAP. Of the SLP-76 associators, Nck and ADAP are notable for pathways coupling back to components at the plasma membrane: Nck to the cortical actin cytoskeleton, and ADAP to integrins (7).

Prior to this work, a good deal of evidence was consistent with a model in which the functionally relevant IgE-FcεRI cluster is formed exclusively through the physical cross-linking of the receptors. A multivalent antigen interacting with a bivalent IgE can, in principle, form a cross-linked receptor aggregate of an arbitrarily large size. Theoretical models found that ligand-receptor interactions are sufficient to form clusters of experimentally observed sizes, or even form a larger gel-like protein aggregate (9). Additional evidence draws correlations between antigen valency, cluster size, and functional response. Bivalent ligands (10, 11) stimulate poor functional responses, trivalent ligands (12, 13) or synergistic cross-linking by multiple bivalent ligands (10), yield stronger responses, and multivalent DNP-BSA yields stronger responses than trivalent ligands of the same type. We explored this rigorously in Chapter 2, quantitatively showing that bivalent ligands form smaller IgE-FcεRI clusters than trivalent ligands, and among trivalent ligands, the spacing of binding sites on the ligand determines density of the clusters. In light of these results, it is tempting to propose the simple model in which an IgE aggregate is formed according to the interactions between the IgE and antigen, and the spatial organization of the aggregate dictates the extent to which downstream signaling proceeds through Syk, LAT, and subsequent components.

Prior to this study, a small amount of evidence suggested that this basic cross-linking model might be an oversimplification. Early reports showed that minimal cross-linking of FcεRI without IgE sensitization, using anti-receptor antibodies (14, 15) or oligomeric IgEs (16), led to strong functional responses. In some cases, when cells were cooled to low temperature after cross-linking with these minimal ligands, optically resolvable patching of FcεRI was seen (17–19) This suggests clusters that are larger than the physically cross-linked structures, but the mechanism remains unclear, and it is unclear whether some level of enhanced FcεRI association exists at physiological temperatures. A more recent observation by electron microscopy (20) found decreased IgE clustering under the inhibition of Lyn, providing the first suggestion that Lyn may be involved in enhancing clustering.

PALM/STORM imaging (21–23) provides the resolution necessary to quantify IgE-FcεRI clustering in intact cells at physiological temperature. The technique has been used previously on live and fixed cells to study IgE clustering (24), and by us in Chapter 2 in conjunction with structurally defined ligands. In this study, we use the direct STORM (dSTORM) (25) implementation.

Here, we use dSTORM to provide clear evidence that downstream signaling events in RBL-2H3 cells work to increase the clustering of ligand-crosslinked IgE-FcεRI. We trace this positive feedback mechanism through the known mast cell signaling pathway, and provide evidence that the entire pathway from Lyn to PLCγ is required for this mechanism. We show that within this pathway, Lyn plays a key, limiting role, such that an increase in Lyn concentration accelerates the entire process, leading to increased antigen-dependent IgE-FcεRI clustering. This novel, positive feedback

mechanism is an important addition to the presently accepted signaling pathway, providing a new perspective on the molecular mechanisms of mast cell signal initiation.

4.3 Results

Overexpression of Lyn leads to increased IgE-FcεRI clustering

We used dSTORM imaging to visualize and quantify IgE-FcεRI clustering in RBL-2H3 cells upon cross-linking with antigen. Cells were sensitized with anti-2,4-dinitrophenyl (DNP) IgE conjugated with Alexa Fluor 647 (AF647-IgE), stimulated with multivalent DNP-BSA for 6 min at 37 °C, and chemically fixed. Cell samples were then imaged by dSTORM in total internal reflection fluorescence (TIRF) to measure the distribution of IgE on the ventral membrane at high resolution.

To evaluate the role of Lyn in IgE-FcεRI clustering, we transfected cells with Lyn-EGFP, and measured the resulting clustering after addition of DNP-BSA. We compared the clustering to that found in cells expressing the construct palmitolyl, myristoyl-EGFP (PM-EGFP), a negative control construct containing a fragment of Lyn including the sites of the palmitoyl and myristoyl membrane anchors, but lacking the rest of the Lyn protein. A TIRF image of each cell in the EGFP (green) channel was collected to show that the cell overexpressed the construct of interest (Fig. 4.1a, EGFP). A dSTORM image of AF647-IgE was collected to measure clustering. As expected, cells overexpressing either construct showed significant IgE clustering upon stimulation, while unstimulated cells did not show clustering. We consistently observed larger IgE clusters in cells overexpressing Lyn-EGFP than in cells overexpressing PM-EGFP (Fig. 4.1a, AF647-IgE), a difference made more clear in the quantification that follows.

IgE clustering was quantified using a pair autocorrelation function analysis, as

Figure 4.1 Overexpression of Lyn leads to an increase in IgE-FcεRI clustering. (a) Example images of chemically fixed cells overexpressing Lyn-EGFP or PM-EGFP, and stimulated 6 minutes at 37°C with with 0.5 μg/mL DNP-BSA, or unstimulated. TIRF images of EGFP verify that the cells express the constructs. EGFP expression level had some cell to cell variability; visible differences here (e.g. dimmer unstimulated example) are features of the individual example cells, and do not represent systematic differences between the conditions. dSTORM images of AF647-IgE show puncta in stimulated cases and a uniform distribution in the unstimulated case, indicating stimulation-dependent IgE-FcεRI clustering. Qualitatively, a larger amount of clustering is visible in the Lyn-EGFP sample than in the PM-EGFP sample. (b) Quantification of clustering by autocorrelation analysis. Average autocorrelation functions of AF647-IgE, measured for cells overexpressing Lyn-EGFP, PM-EGFP, or no construct (Blank), and stimulated with DNP-BSA, or unstimulated where indicated. Bar graph of g(25 nm) gives the value of the correlation functions at a radius of 25 nm. Bar graph of Integral gives the integral of the correlation function from radius 25 to 200 nm. This value is proportional to the average number of receptors per cluster. Error bars indicate standard error of the mean. * $p<0.05$, ** $p<0.01$, *** $p<0.001$. Unstimulated cases are significantly lower than all stimulated cases; stars are elided for clarity. Averages of 39 Lyn cells, 11-15 cells per other condition (see Table 4.1).

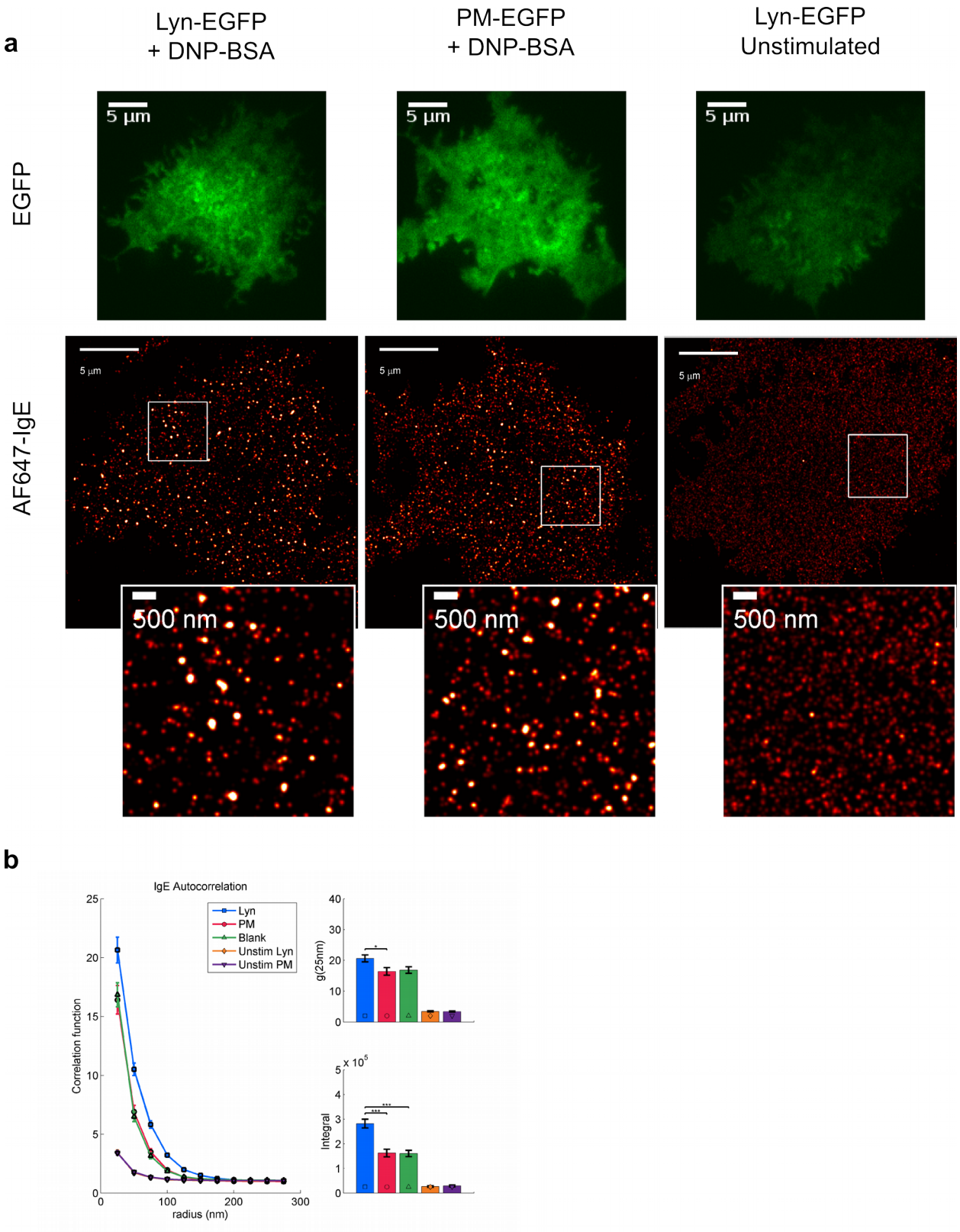
a
Lyn-EGFP
+ DNP-BSA
PM-EGFP
+ DNP-BSA
Lyn-EGFP
Unstimulated
EGFP
AF647-IgE
5 µm
500 nm
b
IgE Autocorrelation
Lyn
PM
Blank
Unstim Lyn
Unstim PM
Correlation function
radius (nm)
g(25nm)
Integral
x 10^5

previously described (Chapter 2 and (26)). The correlation function g(r) gives the increased probability of finding a probe at radius r from a given probe. A correlation function equal to 1 indicates a random distribution of IgE-FcεRI, while a higher value of the correlation function indicates a higher degree of IgE-FcεRI clustering. The decay length of the correlation function is a measure of the average cluster size. The average correlation functions of our AF647-IgE images are given in Fig. 4.1b. From the correlation functions, we extract two key values that we use for comparison among the different samples. First, we take the value of the first point of the correlation function, g(25 nm), giving a measure of the density of IgE-FcεRI clusters at short length scales. Second, we take the integral of the correlation function over a radius of 25-200 nm. This value is proportional to the average number of IgE-FcεRI that are correlated with a given IgE-FcεRI, or more intuitively, the number of IgE-FcεRI per cluster. The quantification of these parameters is shown in the bar graphs in Fig. 4.1b. A table of values giving g(25 nm) and the integral for each graph shown in the figures of this study is included at the end of the Results section (Table 4.1).

From this quantification, we see that Lyn-EGFP-expressing cells show a significantly higher level of IgE-FcεRI clustering than PM-EGFP-expressing cells. The difference is most notable in the integral of the correlation function, indicating that Lyn-EGFP cells form larger clusters containing more IgE-FcεRI, but also significant in g(25 nm), indicating that Lyn-EGFP cells form clusters with a higher local receptor density. As an additional negative control, throughout this study, we used “Blank” cells, which were subjected to the same transfection conditions, but did not express any fluorescent construct (Materials and Methods, Cell sample preparation). In Fig. 4.1b, Blank cells

showed similar clustering to PM-EGFP cells. This suggests that PM-EGFP causes no perturbation affecting IgE-FcεRI, while some activity specific to Lyn leads to the observed increase in clustering.

Our measured autocorrelation functions for Lyn- and PM-transfected, unstimulated cells are much lower than for any stimulated cases, but show a low level of correlation. This level of signal is likely due to over-counting of probes, which is an issue in any one-color PALM/STORM experiment. For this reason, we must be cautious in interpreting the absolute autocorrelation values obtained from our analysis. To verify that over-counting does not affect the conclusions of this study, we performed two-color dSTORM imaging with cross-correlation analysis, which is not subject to over-counting (26), of a similar set of samples overexpressing Lyn-mRFP (Fig. 4.3b-c). We still observe a significantly higher level of clustering in Lyn-mRFP cells compared to non-expressing cells. However, in the two-color experiment, the low level of correlation in unstimulated samples is no longer present.

We observed the same difference in IgE clustering between Lyn and PM cells using a different antigen (Y16, described in Chapter 2) and different fluorescent constructs (Lyn and PM conjugated to mEos 3.2), indicating that this is a general phenomenon, and not an artifact associated with one particular reagent (Fig. 4.2).

For completeness, we also provide in Table 4.1 a measure of the decay length of the correlation function: $r_{1/2}$, defined as the radius at which half the decay between g(25 nm) and g(200 nm) occurs. In 1-color experiments, this value was not reliably different between Lyn-EGFP-expressing cells and control (Blank or PM-expressing) cells. This may be because of overcounting, it represents a convolution between the true length

Figure 4.2 Other reagents reproduce the same results of Lyn-mediated enhancement of IgE-FcεRI clustering. Autocorrelation functions and bar graphs are shown as in Fig. 4.1. Cells were stimulated for 6 minutes at 37 °C and chemically fixed. (a) Cells overexpressing Lyn-EGFP or PM-EGFP were stimulated with the trivalent, dsDNA-based ligand Y16 (Chapter 2) at a concentration of 50 nM, instead of DNP-BSA. (b) Cells were transfected with Lyn-mEos or PM-mEos instead of the corresponding EGFP constructs, and stimulated with Y16. In both cases, we still observed increased clustering in the Lyn sample compared to the PM construct, indicating that this is a general phenomenon not specific to one antigen or protein construct.

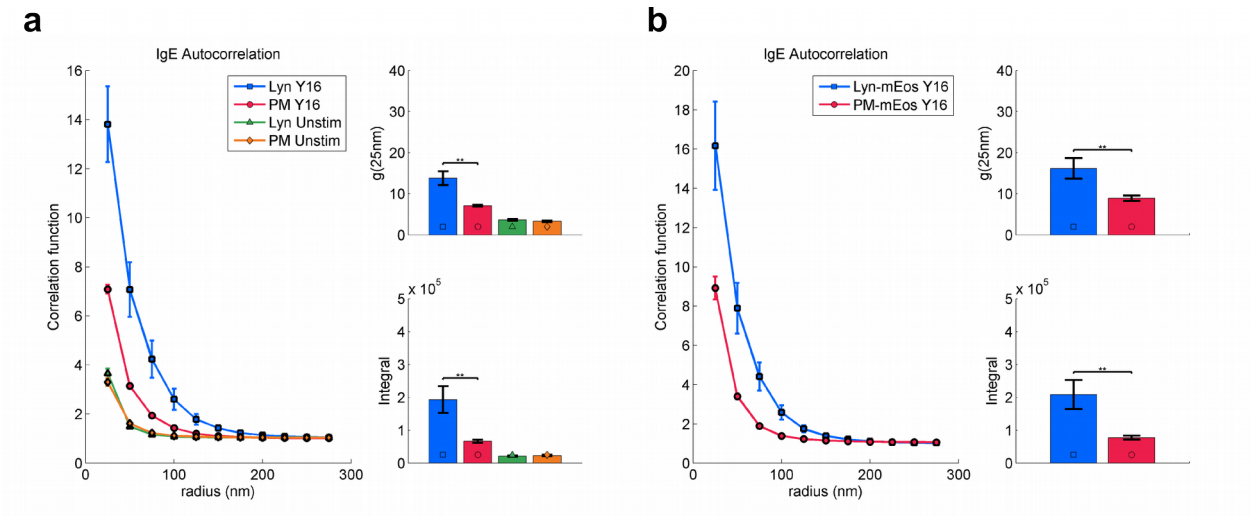
a
IgE Autocorrelation
Lyn Y16
PM Y16
Lyn Unstim
PM Unstim
Correlation function
radius (nm)
g(25nm)
Integral
x 10^5
**
b
IgE Autocorrelation
Lyn-mEos Y16
PM-mEos Y16
Correlation function
radius (nm)
g(25nm)
Integral
x 10^5
**

scale of clusters and the ~ 25 nm size of the super-resolved point-spread function. We note that the integral metric is more reliable, and incorporates information about the cluster length scale: A longer length scale manifests as a higher value of the integral. However, in the two-color cross-correlation experiment (Table 4.1, section 4.3c), where over-counting is not an issue, Lyn-mRFP-expressing cells show a somewhat higher $r_{1/2}$ than Blank cells. This suggests that Lyn-mRFP expression enhances the radius of IgE-FcεRI clusters, in addition to the other structural features.

Inhibition of Lyn by PP2 reduces IgE clustering

Next we asked whether the kinase activity of Lyn is necessary for mediating the observed enhancement in IgE clustering. To do so, we treated cells with PP2, an inhibitor of Src family kinases including Lyn. Our chosen PP2 concentration of 20 μM is optimal for inhibition of the degranulation response in RBL cells (Fig. 4.4). Lyn-EGFP and non-expressing cell samples were prepared with or without PP2 treatment, and were imaged by dSTORM and analyzed as before.

PP2 reduced the autocorrelation function in Lyn-EGFP samples, as measured by a significantly lower value of g(25 nm) in Lyn+PP2 cells compared to Lyn cells. A PP2-dependent reduction in autocorrelation was also observed for the non-expressing cells, with a significantly lower value of g(25 nm) in Blank+PP2 cells than in Blank cells. This suggests that not only the overexpressed Lyn-EGFP, but also endogenous Lyn, is involved in the enhancement of IgE clustering.

These results were reproduced in two-color cross-correlation experiments with Lyn-mRFP samples (Fig. 4.3c), confirming that they are not an artifact of over-counting.

Anti-FcεRI antibody CD3 forms FcεRI clusters by a different mechanism

Figure 4.3 The catalytic activity of Lyn is required for the enhancement of IgE-FcεRI clustering. (a) Autocorrelation quantification of IgE clustering in cells overexpressing Lyn-EGFP or no construct, stimulated with DNP-BSA as in Fig. 4.1. Where indicated, cells were preincubated 5 minutes at 37°C with 20 μM PP2, an inhibitor for Src family kinases including Lyn. Incubation with PP2 continued during DNP-BSA stimulation. Autocorrelation functions and bar graphs are shown as in Fig. 4.1. (b) Clustering analysis was performed for the same cases using two-color samples. Example two-color image of AF488-IgE and AF647-IgE in a cell overexpressing Lyn-mRFP and stimulated with DNP-BSA. Colocalization of the two colors indicates IgE clustering. (c) Quantification of clustering by the cross-correlation function between AF488-IgE and AF647-IgE. Cells overexpressed Lyn-mRFP or no construct (Blank), were stimulated with DNP-BSA or unstimulated where indicated, and were treated with PP2 where indicated. Average of 6 cells per condition.

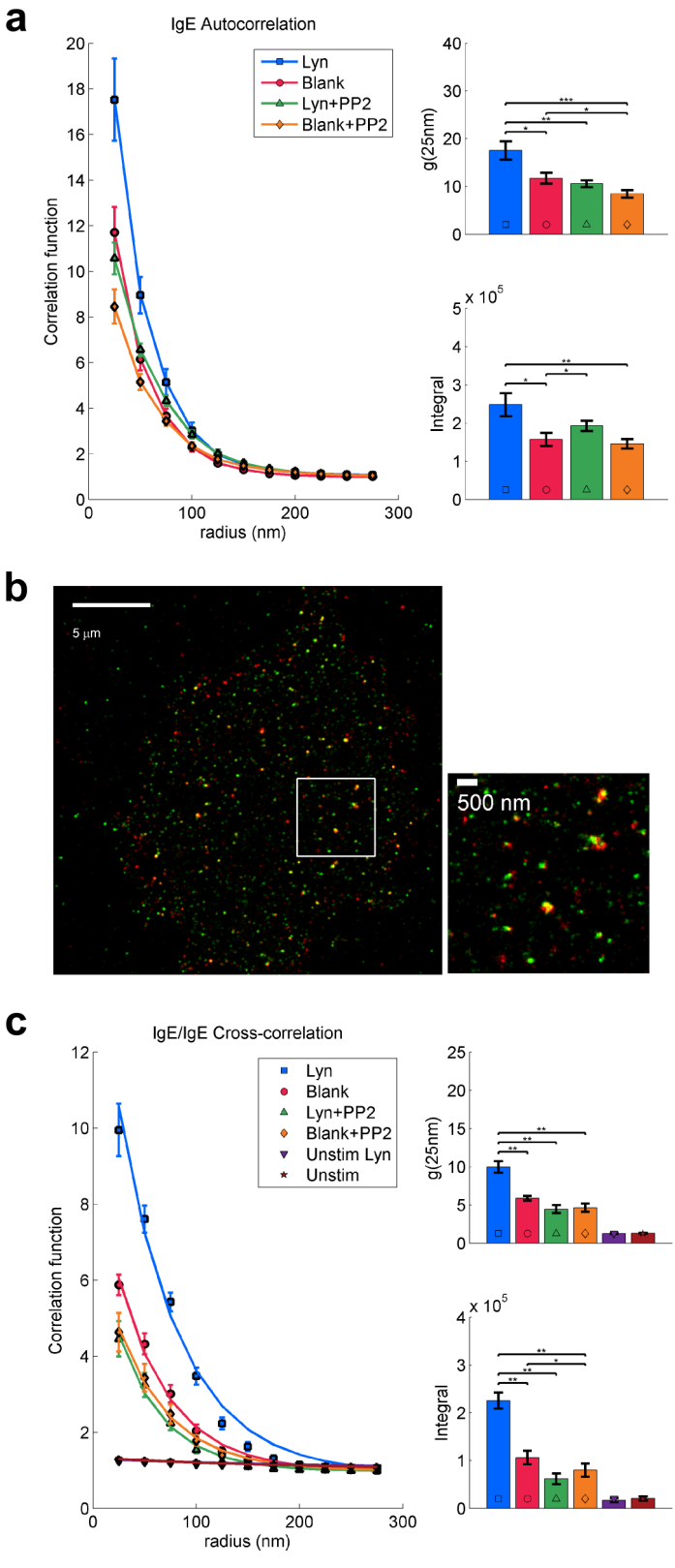
a
IgE Autocorrelation
Lyn
Blank
Lyn+PP2
Blank+PP2
Correlation function
radius (nm)
g(25nm)
Integral
x 10^5
b
5 μm
500 nm
c
IgE/IgE Cross-correlation
Lyn
Blank
Lyn+PP2
Blank+PP2
Unstim Lyn
Unstim
Correlation function
radius (nm)
g(25nm)
Integral
x 10^5

Figure 4.4 The efficacy of the inhibitors used in this study was assessed by a degranulation assay. We measured the amount of beta-hexosiminidase release (degranulation) when RBL cells were stimulated in the presence of varying concentrations of the inhibitors. For the dsRed-GBF panel, cells were sorted by fluorescence-activated cell sorting (FACS) to give negative and positive populations. Cells were stimulated 30 minutes with 0.5 µg/mL DNP-BSA at 37 °C. An unstimulated control sample is also included for each assay. Degranulation is plotted as a percentage of the total beta-hexosiminidase released when cells were permeablized with Triton-x100. Average of 5 technical replicates per condition. Error bars inidicate standard error of the mean.

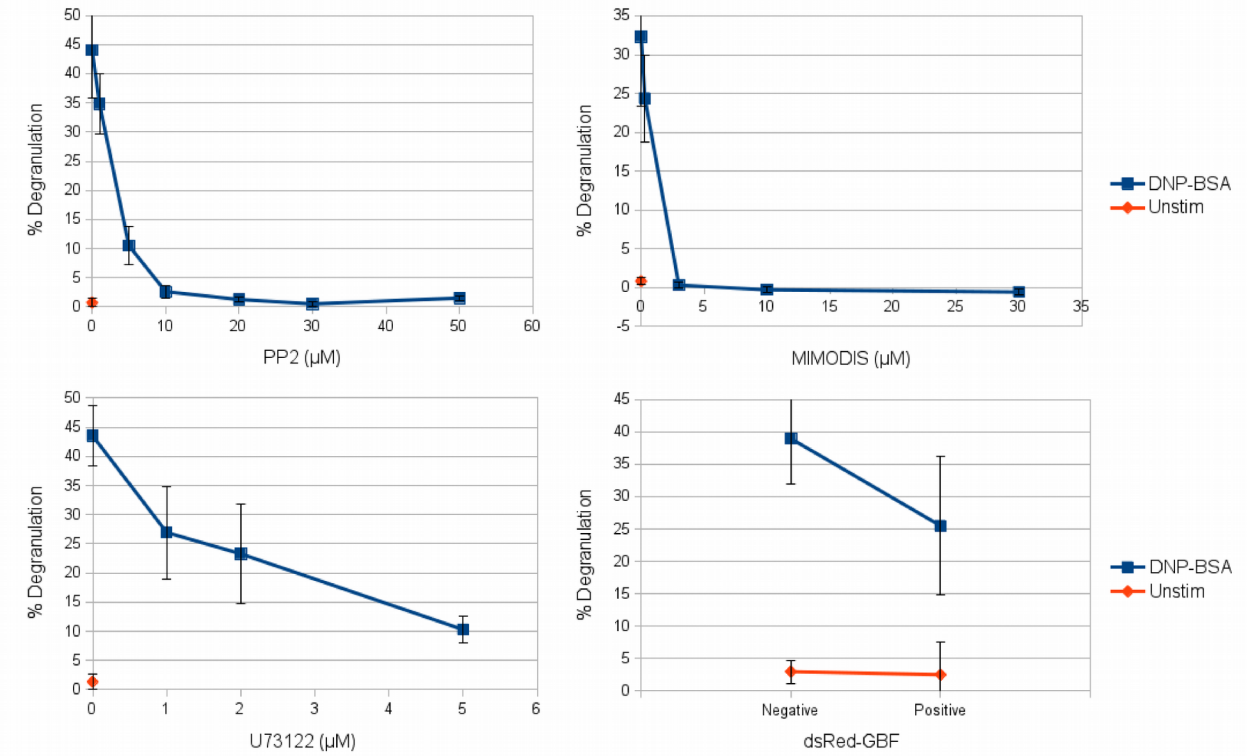
% Degranulation
PP2 (μM)
% Degranulation
MIMODIS (μM)
DNP-BSA
Unstim
% Degranulation
U73122 (μM)
% Degranulation
Negative
Positive
dsRed-GBF
DNP-BSA
Unstim

Having established a role for Lyn in positive feedback on IgE-FcεRI clustering, we were curious whether this is the same mechanism as was previously observed indirectly, in which antibodies to FcεRI produced clusters that were larger than physical cross-linking (18), possibly due to some cellular positive feedback process. We studied the anti-FcεRI antibody CD3 (15). We imaged CD3 using structured illumination microscopy (Fig. 4.5a) and two-color dSTORM (Fig. 4.5b-c). With both imaging techniques, we clearly observed clustering of CD3, to a larger extent than clustering of IgE with a normal bivalent antigen, confirming previous results with diffraction-limited techniques (18). To test whether CD3 acted through the same, Lyn-mediated mechanism that we described here, we imaged CD3 samples treated with PP2 (Fig. 4.5d). We expected PP2 treatment to reduce CD3 clustering, as was the case with our IgE experiments, but PP2 instead increased CD3 clustering. This suggests that the mechanism behind CD3 clustering, while potentially interesting, is different from the Lyn-mediated clustering that we observed for IgE. We chose to focus the remainder of the study on the more physiological means of stimulus by IgE and antigen, for which we have established a positive role for Lyn in feedback on IgE clustering.

Inhibition of Syk reduces IgE clustering, but overexpression of Syk has no effect

We next asked whether Syk, the next kinase in the canonical IgE signaling pathway, is involved in the enhanced clustering that we observed. We treated cells with 3-(1-Methyl-1H-indol-3-yl-methylene)-2-oxo-2,3-dihydro-1H-indole-5-sulfonamide (MIMODIS), a Syk inhibitor (described as compound 2 in (27), and subsequently used in cell studies (28)). Our chosen MIMODIS concentration of 3 μM is optimal for inhibition of degranulation in RBL cells (Fig. 4.4). We performed dSTORM imaging and analysis

Figure 4.5 Assessment of cell-mediated clustering in response to the anti-IgE antibody CD3. (a) Structured Illumination Microscopy (SIM) shows images of CD3 clustering. Cells labeled and stimulated with AF488-CD3 show more prominent puncta than those sensitized with AF488-IgE and left unstimulated or stimulated with the bivalent dsDNA-based ligand Y16bi. (b) CD3 clustering is also apparent in two-color STORM images. Cells were stimulated with AF488-CD3 and AF647-CD3 (3 nM total, 15 min), or sensitized with AF488-IgE and AF647-IgE and stimulated with Y16bi (50 nM, 6 min). In both experiments, clustering is indicated by colocalization of the two labels (yellow). Colocalization is more apparent in the CD3 sample. (c) Two-color cross-correlation functions for single cell experiments as shown in (b). Each curve represents the correlation function measured for one individual cell. CD3 cells show considerably higher cross-correlation than IgE+Y16bi cells, indicating that CD3 forms larger clusters. As CD3 is expected to form smaller physically cross-linked structures than Y16bi (CD3 can only form receptor dimers, while Y16bi can form linear chains of receptors), these results suggest that there is some cell-mediated process that increases CD3 cluster size.

(Figure 4.5, continued) (d) Cells were stimulated with AF488-CD3 and AF647-CD3 in the presence or absence of the Lyn inhibitor PP2 (20 μM, 5 min pre-incubation). An unstimulated sample with AF488-IgE and AF647-IgE was included as a control. Cross-correlation functions and bar graphs as in Fig. 4.3c are shown. CD3 cross-correlation, indicating CD3 clustering, is higher in the presence of PP2. This result suggests that the mechanism behind CD3 clustering is not the same as the mechanism described in the rest of this study. In the rest of the study, we describe a process in which IgE-FcεRI clustering is enhanced by Lyn, while CD3 clustering appears to be inhibited by Lyn. Still, it is a striking result that bivalent CD3 has the capacity to form large receptor clusters without extensive physical cross-linking, and this could warrant future investigation. Cells in this figure were stimulated and fixed at room temperature.

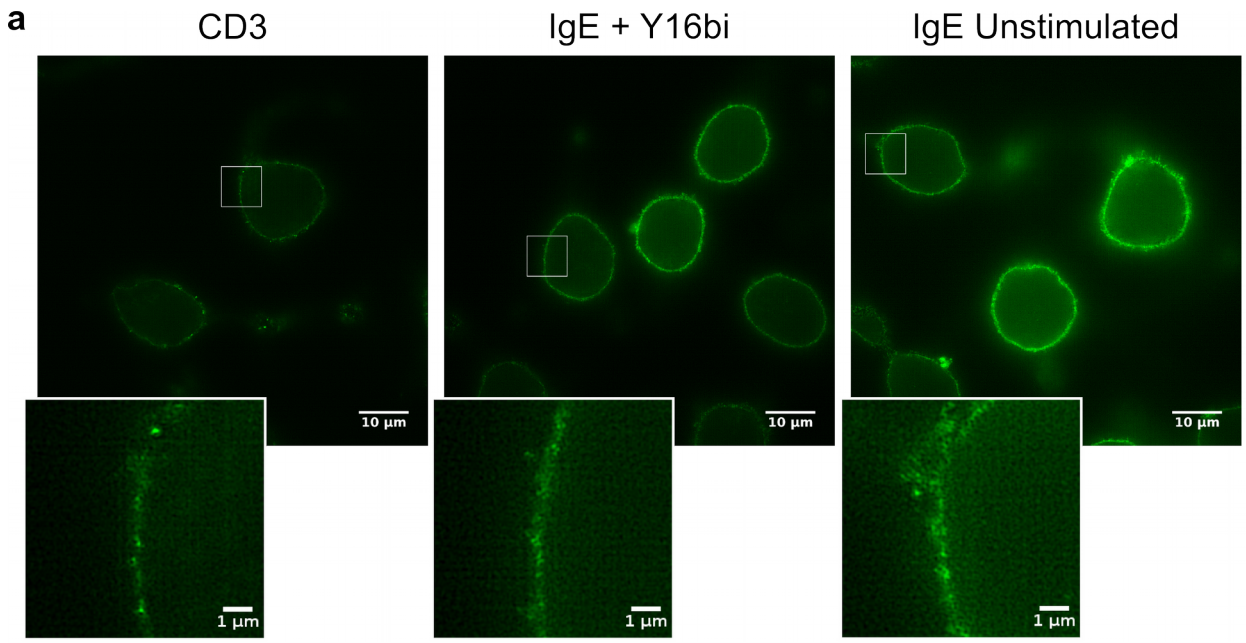
a
CD3
IgE + Y16bi
IgE Unstimulated
10 µm
1 µm

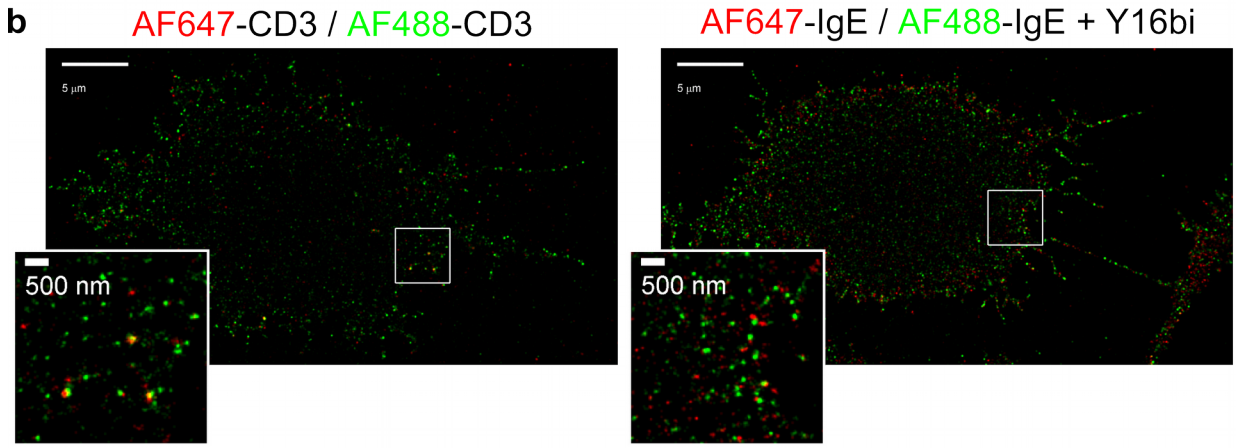
b
AF647-CD3 / AF488-CD3
AF647-IgE / AF488-IgE + Y16bi
5 µm
500 nm

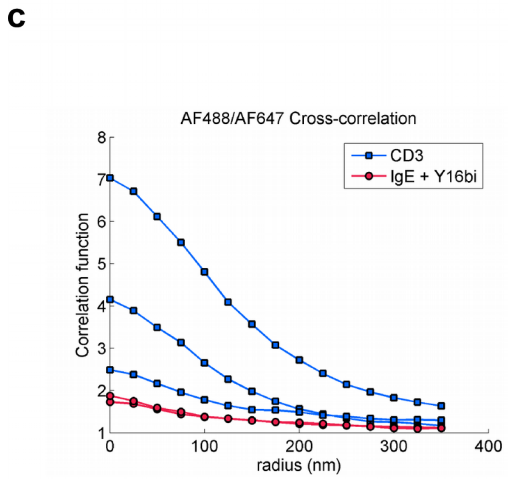
c
AF488/AF647 Cross-correlation
CD3
IgE + Y16bi
Correlation function
radius (nm)

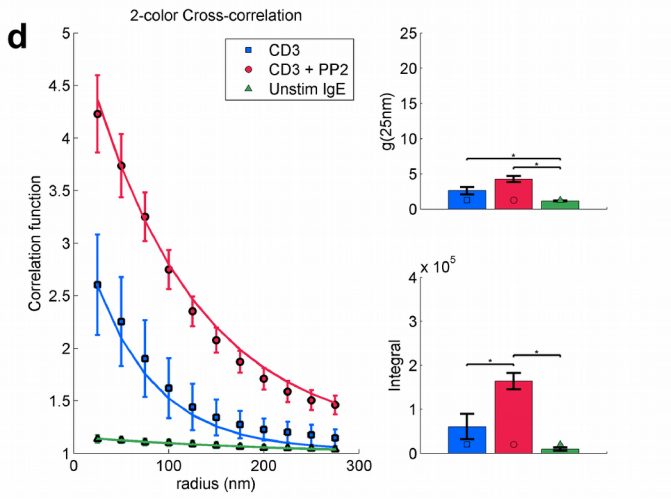
d
2-color Cross-correlation
CD3
CD3 + PP2
Unstim IgE
Correlation function
radius (nm)
g(25nm)
Integral
x 10^5

(Fig. 4.6a), and found that MIMODIS treatment results in significantly lower IgE clustering, as shown by a reduced value of g(25 nm). This difference is present both in cells overexpressing Lyn-EGFP and Blank cells. This suggests that the process responsible for increasing IgE clustering continues downstream of Syk. Surprisingly, this particular set of experiments did not show a difference between the Lyn-EGFP and Blank cases. This may be a consequence of selecting Blank cells as cells from the Lyn dish that were not visibly transfected, rather than using separate samples. However, this does not affect our conclusion, based on the effect of MIMODIS, that Syk plays a role in the positive feedback process.

As a complementary test, we transfected cells with YFP-Syk, and compared the IgE clustering to that in cells overexpressing Lyn-EGFP or Blank (Fig. 4.6b). In this case, we did not see a Syk-dependent difference: IgE clustering in YFP-Syk cells was indistinguishable from clustering in blank cells. Although Syk appears to be involved in the positive feedback pathway based on the inhibition by the Syk inibitor MIMODIS, the YFP-Syk result suggests that increasing the concentration of Syk does increase the activity of the pathway.

Overexpression of LAT has no effect on IgE clustering

We continued our analysis to the next stages of the IgE signaling pathway, which occur on the LAT scaffold. We imaged IgE on cells overexpressing LAT-mEos, and compared to cells overexpressing Lyn-EGFP or Blank (Fig. 4.6c). We found no significant difference between LAT-mEos cells and Blank cells, indicating that an increase in LAT concentration does not lead to an increase in IgE clustering.

Downstream of LAT, IgE clustering is affected by PLCγ but not SLP-76

Figure 4.6 Analysis of the role of further downstream signaling partners on IgE-FcεRI clustering. AF647-IgE autocorrelation functions and bar graphs as in Fig. 4.1. All samples were stimulated with DNP-BSA, as in Fig. 4.1. (a) Stimulated cells overexpressing Lyn-EGFP or no construct (Blank). Where indicated (MIM), cells were preincubated with 3 μM of the Syk inhibitor MIMODIS, 5 minutes at 37°C, with continued incubation with MIMODIS during DNP-BSA stimulation. Average of 8-12 cells per condition. Cells from Lyn dishes with no visible EGFP expression were use as Blank cells. (b) Stimulated cells overexpressing Lyn-EGFP, no construct (Blank), or YFP-Syk. Average of 12 cells per condition. Blank cells included 6 from Lyn-EGFP or YFP-Syk dishes with no visible expression, and 6 from a separate sample. (c) Stimulated cells overexpressing Lyn-EGFP, no construct (Blank), or LAT-mEos. Average of 10-12 cells per condition. All Blank cells come from separate samples.

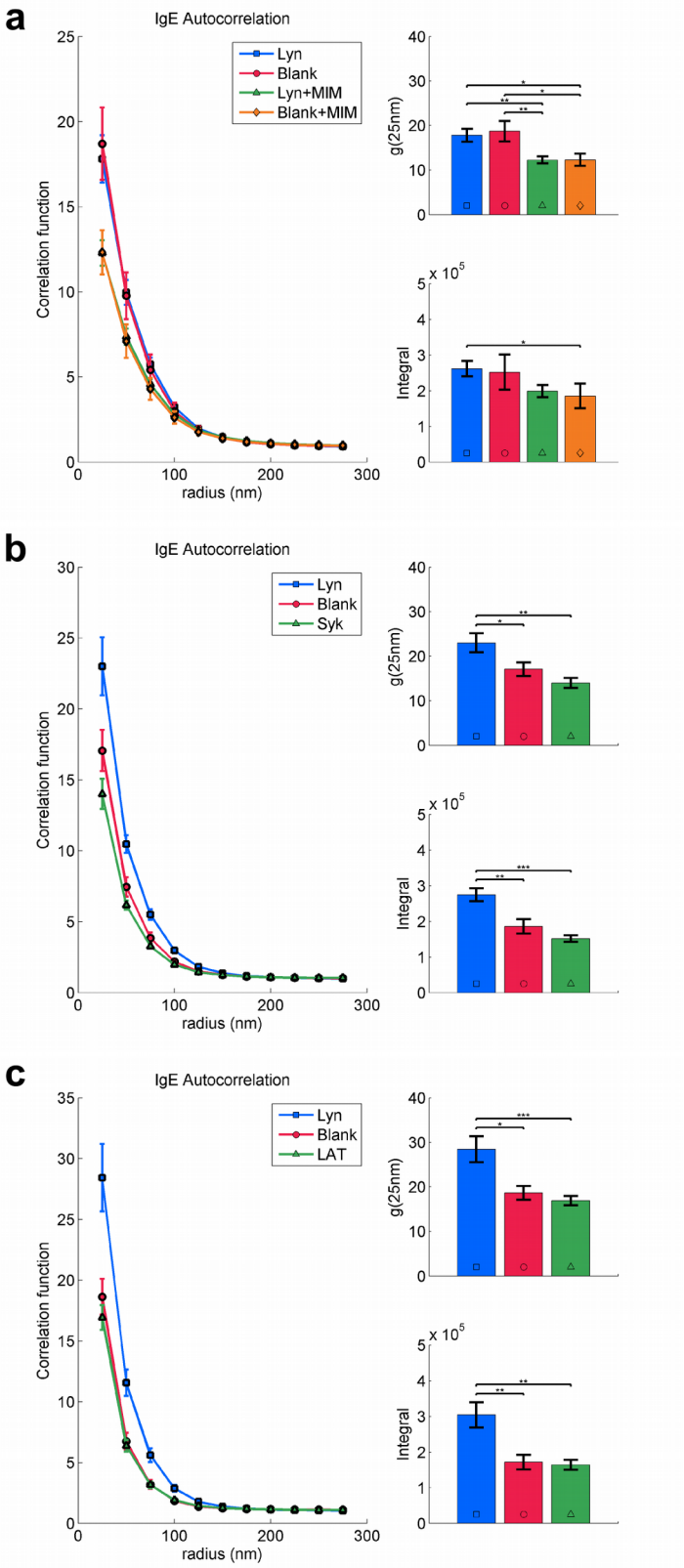
a
IgE Autocorrelation
Lyn
Blank
Lyn+MIM
Blank+MIM
Correlation function
radius (nm)
g(25nm)
x 10^5
Integral
b
IgE Autocorrelation
Lyn
Blank
Syk
Correlation function
radius (nm)
g(25nm)
x 10^5
Integral
c
IgE Autocorrelation
Lyn
Blank
LAT
Correlation function
radius (nm)
g(25nm)
x 10^5
Integral

Downstream of LAT, we examined the two distinct pathways mediated by PLCγ and SLP-76 respectively. To study the role of PLCγ, we used U73122, a pharmacological inhibitor for PLCγ activity. To disrupt the SLP-76 pathway, we overexpressed a construct consisting of dsRed attached the Gads binding fragment of SLP-76 (dsRed-GBF). As described previously (29, 30),this construct binds to Gads, outcompetes endogenous SLP-76 for Gads binding and thereby inhibits SLP-76 recruitment to LAT. This inhibition results in the loss of functional activity of RBL cells (30). In our study, we found that both dsRed-GBF and U73122 cause a partial inhibition of degranulation responses (Fig. 4.4). While U73122 might cause greater, even complete inhibition at higher concentration, we used a concentration of 2 μM to minimize non-specific effects on other proteins with free thiol groups.

We imaged cells treated with U73122 (Fig. 4.7a), and cells overexpressing dsRed-GBF (Fig. 4.7b), in both cases considering cells with Lyn-EGFP or Blank cells. Treatment with U73122 gave a significant reduction in IgE clustering, in both g(25 nm) and the integral, for both Lyn-EGFP and Blank cells. Overexpression of dsRed-GBF did not lead to a significant reduction in clustering by any metric. These results suggest that downstream of LAT, the positive feedback on IgE-FcεRI clustering acts through the PLCγ pathway, and not through the SLP-76 pathway.

4.4 Discussion

Our data suggests a mechanism of positive feedback in RBL mast cells, in which downstream signaling events cause an increase in IgE-FcεRI clustering, beyond what would be achieved by simple cross-linking by antigen. dSTORM imaging is an excellent

Figure 4.7 Analysis of the role of signaling partners of LAT on IgE-FcεRI clustering. AF647-IgE autocorrelation functions and bar graphs as in Fig. 4.1. All samples were stimulated with DNP-BSA, as in Fig. 4.1. (a) Cells transfected with Lyn-EGFP, dsRed-GBF, both constructs, or neither construct (Blank). dsRed-GBF is an inhibitor for the interaction between SLP76 and Gads. Average of 12 cells per condition. (b) Cells overexpressed Lyn-EGFP or no construct. Where indicated, cells were preincubated for 5 min at 37 °C with 2 μM U73122, a PLCγ inibitor, with U73122 incubation continued during DNP-BSA stimulation. Average of 12 cells per condition.

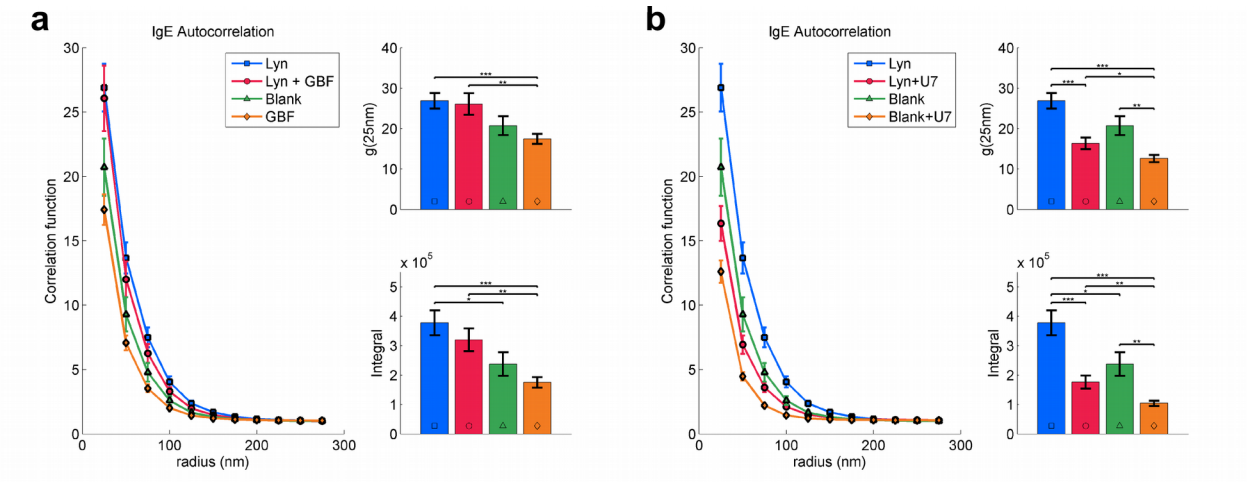
a
IgE Autocorrelation
Lyn
Lyn + GBF
Blank
GBF
Correlation function
radius (nm)
g(25nm)
x 10^5
Integral
b
IgE Autocorrelation
Lyn
Lyn+U7
Blank
Blank+U7
Correlation function
radius (nm)
g(25nm)
x 10^5
Integral

Table 4.1 (2 pages) Values shown in bar graphs quantifying correlation functions throughout this study. The bold heading of each section indicates the figure number corresponding to that section. “n” gives the number of cells imaged. “Std Err” gives the standard error of the mean. We also tabulate the value of $r_{1/2}$, the radius corresponding to half of the decay from g(25 nm) to g(200 nm).

	n	g(25)	Std Err	Integral / 10^5	Std Err / 10^5	$r_{1/2}$(nm)	Std Err
4.1b							
Lyn	39	20.6	1.1	2.81	0.18	51.0	0.8
PM	15	16.4	1.2	1.63	0.16	45.5	0.6
Blank	12	16.8	1.1	1.60	0.13	44.3	0.7
Lyn Unstim	11	3.4	0.2	0.26	0.03	45.0	2.4
PM Unstim	11	3.4	0.2	0.29	0.04	43.6	1.0
4.2a							
Lyn Y16	6	13.8	1.7	1.93	0.41	50.1	3.1
PM Y16	6	7.1	0.2	0.66	0.04	44.2	0.5
Lyn Unstim	6	3.7	0.2	0.21	0.02	40.1	0.2
PM Unstim	6	3.3	0.2	0.23	0.03	41.8	0.4
4.2b							
Lyn mEos Y16	5	16.2	2.5	2.08	0.44	47.4	0.9
PM mEos Y16	5	8.9	0.7	0.77	0.06	42.9	0.4
4.3a							
Lyn	10	17.5	1.9	2.48	0.30	52.2	2.2
Blank	15	11.7	1.1	1.57	0.17	53.8	2.6
Lyn PP2	16	10.6	0.7	1.92	0.14	62.1	2.8
Blank PP2	20	8.5	0.8	1.46	0.12	59.0	2.2
4.3c (2-color)							
Lyn	6	10.0	0.8	2.25	0.17	75.2	4.1
Blank	6	5.9	0.3	1.06	0.14	65.5	2.5
Lyn PP2	6	4.5	0.5	0.62	0.11	62.6	0.9
Blank PP2	6	4.6	0.6	0.80	0.14	64.9	1.5
Lyn Unstim	6	1.2	0.1	0.17	0.04	82.1	11.9
Blank Unstim	6	1.3	0.0	0.21	0.04	89.0	5.8

	n	g(25)	Std Err	Integral / 10^5	Std Err / 10^5	$r_{1/2}$(nm)	Std Err
4.5c (2-color)							
CD3	5	2.6	0.5	0.61	0.29	68.7	7.4
CD3 + PP2	4	4.2	0.4	1.64	0.19	90.2	3.2
IgE Unstim	4	1.1	0.0	0.10	0.04	106.4	16.6
4.6a							
Lyn	10	17.8	1.5	2.62	0.22	53.8	1.3
Blank	8	18.7	2.3	2.52	0.50	50.2	1.7
Lyn MIMODIS	12	12.3	0.8	1.99	0.17	56.2	1.5
Blank MIMODIS	10	12.3	1.4	1.85	0.34	52.5	1.8
4.6b							
Lyn	12	23.0	2.1	2.74	0.18	49.7	1.7
Blank	12	17.1	1.5	1.86	0.20	47.1	1.4
Syk	12	14.0	1.1	1.52	0.10	47.0	1.2
4.6c							
Lyn	10	28.4	2.9	3.04	0.35	45.6	0.7
Blank	12	18.6	1.5	1.72	0.20	43.5	0.6
LAT	12	16.9	1.1	1.64	0.14	43.9	0.6
4.7							
Lyn	12	26.9	1.9	3.78	0.42	49.9	1.0
Lyn + GBF	12	26.1	2.7	3.20	0.39	47.1	0.8
Blank	12	20.7	2.3	2.37	0.40	45.9	0.9
GBF	12	17.4	1.2	1.75	0.18	44.7	0.4
Lyn + U7	12	16.3	1.4	1.76	0.22	45.1	0.6
Blank + U7	12	12.6	0.9	1.04	0.09	42.9	0.5

experimental tool to characterize this mechanism, as it enables nanoscale quantification of IgE-FcεRI cluster sizes for comparisons between different conditions.

Our chosen method for cluster size quantification is a new variant on the established technique of pair correlation analysis. After calculating the autocorrelation function as previously described (Chapter 2 and (26)), we extract two new values in order to perform statistical analysis: the value at radius 25 nm, and the integral from 25 nm to 200 nm. These two values have the advantage that they do not require fitting the correlation function to any assumed equation, which could lead to error if the correlation function is not well-fit by that equation. The disadvantage is that in both cases, we had to choose a specific radius value (25 nm and 200 nm), but we believe these choices are reasonable. 200 nm was chosen for the integral cutoff because all correlation functions measured in this study reach a value close to 1 by this radius, and so the signal at radius greater than 200 nm is likely to be dominated by noise. 25 nm was chosen as a short length scale that avoids some of the over-counting artifact that would be found at radius 0. In practice, these two values effectively encompassed the features visibly apparent from the correlation functions themselves.

Using this powerful microscopy and analysis framework, we walked through a large part of the known IgE-FcεRI signaling pathway, and asked how components at each stage of the pathway affected the amount of IgE-FcεRI clustering. Our initial, striking result is that an increase in the cellular concentration of Lyn via transient transfection leads to a significant increase in DNP-BSA-mediated IgE-FcεRI clustering. We additionally established that the increase in clustering is specific to the portion of the Lyn protein that is not part of the PM construct (including the catalytic and SH2

domains): Our parallel experiments with PM-EGFP excludes any process specific to overexpression or transfection in general, and our similar results with Y16 and Lyn-mEos exclude any ligand-specific or construct-specific effects.

After obtaining these results with Lyn overexpression, we proceeded down the known IgE-FcεRI signaling pathway in search of the mechanism behind IgE-FcεRI clustering enhancement. Our results with PP2 showed that Lyn kinase activity is required. At the next stage of signaling, our results with MIMODIS showed that Syk kinase activity is required as well. This suggested not simply a local effect mediated by Lyn at the membrane, but a more downstream process that feeds back on IgE-FcεRI clustering.

We saw no effect of Syk overexpression, which was surprising given the result with MIMODIS. To explain this difference, we suggest that endogenous Syk may already be expressed in excess compared to other components in the positive feedback pathway. Then, expressing extra Syk does not increase the feedback on IgE-FcεRI clustering, but suppression of the endogenous Syk activity does suppress the feedback mechanism. Conversely, active Lyn (i.e. Lyn in the open conformation with phosphorylated tyrosine 397, able to phosphorylate FcεRI-β) must be present at a limiting concentration, such that an increase in Lyn concentration leads to an increase in the activity of the entire pathway. When cells overexpress a Lyn construct, the total Lyn concentration is increased, which, assuming equilibrium between active and inactive Lyn, increases the active Lyn concentration as well. Alternatively, the presence of a fluorescent protein at the C-terminus may make it more difficult for the transfected Lyn-EGFP to adopt the closed, inactive conformation, in which case overexpression directly

increases the active Lyn concentration. It is likely that concentration of active Lyn is limiting for FcεRI signaling in general, not just positive feedback. This is consistent with results indicating a small concentration of active Lyn in comparison to concentration of FcεRI (31, 32), although the total concentration of Lyn is comparable.

We showed that downstream of LAT, the positive feedback mechanism acts through PLCγ but not SLP-76. This result was somewhat surprising, given that SLP-76 has been established to couple to the plasma membrane: to cortical actin via its association with Nck and to integrins via ADAP. Our results therefore do not support a model in which actin facilitates FcεRI clustering at this stage. While the result is unexpected, it is reasonable that only one of these two pathways emanating from LAT is involved in positive feedback for IgE-FcεRI clustering. While they both contribute to functional responses as coarsely measured by a degranulation assay, SLP-76 and PLCγ activate different downstream events. Our results suggest that only those events activated by PLCγ are necessary to enhance the IgE-FcεRI clustering we observe.

Open questions remain about how the positive feedback mechanism proceeds downstream from PLCγ. Canonically, store-operated Ca^{2+} entry and degranulation occur downstream of this point, both of which are complex processes with some plasma membrane involvement. It is even possible that the positive feedback acts downstream of degranulation, through an autocrine/paracrine signaling process after cytokine release, though it would remain to be shown how such a stimulus could lead to reorganization of FcεRI. In any case, our findings warrant a search for new mechanisms, downstream of PLCγ in the mast cell signaling system, which can exert feedback back on membrane receptor organization.

To our knowledge, this study is the first in which a positive feedback mechanism is described for IgE-FcεRI clustering. Many feedback processes have been described in more downstream mast cell signaling (33), so it is reasonable that IgE-FcεRI is affected by feedback as well. Our results are consistent with electron microscopy results showing inhibition of clustering by the Lyn inhibitor PP1 (20). We addressed the data on large cluster formation by low-valency cross-linking of FcεRI without IgE (18) by showing that such clusters do form in response to the antibody CD3. For the first time, we were able to observe clustering of an anti-FcεRI antibody at room temperature on a time scale of 15 minutes, rather than at 4°C or a time scale of hours. However, this process is not inhibited by PP2, suggesting a different mechanism for the clustering. The CD3 mechanism is likely less physiologically relevant than our newly described Lyn-dependent mechanism acting on IgE cross-linked with ligand.

Although the concept is novel for FcεRI, positive feedback on clustering is a reasonable mechanism to expect in light of what is known for other signaling systems. Many membrane proteins form clusters (34), many of which do not require physical cross-linking for formation. In particular, the T cell receptor, part of the same superfamily as FcεRI, is activated by a monovalent interaction with a target cell's major histocompatibility complex, and yet forms microclusters (35, 36), and subsequently participate in the larger central supramolecular activation cluster (cSMAC) (37), as a consequence of activation. The formation of the cSMAC is actin-mediated (38), while the mechanism of microcluster formation remains unclear, with lipid- and protein-based models proposed (35). It is possible that the same processes involved at some stage of T cell receptor clustering are also responsible for the enhancement of IgE-FcεRI

clustering that we observed.

In summary, our newly described positive feedback mechanism on IgE-FcεRI clustering provides an important expansion on the current understanding of mast cell signaling. Lyn has a key role in the process, with higher concentrations of Lyn causing higher clustering, while components through PLCγ in the mast cell signaling cascade are required to mediate the process. We have not yet fully identified the cellular machinery responsible for increased clustering, but have shown that it is activated downstream of PLCγ, downstream of Syk, LAT, and other key players in membrane reorganization. Future work is required to determine which downstream components are involved and how they influence membrane receptor reorganization.

4.5 Materials and Methods

Reagents

Anti-DNP IgE was prepared as described in (39). Fluorescent IgE was synthesized by reaction of an N-hydroxy-succidimidyl ester derivative of the dye (Alexa Fluor 647 or Alexa Fluor 488), at room temperature overnight in borate buffered saline solution (200 mM boric acid, 160 mM NaCl, pH adjusted to 8.5 with NaOH), followed by dialysis into storage buffer (phosphate buffered saline (PBS) with 1 mM ethylenediaminetetraacetic acid (EDTA)) at 4 °C for 3 days in the case of AF488 or 7 days in the case of AF647. Successful dye conjugation was confirmed by UV-Vis spectroscopy, and the average dye:protein ratio was measured as 1.3 for AF647-IgE and 7.6 for AF488-IgE.

DNP-BSA was prepared as described in (40).

Pharmacological inhibitors were purchased: PP2 from Tocris Bioscience, MIMODIS from EMD Millipore, U73122 from Sigma-Aldrich.

Lyn-EGFP plasmid is described in (41). Lyn-mRFP was obtained by molecular cloning of the EGFP construct to exchange the fluorescent protein. PM-EGFP plasmid is described in (42). YFP-Syk plasmid (43) was a gift from Tobias Meyer (Stanford University). LAT-mEos 3.2 plasmid was obtained of molecular cloning of the Lyn-mEos 3.2 construct described in (44), exchanging the Lyn sequence for a LAT sequence. dsRed-GBF plasmid (30) was a gift from Martha Jordan (University of Pennsylvania) and Gary Koretzky (Weill Cornell Medical College).

CD3 anti-FcεRI IgG antibody (15) was a gift from Reuben Siriganian (NIH), and was conjugated to Alexa Fluor 647 or Alexa Fluor 488 by the same procedure as for IgE. The dye:protein ratio was 0.7 for AF647-CD3 and 1.1 for AF488-CD3.

Y16bi, a bivalent ligand based on a dsDNA scaffold, was prepared as described in Chapter 2.

Cell sample preparation

RBL-2H3 cells were cultured in media consisting of 80% MEM with glutamine and phenol red (Gibco), 20% fetal bovine serum (Atlanta Biologicals) and 50 µg/mL gentamicin. Samples were prepared on 35 mm imaging dishes (MatTek, 14 mm microwell, no. 1.5 coverglass), plasma cleaned for 6 minutes before use. Cells were harvested with trypsin (Gibco), plated at a density of 110,000 cells per dish, and left overnight to adhere and spread.

For all samples but those used in dsRed-GBF experiments (Fig. 4.7), cells were transfected by chemical transfection. Each dish was placed in 1 mL OptiMEM (Gibco). To each dish, transfection solution was added consisting of 2µg plasmid and 6µL Fugene HD chemical transfection reagent (Promega) diluted in 100 µL OptiMEM. After 1 hour incubation at 37 °C, 1 mL 0.1 µg/mL phorbol dibutyrate was added to each dish. After an additional 3 hours, transfection reagents were replaced with regular media, and cells were left at 37 °C for ~ 24 hours for recovery and synthesis of the transfected protein.

For dsRed-GBF, along with all samples in Fig. 4.7, which were prepared in parallel, electroporation was used instead of chemical transfection. A flask containing ~ 30 million cells was resuspended in 2 mL electroporation buffer (137 mM NaCl, 2.7 mM KCl, 1 mM $MgCl_2$, 5.6 mM glucose, 20 mM HEPES, pH 7.4) cooled on ice. For each electroporation, 0.5 mL cells were added to 10 µg plasmid in an electroporation cuvette (BioRad). The 4 mm cuvette was pulsed on a BioRad GenePulser Xcell electroporator at 280 V, 950 µF. Electroporated cells were diluted in 12 mL media, then 1 mL cell solution plus 1 mL media was plated on each imaging dish. Media was changed ~ 3 hours after plating. Cells were used in experiments after ~ 24 hours.

Negative control “Blank” cell samples were prepared by one of two methods. In early experiments (Fig. 4.3, Fig. 4.6a, one of two replicates in Fig. 4.6b), the Blank cells were acquired by finding cells in a Lyn-EGFP, Lyn-mRFP, or YFP-Syk dish that did not visibly express the construct (less than 1/5 of the brightness of cells that we used for the Lyn-overexpressing case). In all other cases, a separate dish was prepared that was subjected to the same transfection conditions as the others, but had no plasmid added.

We prefer the latter method; with the former, there are concerns that the Blank cells might express some lower, undetectable concentration of the construct, or that the presence of overexpressed Lyn in some cells has some effect on the response of other cells in the dish.

We note that in our experience, transient transfection of RBL-2H3 cells by the methods used here results in a somewhat lower degree of overexpression, compared to transfection of other commonly used mammalian cell lines such as COS-7 or NIH 3T3. However, expression of Lyn constructs at these levels was sufficient to give the increase we report in IgE-FcεRI clustering.

Cells were sensitized 40 min at room temperature with 2 μg/mL AF647-IgE diluted in buffered salt solution with BSA (BSS-BSA, 135 mM NaCl, 5 mM KCl, 1 mM $MgCl_2$, 1.8 mM $CaCl_2$, 5.6 mM glucose, 20 mM HEPES pH 7.4, 1 mg/mL BSA). For two-color samples, the solution contained instead a 1:1 mixture of AF647-IgE and AF488-IgE for a final concentration of 2 μg/mL.

Cells were preincubated 5 min at 37 °C in BSS-BSA. For trials that included inhibitors PP2, MIMODIS, or U73122, the inhibitor was included at the desired concentration in the preincubation solution. Following preincubation, the solution was replaced with antigen solution 0.5 μg/mL DNP-BSA in BSS-BSA, plus any applicable inhibitor. For unstimulated samples, DNP-BSA was omitted. Cells were incubated in antigen solution 6 min at 37 °C. Then dishes were rinsed with PBS and fixed with a solution of 4% paraformaldehyde, 0.04% gluteraldehyde. After 10 min incubation at room temperature, the fixation reaction was quenched with blocking buffer (PBS + 10 mg/mL BSA + 0.02% NaN_3). After an additional 10 min incubation, the quench was

replaced with fresh blocking buffer, and the sample was stored at 4 °C until imaged (no more than ~ 2 weeks after preparation).

For trials with U73122, BSA was omitted from the preincubation and antigen solutions, as the free thiol groups on BSA could potentially interfere with U73122.

For experiments with CD3, RBL cells, without IgE sensitization, were stimulated with a 1:1 mixture of AF647-CD3 and AF488-CD3, total concentration of 3 nM, at room temperature for 15 minutes, and then chemically fixed. The time point of 15 minutes was chosen as the earliest time point that gave an acceptably high level of fluorescent label on the cells. For the parallel IgE samples in Fig. 4.5a-c, a custom IgE mixture was used consisting of 25% AF647-IgE, 12.5% AF488-IgE, and the remainder unlabeled IgE, in order to produce a label density that roughly matched the CD3 samples. Fig. 4.5d used an ordinary 1:1 IgE mixture. Parallel IgE samples were sensitized with IgE for 40 minutes at room temperature as in other experiments, then stimulated for 6 minutes at room temperature with buffer or 50 nM Y16bi. The same samples were used for 1-color SIM and 2-color STORM (Fig. 4.5a-c). For SIM, we used only the AF488 channel because it gives higher resolution.

dSTORM imaging

All dSTORM imaging was performed on a home-built system consisting of a Leica DM-IRB inverted fluorescence microscope, laser lines at 488 nm (Coherent), 561 nm (Coherent) and 647 nm (CrystaLaser), mercury arclamp, 1.47 NA 100x TIRF objective (Leica), Optosplit (89 North), and Andor iXon DU-897 EMCCD camera. With this camera and objective, raw images have a pixel size of 145 nm. Image acquisition was performed using home-built MATLAB software.

Samples were put in 1 mL dSTORM imaging buffer consisting of 50 mg/mL glucose, 1 % beta-mercaptoethanol, 0.5 mg/mL glucose oxidase, and 0.04 mg/mL catalase in 0.1 M Tris adjusted to pH ~ 8.0-8.5 . The buffer was exchanged after imaging every two cells.

The mercury arclamp was used to locate cells in the sample expressing the construct of interest. A single two-color TIRF image showing AF647-IgE and the construct's fluorescent protein (EGFP, YFP, mRFP, or dsRed) was saved.

One-color dSTORM was performed on AF647-IgE. The 642 nm excitation laser was used at 100 mW, and 561 nm was used as an activation laser at 100 mW. Both lasers were attenuated with a neutral density filter of 0.44 . Imaging was performed with an exposure time of 10 ms, and a frame rate of 57-85 Hz, the maximum camera speed depending on the size of the region of interest. A total of 10000 raw frames were acquired for each cell imaged.

Two-color dSTORM imaging was performed by a similar method. Before and after imaging each two-color sample, an alignment sample was used consisting of 200 µm TetraSpeck beads (ThermoFisher) adhered to an imaging dish at a density in order to give ~ 10-30 beads per field of view. Two-color TIRF images of 80-100 fields of view in the alignment sample were collected.

The two-color dSTORM was performed simultaneously with both the 488 nm laser (70 mW) and 642 nm laser (100 mW) active with a neutral density filter of 0.44, with the Optosplit projecting the two colors on two halves of the EMCCD. 10000 raw frames were collected at a frame rate of 31 Hz. As both channels were in use for dSTORM, it was not possible to take a TIRF image of mRFP in these experiments.

Image processing and analysis

dSTORM image processing and analysis were performed using home-built Matlab software. To identify candidate localizations, images were first subjected to Gaussian bandpass filtering, which suppressed information on a short length scale of 0.75 px (109 nm) and a long length scale of 10 px (1450 nm), leaving features of size similar to the expected point-spread function. Candidate localizations were taken as local maxima at least 5 standard deviations (7 standard deviations in the case of AF488 channels) above the mean intensity in the filtered image. Localizations were fit in the unfiltered image, with a two-dimensional Gaussian by least squares fitting. Localizations were culled to exclude those abnormal in intensity, radius, or localization error. Correction for stage drift was performed by, each 500 raw frames, computing the spatial offset that maximized the cross-correlation between consecutive blocks of 500 frames. Localizations were binned into pixels of size 25 nm x 25 nm. For image display purposes, a Gaussian blur of 40 nm (large images) or 30 nm (insets) was applied to represent the localization uncertainty.

The two-dimensional autocorrelation function (Chapter 1, Fig. 1.2b) was computed from the unblurred image for a manually defined polygonal region of interest encompassing the entire cell. The calculation was performed using fast Fourier transforms (Chapter 2, equation 1), with the code provided in (26). Cross-correlation functions in two-color imaging were computed by an analogous method (Chapter 2, equation 2).

The two-dimensional correlation function was radially averaged to generate plots shown throughout this study. g(25 nm) was extracted from this radially averaged plot.

The integral was computed by multiplying each g(r) value by a factor of 2πr*25 nm, representing the area of the two-dimensional disc at that radius of width 25 nm (the bin size of the correlation function), from radius 25 to 200 nm.

Statistical tests were performed using the Wilcoxon rank-sum test, using the function *ranksum()* from MATLAB's Statistics Toolbox. We chose this test because it requires no assumptions about the underlying distribution of the data. As our data are not normally distributed (high outliers are more common than low outliers), parametric tests such as a t-test would be misleading.

dSTORM localization precision was evaluated as described in (26), by subtracting the true autocorrelation function from the autocorrelation function of an image in which probes are intentionally overcounted. We found the standard deviation of our super-resolved point-spread function is 20-30 nm (Fig. 4.8).

For each condition tested in this study, at least two biological replicates were prepared and imaged, and all samples were averaged to produce the final graph. Two-color imaging (Fig. 4.3c) had only one replicate. In each biological replicate, typically 6 individual cells were imaged. The total number of cells imaged for each condition is given in Table 4.1. From one run to the next, we observed some variability in the absolute magnitude of autocorrelation functions. Therefore, for each new condition tested in Figures 2 through 4, new Lyn and “Blank” samples were prepared in parallel. Only the Lyn and Blank samples from parallel runs are included in each graph.

Structured Illumination Microscopy

SIM was performed on a Zeiss Elyra super-resolution microscope. Image

Figure 4.8 Quantification of STORM localization precision. The super-resolved point-spread function was calculated as described previously (26). (a) Super-resolved point-spread function for one example cell. Scale is 25 nm per pixel. (b) The radially averaged point-spread function is well fit with a Gaussian, and the standard deviation σ of the Gaussian fit is reported. (c) Histogram of the standard deviation of the point-spread function for many cell images (all 72 cells that are part of Fig. 4.7). We consistently achieve localization precision with σ in the range of 20-30 nm.

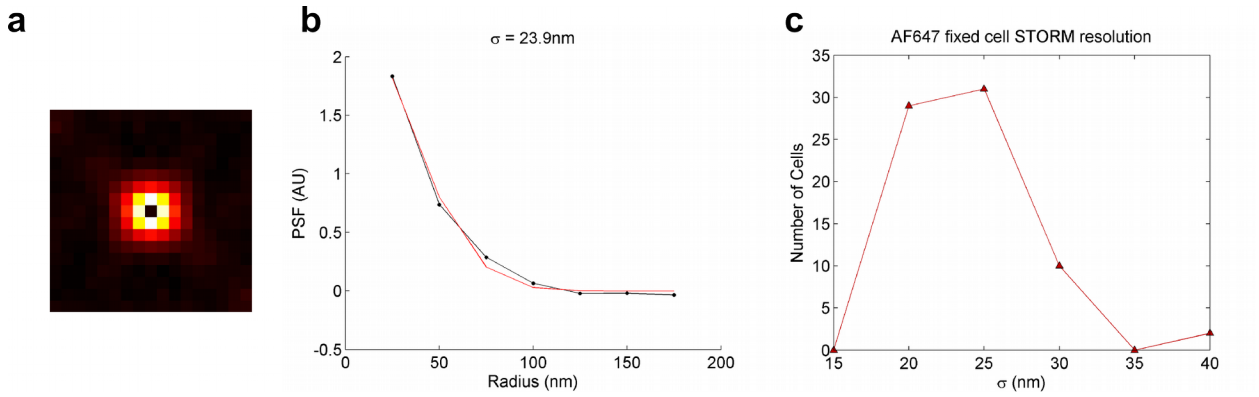
a
b
σ = 23.9nm
PSF (AU)
Radius (nm)
c
AF647 fixed cell STORM resolution
Number of Cells
σ (nm)

acquisition was performed with Zeiss ZEN software, using a 488 nm excitation laser with 5 phases and 5 rotations per SIM image. Processing and rendering were performed using automatic methods in the ZEN software.

Degranulation assays

Degranulation assays were performed as previously described (45). Briefly, β-hexosiminidase released due to degranulation was reacted with methylumbelliferyl-N-acetyl-β-D-glucosaminide substrate to generate a fluorescent signal, read by a 96-well plate reader.

Samples were stimulated 30 minutes at 37 °C with 0.5 μg/mL DNP-BSA in BSS-BSA. For samples subject to an inhibitor, the inhibitor was included as part of the antigen solution. BSA was omitted from the solution for the experiment with U73122.

For the assay involving dsRed-GBF, cells were electroporated with the construct on the day before the assay. FACS was performed on a BD FACSAria Fusion cell sorter. Cells with red fluorescence in the top 18% were collected as positive cells, and those in the bottom 20% were collected as negative cells. The two populations were then plated on the same 96-well plate at the same density, and the assay was completed as normal.

Acknowledgements

David Holowka and Barbara Baird made contributions to this work.

EM, DH, and BB were supported by National Institutes of Health grants R01-AI018306 followed by R01-GM117552. EM was additionally supported by the National Institutes of Health under Ruth L. Kirschstein National Research Service Award

(2T32GM008267) from the National Institute of General Medical Sciences.

Structured illumination microscopy and fluorescence-activated cell sorting were performed in the Cornell University Biotechnology Resource Center. For structured illumination microscopy, we acknowledge NSF funding (1428922) for the shared Zeiss Elyra Microscope.

Felix Chin performed some dSTORM imaging experiments that were included in this study (Fig. 4.3a, and some of Fig. 4.1b). Alice Wagenknecht-Wiesner performed molecular biology work associated with preparation of the DNA constructs used in this study.

We thank Sarah Veatch (University of Michigan) for PALM/STORM analysis software that was adapted for use in this study. We thank Martha Jordan (University of Pennsylvania) and Gary Koretzky (Weill Cornell Medical School) for providing the dsRed-GBF construct, and subsequent helpful discussions regarding its use. We additionally thank Nirmalya Bag for useful discussions.

References

1. Stone, K.D., C. Prussin, and D.D. Metcalfe. 2010. IgE, mast cells, basophils, and eosinophils. J. Allergy Clin. Immunol. 125: S73–S80.

2. Blank, U., and J. Rivera. 2004. The ins and outs of IgE-dependent mast-cell exocytosis. Trends Immunol. 25: 266–273.

3. Gilfillan, A.M., and J. Rivera. 2009. The tyrosine kinase network regulating mast cell activation. Immunol. Rev. 228: 149–169.

4. Ingley, E. 2008. Src family kinases: regulation of their activities, levels and identification of new pathways. Biochim. Biophys. Acta. 1784: 56–65.

5. Siraganian, R.P., R.O. De Castro, E.A. Barbu, and J. Zhang. 2010. Mast cell signaling : The role of protein tyrosine kinase Syk , its activation and screening methods for new pathway participants. FEBS Lett. 584: 4933–4940.

6. Saitoh, S., R. Arudchandran, T.S. Manetz, W. Zhang, C.L. Sommers, P.E. Love, J. Rivera, and L.E. Samelson. 2000. LAT Is Essential for FcεRI-Mediated Mast Cell Activation. Immunity. 12: 525–535.

7. Balagopalan, L., N.P. Coussens, E. Sherman, L.E. Samelson, and C.L. Sommers. 2010. The LAT story: a tale of cooperativity, coordination, and choreography. Cold Spring Harb. Perspect. Biol. 2.

8. Gilfillan, A.M., and C. Tkaczyk. 2006. Integrated signalling pathways for mast-cell activation. Nat. Rev. Immunol. 6: 218–230.

9. Monine, M.I., R.G. Posner, P.B. Savage, J.R. Faeder, and W.S. Hlavacek. 2010. Modeling multivalent ligand-receptor interactions with steric constraints on configurations of cell-surface receptor aggregates. Biophys. J. 98: 48–56.

10. Posner, R., K. Subramanian, B. Goldstein, J.L. Thomas, T. Feder, D. Holowka, and Baird. 1995. Simultaneous Cross-Linking by Two Nontriggering Bivalent Ligands Causes Synergistic Signaling of IgE FcεRI Complexes. J. Immunol. 155: 3601–3609.

11. Paar, J.M., N.T. Harris, D. Holowka, and B. Baird. 2002. Bivalent ligands with rigid double-stranded DNA spacers reveal structural constraints on signaling by FcεRI. J. Immunol. 169: 856–864.

12. Sil, D., J.B. Lee, D. Luo, D. Holowka, and B. Baird. 2007. Trivalent ligands with rigid DNA spacers reveal structural requirements for IgE receptor signaling in RBL mast cells. ACS Chem. Biol. 2: 674–684.

13. Mahajan, A., D. Barua, P. Cutler, D.S. Lidke, F.A. Espinoza, C. Pehlke, R. Grattan, Y. Kawakami, C.-S. Tung, A.R.M. Bradbury, W.S. Hlavacek, and B.S. Wilson. 2014. Optimal Aggregation of FcεRI with a Structurally Defined Trivalent Ligand Overrides Negative Regulation Driven by Phosphatases. ACS Chem. Biol. 9: 1508–1519.

14. Ortega, E., M. Lara, I. Lee, C. Santana, M. Martinez, J.R. Pfeiffer, R.J. Lee, S. Wilson, J.M. Oliver, A.M. Martinez, and B.S. Wilson. 1999. Lyn Dissociation from Phosphorylated FcεRI Subunits: A New Regulatory Step in the FcεRI Signaling Cascade Revealed by Studies of Fc εRI Dimer Signaling Activity. J. Immunol. 162: 176–185.

15. Basciano, L.K., E.H. Berenstein, L. Kmak, and R.P. Siraganian. 1986. Monoclonal antibodies that inhibit IgE binding. J. Biol. Chem. 261: 11823–31.

16. Menon, A.K., D. Holowka, W.W. Webb, and B. Baird. 1986. Clustering, mobility, and triggering activity of small oligomers of immunoglobulin E on rat basophilic leukemia cells. J. Cell Biol. 102: 534–40.

17. Menon, A.K., D. Holowka, and B. Baird. 1984. Small oligomers of immunoglobulin E (IgE) cause large-scale clustering of IgE receptors on the surface of rat basophilic leukemia cells. J. Cell Biol. 98: 577–83.

18. Robertson, D.J. 1990. Association of aggregated receptors for immunoglobulin E with the cytoskeleton of rat basophilic leukemia cells: detergent insolubility and lateral mobility studies. Thesis. .

19. Thomas, J.L., D. Holowka, B. Baird, and W.W. Webb. 1994. Large-Scale Co-aggregation of Fluorescent Lipid Probes with Cell Surface Proteins. J. Cell Biol. 125: 795–802.

20. Veatch, S.L., E.N. Chiang, P. Sengupta, D.A. Holowka, and B.A. Baird. 2012. Quantitative nanoscale analysis of IgE-FcεRI clustering and coupling to early signaling proteins. J. Phys. Chem. B. 116: 6923–6935.

21. Betzig, E., G.H. Patterson, R. Sougrat, O.W. Lindwasser, S. Olenych, J.S. Bonifacino, M.W. Davidson, J. Lippincott-Schwartz, and H.F. Hess. 2006. Imaging intracellular fluorescent proteins at nanometer resolution. Science. 313: 1642–1645.

22. Rust, M.J., M. Bates, and X. Zhuang. 2006. Sub-diffraction-limit imaging by stochastic optical reconstruction microscopy (STORM). Nat. Methods. 3: 793–795.

23. Hess, S.T., T.P.K. Girirajan, and M.D. Mason. 2006. Ultra-high resolution imaging by

fluorescence photoactivation localization microscopy. Biophys. J. 91: 4258–4272.

24. Shelby, S.A., D. Holowka, B. Baird, and S.L. Veatch. 2013. Distinct stages of stimulated FcεRI receptor clustering and immobilization are identified through superresolution imaging. Biophys. J. 105: 2343–54.

25. Heilemann, M., S. van de Linde, M. Schüttpelz, R. Kasper, B. Seefeldt, A. Mukherjee, P. Tinnefeld, and M. Sauer. 2008. Subdiffraction-resolution fluorescence imaging with conventional fluorescent probes. Angew. Chem. Int. Ed. Engl. 47: 6172–6176.

26. Veatch, S.L., B.B. Machta, S.A. Shelby, E.N. Chiang, D.A. Holowka, and B.A. Baird. 2012. Correlation functions quantify super-resolution images and estimate apparent clustering due to over-counting. PLoS One. 7: e31457.

27. Lai, J.Y.Q., P.J. Cox, R. Patel, S. Sadiq, D.J. Aldous, S. Thurairatnam, K. Smith, D. Wheeler, S. Jagpal, S. Parveen, G. Fenton, T.K.P. Harrison, C. McCarthy, and P. Bamborough. 2003. Potent small molecule inhibitors of spleen tyrosine kinase (Syk). Bioorganic Med. Chem. Lett. 13: 3111–3114.

28. Thomson, C.W., W.A. Teft, W. Chen, B.P.-L. Lee, J. Madrenas, and L. Zhang. 2006. FcR Presence in TCR Complex of Double-Negative T Cells Is Critical for Their Regulatory Function. J. Immunol. 177: 2250–2257.

29. Singer, A.L., S.C. Bunnell, A.E. Obstfeld, M.S. Jordan, J.N. Wu, P.S. Myung, L.E. Samelson, and G.A. Koretzky. 2004. Roles of the Proline-rich Domain in SLP-76 Subcellular Localization and T Cell Function. J. Biol. Chem. 279: 15481–15490.

30. Silverman, M.A., J. Shoag, J. Wu, and G.A. Koretzky. 2006. Disruption of SLP-76 Interaction with Gads Inhibits Dynamic Clustering of SLP-76 and FcεRI Signaling in Mast Cells †. Mol. Cell. Biol. 26: 1826–1838.

31. Wofsy, C., C. Torigoe, U.M. Kent, H. Metzger, and B. Goldstein. 1997. Exploiting the difference between intrinsic and extrinsic kinases: implications for regulation of signaling by immunoreceptors. J. Immunol. 159: 5984–5992.

32. Wofsy, C., B.M. Vonakis, H. Metzger, and B. Goldstein. 1999. One lyn molecule is sufficient to initiate phosphorylation of aggregated high-affinity IgE receptors. PNAS. 96: 8615–8620.

33. Chylek, L.A., D.A. Holowka, B.A. Baird, and W.S. Hlavacek. 2014. An Interaction Library for the FcεRI Signaling Network. Front Immunol. 5: 172.

34. Nussinov, R., H. Jang, and C.J. Tsai. 2015. Oligomerization and nanocluster organization render specificity. Biol. Rev. 90: 587–598.

35. Sherman, E., V. Barr, and L.E. Samelson. 2013. Super-resolution characterization of TCR-dependent signaling clusters. Immunol. Rev. 251: 21–35.

36. Yokosuka, T., K. Sakata-Sogawa, W. Kobayashi, M. Hiroshima, A. Hashimoto-Tane, M. Tokunaga, M.L. Dustin, and T. Saito. 2005. Newly generated T cell receptor microclusters initiate and sustain T cell activation by recruitment of Zap70 and SLP-76. Nat. Immunol. 6: 1253–62.

37. Brownlie, R.J., and R. Zamoyska. 2013. T cell receptor signalling networks: branched, diversified and bounded. Nat. Rev. Immunol. 13: 257–269.

38. Burkhardt, J.K., E. Carrizosa, and M.H. Shaffer. 2008. The Actin Cytoskeleton in T Cell Activation. Annu. Rev. Immunol. 26: 233–259.

39. Posner, R.G., B. Lee, D.H. Conrad, D. Holowka, B. Baird, and B. Goldstein. 1992. Aggregation of IgE-receptor complexes on rat basophilic leukemia cells does not change the intrinsic affinity but can alter the kinetics of the ligand-IgE interaction. Biochemistry. 31: 5350–5356.

40. Weetall, M., D. Holowka, and B. Baird. 1993. Heterologous Desensitization of the High Affinity Receptor for IgE (FcεRI) on RBL Cells. J. Immunol. 150: 4072–4083.

41. Hess, S.T., E.D. Sheets, A. Wagenknecht-Wiesner, and A.A. Heikal. 2003. Quantitative analysis of the fluorescence properties of intrinsically fluorescent proteins in living cells. Biophys. J. 85: 2566–2580.

42. Pyenta, P.S., D. Holowka, and B. Baird. 2001. Cross-correlation analysis of inner-leaflet-anchored green fluorescent protein co-redistributed with IgE receptors and outer leaflet lipid raft components. Biophys. J. 80: 2120–32.

43. Wakefield, D.L., D. Holowka, and B. Baird. 2017. The FcεRI Signaling Cascade and Integrin Trafficking Converge at Patterned Ligand Surfaces. Mol. Biol. Cell. (In Press).

44. Shelby, S.A., S.L. Veatch, D.A. Holowka, and B.A. Baird. 2016. Functional nanoscale coupling of Lyn kinase with IgE-FcεRI is restricted by the actin cytoskeleton in early antigen-stimulated signaling. Mol. Biol. Cell. 27: 3645–3658.

45. Naal, R.M.Z.G., J. Tabb, D. Holowka, and B. Baird. 2004. In situ measurement of degranulation as a biosensor based on RBL-2H3 mast cells. Biosens. Bioelectron. 20: 791–796.

CHAPTER FIVE

CONCLUSIONS

5.1 Signal initiation through IgE-FcεRI

The present work contributes to a growing picture suggesting that signal initiation by IgE-FcεRI in mast cells involves an interplay between lipid-mediated and protein-mediated processes. Using molecular-scale experimental and theoretical techniques, we have arrived at several new findings about the initial events in IgE-FcεRI signaling.

In Chapter 2, we related the spatial configuration of IgE-FcεRI in receptor clusters to the signaling capacity of clusters. Structurally defined ligands allowed us to control the spatial organization of the clusters. With PALM/STORM imaging of live and fixed cells, we visualized the resulting configuration of receptors at a resolution that was not possible with previous methods. Using different trivalent ligands made from dsDNA, we formed receptor clusters that varied in the density of receptors and radius of the clusters. We showed that clusters containing a higher density of receptors are more effective in signaling, including at the early stage of Lyn recruitment to clusters.

As part of this microscopy work, we uncovered new technical issues of channel cross-talk in PALM/STORM, which must be considered when working with very weak colocalization signals. By addressing these issues, we were able to detect a small, 20% increase in colocalization between IgE-FcεRI and Lyn, and be sure that this signal was not an artifact of the microscope system.

Even with the capabilities of new biophysical techniques, direct detection of lipid reorganization continues to be challenging. Although lipid reorganization in RBL cells

has been detected by PALM/STORM imaging in the past (1), the same phenomenon was not detectable in the present studies. We detected the immediate consequence of the lipid-mediated signaling – the recruitment of Lyn – but rely on existing data to support our claim that this is a lipid-mediated process. This result reinforces the point that stimulus-mediated lipid reorganization in intact cells is a subtle process, that still remains at the limits of detection of current techniques.

Theoretical modeling allows to evaluate hypotheses about lipid domains despite the limitations of the available experimental data. In Chapter 2, we addressed the dependence of receptor density on intensity of signaling. Previously, this was hypothesized to be due to a transphosphorylation after Lyn binds to FcεRI (2), or in the case of the T cell receptor, due to conformational changes of the receptor (3). We showed that, in addition, it is possible for lipid phase behavior of the plasma membrane to mediate the density dependence. By stabilizing a liquid ordered (Lo)-like domain, the cluster of receptors makes it energetically favorable for a Lo-preferring kinase to enter the cluster, and the magnitude of this effect depends on the density of receptors. We extended this model in Chapter 3 to ask how the lipid contribution to kinase recruitment depends on the phase state of the membrane. We characterized a model that exhibits a rich variety of phase states depending on parameter choices, and drew the phase diagram for several parameter sets. We then compared the implications of different prominent hypotheses for the physical basis of membrane lipid domains. It has been suggested that the membrane might exist as a microemulsion or near a 2D Ising critical phase transition. We found that these two arguments are in fact similar: the states occupy adjacent regions on the phase diagram, and provide similar binding energy for

Lyn entering an IgE-FcεRI cluster. At the same time, we found that the tricritical point provides a much stronger kinase binding energy, apparently the global maximum in this parameter space. This led us to make the novel hypothesis that the membrane might exist near a tricritical point, as this would be the strongest means for the cell to use lipids to control protein localization. However, it is also possible that finely tuned regulation of cell signaling events may favor a lower binding energy. We expect that our result will motivate future experimental studies focused on the possibility of a tricritical point.

Finally, we show that the clustering of membrane proteins is not controlled by the initial interactions among membrane components alone. In Chapter 4, we describe a novel positive feedback pathway that increases IgE-FcεRI clustering after the initial antigen cross-linking events. We show that signaling partners involved in this pathway that lie farther downstream of the initial receptor cross-linking, as far downstream as PLCγ activity. Lyn plays a key, limiting role in this process, such that the overexpression of Lyn alone leads to an increase in IgE-FcεRI clustering. This is, to our knowledge, the most direct evidence to date that IgE-FcεRI clustering at physiological temperatures is not mediated solely by cross-linking by antigen.

Our results here add to the understanding of the complicated role of Lyn in IgE-mediated signaling. Biochemical studies demonstrated both positive and negative roles for Lyn in mast cell signaling (4). Theoretical work (5, 6), and our microscopy results in Chapter 2, suggest a weak interaction between Lyn and FcεRI, with only a small percentage of Lyn involved, while our result in Chapter 4 suggests that the total concentration of Lyn crucially affects its function. One might conjecture that a balance

exists between inactive and active Lyn, which favors inactive Lyn, but allowed us to increase the concentration of active Lyn by increasing the total Lyn concentration. Further studies of Lyn will be necessary to create a more complete model to explain the many disparate activities attributed to this kinase.

In sum, we arrive at a model for the initiation of IgE-FcεRI signaling at the plasma membrane. The system is initiated when a multivalent ligand, with binding sites at a particular spacing, cross-links the IgE-FcεRI. When a sufficient number of receptors amass with a sufficiently small spacing between them, a lipid domain with increased Lo character is stabilized. The nature of this Lo stabilization depends on the phase state of the membrane – it might exist near a critical point, as a microemulsion, in a phase-separated state, or near a tricritical point. We do not know which phase state it is, but note that if it is a tricritical point, the next stage of signaling for this pathway is most effective. Lyn is energetically favored to enter the Lo region surrounding the cluster. This allows Lyn to phosphorylate and bind to FcεRI, activating further downstream signaling events. Following this initial activation, a PLCγ-dependent positive feedback mechanism is activated, which leads to additional IgE-FcεRI clustering and further enhances the response.

5.2 Future directions

PALM/STORM is a powerful technique, but we must recognize its limitations, and consider how to address them with the help other techniques. PALM/STORM has its power in extremely high spatial resolution, at the expense of temporal resolution. In some cases, in particular in two-color PALM/STORM experiments with low cross-

correlation signal, the temporal resolution limited us to observing only chemically fixed cells. The PALM/STORM results in the present study would be well complemented with results from techniques with other strengths, in particular temporal resolution. Several modern techniques have the potential to provide this functionality. Single particle tracking, which we used in Chapter 2 in combination with PALM/STORM (7), could be used in more depth to study live cells with higher time resolution. The new technique of time-resolved cross-correlation (8) is another promising method, which uses novel analysis methods to measure two-color colocalization with high time-resolution in a PALM/STORM-like experiment. Other super-resolution microscopy techniques, in particular structured illumination (9) and lattice light sheet (10) microscopy, are better suited for imaging of live cells in their native environment. Imaging fluorescence correlation spectroscopy (11), a high time resolution, diffraction-limited method in which super-resolution information can be obtained by extrapolation, is currently in use in this lab (12), and is another choice to obtain data complementary to this study. Key conclusions from the experiments in the present study – IgE-FcεRI cluster density controls the level of Lyn recruitment, Lyn recruitment is only a weak, 10-20% increase in concentration, Lyn is a key component of a positive feedback mechanism that enhances IgE clustering – would be strengthened with additional information from one of these better time-resolved methods.

When describing new biological principles, it is always useful to work with a system that is as physiologically relevant as possible. In our studies, we must understand the limitations of the model cell system used. Due to technical constraints, all of our experiments were either performed at room temperature on live cells, or

performed at physiological temperature on cells that were subsequently chemically fixed. The limited time resolution of PALM/STORM makes imaging of live cells challenging, but this is a necessary trade-off in order to obtain quantifiable PALM/STORM images with very high spatial resolution. It would be helpful in future work to study live cells at physiological temperature, especially in the context of lipid organization. We know that lipid phases are highly sensitive to temperature (13), and that chemical fixatives do not immobilize lipid components (although the fixation conditions that we used do immobilize the membrane proteins that we imaged) (14). This makes it especially valuable to work with live cells at physiological temperature when seeking to detect physiologically relevant lipid-mediated phenomena. We also note that, while RBL-2H3 cells are a powerful cell line for the study of mast cell signaling (15), there are limitations to using this cell line (16), and key conclusions should be validated in more physiological cell systems, such as bone marrow-derived mast cells.

Our theoretical results provide suggestions for future experimental work to elucidate the true phase state of the membrane. Our work considered the phase diagram of many possible membrane states, and contrasted how they would affect kinase recruitment to a cluster of receptors. If the membrane exists as a microemulsion, there should exist some characteristic domain size in that microemulsion. It would be a compelling argument for microemulsions to experimentally show that receptors held at a distance larger than the domain size exclude rather than recruit kinase, as predicted by our model.

It is also worth addressing the possibility of a tricritical point, given our discovery that this would lead to much stronger kinase recruitment than other phase states. Likely

the most convincing way to show this would be to show that the critical exponents associated with physical properties of the membrane (e.g. correlation length), as the transition temperature is approached, are consistent with the tricritical Ising model. Previous work found that, on long length scales, exponents are consistent with an Ising critical point (13). We note that from renormalization group theory, a system near a tricritical point, when coarse grained, begins to look like a regular Ising critical point (17). In practice, this means that a super-resolution technique might be able to detect tricritical exponents, even though coarser diffraction-limited methods detect Ising critical exponents.

With current technology, designing such experiments is nontrivial, as it remains challenging to extract quantitative data on lipid-mediated processes in cells. Still, we expect that the continued innovation in the microscopy community will soon provide tools to address these important questions about cell membrane structure.

References

1. Shelby, S.A., S.L. Veatch, D.A. Holowka, and B.A. Baird. 2016. Functional nanoscale coupling of Lyn kinase with IgE-FcεRI is restricted by the actin cytoskeleton in early antigen-stimulated signaling. Mol. Biol. Cell. 27: 3645–3658.

2. Sil, D., J.B. Lee, D. Luo, D. Holowka, and B. Baird. 2007. Trivalent ligands with rigid DNA spacers reveal structural requirements for IgE receptor signaling in RBL mast cells. ACS Chem. Biol. 2: 674–684.

3. Pageon, S. V, T. Tabarin, Y. Yamamoto, P.R. Nicovich, J.S. Bridgeman, A. Cohnen, C. Benzing, Y. Gao, D. Michael, K. Tungatt, G. Dolton, A.K. Sewell, D.A. Price, O. Acuto, R.G. Parton, J.J. Gooding, J. Rossy, J. Rossjohn, and K. Gaus. 2016. Functional role of T-cell receptor nanoclusters in signal initiation and antigen discrimination. PNAS. 113: E6905–E6905.

4. Gilfillan, A.M., and J. Rivera. 2009. The tyrosine kinase network regulating mast cell activation. Immunol. Rev. 228: 149–169.

5. Wofsy, C., C. Torigoe, U.M. Kent, H. Metzger, and B. Goldstein. 1997. Exploiting the difference between intrinsic and extrinsic kinases: implications for regulation of signaling by immunoreceptors. J. Immunol. 159: 5984–5992.

6. Wofsy, C., B.M. Vonakis, H. Metzger, and B. Goldstein. 1999. One lyn molecule is sufficient to initiate phosphorylation of aggregated high-affinity IgE receptors. PNAS. 96: 8615–8620.

7. Manley, S., J.M. Gillette, G.H. Patterson, H. Shroff, H.F. Hess, E. Betzig, and J. Lippincott-Schwartz. 2008. High-density mapping of single-molecule trajectories with photoactivated localization microscopy. Nat. Methods. 5: 155–157.

8. Stone, M.B., and S.L. Veatch. 2015. Steady-state cross-correlations for live two-colour super-resolution localization data sets. Nat. Commun. 6: 7347.

9. Gustafsson, M.G.L. 2000. Surpassing the lateral resolution limit by a factor of two using structured illumination microscopy. J. Microsc. 198: 82–87.

10. Chen, B.-C., W.R. Legant, K. Wang, L. Shao, D.E. Milkie, M.W. Davidson, C. Janetopoulos, X.S. Wu, J.A. Hammer, Z. Liu, B.P. English, Y. Mimori-Kiyosue, D.P. Romero, A.T. Ritter, J. Lippincott-Schwartz, L. Fritz-Laylin, R.D. Mullins, D.M. Mitchell, J.N. Bembenek, A.-C. Reymann, R. Bohme, S.W. Grill, J.T. Wang, G. Seydoux, U.S. Tulu, D.P. Kiehart, and E. Betzig. 2014. Lattice light-sheet microscopy: Imaging molecules to embryos at high spatiotemporal resolution. Science. 346: 1257998.

11. Kannan, B., L. Guo, T. Sudhaharan, S. Ahmed, I. Maruyama, and T. Wohland. 2007. Spatially Resolved Total Internal Reflection Fluorescence Correlation Microscopy Using an Electron Multiplying Charge-Coupled Device Camera. Anal. Chem. 79: 5013–5020.

12. Bag, N., D. Holowka, and B. Baird. 2017. Plasma Membrane Diffusion Modes of FcεRI Receptor for Immunoglobin E Measured with Imaging Fluorescence Correlation Spectroscopy. Biophys. J. 112: 28a.

13. Veatch, S.L., P. Cicuta, P. Sengupta, A. Honerkamp-Smith, D. Holowka, and B. Baird. 2008. Critical fluctuations in plasma membrane vesicles. ACS Chem. Biol. 3: 287–293.

14. Tanaka, K.A.K., K.G.N. Suzuki, Y.M. Shirai, S.T. Shibutani, M.S.H. Miyahara, H. Tsuboi, M. Yahara, A. Yoshimura, S. Mayor, T.K. Fujiwara, and A. Kusumi. 2010. Membrane molecules mobile even after chemical fixation. Nat. Methods. 7: 865–866.

15. Passante, E., and N. Frankish. 2009. The RBL-2H3 cell line: Its provenance and suitability as a model for the mast cell. Inflamm. Res. 58: 737–745.

16. Passante, E., C. Ehrhardt, H. Sheridan, and N. Frankish. 2009. RBL-2H3 cells are an imprecise model for mast cell mediator release. Inflamm. Res. 58: 611–618.

17. Cardy, J. 1996. Scaling and Renormalization in Statistical Physics. New York, New York, USA: Cambridge University Press.